

TECHNISCHE UNIVERSITÄT MÜNCHEN  
MAX-PLANCK-INSTITUT FÜR ASTROPHYSIK

# The Formation of Nebular Spectra in Core-Collapse Supernovae

Jakob Immanuel Maurer

Vollständiger Abdruck der von der Fakultät für Physik der Technischen Universität München zur Erlangung des akademischen Grades eines

*Doktors der Naturwissenschaften*

genehmigten Dissertation.

Vorsitzender: Univ.-Prof. Dr. St. Paul

Prüfer der Dissertation:

1. Hon.-Prof. Dr. W. Hillebrandt
2. Univ.-Prof. Dr. H. Friedrich

Die Dissertation wurde am 13.10.2010 bei der Technischen Universität München eingereicht und durch die Fakultät für Physik am 26.11.2010 angenommen.



# Contents

<b>1. Supernovae</b>	<b>1</b>
1.1. History of Supernova Astronomy . . . . .	1
1.2. Classification . . . . .	4
1.2.1. Thermonuclear Supernovae . . . . .	5
1.2.2. Core-Collapse SNe . . . . .	8
1.2.3. Pair-Instability SNe . . . . .	11
1.3. Supernovae & Astrophysics . . . . .	11
<b>2. Atomic Physics</b>	<b>15</b>
2.1. Radiative Processes . . . . .	15
2.2. Radiative Data . . . . .	18
2.2.1. Hydrogen . . . . .	18
2.2.2. Oxygen . . . . .	20
2.3. Collisional Processes & Data . . . . .	23
<b>3. The Nebular Phase</b>	<b>27</b>
3.1. Nebular Physics . . . . .	27
3.2. The One-Dimensional Nebular Code . . . . .	28
3.3. The Three-Dimensional Nebular Code . . . . .	30
3.3.1. Three-dimensional heat transport . . . . .	30
3.3.2. Three-dimensional line profiles . . . . .	31
3.3.3. The new ionisation treatment . . . . .	33
<b>4. Characteristic Velocities Of Stripped-Envelope Core-Collapse Supernovae</b>	<b>37</b>
4.1. Data Set . . . . .	38
4.2. Spectral Modelling . . . . .	40
4.3. Discussion . . . . .	45
4.3.1. Tests . . . . .	45
4.3.2. Discussion of the Method . . . . .	45
4.4. Results . . . . .	49
4.5. Summary . . . . .	53
<b>5. Oxygen Recombination in Stripped-Envelope Core-Collapse Supernovae</b>	<b>55</b>
5.1. Oxygen lines in the nebular phase of CC-SNe . . . . .	55
5.1.1. Effective recombination rates for neutral oxygen . . . . .	55
5.1.2. Recombination line formation . . . . .	59
5.1.3. Excitation of the O I 7774 Å line . . . . .	61
5.1.4. Test Model . . . . .	63
5.1.5. Emission versus absorption line shapes . . . . .	65
5.2. A shell model of SN 2002ap . . . . .	66
5.3. A 2D model of SN 1998bw . . . . .	67
5.4. Discussion . . . . .	70
5.5. Summary . . . . .	74

<b>6. Hydrogen and Helium In Stripped-Envelope Core-Collapse Supernovae</b>	<b>77</b>
6.1. H and He in the nebular phase	78
6.1.1. Hydrogen	78
6.1.2. Helium	79
6.1.3. Mixed H/He layers	79
6.2. SN 2008ax	83
6.3. Other SNe of Type IIb	88
6.3.1. SN 1993J	89
6.3.2. SNe 2001ig & 2003bg	89
6.3.3. SNe 2007Y	90
6.4. An alternative to shock interaction	91
6.5. Discussion	95
6.5.1. Late $H\alpha$ emission	95
6.5.2. Nebular line profiles of SNe IIb	96
6.5.3. SN 2008ax	96
6.6. Summary	97
<b>7. Supernova 1987A</b>	<b>99</b>
7.1. Nebular Modelling of SN 1987A	100
7.2. Summary	104
<b>8. Conclusions</b>	<b>105</b>
<b>Bibliography</b>	<b>109</b>

# 1. Supernovae

## 1.1. History of Supernova Astronomy

The term 'nova' stems from the Latin denomination for 'new star' (stella nova) since to observers of yesteryear novae appeared to be momentary appearances of star-like spots in the night skies. The term 'supernova' was coined much later in the 1930s, to high-light the extraordinary luminosity of those events.

The earliest records of 'new stars' reach back up to three thousand years and essentially hail from the Far East, but also from the Near East and Europe. A clear identification of historical supernovae is often not possible, since confusion with comets and classical novae cannot be excluded. However, some have been identified unambiguously. The best known examples are dated to the years 1006, 1054, 1572 and 1604 A.D.

Supernova 1006 is to this day the brightest (apparent magnitude) supernova recorded. Contemporary witnesses compared its luminance with that of the moon in the first quarter. Scores of reports from all over the world are available. Thanks to these records supernova 1006 can be linked to the remnant PKS 1459-41 (e.g. [Clark & Stephenson 1977](#)).

Only 48 years later supernova 1054 was observed. Its luminance was comparable to that of Venus at maximum light. Thanks to numerous reports mainly from Asia and the Near East, today supernova 1054 can be associated with the Crab Nebula ([Mayall & Oort 1942](#), [Clark & Stephenson 1977](#)), discovered by John Bevis in 1731. The Crab Nebula has played an important role for the development of modern astronomy. It is the strongest persistent source of  $\gamma$ -rays in the sky and has provided astronomers with observations of various radiation phenomena, which were hardly observed before, like synchrotron radiation and pulsar emission. The centre of the Crab Nebula hosts the Crab Pulsar, which was among the first neutrons stars discovered in the 1960s and has been studied intensively since then.

Supernova 1572 occurred near the constellation Cassiopeia and was comparable in brilliance to supernova 1054. In contrast to the Far and the Near East, astronomy in Europe had undergone a rapid development during the Renaissance in the 15th and 16th century. Particularly thanks to the work of the Danish astronomer Tycho Brahe there is more information about supernova 1572 than for any other recorded before. An amelioration of the Sextant allowed him to determine the position of this supernova relative to other stars accurately. For that reason its remnant (3C10) can be unambiguously identified with the supernova ([Argelander 1864](#), [Hanbury Brown & Hazard 1952](#)). Furthermore it was possible to reconstruct the light curve of supernova 1572 ([Baade 1945](#)), since detailed comparisons between the apparent luminosity of the supernova and other planets and stars over a period of one year exist. Supernova 1572 is a 'normal' Type Ia (see below), as it was found from its light echos ([Rest et al. 2008](#), [Krause et al. 2008](#)).

In 1604, just 32 years later, another bright supernova appeared at the firmament. Detailed reports from Fabricius, Kepler and other European astronomers, but also from Korea allow to reconstruct the light curve of supernova 1604 ([Baade 1943](#)) and to identify its remnant ([Schlier 1935](#), [Baade 1943](#)). Kepler's Supernova was the last galactic one observed to this day. Although the galactic remnants Cas A and G1.9+03 suggest that some light from Milky Way supernovae might have reached earth in the last centuries, none of those had been recorded.

Beginning with the 17th century, the invention of the telescope heralded a new era of astronomy. Thanks to steadily improving instrumentation a rising number of 'new stars' has been observed since then. As it became possible to determine the distance of novae at the beginning of the 20th century (e.g. [Lundmark 1919](#)) it was realised that they can be separated into two groups differing in absolute brightness. The brighter class, which exceeds other novae by several orders in magnitude was termed supernova ([Baade & Zwicky 1934b](#)), to emphasise their extraordinary luminosity. This subdivision is relevant since it turned out that novae and supernovae are physically distinct phenomenons. While novae results from the explosion of thin layers of material accreted onto white dwarf surfaces (e.g. [Bode 2010](#)), supernovae mark the death of white dwarfs or more massive stars (e.g. [Hillebrandt & Niemeyer 2000](#), [Janka et al. 2007](#), [Podsiadlowski et al. 2008](#), [Nomoto et al. 2010](#)).

The rapid improvement of observational methods and fundamental physical theories in the 20th century was

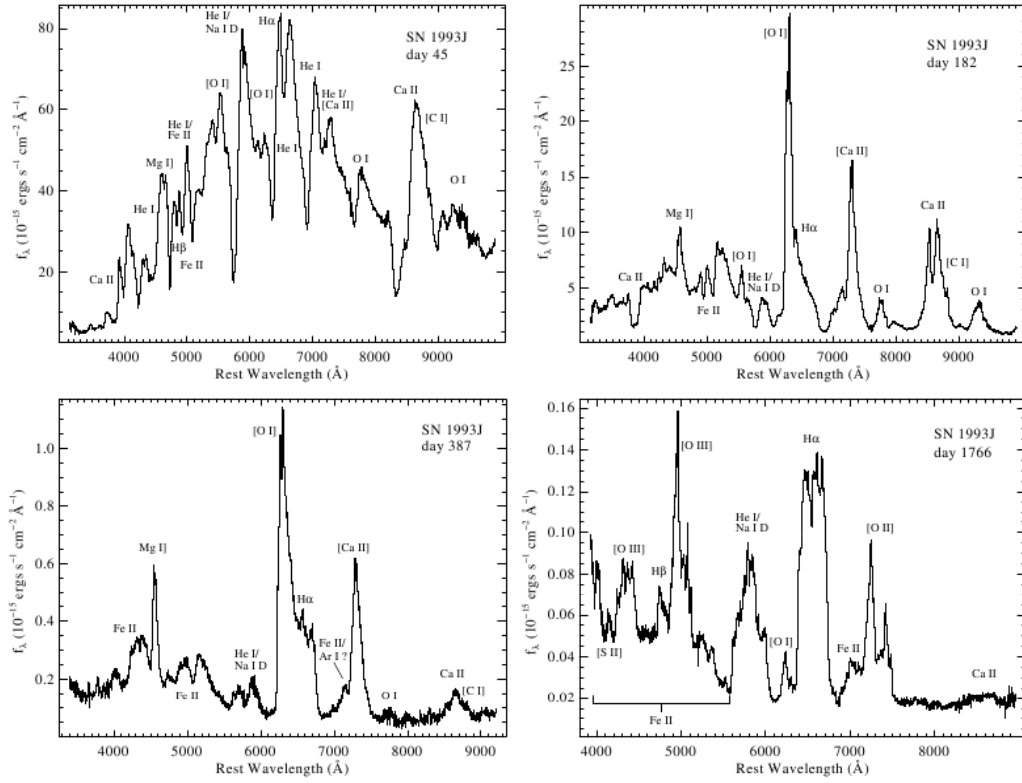


**Figure 1.1.:** Spectra of core-collapse supernova 1993J at 45 (early), 182 (early nebular), 387 (late nebular) and 1766 (remnant) days after explosion taken from [Matheson et al. \(2000\)](#). While the early time spectrum is dominated by absorption, the nebular spectra show strong O [I]  $\lambda\lambda$  6300, 6363 and some H I  $\lambda$  6583 (H $\alpha$ ) emission, which becomes increasingly stronger with time. The remnant phase is dominated by O [III] and H $\alpha$  emission.

accompanied by a growing theoretical understanding of supernovae. Shortly after coining the term supernova, [Baade & Zwicky \(1934a\)](#) proposed the idea that supernovae could be powered by the gravitational energy released by the transition of 'ordinary' to neutron stars. In the following years it was discovered that neutron stars may collapse to even more compact objects (black holes) ([Schwarzschild 1916](#), [Tolman 1934](#), [Oppenheimer & Volkoff 1939](#)) and the importance of neutrinos in the context of supernovae was first realised ([Gamow & Schoenberg 1941](#)). Until that time spectral observations showed that there are different classes of supernovae, some showing hydrogen lines (Type II), others not (Type I) ([Minkowski 1940, 1941](#)). The idea that supernovae could be exploded by nuclear burning processes was developed later ([Borst 1950](#), [Burbidge et al. 1956](#), [Baade et al. 1956](#), [Hoyle & Fowler 1960](#), [Colgate & White 1966](#)). Today, it is commonly accepted that different types of supernovae exist and that some are powered by gravitational energy and some by thermonuclear burning. Advanced calculations of silicon nucleosynthesis ([Truran et al. 1967](#), [Bodansky et al. 1968](#)) led to the recognition that the decay chain  $^{56}\text{Ni} \rightarrow ^{56}\text{Co} \rightarrow ^{56}\text{Fe}$  is the radioactive source of supernova light-curves ([Colgate & McKee 1969](#)). Today it is believed that both gravitational and thermonuclear supernovae produce  $^{56}\text{Ni}$ , which is the cause of their outstanding brightness. In the last decades the understanding of supernovae has further improved owing to advances of observational methods, particle and atomic physics, supernova theory and computational facilities. The modern picture of supernovae is discussed in Section 1.2 in more detail.

Although there is consensus about the fundamentals of supernova physics, many details remain unclear to this day. A key role in the progress of astrophysics has always been played by the comparison of theory and observations. In the case of supernova astronomy this also demands an accurate and reliable understanding of the formation of supernova light curves, spectra and other observables such as polarisation, neutrinos or gravitational waves.

In the 19th century the existence of electromagnetic waves was observed in interference experiments (Young

1802), predicted by Maxwell's theory of electromagnetism and confirmed by experiments of Hertz and others. Maxwell's theory describes light by transversal waves, which means that they oscillate in a direction perpendicular to the direction of propagation. The orientation of these oscillations is called polarisation. The conditions generating a radiation field have direct influence on its polarisation state. Therefore, certain physical properties of light sources can be inferred from polarisation measurements. Polarisation measurements of supernova light have been used to detect synchrotron radiation or ejecta asymmetries, for example.

The neutrino was proposed by Pauli in the 1930s to explain the energy spectrum of the  $\beta$ -decay, but was not experimentally detected before 1956. Today, the neutrino plays an important role in the standard model of particles and various other areas of physics. In modern particle physics the neutrino is described as weakly interacting, which means that it is hard to detect but it can escape from high density regions which are obscured for electromagnetic observations. It is predicted that more than 99% of the explosion energy of core-collapse supernovae escapes as neutrinos, which in principle makes them attractive for direct observations of the centre of the explosion. However, since they are hard to detect the only supernova where neutrinos could be verified unambiguously so far is SN 1987A (Bionta et al. 1987, Hirata et al. 1987, Aglietta et al. 1987).

In 1915 Albert Einstein proposed 'general relativity', a theory which predicts the existence of gravitational waves, i.e. a deformation of space-time, which travels detached from its source. Today, general relativity is one of the best tested theories of physics and there is little doubt that gravitational waves exist. However, their detection is difficult. Gravitational waves are expected if the quadrupole (or any higher) moment of a gravitational system is changed. Therefore, compact binaries but also certain deformations of supernova cores during the explosion and the formation of compact objects are expected to generate gravitational waves. Although gravitational waves eluded direct detection to this day, observations of the rotational period of close binary systems consisting of two compact objects (Hulse & Taylor 1974) allowed to confirm their existence indirectly.

Supernova light curves describe the time resolved luminosity of a supernova. A bolometric light curve is obtained by integrating the luminosity at all wavelengths, but also light curves of specific wavelength intervals are common (e.g.  $V$ -,  $B$ -,  $R$ - band). If these wavelength intervals become very small, i.e. there are several bands observed simultaneously one speaks of a spectrum. The characteristics of supernova spectra evolve with the epoch (the time since explosion). Although these transitions are gradual, at least three distinct phases can be identified.

In the 'early' phase, which describes about the first 100 days of a supernova, the inner parts of the ejecta are optically thick at all observable wavelengths. Light emitted from this region is scattered in the outer parts. The resulting spectra resemble a black-body rugged by absorption valleys and emission bumps (see Figure 1.1). The typical shape of these scattering lines is called a P-Cygni profile, which is characteristic for expanding, centrally illuminated atmospheres. Photons emitted in the optical thick centre are line-scattered in the outer regions if they come into resonance with any optical thick line. Since the expansion velocity increases from the inside to the outside, the flux bluewards of the line's rest wavelength is reduced by the absorption. The wavelength of the re-emitted photons in the frame of the observer depends on the relative velocity of the gas and the observer and is centred around the line's rest wavelength in the observer's frame if the scattering region is approximately spherical symmetric. Therefore, the line is observed by a blueshifted absorption valley and a rest wavelength centred emission bump. Early phase observations can primarily be used to study the outer parts of supernovae, since the inner parts are obscured. Beside possible ejecta inhomogeneities and the composition of the outer layers, the total mass and kinetic energy can be best estimated from this phase.

Between 100 and 200 days after explosion supernovae change into the 'nebular' phase. As the supernova ejecta expand with time they become transparent to optical light, the continuum emission ceases and absorption becomes a subordinate process. Instead, strong emission lines, powered by electron collisions and recombination form. The spectra are dominated by blends of numerous weak and scattered strong emission lines (see Figure 1.1). In principle all parts of the supernova can be observed in this phase. However, because of the lower density of the outer regions, a clear interpretation of the data is often restricted to the core of the supernova. Early and nebular phase observations are therefore complementary. While the outer parts can be studied from early time observations more accurately, interesting observables of supernova cores, like asymmetries in the ejecta or the products of the central nucleosynthesis, which link most directly to the explosion mechanism, can be accessed best during this late phase.

The nebular phase is followed by the 'remnant' phase but this transition is subtle. Like in the nebular phase the spectra are dominated by emission lines, but the gas is more ionised and the characteristic emission lines of both phases are different (see Figure 1.1). The gas falls out of ionisation equilibrium and the interaction with the circumstellar medium becomes dominant causing compression, heating and mixing of the gas. Physical processes,

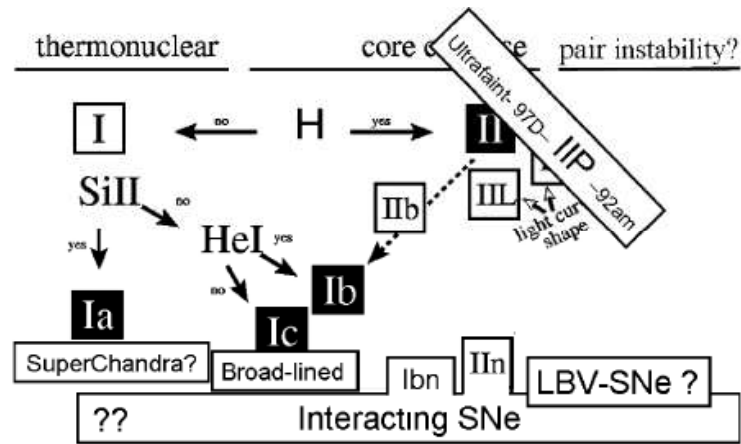


**Figure 1.2.:** Classification scheme of various types of supernovae taken from [Turatto et al. \(2007\)](#).

which elude direct observations, like the formation of magnetic fields, the deceleration and annihilation of positrons or shocks, become important. Since the supernova ejecta are decelerated considerably, it is more difficult to trace back the original structure of the supernova ejecta from remnant phase observations. On the other hand, such observations can be used to obtain information about compact remnants of the supernova (neutron stars, black holes) or to study physical processes like synchrotron radiation. An important example is the Crab Nebula, which has extensively been used as an astrophysical laboratory.

This work is exclusively devoted to the formation of spectra in the nebular phase of supernovae.

## 1.2. Classification

With the possibility of spectral observations it became evident that Supernovae (SNe) can be separated into different groups by their early spectral characteristics. Initially, SNe had been separated into SNe I and II, depending on the presence of hydrogen absorption lines in their early spectra ([Minkowski 1940, 1941](#)). However, later it turned out that the classification scheme had to be refined. Today, supernovae are grouped into Type Ia, Ib, Ic, IIP, IIL and IIn (e.g. [Barbon et al. 1979](#), [Wheeler & Harkness 1986](#), [Branch et al. 1991](#), [Filippenko 1991, 1997](#)). While SNe I show no obvious signs of hydrogen, SNe II do. Among the SNe I, some show strong Si  $\pi$   $\lambda$ 6355 absorption. These are called SNe Ia (see Section 1.2.1). The remaining SNe I are divided into SN Ib and Ic depending on whether there is helium absorption (especially He I  $\lambda$ 5876) or not, respectively. Among the SNe II, SNe showing only weak signs of hydrogen are classified as SNe IIP, while the others are distinguished by their light curves (IIP 'plateau like' and II-L 'linear decreasing' light curves) and the width of their spectral lines (IIn 'narrow' emission lines, almost no absorption lines, slow decline of the light curve) (see Section 1.2.2). SNe Ib, Ic and IIP are often called stripped-envelope core-collapse (SECC) supernovae, since they lost all or most of their hydrogen before explosion.

Although the classification is sometimes not unambiguous (for example it can be difficult to distinguish between SNe Ib and Ic or between SNe Ib and IIP), a connection between physical properties of SNe and their classification can be established (e.g. [Nomoto et al. 1996](#), [Filippenko 1997](#), [Heger et al. 2003](#)). While SNe Ia originate from white dwarf explosions, SNe Ib, Ic and II are associated with the collapse of massive stars. While the progenitor system and the details of the stellar mass loss and evolution decide which type of SN is produced, the details of this chaining are not understood completely.

In addition to the types of supernovae listed here there are others, which are however poorly established, as for example supernovae Ibn (e.g. [Pastorello et al. 2008](#)). An interesting supernova species, which has however no spectral classification yet since these events are rarely observed and since there is still debate about these detections (e.g. [Woosley et al. 2007](#), [Umeda & Nomoto 2008](#), [Blinnikov 2010](#), [Moriya et al. 2010](#)), are pair-instability supernovae (see Section 1.2.3). Pair-instability supernovae have been predicted by theory, but so far the only possible detections are SNe 2006gy (e.g. [Smith et al. 2007](#)) and 2007bi (e.g. [Gal-Yam et al. 2009](#)).



### 1.2.1. Thermonuclear Supernovae

SNe Ia are classified by the absence of obvious hydrogen and by the presence of clear Si II features in their early spectra. While the spectra are dominated by absorption lines of neutral and singly ionised intermediate-mass elements (O, Mg, Si, S, Ca) directly after the explosion, the relative contribution of iron-group elements quickly increases as the photosphere recedes into the core of the SN (e.g. [Filippenko 1997](#)). About two weeks after maximum light the spectra are dominated by Fe II. In the nebular phase the spectra are dominated by blends of dozens of forbidden Fe, but also Co lines.

Although there is growing evidence for diversity among SNe Ia, their physical properties are probably more homogeneous than those of core-collapse supernovae. It was noted by [Branch et al. \(1993\)](#), [Filippenko \(1997\)](#) that about 80% of all SNe Ia belong to the 'normal' type, which is defined by a sample of well observed events. More recent studies suggest that about 60% – 70% of all SNe Ia belong to that 'normal' type (e.g. [Li et al. 2001](#), [Foley et al. 2009](#)), which may however be affected by selection effects.

Supernovae Ia, which are not of 'normal' type by their spectral characteristics can be divided into sub- and super-luminous events. The luminosity of supernovae Ia varies by roughly a factor of ten but only by about a factor of two among 'normal' supernovae Ia.

#### 1.2.1.1. Progenitors and explosion mechanism

It is commonly accepted that supernovae Ia are thermonuclear explosions of white dwarfs (e.g. [Nomoto et al. 2009](#)) but the details are still under debate.

White dwarfs (WDs) can consist of various light and intermediate mass elements (e.g. He, C, O, Ne, Mg) (e.g. [Iben & Tutukov 1985](#)) but the most promising candidates for SNe Ia are 'C + O' WDs (e.g. [Hillebrandt & Niemeyer 2000](#)), since He WDs explode when reaching about  $0.7 M_{\odot}$  (e.g. [Woosley et al. 1986](#)) inconsistent with the observations and O+Ne+Mg WDs tend to collapse to neutron stars instead of exploding in SNe Ia (e.g. [Nomoto & Kondo 1991](#), [Saio & Nomoto 1998](#)).

All WDs have in common that their material is completely ionised and that most of the free electron gas is degenerate to varying degrees (e.g. [Hillebrandt & Niemeyer 2000](#), [Hansen 2004](#)). Because of the quantum mechanical uncertainty principle, the momentum of a particle becomes increasingly indefinite the more localised in space it is. If this quantum mechanical momentum exceeds the thermal momentum or the rest mass energy of the particle it is called degenerate or relativistically degenerate, respectively. Because of this quantum effect degenerate electrons cause a pressure, which can stabilise a white dwarf against gravitational collapse up to a critical mass, known as the Chandrasekhar (CS) limit (e.g. [Chandrasekhar 1931](#)).

Since WDs are inert systems ('C + O' WDs are born with typical masses of  $0.6 M_{\odot}$  [Homeier et al. 1998](#), well below the CS limit), an external mechanism is needed to trigger the explosion. Supernova Ia models can be divided into two classes (e.g. [Hillebrandt & Niemeyer 2000](#)). In single degenerate (SD) scenarios ([Whelan & Iben 1973](#), [Nomoto 1982b](#)) the WD has a stellar companion from which mass is accreted and the WD is heated by compression. Initially the heating process can be compensated by neutrino losses (e.g. [Woosley & Weaver 1986](#)). When the mass of the WD increases towards the CS limit  $M_{CS} \sim 1.4 M_{\odot}$  it contracts significantly. At such high densities the generation of nuclear energy is enhanced by electron-screening (e.g. [Woosley & Weaver 1986](#)). Nuclear carbon burning is triggered, which can become unstable and disrupt the WD (e.g. [Arnett 1969](#)). Explosive burning is preceded by a phase of convective carbon burning and neutrino cooling lasting for about 1000 years (e.g. [Paczynski 1973](#), [Hillebrandt & Niemeyer 2000](#)). Over this period the temperature rises while the convective turnover timescales become increasingly shorter. Finally the conditions for explosive carbon burning are reached at temperatures of  $T \sim 1.5 \times 10^9$  K (e.g. [Hillebrandt & Niemeyer 2000](#)). The ignition of the WD may occur close to its centre, where the density and the temperature are highest, but it could also ignite slightly off-centre because of burning bubbles rising several 100 kilometres from the core (e.g. [Garcia-Senz & Woosley 1995](#), [Niemeyer et al. 1996](#)) before triggering the explosion.

After ignition the nuclear burning front can transverse the star either by deflagration [Nomoto et al. \(1976\)](#) or detonation (e.g. [Arnett 1969](#)). Pure detonation scenarios seem to be inconsistent with the observations. Since detonations cross the WD super-sonically, which means that the unburned material cannot expand before the burning is initiated, too little mass is burned to intermediate mass elements (e.g. [Arnett et al. 1971](#)). Deflagrations on the other hand propagate sub-sonically. In this case the material expands prior to burning enhancing the burning of low density material. Depending on the velocity of the deflagration front different ratios of intermediate and iron-group

elements are produced (e.g. Hillebrandt & Niemeyer 2000). Turbulence could be important for accelerating the propagation of the flame (e.g. Niemeyer & Hillebrandt 1995, Gamezo et al. 2003). Alternatively the deflagration could develop into a detonation at some point of the explosion (e.g. Khokhlov 1991), which may also allow the observed chemical abundances to be produced.

Alternatively to the Chandrasekhar model, a WD could also explode accreting a helium layer, which can detonate and possibly ignite the 'C + O' white dwarf (e.g. Shen et al. 2010). Carbon could be ignited close to the centre as a shock-focused detonation (e.g. Livne & Glasner 1990, Woosley & Weaver 1994, Fink et al. 2007) or off-centre at the core-envelope interface (e.g. Nomoto 1982a, Wiggins et al. 1998).

The second class of explosion scenarios are the double-degenerate (DD) scenarios, i.e. the merger of two WDs (e.g. Iben & Tutukov 1984, Webbink 1984). A close binary can merge losing the orbital energy of its components by gravitational wave emission. Population synthesis calculations have shown that the rate of WD mergers could be comparable to the rate of SNe Ia (e.g. Branch et al. 1995). Double-degenerate scenarios could also explain the absence of hydrogen in the spectra of SNe Ia. However, it is not clear if all such mergers can produce SNe Ia. Simulations show that in systems with a mass ratio different from one the less massive WD is disrupted in the gravitational field of the companion, forming an accretion disc (e.g. Benz et al. 1990). Consequent accretion can trigger carbon burning in the outer layers of the WD (e.g. Saio & Nomoto 2004, Yoon et al. 2007). The WD is converted into O+Ne+Mg which is likely to collapse to a neutron star instead of exploding by a SN Ia (e.g. Saio & Nomoto 1985, Nomoto & Kondo 1991, Saio & Nomoto 1998). However, WD binaries with a mass ratio close to one can probably produce Ia explosions by violently merging their components (Pakmor et al. 2010).

All the different scenarios have their merits. Although there are issues concerning the stability of the accretion process in the SD Chandrasekhar scenario (e.g. Branch et al. 1995, Hillebrandt & Niemeyer 2000), it could account for the observed homogeneity of 'normal' SNe Ia best. On the other hand, the observed range of  $^{56}\text{Ni}$  masses (roughly a factor of ten) can hardly be explained by this scenario alone. Sub-luminous SNe Ia may originate from the SD helium-shell scenario, since the ignition is expected at WD masses much lower than the CS limit. The DD scenario could produce a range of events, since the mass and composition of the involved white dwarfs could vary (e.g. Pakmor et al. 2010). There is observational evidence that SN Ia could originate from two different types of progenitors (e.g. Mannucci 2005, Scannapieco & Bildsten 2005, Brandt et al. 2010), characterised by very different delay times (the time between progenitor star formation and SN Ia explosion).

### 1.2.1.2. SN Ia & Cosmology

In 1929 Hubble (1929) discovered that cosmological objects are increasingly redshifted with their distance to earth, which can be interpreted as a relative motion of distant objects with their velocity  $v$  increasing with their distance  $d$ . Assuming that this relative motion can be observed at any point of the universe one obtains the Hubble Law

$$v = H \cdot d \quad (1.1)$$

which is compatible with an expanding, homogeneous and isotropic universe. The general relativistic description of homogeneous and isotropic space was found by Friedmann and later Lemaitre in the 1920s. Lemaître (1931) proposed the idea that our universe may originate from a single point in an explosion, which was later termed 'big bang'. The expansion process is described by the Friedman equations (e.g. Carroll et al. 1992)

$$\begin{aligned} \left(\frac{\dot{a}}{a}\right)^2 &= \frac{8\pi G}{3}\rho - \frac{kc^2}{a^2} + \frac{\Lambda c^2}{3} \\ \left(\frac{\ddot{a}}{a}\right) &= -\frac{4\pi G}{3}\left(\rho + \frac{3p}{c^2}\right) + \frac{\Lambda c^2}{3} \end{aligned} \quad (1.2)$$

which relate the scale parameter of the universe  $a$  to its density  $\rho$  and pressure  $p$ . Here  $G$  is the gravitational constant,  $c$  the speed of light,  $\Lambda$  the cosmological constant (a term originally introduced by Einstein, which can be interpreted as an intrinsic energy density of the vacuum) and  $k = (-1, 0, 1)$  is a spatial curvature-dependent integer.

The expansion (or contraction) of space is described by the scale parameter  $a$ , which relates to the Hubble parameter  $H$  by (e.g. Carroll et al. 1992)

$$H(t) = \frac{\dot{a}(t)}{a(t)} \quad (1.3)$$

Today, the observed redshift  $z$  of distant objects is interpreted as the stretching of wavelength owing to the cosmological expansion of space, i.e.

$$z = \frac{a_o}{a_e} \quad (1.4)$$

where  $a_o$  and  $a_e$  are the scale factors of space at the time and location of observation and emission, respectively. Therefore, the modern interpretation of the Hubble Law is not a peculiar motion of distant objects but an expansion of general relativistic space-time.

Assuming that our universe is homogeneous and isotropic on large scales (Cosmological Principle) the relation between the luminosity distance  $d_L = \left(\frac{L}{4\pi F}\right)^{1/2}$  ( $L$  is the rest-frame luminosity and  $F$  the apparent flux) and the redshift  $z$  of cosmological objects is given by (e.g. [Carroll et al. 1992](#))

$$d_L = \frac{(1+z)c}{H_0|\Omega_k|^{1/2}} S\left(|\Omega_k|^{1/2} \int_0^z [(1+z')^2(1+z'\Omega_M) - z'(2+z')\Omega_\Lambda]^{-1/2} dz'\right) \quad (1.5)$$

where  $\Omega_k \equiv -\frac{kc^2}{a_0^2 H_0^2}$ ,  $\Omega_M \equiv \frac{8\pi G}{3H_0^2} \rho$  and  $\Omega_\Lambda \equiv \frac{\Lambda c^2}{3H_0^2}$  are the energy density contributions from curvature, matter and cosmological constant adding up to  $\Omega_k + \Omega_M + \Omega_\Lambda = 1$ ,  $H_0$  is the Hubble constant at the present epoch and  $S$  is the function

$$S(x) = \begin{cases} \sin(x) & \Omega_k < 0 \\ x & \Omega_k = 0 \\ \sinh(x) & \Omega_k > 0 \end{cases} \quad (1.6)$$

One can turn this around to determine the energy density of the universe by measuring the relation between  $d_L$  and  $z$ .

The redshift of an object can be determined spectroscopically. For nearby objects it is strongly influenced by peculiar motions caused by the local gravitational potential (e.g. [Dressler & Faber 1990](#)). However, the relative importance of this effect decreases with the cosmological redshift of the observed objects. For a large sample of objects this effect can be treated statistically (e.g. [Riess et al. 1995](#)).

Determining the distance of astronomical objects can be difficult. For the closest objects ( $< 1000$  light years) one can use the parallax method which makes use of the fact that the relative position of extraterrestrial objects changes as a consequence of the earth's motion around the sun (e.g. [Rowan-Robinson 1985](#)). For larger distances so-called standard candles are used. Standard candles are classes of objects with constant luminosity, which allow us to obtain their distance from comparing absolute and apparent magnitudes. Depending on their luminosity the maximum distance, which can be measured by this method is limited by the sensitivity of our observational facilities.

Using the parallax method to calibrate RR Lyrae stars and other standard candles in our neighbourhood, these can be used to calibrate Cepheids and novae out to distances of more than  $10^5$  light years. Cepheids are massive stars that became pulsationally unstable at the end of their lives. Remarkably, there is a tight correlation between their luminosity and their pulsational period (e.g. [Rowan-Robinson 1985](#)). Therefore, Cepheids can be used to measure distances out to about  $10^7$  light years and to calibrate other standard candles like SNe or H II regions (e.g. [Rowan-Robinson 1985](#)). Using increasingly bright objects to extend the calibration of standard candles out to cosmological distances is called the ‘‘cosmological distance ladder’’ ([Rowan-Robinson 1985](#)). This method makes it possible to calibrate the luminosity of SNe Ia although they have never been observed in our own galaxy in the last few centuries.

Although SNe Ia show some dispersion of their luminosities (see above) and therefore are not ‘true’ standard candles, it turned out that they can be standardised, which makes them of great use for determining redshift to distance relations (e.g. [Leibundgut 2000](#)).

In a first step supernovae Ia which can be identified to be of the ‘normal’ type by spectroscopy are selected. This sub-sample still shows a dispersion of about a factor of two in luminosity, still too large for cosmological use. To reduce this uncertainty one can use empirical relations between peak luminosity and the light curve decline rate ([Phillips 1993](#), [Phillips et al. 1999](#)), which allows us to determine the peak luminosity of an observed event more precisely. The ‘‘Phillips’ relation’’ has been refined later (e.g. [Riess et al. 1995](#), [Perlmutter et al. 1997](#)), but the general principle of all standardisation attempts is to relate the luminosity to quantities which can be observed directly and are independent of distance (e.g. spectral characteristics, redshift corrected timescales). Thanks to these relations, SNe Ia are currently the best distance indicators beyond the Virgo cluster (distances larger than about  $10^7$  light years) (e.g. [Leibundgut 2000](#)) and are used out to distances of  $10^{10}$  light years (e.g. [Riess et al. 2007](#)).

Using SNe Ia several groups (e.g. [Riess et al. 1998](#), [Perlmutter et al. 1999](#), [Conley et al. 2006](#), [Riess et al. 2007](#), [Kowalski et al. 2008](#)) derived constraints on cosmological parameters, which seem to be consistent with results obtained from cosmic microwave background (e.g. [Spergel et al. 2003](#), [Dunkley et al. 2009](#), [Komatsu et al. 2009](#)), baryon acoustic oscillations (e.g. [Eisenstein et al. 2005](#)) and gravitational lensing ([Jullo et al. 2010](#)) measurements. Combining different methods is especially powerful (e.g. [Komatsu et al. 2009](#)) since the degeneracy of the cosmological parameters  $\Omega_M$  and  $\Omega_\Lambda$  obtained from SN Ia (luminosity distance) measurements is orthogonal to the one obtained from cosmic microwave background (angular diameter distance, see e.g. [Mukhanov 2005](#), page 60 – 65 for a definition) measurements (e.g. [White 1998](#), [Leibundgut 2001](#)).

Apart from observational errors (e.g. [Leibundgut 2001](#)) the luminosity distance relation observed by SNe Ia could be influenced by an evolution of SN Ia properties with the age of the universe (distance), dust absorption or gravitational lensing effects (e.g. [Leibundgut 2001](#)). For example, [Sullivan et al. \(2010\)](#) find a dependence of SN Ia luminosity on the host galaxy properties, which are in turn expected to evolve with time (e.g. [White & Rees 1978](#)). Improving our understanding of SNe Ia explosions and light curve formation will help to clarify this issue.

## 1.2.2. Core-Collapse SNe

Core-collapse supernovae are classified by the presence of hydrogen (SNe II) or by the simultaneous absence of hydrogen and silicon (SNe Ib/c) features in their early spectra ([Filippenko 1997](#)). SNe Ib/c are thought to result from pre-explosive mass loss causing the absence of hydrogen (SNe Ib/c) and helium (SNe Ic). SNe I Ib, showing helium and weak hydrogen features mark the transition from Type II to Type Ib.

Core-collapse supernovae are much more inhomogeneous than supernovae Ia with respect to their masses, energies and abundances and consequently their light curves and spectra. The light curves of supernovae Ib, Ic and I Ib are dominated by radioactive processes, while the light curves of supernovae II-L and II-P are strongly influenced by energy released from hydrogen recombination. The  $^{56}\text{Ni}$  mass and kinetic energy of core-collapse supernovae can vary by factors of more than 1000 and 100, respectively (e.g. [Mazzali et al. 2005](#), [Maurer et al. 2010](#)).

Core-collapse supernovae are in general iron-group poor (as compared to SNe Ia) and show more variety regarding their relative element abundances. The characteristic core velocities of stripped core-collapse SNe vary between 3000 and 7000 km s<sup>-1</sup> ([Taubenberger et al. 2009](#), [Maurer et al. 2010](#)) and can be even lower for SNe II, which causes a strong variance of the observed nebular line widths. The nebular spectra of stripped core-collapse SNe are dominated by forbidden oxygen emission, those of SNe II-L and II-P by H $\alpha$ .

The oxygen [O I]  $\lambda\lambda$  6300, 6363 Å doublet of stripped-envelope core-collapse supernovae (which is the most prominent nebular line in those events) often deviates from the parabola-like shape, which is expected from spherical symmetric ejecta geometries. Double or even triple peaks can be observed. There are several explanations for this deformation. The most promising one is ejecta geometry ([Mazzali et al. 2005](#), [Maeda et al. 2008](#), [Modjaz et al. 2008](#), [Taubenberger et al. 2009](#), [Maurer et al. 2010](#)), but also the doublet nature of [O I]  $\lambda\lambda$  6300, 6363 Å in supernovae II (e.g. [Li & McCray 1992](#)) and H $\alpha$  absorption in supernovae I Ib ([Maurer et al. 2010](#)).

### 1.2.2.1. Progenitors and explosion mechanism

There is consensus that all supernovae except Type Ia are produced by the death of massive stars ( $> 8 M_\odot$ ) but a physical description of the details of this process is difficult to this day (e.g. [Janka et al. 2007](#), [Nomoto et al. 2010](#)).

At birth, stars mainly consist of hydrogen and helium. After the central hydrogen reservoir of a star has been burned to helium, the core contracts since there is no further nuclear energy release working against gravity. The compression of the core material converts gravitational energy into heat (Virial theorem), which can ignite helium burning (e.g. [Woosley & Janka 2005](#)) if the star is sufficiently massive. The mechanism of compression and subsequent nuclear burning to heavier elements continuous in increasingly dense regions of the core and on increasingly shorter time scales at the end of a stars life (e.g. [Woosley & Janka 2005](#)).

Therefore, at the time of their death massive stars consist of onion-like structures of relics of previous burning phases (hydrogen, helium, carbon, neon, oxygen, silicon) (e.g. [Woosley & Janka 2005](#), [Janka et al. 2007](#)). The burning of nuclear matter becomes less efficient with increasing proton number of the nuclei until the most tightly bound nuclei are reached with  $^{62}\text{Ni}$  and other iron-group elements like  $^{56}\text{Fe}$  (e.g. [Fewell 1995](#)), because of the balance of the electromagnetic and the strong force. Therefore nuclear burning stops when reaching the iron group. Which iron-group elements are preferentially produced depends on the exact burning conditions (density, temperature, proton to neutron ratio) (e.g. [Clifford & Tayler 1965](#)). The details of the final evolution of massive stars depend on their

mass and on their rotation and for very massive stars ( $M > 40 M_{\odot}$ ) also on their metallicity, which influences stellar mass loss (e.g. [Heger et al. 2003](#))

Stars with  $\sim 8 - 10 M_{\odot}$  cannot burn their core material up to the iron-group, since their gravity is too low to produce the required densities and temperatures. Instead, a O+Ne+Mg core forms in the centre of the progenitor (e.g. [Miyaji et al. 1980](#), [Nomoto 1984, 1987](#)), which is stabilised against collapse by electron degeneracy pressure. Nuclear burning in the outer regions increases the mass of the core to  $\sim 1.38 M_{\odot}$ , at which point the collapse of the core is triggered by electron captures on Ne and Mg. During the collapse explosive O burning is ignited, but it is too weak to stop the collapse (e.g. [Nomoto 1984](#)).

Between 10 and 12  $M_{\odot}$  a O+Ne+Mg core is also formed, but gravity is strong enough to allow Ne burning (e.g. [Nomoto & Hashimoto 1986](#), [Nomoto et al. 1988](#)). The core is semi-degenerate and a temperature inversion develops in the centre of the progenitor because of neutrino cooling of the innermost regions ([Nomoto & Hashimoto 1986](#)). Therefore, Ne burning starts in a layer off-centre and propagates inwards triggering O burning. Electron captures in the burning region reduce the degeneracy pressure and the flame propagates by gravitational compression ([Nomoto & Hashimoto 1986](#)) producing silicon and sulphur. Depending on the properties of the progenitor the flame may reach the centre of the progenitor or is quenched by neutrino cooling leaving behind a O+Ne+Mg core surrounded by a massive Si+S shell ([Nomoto & Hashimoto 1986](#)). If the flame can propagate to high enough densities Ne burning becomes so violent that some material could be expelled from the progenitor ([Nomoto & Hashimoto 1986](#)). Otherwise the core contracts until central O burning is ignited producing iron group elements ([Wilson et al. 1986](#)). Since those capture electrons efficiently, the central pressure is further reduced and the core starts to implode. The rest of the O+Ne+Mg core and parts of the Si+S shell are heated by compression and burn explosively when falling through a standing combustion front that develops at a radius of about 100 to 200 km ([Wilson et al. 1986](#)).

Stars between 12 and about 25  $M_{\odot}$  form degenerate iron cores in their centres (e.g. [Wilson et al. 1986](#), [Janka et al. 2007](#), [Umeda & Nomoto 2008](#)) by subsequent burning of low and intermediate-mass elements. Central He burning is followed by convective carbon burning, which greatly reduces the entropy of the central region via neutrino losses. The core contracts. A strong carbon shell burning develops at the edge of the (semi-)degenerate core separating core and envelope by a strong entropy gradient (e.g. [Wilson et al. 1986](#)). Consequent oxygen and silicon burning in the centre converts the core material into iron. Because of its low entropy the iron core is stabilised by degenerate electrons. The nuclear burning continues outside the iron core, increasing the core mass with time. Finally, the iron core collapses when reaching about the CS mass (e.g. [Bethe 1990](#), [Janka et al. 2007](#)).

Accelerated by electron capture and photodisintegration of iron-group nuclei, which lower the electron density and the radiation pressure in the core (e.g. [Wilson et al. 1986](#), [Janka et al. 2007](#)), the core collapses on the free-fall time scale until the densities become high enough to efficiently neutronise the material. Neutronisation causes the release of neutrinos which cannot escape from the core when its density increased to about than  $10^{12} \text{ g cm}^{-3}$  since their diffusion timescale now exceeds the duration of the collapse. The collapse proceeds to densities of  $\sim 10^{14} \text{ g cm}^{-3}$  when all the material has been converted to free neutrons (neutron star) (e.g. [Bethe 1990](#), [Janka et al. 2007](#)). Since this neutron fluid is highly incompressible, the collapse of the core stalls quasi instantaneously at this point, producing a shock wave travelling outwards. This is called core-bounce (e.g. [Janka et al. 2007](#)). Although it had been thought initially that this shock wave may cause the star to explode, it was found in numerical simulations later that it is too weak to unbind stellar material (e.g. [Janka et al. 2007](#)). Numerical calculations often show that the shock stalls and no material is expelled from the progenitor (e.g. [Rampp & Janka 2000](#), [Thompson et al. 2003](#), [Liebendörfer et al. 2005](#), [Buras et al. 2006](#)).

Most of the gravitational energy released by the collapse is emitted in neutrinos, which deposit some small fraction of their energy in the shock region mainly by neutrino captures on free nucleons (e.g. [Bethe & Wilson 1985](#)). The neutrino energy deposition can probably revive the outgoing shock wave, depending on the luminosity and the hardness of the neutrino spectrum (e.g. [Bethe & Wilson 1985](#), [Burrows & Goshy 1993](#), [Janka 2001](#)). Eventually, neutrino energy deposition could lead to the explosion of the progenitor star (e.g. [Marek & Janka 2009](#)). Neutrino heating could be enhanced by the so-called standing accretion shock instability (SASI; [Blondin et al. 2003](#)), which may cause a bi-polar oscillation of the shock front. Instabilities (e.g. magnetic buoyancy instabilities [Wilson et al. 2005](#)) and convection (e.g. [Burrows 1987](#), [Keil et al. 1996](#)) in the newly born neutron star, which could increase the neutrino luminosity in the central region or oscillations of the neutron star driving acoustic waves into the envelope (e.g. [Burrows et al. 2006](#)) could also be important for supporting the explosion. Recent studies indicate that the energy deposited by neutrinos increases with the dimension of the simulation, i.e. that the explosions become strongest when treated three-dimensionally ([Nordhaus et al. 2010](#)). Since currently all the simulations treating neutrino transport in detail are done in one or two dimensions, further development is necessary to reach final

conclusions.

Stars in a range between  $\sim 25$  and  $90 M_{\odot}$  also form iron cores (e.g. [Nomoto et al. 2010](#)), but those can become more massive than the CS limit (e.g. [Wilson et al. 1986](#)). Since the production of oxygen relative to carbon is efficient in these cores (e.g. [Wilson et al. 1986](#)), the carbon fraction is too low for convective carbon burning to develop, which would cool the core. The cores sustain high entropy and are supported by thermal pressure during oxygen and subsequent silicon burning (e.g. [Wilson et al. 1986](#)). The iron core can become much larger than the CS mass (e.g. [Wilson et al. 1986](#)) and the collapse results in a black hole instead of a neutron star either by fall back ( $\sim 25 - 40 M_{\odot}$ ) or by direct collapse ( $> 40 M_{\odot}$ ) (e.g. [Nomoto et al. 2010](#)). Because of the high entropy photodisintegration is more important than electron capture for triggering core collapse (e.g. [Muller 1990](#)).

If the progenitor is rotating rapidly, a Kerr black hole or a rapidly rotating neutron star possibly surrounded by a massive accretion disc may form in the central region. Magnetic fields could also become important. It is possible that the rotational energy of such a system is converted into an outwards directed energy flow (e.g. [Woosley et al. 2003](#)), which could contribute to the explosion energy of the SN (e.g. [Heger et al. 2003](#)). In this regime hypernovae and GRB-SNe could occur, which is however not understood in detail. Even more massive stars ( $> 90 M_{\odot}$ ) can be affected by pulsational mass loss or pair-instability (e.g. [Nomoto et al. 2010](#), also see Section 1.2.3)

Since the explosion energy of core-collapse supernovae is not produced by thermonuclear burning and since significant amounts of the synthesised iron-group elements can disappear in the central compact object, the ejected  $^{56}\text{Ni}$  mass of CC-SNe can vary much more than in SNe Ia (e.g. [Mazzali et al. 2005](#), [Maurer et al. 2010](#), [Moriya et al. 2010](#)).

### 1.2.2.2. SN-GRB connection

Gamma-ray bursts are the most luminous events in the skies, reaching 'isotropic' energies up to almost  $10^{55}$  ergs (e.g. [Amati et al. 2009](#)). Since they are likely collimated (jets) their 'true' energy could be significantly lower. From jet-break measurements the opening angles of long GRBs are estimated to be about  $1 - 10$  degrees (e.g. [Nava et al. 2006](#)). However the jet-break method is not undisputable. Theoretically, a break in the slope of a GRB light curve is expected when the relativistic collimation factor of radiation becomes wider than the opening angle of the jet owing to deceleration. This light-curve break is expected to be mono-chromatic and is called jet-break (e.g. [Rhoads 1998](#)). Unfortunately in many GRBs the jet-breaks are chromatic or are not observed at all (e.g. [Racusin et al. 2008](#), [Curran et al. 2008](#)). Some constraints on the degree of collimation can also be derived from radio observations (e.g. [Soderberg et al. 2010](#)).

GRBs can be observed out to redshifts of at least  $z \sim 8$  ([D'Avanzo & Salvaterra 2010](#)). The duration of GRBs shows a bimodal distribution with a separation at about 2 s, therefore dividing into short and long GRBs ([Kouveliotou et al. 1993](#)). The spectrum of short GRBs is harder than that of long GRBs. This separation has physical relevance, since short and long GRBs most likely originate from different progenitors. While short GRBs are identified with the merger of two compact objects (e.g. two neutron stars), long GRBs are associated with the core-collapse of massive stars (e.g. [Piran 2004](#), [Mészáros 2006](#)). Short GRBs are distributed homogeneously over their host galaxies, indicating that they occur independently of on-going star formation, which is explained best by the compact-object scenario (e.g. [Prochaska et al. 2006](#), [Bloom & Prochaska 2006](#), [Gehrels & the Swift Team 2008](#)). The distributions of long GRBs follows that of star-forming regions and SNe Ic (e.g. [Bloom & Prochaska 2006](#), [Gehrels & the Swift Team 2008](#), [Svensson et al. 2010](#)). In addition at least a few long GRBs can be associated with supernovae of type Ic directly, which suggest that long GRBs and supernovae Ic have similar (and sometimes identical) progenitors (e.g. [Woosley & Bloom 2006](#)).

Although GRBs are most likely collimated events (and therefore a GRB can miss an observer), it can be excluded by statistical arguments and radio observations that all supernovae Ic are accompanied by GRBs. Also long GRBs, which clearly were not accompanied by a supernova (at least not by a supernova of regular luminosity) have been observed. Summarising, some supernovae Ic are accompanied by long GRBs and some long GRBs are accompanied by supernovae Ic, while both can occur without the other (e.g. [Woosley & Bloom 2006](#)). Supernovae Ic accompanied by GRBs are extremely energetic, with extraordinary high ratios of kinetic energy to mass, therefore terming them 'hypernovae'.

The details of GRB formation are poorly understood (e.g. [Lyutikov 2009](#)). Long GRBs are probably powered by the accretion onto black holes, extracting energy from the accretion disc (Blandford-Payne mechanism) or directly from black hole rotation (Blandford-Znajek mechanism). Alternatively they could be powered by magnetar (rapidly spinning, highly magnetised neutron star) spin-down (e.g. [Lyutikov 2009](#)). Many exotic alternatives exist. The

central engine is thought to launch a kinetic or pointing-flux dominated flow in the polar regions of the progenitor (e.g. Piran 2004, Mészáros 2006). The details of this process as well as the propagation through the stellar envelope are highly uncertain. Outside of the star, internal and external shocks could accelerate electrons and produce the observed  $\gamma$ -radiation by synchrotron or Compton radiation. Again, uncountable variations and alternatives of these scenarios exist, but none of those can explain the phenomenon satisfactorily (Lyutikov 2009).

From the perspective of supernova spectra the SN-GRB connection is interesting, since GRBs are expected to leave some imprint of the stellar envelope and consequently on the associated supernovae. GRB-SNe may be strongly deformed and enriched with iron-group elements along their polar axis (where the GRB is expected to penetrate the stellar envelope). This could influence the line profiles (Mazzali et al. 2005, Maeda et al. 2008, Modjaz et al. 2008, Taubenberger et al. 2009, Maurer et al. 2010) and the line width ratios of various intermediate and heavy mass elements (Mazzali et al. 2001).

### 1.2.3. Pair-Instability SNe

While the spectral characteristics of Type Ia and core-collapse supernovae are well known, there is no classification scheme for pair-instability supernovae (PISN) yet. Pair-instability supernovae have been predicted theoretically to be the final explosion of extremely massive stars. Although these events are expected to be very energetic, their large mass may cause moderate ejecta velocities, which means that their spectral lines are not expected to be extremely broad.

So far, there are only two pair-instability supernovae candidates, 2006gy and 2007bi but this identification is not undisputable (e.g. Woosley et al. 2007, Umeda & Nomoto 2008, Blinnikov 2010, Moriya et al. 2010). The nebular spectra of 2006gy and 2007bi show stronger (relative to light elements) iron lines than usually found in core-collapse supernovae and from the light curve and spectra their ejecta masses can be estimated to be extraordinarily high ( $M \sim 50 M_{\odot}$ ). Currently it seems unclear whether these SNe result from the collapse of a massive star or from a pair-production induced explosion.

#### 1.2.3.1. Progenitors and explosion mechanism

The pair-instability mechanism is expected to operate in massive metal-poor stars with initial masses of  $\sim 100 - 300 M_{\odot}$  (e.g. Barkat et al. 1967, Fraley 1967, Ober et al. 1983, Heger & Woosley 2002, Heger et al. 2003). Main sequence stars are stabilised by radiation pressure against gravitational collapse. The more massive the star the higher is its temperature and the more highly energetic photons are produced. Photons interacting with atomic nuclei can create electron-positron pairs if their energies exceed the rest mass energy of two electrons (1.022 MeV). If pair creation is efficient, the radiation pressure is reduced significantly, which leads to the contraction of the star and therefore further increases its temperature and consequently the production of highly energetic photons (Barkat et al. 1967). Consequently, the process can become unstable causing the implosion of the star followed by explosive oxygen burning of the core as a result of compression. In the PISN scenario the whole star is destroyed. The energy released by explosive oxygen burning can be as high as  $10^{52}$  ergs (e.g. Barkat et al. 1967, Ober et al. 1983).

Under certain conditions the energy released by the oxygen burning is not sufficient to disrupt the whole star, but can stop the collapse (e.g. Ober et al. 1983). In this case only a fraction of the star is expelled forming a thick shell of material around the stellar core. The remnant star may undergo further pulsational mass loss and finally end in a core-collapse supernova (e.g. Ober et al. 1983, Heger & Woosley 2005). These 'pulsational' supernovae therefore are hybrids of both types of explosion scenarios.

In even more massive stars ( $\sim 10^3 - 10^4 M_{\odot}$ ), the thermonuclear explosion of the core cannot stop the collapse and a black hole is formed, without supernova explosion (e.g. Wheeler 1977, Heger et al. 2003). It depends on mass and metallicity of the star whether it ends as a supernova and whether the progenitor explodes because of core-collapse or pair-instability.

## 1.3. Supernovae & Astrophysics

Beside their importance for cosmology, their general role as astrophysical laboratories for all kind of experiments and their connection to GRBs (see Sections 1.2.1.2 and 1.2.2.2), supernovae also influence various areas of astrophysics directly. Supernovae interact with their environment by emitting all kinds of highly energetic radiation like

$\gamma$ -rays, neutrinos and positrons and heat and enrich their surroundings with intermediate-mass and heavy elements, which can influence star (e.g. Larson 1985, Vanhala & Cameron 1998, Loewenstein 2006, Bate 2009) and galactic disc (e.g. Abadi et al. 2003, Robertson et al. 2004, Scannapieco et al. 2007) formation.

One of the predictions of 'big bang' theory is the absence of heavy elements in the early universe (e.g. Iocco et al. 2009). After space-time has expanded and the temperatures became low enough to allow the formation of deuterium, two-body reactions can form isotopes of hydrogen and helium and traces of heavier elements (Alpher et al. 1948, Peebles 1966, Schramm & Turner 1998, Burles et al. 2001, Iocco et al. 2009). Nuclei consisting of five nucleons are unstable because of the fifth nucleon's angular momentum, which has to be larger than zero (Pauli exclusion principle). For similar reasons  ${}^8\text{Be}$  is unstable (e.g. Fowler 1984). Since under the conditions of 'big-bang' nucleosynthesis (density, temperature, duration) three- (or more) body collisions do not become efficient almost no elements heavier than helium are synthesised (e.g. Iocco et al. 2009).

The most abundant elements in (the observed part of) our universe are H, He, O and C followed by intermediate mass (Mg – Ca) and the iron-group elements. Most of these elements have likely been formed in stars and (super)nova explosions (e.g. Burbidge et al. 1957, Fowler 1984, Wallerstein et al. 1997). In stars hydrogen is fused to helium by  $pp$ -reactions or the (H)CNO-cycle, depending on the star's temperature (e.g. Wallerstein et al. 1997). From helium carbon can be produced by the triple- $\alpha$  reaction, which is possible because of the long lifetime of stars. Once carbon has formed all the other (heavier) elements can be formed by proton, neutron and  $\alpha$ -captures or neutron- and  $\alpha$ -photodisintegration (Burbidge et al. 1957, Wallace & Woosley 1981, Wallerstein et al. 1997). These processes allow the formation of isotopes as heavy as  ${}^{209}\text{Bi}$ , which is the heaviest stable element (e.g. Burbidge et al. 1957). Even heavier nuclei like  ${}^{235,238}\text{U}$ , which are unstable, but play an important role in our modern world, can be produced (e.g. Burbidge et al. 1957, Fowler 1984, Wallerstein et al. 1997). Finally, the explosion of supernovae leads to further burning and to the ejection of large fractions of the stellar mass. The ejected heavy elements can mix with hydrogen and helium clouds and can form a new generation of stars more metal rich than their parent population at birth (e.g. Truran & Cameron 1971, Tominaga et al. 2008, Maio et al. 2010)

About at the same time as the importance of the decay chain  ${}^{56}\text{Ni} \rightarrow {}^{56}\text{Co} \rightarrow {}^{56}\text{Fe}$  in supernovae was realised, making them a potential sources of positrons (Colgate 1970, Burger et al. 1970, Ramaty & Lingenfelter 1979), the diffuse Galactic annihilation radiation at 511 keV (Johnson et al. 1972, Haymes et al. 1975, Leventhal et al. 1978) was discovered by balloon-borne experiments. Radioactive  ${}^{56}\text{Co}$  decays on timescales of 111.37 days by electron capture or positron emission in 81% and 19% respectively (e.g. Milne et al. 1999). Additionally, other radio-actives which decay by positron emission like  ${}^{44}\text{Ti}$  can be produced in supernovae.

Because of the short decay time scale of  ${}^{56}\text{Co}$  most of the positrons are emitted shortly after the explosion and the supernova ejecta are eventually too dense to allow efficient positron escape. The escape fraction depends on the magnetic field of the supernova ejecta sensitively (Chan & Lingenfelter 1993, Milne et al. 1999) which introduces large uncertainties. Modelling late-time light-curves of SNe Ia by positron deposition Milne et al. (1999) estimated an average escape fraction of  $3.5\% \pm 2\%$ . Owing to the larger decay time-scales of the chains  ${}^{44}\text{Ti} \rightarrow {}^{44}\text{Sc} \rightarrow {}^{44}\text{Ca}$  ( $\sim 89$  yr) and  ${}^{26}\text{Al} \rightarrow {}^{26}\text{Mg}$  ( $10^6$  yr) the escape fractions of their positrons are more certain (approximately one), but the abundance of these elements is not constrained well. Independently from these problems the importance of the contribution of supernovae to the galactic 511 keV annihilation line is commonly accepted (Higdon et al. 2009, Lingenfelter et al. 2009).

In addition to positrons, each decay of  ${}^{56}\text{Co}$  leads to the direct emission of  $\sim 3.61$  MeV in  $\gamma$ -rays of energies between 0.26 and 3.6 MeV. The decay of other radio-actives also produces a rich spectrum of  $\gamma$ -rays, which are Compton-scattered in the ejecta during the first few hundred days after the explosion but can escape freely later.

In addition to the emission from nuclear processes, supernovae can contribute to the cosmic spectrum of high energy radiation (Baade & Zwicky 1934a) by their (compact) remnants (e.g. pulsars, black holes, shocks). Today it is believed that shocks from supernovae propagating into the interstellar medium can efficiently accelerate particles by first-order Fermi processes (e.g. Axford et al. 1977, Blandford & Ostriker 1980, Higdon et al. 1998, Lingenfelter et al. 2000, Zatsepin & Sokolskaya 2006).

Because of their influence on the metallicity and the production of energetic particles supernovae have an important influence on the formation of stars and galaxies. Stars predominantly form in regions which have cooled by radiative losses, since the density increases at low temperatures. Energy injection and metal enrichment heat these clouds, which can moderate the star formation rate (e.g. Bate 2009). The heating also allows gas to preserve its angular momentum for a longer period, facilitating the formation of galactic discs, which may not form without this supernova feed-back (e.g. Abadi et al. 2003, Robertson et al. 2004, Scannapieco et al. 2007) and the structure of dwarf galaxies could also be influenced by SNe (e.g. Ferrara & Tolstoy 2000).



Also the properties of stars themselves are changed. It is expected that supernovae influence the initial mass function since the Jeans mass - the typical fragmentation mass - of the star forming cloud increases with its temperature (e.g. [Larson 1985](#), [Bate 2009](#)). Also, supernova shocks can possibly trigger star formation (e.g. [Vanhala & Cameron 1998](#)). Furthermore, the metallicity of a star at birth has strong influence on its evolution, since it alters its nucleosynthesis (e.g. [Burbidge et al. 1957](#)) and mass and angular momentum loss rates (e.g. [Meynet & Maeder 2005](#), [Eldridge & Vink 2006](#)).

The impact of supernovae certainly reaches beyond the points out-lined in this section. There are even speculations that supernovae and GRBs could have influenced the history of life on our planet in the past billions of years (e.g. [Bailer-Jones 2009](#)). All the more it seems important to understand these phenomena in detail.



## 2. Atomic Physics

The Greeks have used the term 'atomos' more than 2500 years ago to describe prime particles. Of course, this idea originated from philosophical belief, but not from scientific reasoning. Our modern understanding of atoms started to develop in the 19th century with the rise of spectroscopy. At the beginning of the 20th century the classical understanding of radiation and matter was challenged by the cognisance of the equivalence of mass and energy on the one side and by the development of quantum mechanics on the other side.

About 100 years after Young had demonstrated the interference of light, Planck and Einstein used the concept of light 'quanta' around 1900 to explain the black-body spectrum and the photo-effect, respectively. And in 1924 de Broglie proposed the wave-like character of matter, which was confirmed by electron interference experiments of Germer & Davisson in 1927.

This new understanding of matter and light finally led to the mathematical formulation of quantum mechanics in the 1920s. One of quantum mechanic's important applications is the mathematical description of atomic physics, which made it possible to treat atomic processes quantitatively.

Today it is commonly accepted that atoms actually can be divided, most trivially in their nuclei and electrons, which were discovered around 1900 by Thompson and others. In 1911 and 1913 the first physical models of atoms had been developed by Rutherford and Bohr respectively, but around 1930 these models were replaced by a quantum mechanical description, which is valid to this day.

### 2.1. Radiative Processes

To explain the photo-effect Einstein introduced the absorption and emission coefficients usually called  $A$  and  $B$  in the literature. The coefficient  $A$  describes spontaneous emission, while the coefficient  $B$  describes absorption and stimulated emission processes. Two atomic states  $n_{1,2}$  connected by radiative processes in a radiation field of energy density  $\rho(\nu)$  are described in equilibrium by

$$n_1 B_{12} \rho(\nu_{21}) = n_2 [A_{21} + B_{21} \rho(\nu_{21})] \quad (2.1)$$

Assuming thermal equilibrium  $\frac{n_1}{n_2} = \frac{g_1}{g_2} \exp(h\nu_{21}/k_B T)$  one can derive the Einstein relations

$$\begin{aligned} g_1 B_{12} &= g_2 B_{21} \\ A_{21} &= \frac{8\pi h \nu^3}{c^3} \left[ \frac{c}{4\pi} \right] B_{21} \end{aligned} \quad (2.2)$$

where  $g_1$  and  $g_2$  are the statistical weights of the corresponding states. The Einstein relations have no reference to the temperature and also hold if the system is not in thermal equilibrium. The relation between  $A$  and  $B$  is sometimes defined by the intensity  $J$  of the radiation field (rather than by its energy density  $\rho$ ), which leads to a definition different by a factor of  $c/4\pi$ .  $A$  and  $B\rho(\nu_{21})$  describe the transition probability per particle per unit time.

These coefficients as well as the energy of a transition can be determined experimentally in principle, which allows to describe the interaction of atoms with arbitrary radiation fields. However, especially transitions rates between highly excited states can hardly be determined in experiments and one has to rely on theoretical calculations.

To understand the principals of atomic calculations it is useful to consider a one-electron system. The Schrödinger Equation of hydrogen describes an electron in the Coulomb potential of a proton. The atomic states of the hydrogen atom can be decomposed into a radial and a spherical part  $\Phi^0(\mathbf{r}) = r^{-1} R_n^l(r) Y_l^m(\theta, \phi)$ . While the spherical part is described by spherical harmonic functions of the quantum numbers  $l$  and  $m$  (corresponding to the  $\theta$  and  $\phi$  coordinates), the radial part can be obtained from solving the radial part of the Schrödinger Equation with an appropriate potential (see Section 2.2.1).

An electromagnetic wave (photon) can be considered as a perturbation to the atomic potential, which can cause the transition from one state to another. To obtain the probability of a photon induced transition between two different

states (Einstein coefficients) one can use time-dependent perturbation theory (e.g. [Atkins 1970](#), [Rybicki & Lightman 1979](#)). It is assumed that there is a solution for the unperturbed system,

$$H^0 \Phi_n^0 = E_n^0 \Phi_n^0 \quad (2.3)$$

where  $H^0$  is its Hamiltonian,  $E_n^0$  are its Eigenvalues (energies) and  $\Phi_n^0$  are its Eigenstates. The state of the perturbed system can be expressed as superposition of unperturbed states

$$\Phi(\mathbf{r}, t) = \sum_n c_n(t) \Phi_n^0(\mathbf{r}, t) = \sum_n c_n(t) e^{-i\omega_n t} \Phi_n^0(\mathbf{r}) \quad (2.4)$$

and the Schrödinger Equation  $i\hbar \frac{\partial}{\partial t} \Phi = H\Phi$  can be written as ([Atkins 1970](#), page 218)

$$i\hbar \sum_n [\dot{c}_n e^{-i\omega_n t} - i\omega_n c_n e^{-i\omega_n t}] \Phi_n^0 = \sum_n c_n(t) e^{-i\omega_n t} [H^0 + H^P(t)] \Phi_n^0 \quad (2.5)$$

where the Hamiltonian of the disturbed system is given by  $H = H^0 + H^P(t)$ . Multiplication with the complex conjugate  $\Phi_k^{0,*} e^{i\omega_k t}$  gives

$$\sum_n c_n(t) e^{i\omega_{kn} t} \Phi_k^{0,*} H^P(t) \Phi_n^0 = i\hbar \sum_n \dot{c}_n e^{i\omega_{kn} t} \Phi_k^{0,*} \Phi_n^0 = i\hbar \dot{c}_k \quad (2.6)$$

with  $\omega_{kn} = \omega_k - \omega_n$  and  $E_n = \omega_n/\hbar$ . By integration one obtains ( $H_{kn}^P \equiv \Phi_k^{0,*} H^P(t) \Phi_n^0$ )

$$c_k(t) - c_k(0) = -\frac{i}{\hbar} \sum_n \int_0^t dt c_n H_{kn}^P e^{i\omega_{kn} t} \quad (2.7)$$

If the perturbed system had been in the state  $\Phi = \Phi_i^0$  at  $t = 0$ , all other coefficients  $n \neq i$  (also the one of the final state  $n = f$ ) had been 0 and therefore

$$c_f(t) = -\frac{i}{\hbar} \int_0^t dt e^{i\omega_{fi} t} H_{fi}^P(t) \quad (2.8)$$

The time-dependent probability to find a system in the state  $f$  is given by  $P_f(t) = |c_f(t)|^2$ . To investigate the interaction of an atomic state with an electromagnetic wave one has to consider a harmonic perturbation

$$H^P(t) = H_0^P (e^{i\omega t} + e^{-i\omega t}) \quad (2.9)$$

and so ([Atkins 1970](#), page 220)

$$\begin{aligned} c_f(t) &= -i \frac{H_{0,fi}^P}{\hbar} \int_0^t dt e^{i\omega_{fi} t} (e^{i\omega t} + e^{-i\omega t}) \\ &= -i \frac{H_{0,fi}^P}{\hbar} \left[ \frac{e^{i(\omega_{fi} + \omega)t} - 1}{i(\omega_{fi} + \omega)} + \frac{e^{i(\omega_{fi} - \omega)t} - 1}{i(\omega_{fi} - \omega)} \right] \end{aligned} \quad (2.10)$$

This expression is dominated by the contributions from  $\omega \sim \omega_{fi}$  and therefore

$$P_f(t) = |c_f|^2 \sim 4H_{0,if}^P H_{0,fi}^P \left[ \frac{\sin^2 \frac{1}{2}(\omega_{fi} - \omega)t}{\hbar^2(\omega_{fi} - \omega)^2} \right] \quad (2.11)$$

Owing to the uncertainty principle the energy of excited (unstable) states is smeared out because of their finite lifetimes and there is a continuum of states with density  $n(\nu)$  (number of states per frequency  $\nu$ ). Averaging over these states

$$P(t) = \frac{4}{\hbar^2} \int d\nu n(\nu) |H_{0,fi}^P|^2 \left[ \frac{\sin^2 \frac{1}{2}(\omega_{fi} - \omega)t}{(\omega_{fi} - \omega)^2} \right] \quad (2.12)$$

and setting  $x = \frac{1}{2}(\omega_{fi} - \omega)t$  and assuming that neither  $|H_{0,fi}^P|^2$  nor  $n(\nu)$  change significantly over the narrow range, which contributes most to the integral ( $\omega \sim \omega_{fi}$ ) one can write

$$\begin{aligned} P(t) &= \frac{t}{\hbar^2 \pi} |H_{0,fi}^P|^2 n(\nu_{fi}) \int_{-\infty}^{\infty} dx x^{-2} \sin^2(x) \\ &= \frac{t}{\hbar^2} |H_{0,fi}^P|^2 n(\nu_{fi}) \end{aligned} \quad (2.13)$$

Setting the state density  $\rho'(\nu) = \frac{n(\nu)}{h}$  one obtains the transition probability per time  $t$  (transition rate; Fermi's Golden Rule)

$$W_{f \leftarrow i} = \frac{2\pi}{\hbar} |H_{0,fi}^P|^2 \rho'(\nu_{fi}) \quad (2.14)$$

In the case of the interaction of an atom with an electromagnetic wave the perturbation is caused by the electromagnetic force of the wave working on the electron. For dipole-allowed transitions the strongest perturbation is caused by the electric dipole moment  $H^P = \hat{\mathbf{d}}\mathbf{F} = e\mathbf{r} \cdot \mathbf{F}$  where  $\mathbf{F} = 2\mathbf{F}_0 \cos(\omega t)$  is the electric field and  $e$  the electric charge. With the energy of the electromagnetic field  $U(\nu) = \epsilon_0 \langle \mathbf{F}^2(t) \rangle_t = \epsilon_0 2\mathbf{F}_0^2$ ,  $\rho(\nu) = h\rho'(\nu)U(\nu)$  and assuming that the radiation is isotropic (i.e.  $d_{x,y,z}^2 = \frac{1}{3}\mathbf{d}^2$ ,  $F_{x,y,z}^2 = \frac{1}{3}\mathbf{F}_0^2$ ) one finally obtains

$$W_{f \leftarrow i} = \frac{1}{6\epsilon_0 \hbar^2} |\mathbf{d}_{if}|^2 \rho(\nu_{fi}) \quad (2.15)$$

which can be used directly to calculate the Einstein coefficients of dipole allowed transitions. For non-degenerate levels ( $g_1 = g_2 = 1$ )  $W_{f \leftarrow i} = B_{fi}\rho(\nu_{fi}) = B_{if}\rho(\nu_{fi})$  and therefore

$$\begin{aligned} B_{fi} = B_{if} &= \frac{1}{6\epsilon_0 \hbar^2} |\mathbf{d}_{if}|^2 \\ A_{if} &= \frac{8\pi^2 \nu^3}{3\epsilon_0 c^3 \hbar} |\mathbf{d}_{if}|^2 \end{aligned} \quad (2.16)$$

From the above considerations one can directly obtain the selection rules of (electric-dipole) allowed transitions

$$\begin{aligned} \Delta s &= 0 \\ \Delta l &= \pm 1 \\ \Delta m &= 0, \pm 1 \end{aligned} \quad (2.17)$$

The spin  $s$  does not appear in the calculation and therefore does not change, i.e.  $\Delta s = 0$ . Since the 'dipole operator'  $\hat{\mathbf{d}}$  of the perturbation  $\langle nlm | \hat{\mathbf{d}} | n'l'm' \rangle = \int \Phi \hat{\mathbf{d}} \Phi' d\mathbf{r} = e \int \Phi \Phi' \mathbf{r} d\mathbf{r}$  corresponds to a linear multiplication (which has odd parity), the perturbation will vanish unless the term  $\Phi \Phi'$  also has odd parity. The angular states are given by spherical harmonic functions of parity  $(-1)^l$ , which means that  $l$  and  $l'$  have to differ by an odd integer to obtain odd parity. An explicit integration does show that this integer has to be  $\Delta l = \pm 1$ . The constraints on  $\Delta m$  depend on the polarisation of the incident photons. The  $m$  component of the spherical harmonic functions can be written as  $\exp(-im\phi)$  and so

$$W_{f \leftarrow i} \propto \left| \int_0^{2\pi} \mathbf{r} e^{-im\phi} e^{im'\phi} d\phi \right|^2 \quad (2.18)$$

for light polarised in  $z$ -direction ( $z = r \cos \theta$ ) one obtains  $\Delta m = 0$ , while for light polarised in  $x$ - or  $y$ - direction ( $x = r \sin \theta \cos \phi = r \sin \theta \frac{1}{2}(e^{+i\phi} + e^{-i\phi})$ ,  $y = r \sin \theta \frac{1}{2i}(e^{+i\phi} - e^{-i\phi})$ ) one obtains  $\Delta m = \pm 1$ . Depolarised light allows  $\Delta m = 0, \pm 1$ , while circular polarised light allows  $\Delta m = \pm 1$  only.

If a transition is electric dipole-forbidden other transitions (most importantly the magnetic dipole and the electric quadrupole) can become important. To calculate these, one has to consider the more general form of electromagnetic perturbations by replacing  $H^P = \hat{\mathbf{d}}\mathbf{F}$  by the operator form  $H^P = \mathbf{A}\hat{\mathbf{p}}$  (classical physics  $\mathbf{E} = \mathbf{A} \cdot \mathbf{p}$ ; electromagnetic vector potential  $\mathbf{A}$  and momentum  $\mathbf{p}$ ) which can be expanded as a series (as long as  $\mathbf{k} \cdot \mathbf{r} \sim \frac{Z\alpha}{2} \ll 1$ )

$$A\hat{p} = A(t)\mathbf{e}^{i\mathbf{k}\cdot\mathbf{r}} i\hbar \nabla = i\hbar A(t)(1 + i\mathbf{k} \cdot \mathbf{r} + \dots) \mathbf{1} \cdot \nabla \quad (2.19)$$

to obtain higher order terms, analogous to the electric-dipole ( $\mathbf{l}$  is a unit vector pointing in the direction of  $\mathbf{A}$ ). Using the commutation relations ( $H^0 = \frac{1}{2m_e}\mathbf{p}^2 + V(\mathbf{r})$ )

$$\begin{aligned}\mathbf{r}\mathbf{p}^2 - \mathbf{p}^2\mathbf{r} &= 2i\hbar\mathbf{p} \\ (\mathbf{r}H^0 - H^0\mathbf{r}) &= i\frac{\hbar}{m_e}\mathbf{p}\end{aligned}\quad (2.20)$$

the dipole approximation is obtained from the lowest order term

$$\begin{aligned}\int \Phi_f^* \mathbf{l} \cdot \mathbf{p} \Phi_i d\mathbf{r} &= -i\frac{m_e}{\hbar} \int \Phi_f^* \mathbf{l} \cdot (\mathbf{r}H^0 - H^0\mathbf{r}) \Phi_i d\mathbf{r} \\ &= -i\frac{m_e}{\hbar} (E_i - E_f) \int \Phi_f^* \mathbf{l} \cdot \mathbf{r} \Phi_i d\mathbf{r}\end{aligned}\quad (2.21)$$

In addition to dipole allowed and other types of single photon transitions, atomic states can also change into another one by multi-photon transitions. This was predicted by Goepfert-Mayer in 1931 and confirmed experimentally thirty years later after the invention of the laser. Photons can excite 'virtual' states from which other photons can excite the electron to 'real' states. However, since the product of small probabilities is involved in this process, the transition rates are extremely small. Therefore, two-photon (2PE) emission is usually not important in the nebular phase of SNe with the exception of He I (e.g. [Li & McCray 1993b](#), [Maurer et al. 2010](#)).

Ionisation and recombination processes can be calculated in a similar way to excited state transitions considering the free electrons as unbound states of the atom. The recombination cross-sections can be obtained from the ionisation cross-sections by the Milne Relation, which can be derived from detailed balance (e.g. [Nahar 2005](#)), similar to the Einstein relations

$$\sigma_{\text{nl}}^R(\epsilon) = \frac{\alpha^2}{4} \frac{g_i}{g_j} \frac{(\epsilon + I)^2}{\epsilon} \sigma_{\text{nl}}^I(\epsilon) \quad (2.22)$$

where  $g_i$  and  $g_j$  are the statistical weights of the initial (not ionised) and recombining (ionised) state. To obtain recombination rates for an ensemble of thermal electrons one has to integrate the energy-dependent recombination cross-sections

$$R_{\text{nl}}(T) = \int_0^\infty v \sigma_{\text{nl}}^R(v) \mathcal{M}(v, T) dv \quad (2.23)$$

over the Maxwell-Boltzman distribution

$$\mathcal{M}(v, T) = 4\pi \left( \frac{m_e}{2\pi k_B T} \right)^{3/2} v^2 \exp - \frac{m_e v^2}{2k_B T} \quad (2.24)$$

where  $v$  and  $T$  are the electron velocity and temperature.

## 2.2. Radiative Data

In Section 5 radiative rates for highly excited levels of oxygen are needed. Although atomic data for the lower levels of neutral oxygen are available in the literature, the atomic levels  $n > 10$  are not. Radiative rates of hydrogen and helium are needed in Section 6. Therefore, in this section the calculation of hydrogen and oxygen atomic data is described. Helium can be treated analogously to oxygen. Hydrogen radiative data can be obtained from analytic solutions available in the literature. Levels of oxygen with angular quantum number  $l > 2$  can be treated in the hydrogenic approximation, while radiative data for  $l \leq 2$  is obtained using an analytic approximation.

### 2.2.1. Hydrogen

The radial coordinate of the hydrogenic electron is described by a radial wave function  $R_{nl}(r)$  (see Section 2.1), from which the probability of finding the electron at a certain radius  $r$  can be calculated. The radial (bound and free) wave functions  $R_{nl}(r)$  and  $F_{kl}(r)$  can be calculated solving the radial Schrödinger equation for an electron in a potential of  $Z$  protons plus centrifugal correction

$$\left[ \frac{d^2}{dr^2} - \frac{l(l+1)}{r^2} + \frac{2Z}{r} + \left\{ \frac{-Z^2/n^2}{k^2} \right\} \right] \begin{Bmatrix} R_{nl}(r) \\ F_{kl}(r) \end{Bmatrix} = 0 \quad (2.25)$$

where  $k^2$  is the energy of the unbound electron in units of  $I_H = 13.6$  eV. For hydrogen the core consists of a single proton and therefore  $Z$  has to be set equal to one.

Once the radial wave functions are known, the radiative rate for a transition between quantum state  $n, l$  and  $n', l'$  can be obtained from Equation 2.16 by spherical integration and is given by (e.g. [Gordon 1929](#), [Green et al. 1957](#))

$$A_{nl'n'} = \frac{8\pi^2\nu^3}{3\epsilon_0 c^3 \hbar} 4\pi\epsilon_0 e^2 a_0^2 \frac{l_{>}}{2l+1} \left| \int_0^\infty R_{n'l'} R_{nl} r dr \right|^2 \quad (2.26)$$

where  $l_{>}$  is the maximum of  $l$  and  $l'$ . There is an analytic solution for the integral (e.g. [Gordon 1929](#)):

$$\begin{aligned} \left| \int_0^\infty R_{n'l'} R_{nl} r dr \right|^2 &= \left\{ \frac{(-1)^{n'-l}}{4(2l-1)!} \sqrt{\frac{(n+l)!(n'+l-1)! (4nn')^{l+1} (n-n')^{n+n'-2l-2}}{(n-l-1)!(n'-l)! (n+n')^{n+n'}}} \right. \\ &\quad \times \left[ {}_2F_1\left(-n+l+1, -n'+l; 2l; -\frac{4nn'}{(n-n')^2}\right) \right. \\ &\quad \left. \left. - \left(\frac{n-n'}{n+n'}\right)^2 {}_2F_1\left(-n+l-1, -n'+l; 2l; -\frac{4nn'}{(n-n')^2}\right) \right] \right\}^2 \end{aligned} \quad (2.27)$$

with  ${}_2F_1$  the hyper-geometric function (see [Gordon \(1929\)](#), [Whittaker & Watson \(1958\)](#), page 293). To obtain recombination rates one has to calculate the ionisation coefficients first. The radiative ionisation cross-sections can be calculated by (e.g. [Burgess 1965](#))

$$\sigma_{nl}^I(k^2) = \left(\frac{4\pi\alpha a_0^2}{3}\right) \frac{n^2}{Z^2} \sum_{l'=\pm 1}^{l_{>}} \frac{l_{>}}{2l+1} (1+n^2\kappa^2) g(n, l; \kappa, l')^2 \quad (2.28)$$

defining  $\kappa = k/Z$  ( $=k$ ;  $Z=1$  for hydrogen), the analytic expression for photo-ionisation cross section is given by

$$\begin{aligned} g(n, l; \kappa, l' = l \pm 1) &= \left( \frac{\pi}{2} \frac{(n+l)!}{(n-l-1)!(1-e^{-2\pi/\kappa})} \prod_{s=0}^{l'} (1+s^2\kappa^2) \right)^{1/2} \left( \frac{4n}{1+n^2\kappa^2} \right)^{l_{>+1}} \\ &\quad \times \frac{\exp[-\frac{2}{\kappa} \arctan(n\kappa)]}{4n^2(2l \pm 1)!} Y_{\pm} \end{aligned} \quad (2.29)$$

with

$$\begin{aligned} Y_+ &= \eta \left( \frac{n-\eta}{n+\eta} \right)^{n-l} \left[ {}_2F_1\left(l+1-n, l-\eta; 2l+2; \frac{-4n\eta}{(n-\eta)^2}\right) \right. \\ &\quad \left. - \left( \frac{n+\eta}{n-\eta} \right)^2 {}_2F_1\left(l+1-n, l+1-\eta; 2l+2; \frac{-4n\eta}{(n-\eta)^2}\right) \right] \\ Y_- &= \left( \frac{n-\eta}{n+\eta} \right)^{n-l-1} \left[ {}_2F_1\left(l-1-n, l-\eta; 2l; \frac{-4n\eta}{(n-\eta)^2}\right) \right. \\ &\quad \left. - \left( \frac{n+\eta}{n-\eta} \right)^2 {}_2F_1\left(l+1-n, l-\eta; 2l; \frac{-4n\eta}{(n-\eta)^2}\right) \right] \end{aligned} \quad (2.30)$$

with  $\eta = i/\kappa$  and the generalised hyper-geometric function  ${}_2F_1(a1, a2; b; z)$  [Whittaker & Watson \(1958\)](#). Equation 2.30 can in principle be computed numerically. However a numerical computation of the generalised hyper-geometric function is difficult for complex arguments, which occur for the free electron wave functions. It is therefore more convenient to calculate the  $g(n, l; \kappa, l' = l \pm 1)$  using a recursion technique ([Burgess 1965](#))

$$\begin{aligned} 2n \sqrt{[n^2 - (l-1)^2][1 + l^2\kappa^2]} g(n, l-2; \kappa, l-1) &= [4n^2 - 4l^2 + l(2l-1)(1+n^2\kappa^2)] \\ &\quad \times g(n, l-1; \kappa, l) - 2n \sqrt{[n^2 - l^2][1 + (l+1)^2\kappa^2]} g(n, l; \kappa, l+1) \end{aligned} \quad (2.31)$$

$$\begin{aligned} 2n \sqrt{[n^2 - l^2][1 + (l-1)^2\kappa^2]} g(n, l-1; \kappa, l-2) &= [4n^2 - 4l^2 + l(2l+1)(1+n^2\kappa^2)] \\ &\quad \times g(n, l; \kappa, l-1) - 2n \sqrt{[n^2 - (l+1)^2][1 + l^2\kappa^2]} g(n, l+1; \kappa, l) \end{aligned}$$

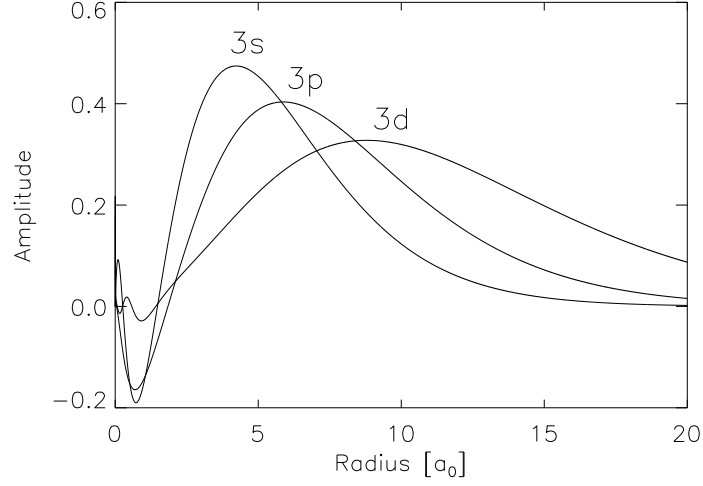


**Figure 2.1:** Radial electron wave-functions of O I 3s, 3p and 3d obtained by the QDM (Maurer & Mazzali 2010). The QDM wave functions are expected to become accurate at  $r \gtrsim 1$ . Unless there is strong term cancellation in the transition integrals, the contribution from  $r < 1$  is weak and the atomic data obtained by the QDM are quite accurate. For most excited states ( $n \gtrsim 4$ ) the transition rates agree to 10% and better with the values obtained from numerical calculations. In the worst case the rates differ by less than 40%.

using starting terms

$$\begin{aligned}
 g(n, n-1; 0, n) &= \sqrt{\frac{\pi}{2(2n-1)!}} 4(4n)^n \exp(-2n) \\
 g(n, n-1; \kappa, n) &= \sqrt{\frac{\prod_{s=1}^n (1+s^2\kappa^2) \exp[2n - 2\kappa^{-1} \arctan(n\kappa)]}{1 - \exp(-2\pi/\kappa) (1+n^2\kappa^2)^{n+2}}} g(n, n-1; 0, n) \\
 g(n, n-2; \kappa, n-1) &= \frac{1}{2} \sqrt{[2n-1][1+n^2\kappa^2]} g(n, n-1; \kappa, n) \\
 g(n, n-1; \kappa, n-2) &= \frac{1}{2n} \sqrt{\frac{1+n^2\kappa^2}{1+(n-1)^2\kappa^2}} g(n, n-1; \kappa, n) \\
 g(n, n-2; \kappa, n-3) &= \frac{4+(n-1)(1+n^2\kappa^2)}{2n} \sqrt{\frac{2n-1}{1+(n-2)^2\kappa^2}} g(n, n-1; \kappa, n-2)
 \end{aligned} \tag{2.32}$$

which constitute a complete set and are therefore sufficient to compute  $g(n, l; \kappa, l' = l \pm 1)$  for any value of  $n, l, \kappa, l'$ .

### 2.2.2. Oxygen

As in classical physics, the description of systems of more than two particles becomes promptly complicated also in quantum mechanics. While analytic solutions are available for a large variety of hydrogenic processes, atoms with more than one electron have to be treated numerically or in approximation.

Although a numerical treatment can give the most accurate results, such a description can become arbitrarily complicated and constitutes its own field of physics. A commonly used numerical method is that developed by Hartree and Fock. It is an ab-initio method, which needs no experimental data by solving the atomic equations iteratively. It can be shown that the energy of an atomic system becomes smaller the better the approximation of its states, which gives the iteration criterion. The atomic states (electrons) contribute to an effective potential, which in turn determines the atomic states. This can be repeated until the solution has converged. Since the method uses an



effective potential, its accuracy has theoretical limitations (Hartree-Fock limit). More recent attempts try to improve the degree of approximation by including electron-electron correlations, but there is no exact solution yet. Typical errors on radiative rates obtained by such numerical calculations are of the order of 5 – 10 %.

A method which is less time demanding in its implementation (but less accurate) is an analytic approximation of the problem, called Quantum Defect Method (QDM) (e.g. [Bates & Damgaard 1949](#), [Seaton 1958](#)). To derive the QDM solution it is assumed that the atom consist of one electron only and an 'effective' core consisting of protons, neutrons and all the other electrons of the atom. Therefore the problem reduces to a two body problem again and one can hope for an analytic solution.

The potential of this 'effective' core converges against its asymptotic form  $r^{-1}$  at large radii and the system can be described in a similar way to hydrogen in this region however with different energy levels owing to the (unknown) structure of the core potential. These energy levels can be determined in experiments and can be used to compensate for the lack of knowledge of the core potential.

The goal of a mathematical description of an atomic system must be the determination of the wave functions of all the atomic states (see [Figure 2.1](#)), since from those the atomic processes can be calculated (see [Section 2.1](#)). In QDM it is assumed that the potential of the atom can be approximated as a Coulomb term plus some additional term which falls to zero at radii larger than  $r_0$ . At large radii the atom can be described by the differential equation (Schrödinger equation) of hydrogen, which can be solved analytically, however with different boundary conditions. Therefore the wave functions of the atom at large radii have the same periodicity, but a different amplitude and phase than the hydrogenic solutions. It has been shown that in the limit  $r \rightarrow \infty$  the new amplitude and phase can be expressed as functions of the quantum defect  $\mu_{nl} = n - \nu_{nl}$  defined as the difference of real and effective main quantum numbers  $n$  and  $\nu_{nl}^2 = \frac{RZ^2}{E_{nl}}$  ( $R$  means the Rydberg constant here). This allows an exact solution of the problem at large and an approximate solution at small radii (the accuracy decreasing with decreasing radius). It cannot be justified from first principles that this approximation is accurate, but comparison with experimental data and numerical calculation indicates reasonable agreement.

At large radii the bound radial wave functions of hydrogen can be expressed by the Whittaker function (e.g. see [Chap. XVI](#), [Whittaker & Watson 1958](#), [Seaton 1958](#), [Burgess & Seaton 1960](#))  $W_{a,b}(c)$ . For effective main quantum numbers  $\nu$  an approximate solution is given by

$$R_{nl}(r) = Z^{1/2} K(\nu, l) W_{\nu, l+1/2}(2Zr/\nu) \quad r \gg 1 \text{ (atomic units)} \quad (2.33)$$

where

$$K(\nu, l) = [\zeta(\nu) \nu^2 \Gamma(\nu + l + 1) \Gamma(\nu - l)]^{-1/2} \quad (2.34)$$

with ( $\epsilon = \nu^{-2}$ )

$$\zeta(\nu) = 1 + \frac{2}{\nu^3} \frac{\partial \mu(\epsilon)}{\partial \epsilon} \quad (2.35)$$

At large radii the Whittaker function has the asymptotic form [Burgess & Seaton \(1960\)](#)

$$W_{\nu, l+1/2}(2Zr/\nu) \sim \left(\frac{2Zr}{\nu}\right)^\nu \exp\left(-\frac{Zr}{\nu}\right) \sum_{t=0}^{t_0} b_t(\nu, l) (Zr)^{-t} \quad (2.36)$$

where  $b_0 = 1$  and

$$b_t = \frac{\nu}{2t} [l(l+1) - (\nu-t)(\nu-t+1)] b_{t-1} \quad (2.37)$$

For  $\nu = n = (l+1), (l+2), \dots$  the series terminates at  $t_0 = n - l$  ( $b_{t_0} = 0$ ) and is then equal to the exact hydrogenic eigenfunction [Burgess & Seaton \(1960\)](#). For non-integer values of  $\nu$  a suitable choice of  $t_0$  can lead to an accurate approximation of the radial wave function. The two zero points of  $b_t$  are given by

$$t_{1,2} = \frac{1}{2} [(1+2\nu) \pm (1+2l)] = \left\{ \begin{array}{l} \nu + l + 1 \\ \nu - l \end{array} \right. \quad (2.38)$$

However, since  $t$  must be an integer,  $b_t$  will not become 0 at all. Therefore  $t_0$  is set to the integer closest to the second zero point, given by

$$\nu_{nl} + l < t_{0,nl} \leq \nu_{nl} + l + 1 \quad (2.39)$$

The wave functions obtained by this series expansion will be inaccurate at small radii but rather exact at  $r \gg 1$  (atomic units). After calculating the radial wave functions the radiative transition rates can be obtained similar to hydrogen

$$A_{nl'n'l'} = \frac{8\pi^2\nu^3}{3\epsilon_0 c^3 \hbar} 4\pi\epsilon_0 e^2 a_0^2 C' \left| \int_0^\infty R_{n'l'} R_{n'l} r dr \right|^2 \quad (2.40)$$

Because of the ground state electrons (which are not present in hydrogen) the statistical factor  $C'$  Burgess & Seaton (1960) of the transition has to be evaluated differently. For atoms which have all their shells, but the excited state, closed or empty (as hydrogen for example)  $C'$  is given by

$$C' = \frac{l_{>}}{2l+1} \quad (2.41)$$

If there is a non-zero ground state term  $S''L''$  and the electron  $nlSL$  makes a transition to  $n'l'S'L'$  then

$$C'_{L'} = (2L' + 1) W_R^2(l'l'LL'; 1L'') l_{>} \quad (2.42)$$

where  $W_R$  means a Racah coefficient Racah (1942). As long as the radial integral does not depend on  $L'$  (or if there is only one possible  $L'$ ), the statistical factor can be calculated as the sum

$$C' = \sum_{L'} C'_{L'} = \frac{l_{>}}{2l+1} \quad (2.43)$$

Finally, if the transition involves a populated state itself (e.g. the ground state) and is therefore of the type  $l^q SL$  to  $l^{q-1} S''L''n'l'S'L'$  then

$$C'(l^q SL \rightarrow l^{q-1} S''L''n'l'S'L') = (2l+1)(2L'+1) W_R^2(l'l'LL'; 1L'') C(l^q SL \rightarrow l^{q-1} S''L''l') \quad (2.44)$$

where  $C(l^q SL \rightarrow l^{q-1} S''L''l')$  is for example tabulated in Burgess & Seaton (1960). For neutral oxygen almost all the electrons are in the  $2p^4(^3P)$  state, while for excited or singly ionised oxygen the 2p electrons are to about 100% in the  $2p^3(^4S)$  state. The  $C'$  coefficients for transitions  $2p^4(^3P) \rightarrow 2p^3(^4S)$  into excited (or unbound) s and d levels are 4/9 ( $2p^4(^3P)$  to  $2p^3(^4S)n, [l=0]$  levels) and 8/9 ( $2p^4(^3P)$  to  $2p^3(^4S)n, [l=2]$  levels).

The QDM can also be used to evaluate recombination rates. First, one has to calculate the free radial wave functions  $F_{nl}$ . The recombination rates can then be calculated as described in Section 2.1. The quantum defect  $\mu(\epsilon)$  of a free electron (with continuous energy  $\epsilon$ ) in the presence of a core potential is obtained by an interpolation between the quantum defects  $\mu_{nl}$  at the eigenvalues of the system at discrete values  $\epsilon_{nl}$  (e.g. Seaton 1958). The quantum defect causes a shift  $\delta(\epsilon) \sim \pi\mu(\epsilon)$  (Seaton 1958) in the phase of the free-electron wave function.

The free wave functions have the asymptotic forms Burgess & Seaton (1960)

$$\begin{aligned} F_{k,l'}(r) &\propto k^{-1/2} \sin[x(r) + \pi\mu] & , r \rightarrow \infty \\ F_{k,l'}(r) &\propto (Zr)^{l'+1} & , r \rightarrow 0 \end{aligned} \quad (2.45)$$

where

$$x = kr - \frac{1}{2}l\pi + \frac{Z}{k} \ln(2kr) + \arg \Gamma(l+1 - iZ/k) \quad (2.46)$$

An approximation of the free wave function is found in the QDM Burgess & Seaton (1960) by setting

$$F_{k,l'}(r) = Z^{-1/2} [G(\epsilon, l', Zr) \cos \pi\mu(\epsilon) - H(\epsilon, l', Zr) \sin \pi\mu(\epsilon)] \quad (2.47)$$

where

$$G(\epsilon, l', Zr) = \left(\frac{\pi A'}{2}\right)^{1/2} y'_1 \quad (2.48)$$

and

$$H(\epsilon, l', Zr) = [1 - \exp(-\tau_l Zr)]^{2l'+1} \left(\frac{\pi}{2A'}\right)^{1/2} y'_3 \quad (2.49)$$

and the Coulomb functions  $y'_1$  and  $y'_3$  (Seaton 1958), which are analytic solutions of the hydrogenic Schrödinger equation. The normalisation factor  $A'$  is given by

$$A' = [1 + \epsilon l'^2][1 + \epsilon(l' - 1)^2] \dots [1 + \epsilon] \quad (2.50)$$

and the cut-off factor  $\tau_{l'}$  is introduced in order to suppress the divergent behaviour of  $y'_3$  at radii smaller than  $\sim l'(l' + 1)/(2Z)$  and is therefore set to

$$\tau_{l'} \sim \frac{10}{l'(l' + 1)} \quad (2.51)$$

The free-electron wave functions obtained by the QDM (Equation 2.47) behave as  $F_{nl} \propto (Zr)^{l'+1}$  at the origin and as  $F_{nl} \propto k^{-1/2} \sin(x + \pi\mu)$  at large radii and therefore have the correct asymptotic forms in the limits  $r \rightarrow 0$  and  $r \rightarrow \infty$ . After the free and bound wave functions have been calculated, the ionisation cross-sections are given by [Burgess & Seaton \(1960\)](#)

$$\sigma_{nl}^1(k^2) = \frac{4\pi\alpha a_0^2}{3}(I + k^2) \sum_{l'=l\pm 1} C_{l'} \left| \int_0^\infty R_{nl} F_{k,l'} r dr \right|^2 \quad (2.52)$$

where the coefficients  $C_{l'}$  have to be chosen as described above.

## 2.3. Collisional Processes & Data

Collisional processes can also be described by quantum mechanics, but the problem is more complicated than for radiative processes. For this thesis the collision of thermal and non-thermal electrons with bound and free electrons is most important. Since these processes involve more than two particles no strictly analytic treatment is possible. However, under certain conditions approximate solutions can be found.

Since these approximations are inaccurate, the problem is solved by experiments and elaborate numerical calculations in general. Fortunately, atomic data for most collisional processes relevant in the nebular phase of a supernova are available in the literature in the form of experimental and numerically calculated data compilations and fit functions.

However, to gain some insight into the collisional processes important for this work it is instructive to study electron-atom collisions by calculating their differential and total cross-sections  $I_n(\theta, \phi)$  and  $\sigma_n$  ([Mott & Massey 1950](#)). In this section a high-energy limit of these cross-section is derived, which will be important in Section 3.3.3 for calculating the non-thermal electron ionisation and excitation of SN nebulae.

It is assumed that the energy of the incident electron moving in direction  $\mathbf{n}_0$  is high  $k_0 = 2\pi m v_0/h$  compared to the typical binding energy of the atom and therefore the state of the incident electron  $F_0$  is hardly influenced by the atomic potential (Born approximation). Its (free) wave function is then given by ([Mott & Massey 1950](#), page 137)

$$F_0 \sim e^{ik_0 r} \quad (2.53)$$

After scattering the (bound) atomic electron to state  $n$  (unbound states included) the incident electron is described by the new wave function

$$F_n \sim r^{-1} e^{ik_n r} f_n(\theta, \phi) \quad (2.54)$$

which again describes a free electron, however with some angular diffraction. The probability per unit time for an incident electron to scatter the bound electron to state  $n$  and to be found in a unit angle  $d\omega = \sin\theta d\theta d\phi$  at coordinates  $\theta, \phi$  is

$$\begin{aligned} P_n(\theta, \phi) &= \frac{d}{dt} \int_V |F_n|^2 dV \\ &= \int_{\theta, \phi} |f_n(\theta, \phi)|^2 r^{-2} \frac{v_n}{V_n} dS \\ &= \int_{\theta, \phi} |f_n(\theta, \phi)|^2 \frac{v_n}{v_0} \frac{v_0}{V_n} d\omega \end{aligned} \quad (2.55)$$

where  $v_0$  and  $v_n$  are the velocities of the incident and scattered electron, respectively. The differential cross-section for scattering an electron to state  $n$  is then given by

$$I_n(\theta, \phi) = \frac{V_n}{v_0} \frac{d}{d\omega} P_n(\theta, \phi) = \frac{v_n}{v_0} |f_n(\theta, \phi)|^2 \quad (2.56)$$

The total cross-section for scattering an electron to state  $n$  is obtained by angular integration of the differential cross-sections

$$\sigma_n = \int_0^{2\pi} \int_0^\pi I_n(\theta, \phi) d\omega \quad (2.57)$$

The radial wave function  $\Phi$  of the two electron system (incident and atomic electron) is a solution of

$$\left[ \frac{\hbar^2}{8\pi^2 m_e} (\nabla_r^2 + \nabla_R^2) + \frac{\epsilon^2}{|r|} + \frac{\epsilon^2}{|R|} - \frac{\epsilon^2}{|r-R|} + E \right] \Phi = 0 \quad (2.58)$$

where  $\mathbf{r}$  denotes the atomic and  $\mathbf{R}$  denotes the incident electron. Writing  $\Phi(\mathbf{r}, \mathbf{R}) = \sum_n \Phi_n(\mathbf{r}) F_n(\mathbf{R})$  with  $\Phi_n$  ( $n$  denotes all the bound and free states) the proper states of the hydrogen atom and combining Equation 2.58 with the Schrödinger equation of the hydrogen atom, multiplying by  $\Phi_n^*(\mathbf{r})$  and integrating over the radial coordinate of the bound electron one obtains

$$\begin{aligned} \left[ \frac{\hbar^2}{8\pi^2 m_e} \nabla_R^2 + E - E_n \right] F_n(\mathbf{R}) &= \int \left( \frac{\epsilon^2}{|r-R|} - \frac{\epsilon^2}{|R|} \right) \Phi(\mathbf{r}, \mathbf{R}) \Phi_n^*(\mathbf{r}) d\mathbf{r} \\ &\equiv \int V(\mathbf{r}, \mathbf{R}) \Phi(\mathbf{r}, \mathbf{R}) \Phi_n^*(\mathbf{r}) d\mathbf{r} \end{aligned} \quad (2.59)$$

Using the Born approximation  $\Phi_0(\mathbf{r}, \mathbf{R}) = \Phi_m(\mathbf{r}) F_0(\mathbf{R}) = \Phi_m(\mathbf{r}) \exp(ik_0 \mathbf{n}_0 \cdot \mathbf{R})$  one can write

$$\left[ \frac{\hbar^2}{8\pi^2 m_e} \nabla_R^2 + E - E_n \right] F_n(\mathbf{R}) = \int V(\mathbf{r}, \mathbf{R}) e^{ik_0 \mathbf{n}_0 \cdot \mathbf{R}} \Phi_m \Phi_n^*(\mathbf{r}) d\mathbf{r} \quad (2.60)$$

which is solved by (Mott & Massey 1950, page 138, 224)

$$F_n \sim r^{-1} e^{ik_n r} \frac{2\pi m_e}{\hbar^2} \iint V(\mathbf{r}, \mathbf{R}) e^{-i(k_{mn} \mathbf{n}_{mn} - k_0 \mathbf{n}_0) \cdot \mathbf{R}} \Phi_m(\mathbf{r}) \Phi_n^*(\mathbf{r}) d\mathbf{r} d\mathbf{R} = r^{-1} e^{ik_n r} f_n(\theta, \phi) \quad (2.61)$$

where  $k_0 \mathbf{n}_0$  and  $k_{mn} \mathbf{n}_{mn}$  are momentum vectors of the incident and the scattered electron. The differential cross section  $I_n(\theta)$  is then given by

$$I_{mn}(\theta) = \frac{4\pi^2 m_e^2}{\hbar^4} \frac{k_{mn}}{k_0} \left| \iint V(\mathbf{r}, \mathbf{R}) e^{i(k_{mn} \mathbf{n}_{mn} - k_0 \mathbf{n}_0) \cdot \mathbf{R}} \Phi_m(\mathbf{r}) \Phi_n^*(\mathbf{r}) d\mathbf{r} d\mathbf{R} \right|^2 \quad (2.62)$$

Substituting

$$\begin{aligned} \exp[i(k_{mn} \mathbf{n}_{mn} - k_0 \mathbf{n}_0) \cdot \mathbf{R}] &= \exp(iKX) \\ K &= |k_{mn} \mathbf{n}_{mn} - k_0 \mathbf{n}_0| = (k_0^2 + k_{mn}^2 - 2k_0 k_{mn} \cos \theta)^{1/2} \\ K dK &= k_0 k_{mn} \sin \theta d\theta \end{aligned} \quad (2.63)$$

and using (Mott & Massey 1950, page 226)

$$\int V(\mathbf{r}, \mathbf{R}) e^{iKX} d\mathbf{R} = \epsilon^2 \int \frac{e^{iKX}}{|\mathbf{R} - \mathbf{r}|} d\mathbf{R} = \frac{4\pi \epsilon^2}{K^2} e^{iKx} \quad (2.64)$$

one can write

$$\begin{aligned} I_{mn}(K) dK &= \frac{128\pi^5 m_e^2 \epsilon^4}{k_0^2 \hbar^4} \frac{dK}{K^3} \left| \int e^{iKx} \Phi_m \Phi_n^* d\mathbf{r} \right|^2 \\ &= \frac{128\pi^5 m_e^2 \epsilon^4}{k_0^2 \hbar^4} \frac{dK}{K^3} \sum_{j=0}^{\infty} \frac{K^{2j} \left| \int x^j \Phi_m \Phi_n^* d\mathbf{r} \right|^2}{j!} \end{aligned} \quad (2.65)$$

The total cross section is given by

$$\sigma_{mn}(k_0) = \int_{K_{\min}}^{K_{\max}} I_{mn}(K) dK \quad (2.66)$$

assuming  $k_0 \sim k_{mn}$  (high energy approximation)

$$\begin{aligned}
 k_0^2 &= k_{mn}^2 + \frac{8\pi^2 m_e}{h^2} (E_n - E_m) \\
 k_{mn} &\sim k_0 - \frac{4\pi^2 m_e}{k_0 h^2} (E_n - E_m) \\
 K_{\max} &= k_0 + k_{mn} \sim 2k_0 \\
 K_{\min} &= k_0 - k_{mn} \sim \frac{4\pi^2 m_e}{k_0 h^2} (E_n - E_m)
 \end{aligned} \tag{2.67}$$

For dipole-allowed transitions the  $j = 1$  term of Equation 2.65 is dominant and the total cross-section is approximately given by (Mott & Massey 1950, page 241)

$$\sigma_{mn} \simeq \frac{64\pi^5 m_e^2 \epsilon^4}{k_0^2 h^4} |x_{mn}|^2 \ln \frac{2m_e v_0^2}{E_n - E_m} \tag{2.68}$$

where  $|x_{mn}|^2$  is one-third of the mean square radius of an electron in the state  $m$ . If the transitions proceeds by the quadrupole moment  $j = 2$  then

$$\sigma_{mn} \simeq \frac{128\pi^7 m_e^3 \epsilon^4}{k_0^2 h^6} |x_{mn}|^2 |E_m| \tag{2.69}$$

Because of the logarithmic energy dependence in Equation 2.68 the total-cross sections of dipole-allowed transitions fall off weaker with energy than that of dipole-forbidden transitions. Therefore, for collisional excitation by highly energetic electrons only dipole-allowed transitions are excited efficiently, which will be useful in Sections 5 & 6.

From Equation 2.68 one can see that the ionisation cross-section for highly energetic electron collisions has the form

$$\sigma_n^i = \frac{\mathcal{A}}{m_e v_0^2} \ln \left( \frac{m_e v_0^2}{\mathcal{B}} \right) \tag{2.70}$$

which is closely related to the Bethe loss-function. These high-energy forms of the ionisation cross-section and the Bethe loss-function are used in Section 3.3.3. In principle  $\mathcal{A}$  and  $\mathcal{B}$  can be calculated in approximation but these calculations are usually not sufficiently accurate. Alternatively  $\mathcal{A}$  and  $\mathcal{B}$  can be obtained from fitting Equation 2.70 to experimental data at energies of  $\sim 10^4$  keV.

The interaction of highly energetic electrons with a thermal electron plasma can also be written in the form of Equation 2.70 (e.g. Axelrod 1980). In this case  $\mathcal{B}$  does not depend on the energy of the atomic levels but on a characteristic energy of the electron plasma, which depends on the electron density.

To calculate the collisions of thermal electrons with bound electrons one cannot use the Born approximation, since the electron velocities are low and the incident electron is influenced by the atomic potential significantly. Starting with Equation 2.59, which is also valid for low energetic collisions one has to make assumptions about  $\Phi(\mathbf{r}, \mathbf{R})$ . The problem becomes quite complex (Mott & Massey 1950). Although analytic approximations exist, the problem is usually solved numerically.



## 3. The Nebular Phase

### 3.1. Nebular Physics

Many physical processes contribute to the formation of SN nebular spectra. Some of these processes are of dominant importance and a physical description of the SN nebular phase becomes pointless neglecting one of those. Others are less important and can be considered as corrections to the dominant processes or become important under certain conditions only.

The dominant processes are radioactive heating by the decay of  $^{56}\text{Co}$ , non-thermal electron ionisation, radiative recombination, thermal electron (de-) excitation, radiative de-excitation, self-absorption and Doppler-broadening. These processes have been discussed in Section 2 or are explained below.

Less important effects are the ejecta geometry and mixing (three-dimensional effects) or clumping of the ejecta, shock interaction, heating by various radio-active isotopes (e.g.  $^{56}\text{Ni}$ ,  $^{57}\text{Ni}$ ,  $^{57}\text{Co}$ ,  $^{44}\text{Ti}$ ) or other energy sources (recombination, compact objects), positron energy deposition, thermal electron ionisation, photo-ionisation & excitation, collisional and di-electronic recombination, charge-exchange reactions, non-thermal electron excitation, line-scattering, continuum destruction, the population of excited states by recombination, two-photon transitions and electron scattering. This list is certainly not complete, but all effects worth consideration are probably mentioned. None of the less important processes is explained here, but some of them are elucidated later, if necessary. Here the formation of nebular spectra is explained qualitatively [see (Axelrod 1980) for a more quantitative description] based on the dominant processes.

Directly after the explosion most of the radioactive material of SNe exists in the form of  $^{56}\text{Ni}$ , which decays to  $^{56}\text{Co}$  with a mean lifetime of 8.77 days. By the transition to the nebular phase, about 100 days later, almost all  $^{56}\text{Ni}$  has decayed to  $^{56}\text{Co}$ . In SNe II-P a lot of the emitted energy comes from hydrogen recombination, but at the time of the nebular phase, radioactive decay is the dominant source of energy. Under certain conditions, shock heating may also be important, and in principle the SNe could be powered by other radio-active isotopes like  $^{57}\text{Ni}$ , but for most of the SNe observed so far it has been sufficient to consider heating by  $^{56}\text{Co}$ .

$^{56}\text{Co}$  decays to  $^{56}\text{Fe}$  with a mean lifetime of 111.37 days by transforming a proton into a neutron. About 81% of the decays are induced by orbital electron capture, while about 19% are by positron emission. Directly after the transition from  $^{56}\text{Co}$  to  $^{56}\text{Fe}$  the atomic core is in an excited state, which decays to the ground state by emitting  $\gamma$ -rays of various energies (0.26 – 3.6 MeV) with an average energy of 3.61 MeV per decay (e.g. Milne et al. 1999). The positrons, which are released in about every fifth decay carry on average about 0.63 MeV of kinetic energy. Most of this energy is lost to the SN gas by positron-electron collisions before the positrons annihilate with electrons [at  $E_{\text{kin}} \leq 10$  keV (e.g. Higdon et al. 2009)] and release two or three photons with a total energy of  $\sim 1.02$  MeV. Since only 19% of all decays emit a positron the total energy of one  $^{56}\text{Co}$  decay is on average distributed 92.0% in direct  $\gamma$ -rays, 3.1% in positron kinetic energy and 4.9% annihilation  $\gamma$ -radiation. Since most of the energy is emitted in  $\gamma$ -rays the contribution from positrons is insignificant as long as  $\gamma$ -rays deposit their energy in the gas efficiently (during the first few hundred days).

The situation changes at late times (several hundred days) when almost 100% of all  $\gamma$ -rays can escape. In this case most of the SN energy is provided by positron kinetic energy deposition. Unfortunately, this process is very sensitive to magnetic fields in the supernova envelope, since they greatly influence the paths of charged particles. Often, it is assumed that the positron kinetic energy is deposited completely, since rather weak magnetic fields are sufficient to trap all the positrons inside the SN volume. The cyclotron radius of a positron is given by

$$r_c = \frac{\gamma v m_\beta c}{qB} = 1.694 \times 10^3 \frac{\gamma \sqrt{1 - \gamma^{-2}}}{B[\text{G}]} [\text{cm}] \quad (3.1)$$

with

$$\gamma = 1 + \frac{E_{\text{kin}}}{m_\beta c^2} \quad (3.2)$$

For typical positron kinetic energies of  $E_{\text{kin}} \sim 1$  MeV and typical magnetic field strengths of the interstellar gas of  $B \sim 10^{-6}$  G the cyclotron radius is  $\sim 10^{10}$  cm, which has to be compared to the typical radius of the supernova  $\sim 10^{16}$  cm (at 100 days after explosion, assuming a typical supernova velocity of  $\sim 10^9$  cm s $^{-1}$ ).

However, radially combed magnetic fields may have quite the opposite effect and could even increase the escape fraction of positrons as they guide the positrons out of the supernova volume. Not much is known about the magnetic fields in SNe and therefore the deposition fraction of positrons is highly uncertain (e.g. Milne et al. 1999). Anyhow, at the epochs of interest for this work, positron energy depositions remains a second-order effect.

As the  $^{56}\text{Co}$  decay  $\gamma$ -rays propagate through the gas, they are Compton-scattered on free and bound electrons. By this scattering process high energetic electrons are produced, which lose most of their energy by electronic (plasma losses) and atomic collision processes (ionisation, excitation). The dominant ionisation process in the nebular phase are these non-thermal electron collisions. Under certain conditions, photo-ionisation can become a dominant process (e.g. Maurer et al. 2010), but usually it can be neglected.

Since the cross-sections for electron-electron collisions increases strongly at low electron energies, the electrons thermalise at low energies. From this thermal pool electrons (de-) excite and recombine to the various ions of the SN gas. Important for both processes are the electron density and temperature. Thermal electron collisional rates increase proportionally to the electron density and also increase with temperature. Radiative recombination rates, which are the most important ones at typical nebular temperatures and densities also increase proportionally to the electron density, but decrease with temperature. During the nebular phase the gas is in ionisation and in thermal equilibrium (e.g. Axelrod 1980).

Electrons in excited states reach the ground state by thermal electron collisions or radiative transitions. Since the ground states are strongly populated in the nebular phase, most photons are absorbed several times before they can leave the SN volume. This effect is called self-absorption. Self-absorption is important for the formation of nebular spectra, since it increases the chance that an excited state is depopulated by electron collisions (producing no radiation, but heating the electrons) and not by photon emission.

Since supernovae expand homologously (the velocity of the ejecta increases constantly from the inside to the outside), absorption processes can be described by the Sobolev approximation (e.g. Sobolev 1960, Rybicki & Hummer 1978, Jeffery 1993). In this approximation it is assumed that a photon interacts with any line only in a small resonance region with constant physical properties, where it is Doppler-shifted into resonance with that line. This approximation is valid as long as the resonance region is sufficiently small that its physical properties (temperature, densities and occupation numbers) do not vary greatly. This means that the thermal velocity of the SN gas must be significantly lower than the characteristic velocity scale of the variation of these quantities. In the nebular phase the gas temperature is about 5000K and therefore the thermal velocity of the atoms and ions is about 1 – 10 km s $^{-1}$ . On the other hand, a typical velocity scale of temperature, density and occupation number variations is  $10^3$  km s $^{-1}$ . Therefore the conditions for the applying the Sobolev approximation are fulfilled in the nebular phase of SNe (e.g. Jeffery 1993).

Since electron density and temperature play the central role for the formation of nebular phase spectra, their physical description must aim on the calculation of these two quantities.

## 3.2. The One-Dimensional Nebular Code

The three-dimensional nebular code (NC3D) developed in this thesis is an advancement of the nebular code of Mazzali et al. (2001, 2007) (NC1D), which in turn is based on the work of Axelrod (1980) and Ruiz-Lapuente & Lucy (1992). The improvements include an implementation of a full three-dimensional structure, an improved treatment of radioactive heating and ionisation, the population of excited states by recombination, two-photon transitions of hydrogen and helium (unimportant for other elements), photo-ionisation of hydrogen (important under special conditions only) and a general treatment of line-scattering. These modifications are presented in Sections 3.3, 4, 5 and 6.

Since the general scheme of NC1D and NC3D is identical, we describe NC1D in this section in detail. The code is available in a one-zone and a shell version and has widely been used in the literature (e.g. Mazzali et al. 2007, Maeda et al. 2008, Silverman et al. 2009, Gal-Yam et al. 2009). In the one-zone version, the SN ejecta are approximated as a sphere of homogeneous density and compositions, while in the shell version several shells with different compositions and densities can be defined in spherical symmetry. To understand the concept of NC1D it is sufficient to look at the one-zone version.



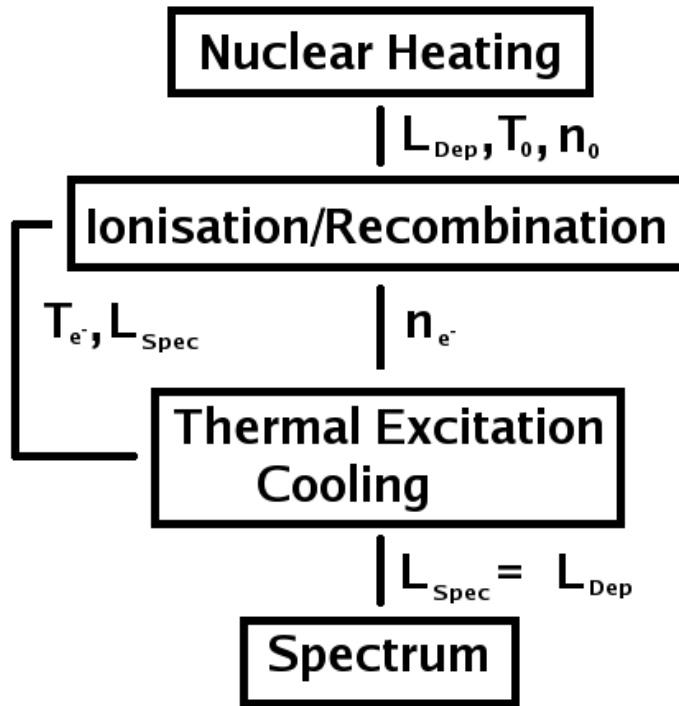


**Figure 3.1.:** Scheme of the nebular code. After the energy deposition has been calculated the electron density  $n_e$  and temperature  $T_e$  are iterated until the integrated luminosity of the synthetic spectrum  $L_{\text{Spec}}$  equals the deposited luminosity  $L_{\text{Dep}}$ .

NCID can treat radioactive heating of the SN ejecta by  $^{56}\text{Ni}$ ,  $^{56}\text{Co}$ ,  $^{57}\text{Ni}$  and  $^{57}\text{Co}$ . The deposition process (Compton-scattering of  $\gamma$ -rays and cascading of high-energetic electrons) is not treated explicitly, but is calculated by computing a density dependent deposition fraction (Axelrod 1980). In the shell version this effective treatment of deposition is combined with a Monte Carlo treatment to calculate the  $\gamma$ -ray transport between different shells.

NCID can treat the neutral and first ionisation state of C, N, O, Ne, Na, Mg, S, Si, Ar and Ca, as well as the first and the second ionisation state of Fe, Co and Ni.

The ionisation rate  $Y$  is determined by assuming that certain fractions of the energy deposited in each shell are lost to ionise the various elements. In NCID these fractions were computed using an analytic formula, which however underestimated the ionisation rates of light elements like carbon and oxygen by roughly a factor of ten. The estimate of the ionisation rate of heavier elements like calcium and iron was more accurate (Maurer & Mazzali 2010, Mazzali et al. 2010). Radiative and di-electronic recombination are considered, but the population of excited states by recombination is neglected. The recombination rates  $R$  depend on the electron density  $n_e$  and temperature  $T_e$  and are taken from the literature.

An iterative scheme is used (see Figure 3.1). After the deposited energy and the non-thermal electron ionisation rates have been evaluated, the ionisation equilibrium equations are solved using an initial guess for the electron density and temperature

$$Yn_{\text{I}} = R(T_e)n_en_{\text{II}} \quad (3.3)$$

where  $n_{\text{I,II}}$  are the densities of the lower and upper ionisation state.

This calculation determines the degree of ionisation of the SN gas and therefore its free-electron density. The nebular emission is predominantly produced by thermal-electron excitation of forbidden lines. Since these rates depend on the electron density and temperature, the electron temperature can be calculated for a given electron density by balancing the energy emitted by all the excited lines with the deposited luminosity.

To calculate the emission of an ion one has to solve the equation system for the fractional population of all the

treated states  $q_j$  of an ion

$$\begin{aligned} 0 &= \dot{q}_j = -q_j \sum_k (A_{jk} + C_{jk}) + \sum_k q_k (A_{kj} + C_{kj}) \\ 1 &= \sum_j q_j \end{aligned} \tag{3.4}$$

where  $A$  and  $C$  are the radiative and collisional transition rates respectively. Equation 3.4 can be written in the form  $\mathcal{A}x = \mathcal{B}$ , which is a linear matrix problem and can be evaluated by an appropriate matrix solver. Calculating all the excited state populations, one obtains the emitted luminosity for the old combination of electron density and temperature. This luminosity has to be compared to the deposited luminosity, which gives the iteration criterion. If the emitted luminosity is lower than the deposited luminosity one has to increase the electron temperature and vice versa. The new electron density and temperature (which influence the recombination rates) can be used to recalculate the ionisation equilibrium. Each cycle produces a new pair of electron density and temperature, which converges after a few iterations only (see Figure 3.1).

Since an analytical solution for the emission profile of a spherical shell of uniform density is available (see Section 3.3), the emission line profiles can be calculated directly as soon as the line luminosities have converged. Therefore, for a given model, the spectra can be calculated from velocity, density and composition information. One can turn this around and try to obtain these quantities from fitting the nebular spectra of an observed SN. This process is called 'nebular modelling'.

To derive a model for an observed SN one can start with an initial guess for the ejecta structure and composition and can then compare the resulting synthetic spectra to the observations. Since the line emission depends on the density of the emitting material and since the velocity can be derived from the line profiles (see Section 3.3), one can obtain the SN properties by iteratively modifying this initial guess until a good reproduction of the spectra is obtained. If the distribution of  $^{56}\text{Ni}$  is known exactly, such a model is unique under the assumption of spherical symmetry. To infer the  $^{56}\text{Ni}$  distribution, one can study the various Fe-group lines, which can however be difficult since these lines are often blended and the Fe-group collisional data are affected by significant uncertainties. More constraints on the  $^{56}\text{Ni}$  distribution can be derived from modelling a series of spectra over (several) hundred days, which demands an accurate guess of the 'real'  $^{56}\text{Ni}$  (and other ejecta) distribution, since otherwise the luminosity and line ratio evolution would not be reproduced correctly.

### 3.3. The Three-Dimensional Nebular Code

#### 3.3.1. Three-dimensional heat transport

As in NC1D the heat transport in NC3D is done by a Monte Carlo routine. Using a Monte Carlo approach one can calculate the influence of a chain of probabilistic processes on a large number of particles by explicitly following a subset of these particles to a representative set of final states. The particle set has to be large enough to cover all relevant outcomes of the chaining with a statistical significant number of events.

In the nebular phase of SNe most of the emitted energy is deposited in the ejecta by Compton scattering of  $\gamma$ -rays (see Section 3.1). Compton scattering has an angle and energy dependent probability. The  $\gamma$ -rays emitted by the radioactive decay must be bundled up to packets containing several  $\gamma$ -rays of the same energy to reduce the computational time. These energy packets are propagated through the SN envelope to calculate the energy deposited in each cell. The chance to scatter a package is determined by the energy of the corresponding  $\gamma$ -rays and by the density and the size of the cell. From all the possibilities (there is also a chance of no scattering) one is chosen randomly according to the corresponding physical probabilities. The size of the packets determine the computational time and the accuracy of the calculation since the number of packages is inversely proportional to the package size. In the nebular code the package size is chosen to guarantee an error of less than 1% on the energy deposited in each cell.

To calculate the absorption probability of a Monte Carlo energy packet, it is necessary to calculate the distances between the energy packet and the walls of the grid cell (at  $R_{\min,\max}$ ,  $\theta_{\min,\max}$ ,  $\phi_{\min,\max}$ ), containing the energy packet, along the line of energy packet propagation. This distance can be calculated by equating the sum of the position vector  $\mathbf{P}$  and the directional unit vector  $\mathbf{E}$  times the distance  $D$  from the walls  $\mathbf{W}$  of the cell and then solving for the

distance.

$$\mathbf{W} = \mathbf{P} + DE \quad (3.5)$$

We decided to use a spherical grid (a Cartesian grid had been another possibility and the choice was arbitrary). The distances to the walls of the cell at  $R_{\min, \max}$  is given by

$$D_R = -\mathbf{P} \cdot \mathbf{E} \pm \sqrt{(\mathbf{P} \cdot \mathbf{E})^2 - \mathbf{P}^2 + R^2} \quad (3.6)$$

with  $R = R_{\min, \max}$ .

The distances to the  $\theta_{\min, \max}$  walls of the cell is given by

$$D_\theta = \frac{-\mathbf{P} * \mathbf{E} \pm \sqrt{(\mathbf{P} * \mathbf{E})^2 - (\mathbf{P} * \mathbf{P})(\mathbf{E} * \mathbf{E})}}{\mathbf{E} * \mathbf{E}} \quad (3.7)$$

with  $\mathbf{a} * \mathbf{b} \equiv a_Z b_Z \tan^2 \theta - a_Y b_Y - a_X b_X$  and  $\theta = \theta_{\min, \max}$  if  $Z \geq 0$  and  $\theta = \theta_{\min, \max} - \pi$  if  $Z < 0$ .

The distances to the  $\phi_{\min, \max}$  walls of the cell is given by

$$D_\phi = \frac{P_Y - P_X \tan \phi}{E_X \tan \phi - E_Y} \quad (3.8)$$

with  $\phi = \phi_{\min, \max}$  if  $Y \geq 0, X \geq 0$ ,  $\phi = \phi_{\min, \max} - \pi$  if  $X < 0$  and  $\phi = \phi_{\min, \max} - 2\pi$  if  $Y < 0, X \geq 0$ . After determining the distance to the cell boundaries, a Monte Carlo routine can be used to decide whether the energy packed is absorbed or propagates into a neighbouring cell.

### 3.3.2. Three-dimensional line profiles

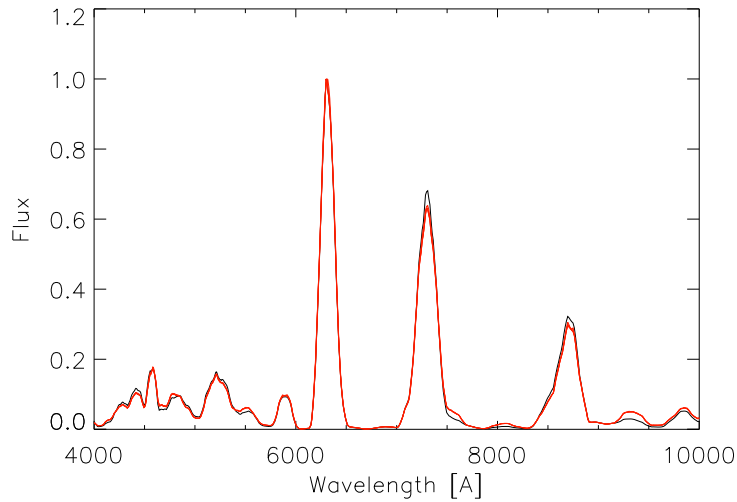


**Figure 3.2.:** A synthetic spectrum calculated for a spherical symmetric ejecta configuration of a SN Ic derived in Section 4 by nebular modelling. The calculation was performed with the 1D code in the stratified version (black) and the 3D code (red) using Equation 3.13 for comparison. The 3D resolution used is  $\sim 1000$  cells. The agreement is excellent.

The formation of line profiles in spherical symmetric geometry is for example described in [Axelrod \(1980\)](#) and can be easily implemented in a code, since an analytic expression can be found for the line profile of a spherical shell.

In three dimensions an analytical solution can be found for the special case of polar observation ( $\theta = 0$ ). The important process for line profile formation during the nebular phase is the Doppler shift caused by the relative

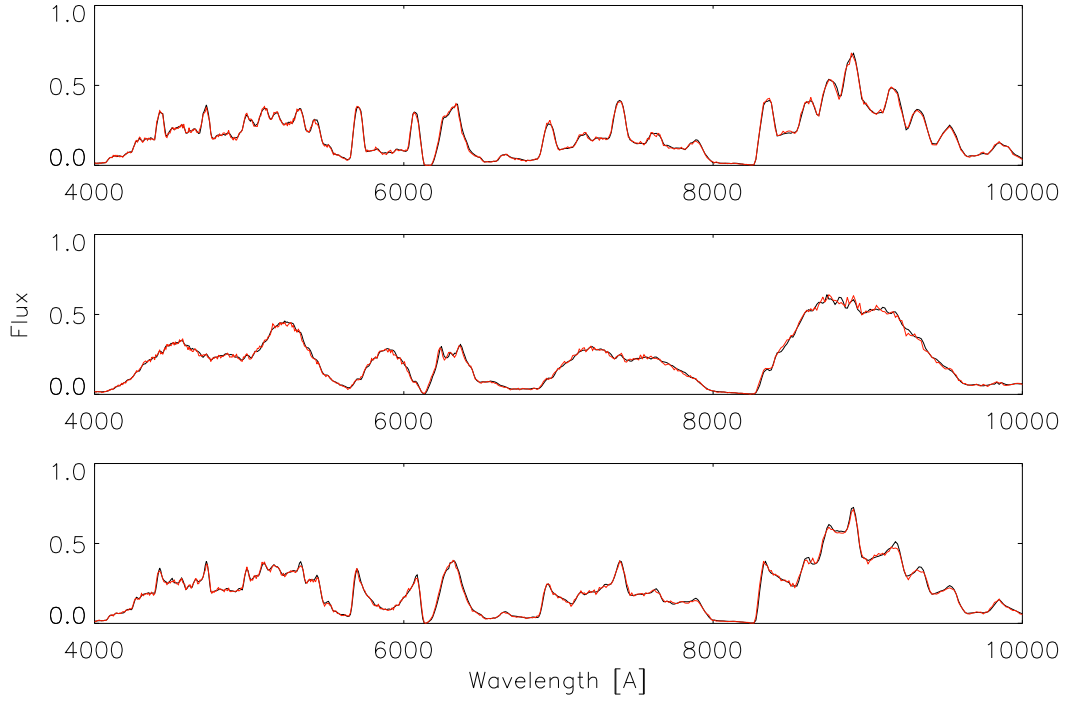


**Figure 3.3.:** An artificial three-dimensional test model with  $\sim 1000$  cells observed from three different angles [ $(\theta = 0^\circ, \phi = 0^\circ)$  top,  $(\theta = 90^\circ, \phi = 0^\circ)$  middle,  $(\theta = 23^\circ, \phi = 86^\circ)$  bottom]. The line profiles obtained from Equation 3.13 are shown in black, the ones obtained by the Monte Carlo routine in red. The agreement is excellent. The model was designed to show very strong asymmetries to allow a meaningful comparison of both methods.

motion of the emitting regions and the observer. Assuming constant density within one cell the line profile  $\Phi(\nu)$  of an individual cell can be calculated by

$$\begin{aligned}
 \Phi(\nu) &= A \int_{R_{\min}}^{R_{\max}} r^2 dr \int_{\mu_{\min}}^{\mu_{\max}} d\mu \int_{\phi_{\min}(\mu)}^{\phi_{\max}(\mu)} \delta(\nu - \nu^*(r, \mu)) d\phi \\
 &= A \int_{R_{\min}}^{R_{\max}} r^2 dr \int_{\mu_{\min}}^{\mu_{\max}} \Delta\phi(\mu) \delta(\nu - \nu^*(r, \mu)) d\mu \\
 &= A \int_{R_{\min}}^{R_{\max}} r^2 dr \int_{\mu_{\min}}^{\mu_{\max}} \Delta\phi(\mu) \delta\left(\nu - \nu_0 \left[1 + \mu \frac{V(r)}{c}\right]\right) d\mu \\
 &= A \int_{R_{\min}}^{R_{\max}} r^2 dr \int_{\mu_{\min}}^{\mu_{\max}} \Delta\phi(\mu) \delta\left(\frac{\nu_0 V(r)}{c} \left[\frac{c}{V(r)} \left(\frac{\nu - \nu_0}{\nu_0}\right) - \mu\right]\right) d\mu \\
 &= A \int_{R_{\min}}^{R_{\max}} r^2 dr \int_{\mu_{\min}}^{\mu_{\max}} \Delta\phi(\mu) \frac{c}{V(r)\nu_0} \delta(\mu - \mu^*(r, \mu)) d\mu
 \end{aligned} \tag{3.9}$$

with  $\mu = \cos \theta$ ,  $\Delta\phi(\mu) = \phi_{\max}(\mu) - \phi_{\min}(\mu)$ ,  $A$  a normalisation constant and

$$\begin{aligned}
 \nu^*(r, \mu) &= \nu_0 \left(1 + \mu \frac{V(r)}{c}\right) \\
 \mu^*(r, \nu) &= \frac{c}{V(r)} \left(\frac{\nu - \nu_0}{\nu_0}\right)
 \end{aligned} \tag{3.10}$$

where  $V(r) = \frac{V_0}{R_{\max}} r$  (homologous expansion) is the radial velocity of the cell.

If the observer's position coincides with the polar axis of the grid,  $\Delta\phi(\mu)$  is a constant and one can simplify Equation 3.9 to (absorbing the constants into the normalisation factor  $A$ )

$$\Phi(\nu) = \begin{cases} A \int_{R_{\min}}^{R_{\max}} r dr & \mu_{\min} \leq \mu \leq \mu_{\max} \\ 0 & \text{else} \end{cases} \quad (3.11)$$

Defining  $R_{\max} \equiv R$ ,  $R_{\min} \equiv (1 - h_R)R$  and

$$x \equiv \frac{c}{V_0} \left( \frac{\nu - \nu_0}{\nu_0} \right) = \frac{r}{R} \mu \quad (3.12)$$

one finally obtains  $(\frac{Rx}{\mu_{\max}} \leq r \leq \frac{Rx}{\mu_{\min}}; R(1 - h_R) \leq r \leq R)$

$$\Phi(x) = A \int_{\max[\frac{x}{\mu_{\max}}, (1-h_R)]}^{\min[\frac{x}{\mu_{\min}}, 1]} r dr \quad (3.13)$$

absorbing  $R^2$  into the normalisation factor  $A$ . In general, one wants to compute spectra from several different observer positions for the same ejecta model and therefore it is not possible to angle the polar axis of the computational grid in the direction of the observer.

In this general case,  $\Delta\phi(\mu)$  (the cell width along the  $\phi$  direction relative to the observer), is a complicated function of  $\mu$ , the position of the observer relative to the grid and the cell boundaries. To obtain the line profiles the computational grid is mapped onto a second spherical grid with its polar axis pointing towards the observer. This mapping basically replaces each cell of the computational grid by a new cell with the same position, volume and physical properties, however with a new orientation. As long as the number of angular cells is much larger than one, this approximation produces the correct line profiles.

Alternatively one can use a Monte Carlo approach, which is also useful for calculating the effect of line-scattering. Packets of photons produced by the various transitions in each computational cell are propagated through the virtual SN envelope until the packets reach the outer boundary of the computational domain. Line-scattering is implemented in the Sobolev approximation by following each photon packet through all the resonance regions of potential scattering lines. The Monte Carlo approach needs more computational time and is especially interesting for small cell numbers, of the order of 1000 or less. For higher grid resolutions the semi-analytical approach described above is faster and becomes very accurate (see Figure 3.3). Therefore both concepts are useful and are used in different situations.

### 3.3.3. The new ionisation treatment

The ionisation of the SN ejecta is mainly caused by non-thermal highly energetic electrons, which are generated in Compton processes following the decay of  $^{56}\text{Co}$  at nebular epochs. Ionisation by thermal electrons is unimportant at typical nebular temperatures ( $T_e \sim 5000$  K) and photo-ionisation is only important under special conditions (e.g. see Section 6).

The high energy electrons are scattered by free electrons and atoms, losing energy to the electron plasma and causing ionisation and excitation. An ionisation reduces the energy of the electron by the ionisation energy of the atom or ion and the kinetic energy of the freed electron, which can be significantly higher than the ionisation energy. Therefore, only a minor fraction of the total deposited energy goes into ionisation, while the larger part heats the thermal electron plasma.

In the nebular code (in previous versions) it was assumed that some constant fraction of the deposited energy goes into ionisation. This fraction was evaluated by a simple formula. While this approach gave approximately correct ionisation rates for iron group elements, the ionisation rates for light elements like carbon or oxygen were underestimated by a factor of ten and more. Since all the light elements are observed by their neutral state (e.g. O I), which is by far dominant, an inaccurate estimate of the ionisation rate has rather small influence on the mass estimates.

For example, if the ratio of the O I ionisation to the recombination rate (which equals the ratio of the ionised and the neutral state) was 0.01 with the old treatment, it is about 0.1 with the new version of the code. The oxygen mass of SN ejecta is estimated from neutral oxygen in the nebular phase since no O II lines can be identified. Both versions of the code produce similar estimates of the O I mass. However, the total mass of oxygen estimated also

depends on the O II fraction. Therefore, in this example the new version of the code estimates a total O mass, which is about 10% larger than the one obtained with the old version, since there is more O II. For the large sample of CC-SNe presented in Section 4 we find that the total O mass estimate increased by 10 – 40% with the new version of the code depending on the ejecta configuration (also see [Mazzali et al. 2010](#)). Since mass estimates obtained by the nebular code are in general not expected to be more accurate than 10 – 20% this error was not quite dramatic.

However, when calculating recombination line formation (as done in Section 5), an accurate treatment of the ionisation becomes important since the strength of the recombination lines depends on the ionisation rates directly. In this section a more accurate estimate of ionisation rates is described. The ionisation rates can be calculated using the concept of 'work per ion'  $W$  (e.g. [Axelrod 1980](#)), which means the amount of energy which is lost to thermal electrons while causing one ionisation. The method presented here is based on an ionisation treatment of [Axelrod \(1980\)](#). The ionisation rate can be calculated directly by dividing the amount of total deposited energy per time and atom by  $W$

$$Y = \frac{L_{\text{Dep}}}{N_{\text{tot}} W} \quad (3.14)$$

The work per ion  $W$  can be calculated by

$$W = \frac{E_{\text{max}}}{\int_{E_{\text{min}}}^{E_{\text{max}}} \frac{\sigma(E')}{L_{\text{atom}}(E') + L_{\text{elec}}(E')} dE'} \quad (3.15)$$

with the total ionisation cross-section (see Section 2.3; the  $\beta = v/c$  terms result from relativistic corrections)

$$\sigma = \frac{2A}{\beta^2 m_e c^2} \sum_i \frac{n_i}{P_i} \left[ \ln \frac{\beta^2 m_e c^2}{2P_i(1-\beta^2)} - \beta^2 \right] \quad (3.16)$$

the loss function due to atomic processes

$$L_{\text{atom}} = \frac{4\pi e^4}{\beta^2 m_e c^2} Z_b \left[ \ln \frac{\beta^2 m_e c^2}{\frac{1}{2} I(1-\beta^2)} - \beta^2 \right] \quad (3.17)$$

and the loss function due to interactions with the free electron plasma

$$L_{\text{elec}} = \frac{4\pi e^4}{\beta^2 m_e c^2} X_e \left[ \ln \frac{\beta^2 m_e c^2}{\frac{1}{2} \hbar \omega_p (1-\beta^2)^{1/2}} - \frac{1}{2} \beta^2 \right] \quad (3.18)$$

$Z_b$  is the number of bound electrons and  $X_e$  the number of free electrons per ion. The plasma frequency  $\omega_p$  is given by

$$\omega_p = \left( \frac{4\pi n_e e^2}{m_e} \right)^{1/2} \sim 5.64 \times 10^4 n_e^{1/2} \text{ [s}^{-1}\text{]} \quad (3.19)$$

$W$  is insensitive to the  $E_{\text{max}}$  and  $E_{\text{min}}$ . For  $E_{\text{max}} \rightarrow \infty$  the logarithmic terms become increasingly similar and the high-energy limit is given by

$$W_{\infty} \sim \frac{2\pi e^4 (Z_b + X_e)}{A \sum_j \frac{q_j}{P_j}} \sim 1.3 \times 10^{-13} \frac{Z_b + X_e}{A \sum_j \frac{q_j}{P_j}} \quad (3.20)$$

$W$  is basically proportional to the ionisation potential and the normalisation constant of the ionisation cross section, which are both element dependent. If the SN gas consists of more than one species of ions 'i' the 'work per ion' of each species is given by

$$W_i = \frac{E_{\text{max}}}{\int_{E_{\text{min}}}^{E_{\text{max}}} \frac{\sigma_i(E')}{\sum_j X_j L_{\text{atom},j}(E') + L_{\text{elec}}(E')} dE'} \quad (3.21)$$

where  $X_i = \frac{n_i}{n_{\text{tot}}}$  is the particle fraction of ion 'i' and

$$\frac{1}{W} = \sum_i X_i \frac{1}{W_i} \quad (3.22)$$

which gives

$$Yn_{\text{tot}} = \frac{L_{\text{Dep}}}{N_{\text{tot}}W}n_{\text{tot}} = \sum_i \frac{L_{\text{Dep}}}{N_{\text{tot}}W_i}X_i n_{\text{tot}} = \sum_i Y_i n_i \quad (3.23)$$

The normalisation constant  $A$  in Equation 3.16 is obtained from fitting the equation to experimental data at 10 keV. The atomic data (ionisation potentials, collisional cross-sections at 10 keV) necessary to calculate these ionisation rates are taken from [Lotz \(1970\)](#) and [Lennon et al. \(1988\)](#).





## 4. Characteristic Velocities Of Stripped-Envelope Core-Collapse Supernovae

In Section 3.2 we described the three-dimensional nebular code (NC3D) developed for this thesis. In this section this code is deployed to study possible ejecta asymmetries and core-velocities for a large sample of stripped-envelope core-collapse supernovae (SECC-SNe). These SNe are the result of the explosion of bare cores of massive stars, which lost part of their envelope before collapse and offer a clearer view of their inner ejecta than other SNe which have retained it. Thus, in this section we exclusively address stripped CC-SNe (Types I Ib, Ic).

Early-time observations ( $< 100$  days) of SECC-SNe have revealed a subclass of very energetic SNe, termed broad-lined (BL) SNe or hypernovae, which are characterised by broad absorption lines in the early-time spectra, indicative of outer ejecta moving at very high velocity ( $v \geq 0.1c$ ). BL-SNe seem to be preferentially of Type Ic [two exceptions are the Type I Ib SN 2003bg (Hamuy et al. 2009) and the Type Ib SN 2008D (Mazzali et al. 2008, Modjaz et al. 2009); see also SN 1987K (Filippenko 1988, Hamuy et al. 2009)]. Some BL-SNe can reach kinetic energies of  $\geq 10^{52}$  ergs. They are sometimes called hypernovae, and can be associated with long-duration gamma-ray bursts (GRBs) [see Woosley & Bloom (2006) and references therein]. However not all BL-SNe are associated with GRBs.

Asphericities in their inner and outer ejecta (e.g., Mazzali et al. 2001) are evident in at least some SECC-SNe. Two main indicators are velocity differences of Fe and lighter-element lines, and polarisation measurements (e.g., Höflich 1991). In GRB scenarios a relativistic outflow is launched by the central engine and deposits some fraction of its energy into the SN ejecta, probably preferentially along the polar axis, which might cause strong asymmetries (e.g., Maeda et al. 2002). The nearest, best-studied GRB-SNe are SN 1998bw / GRB 980425 (Galama et al. 1999), SN 2003dh / GRB 030329 (Matheson 2004), SN 2003lw / GRB 031203 (Malesani et al. 2004), and SN 2006aj / GRB/XRF 060218 (Pian et al. 2006), although it is not fully established that the GRBs (or X-ray flashes) accompanying nearby SECC-SNe can be compared directly to high-redshift GRBs. SECC-SNe may be characterised by asphericities although a jet does not necessarily form (Blondin et al. 2003, Burrows et al. 2007, Kotake et al. 2004, Moiseenko et al. 2006, Takiwaki et al. 2009).

The late-time spectra of SECC-SNe are typically dominated by strong [O I]  $\lambda\lambda 6300, 6363$  emission (the brackets “[ ]” denote forbidden transitions) produced by the innermost, slow-moving ejecta which are not visible at earlier times as they are located below the photosphere. The doublet lines are powered by thermal electron excitation of  $O\ I\ ^1D_2$ , which decays to the ground state sub-levels  $O\ I\ ^3P_1$  (6363 Å) and  $O\ I\ ^3P_2$  (6300 Å). Following Mazzali et al. (2005), who analysed the line-profiles of SN Ic 2003jd, recently, several authors (e.g. Maeda et al. 2008, Modjaz et al. 2008, Taubenberger et al. 2009, Maurer et al. 2010) have studied the shape of the [O I]  $\lambda\lambda 6300, 6364$  doublet (which is produced by much of the mass) and concluded that torus-shaped oxygen distributions may cause the double-peaked [O I] profile observed in many SECC-SNe nebular spectra. However, there is ongoing discussion regarding whether geometry is the dominant reason for this type of line profile (e.g. Milisavljevic et al. 2010).

If there is asymmetry in SECC-SNe or if different explosion scenarios are involved for different types of SECC-SNe, one might expect the largest, most revealing differences to be in the central region of the explosion. Therefore, in contrast to the standard classification of BL-SNe, which is based primarily on early-time spectroscopy and describes the velocity field of the outer SN layers, here we focus on the centre of the explosion. In this section, we model the nebular spectra of 56 SECC-SNe, the largest sample of SECC-SNe so far, to obtain a statistically significant representation of their core velocities. Using NC3D, we show that the derived relation between inner and outer ejecta velocities can be interpreted as evidence of non-spherical SN core geometry.

We describe our data set in Section 4.1 and the modelling procedure in Section 4.2. In Section 4.3 we test the reliability of the modelling approach and discuss our results.

SN	$\log(L_{\text{Bol}})$	$M_{\text{Ni}} (M_{\odot})$	$\beta$	$M_{\text{ej,tot}} (M_{\odot})$	$E_{\text{kin,tot}} (10^{51} \text{ ergs})$	References ( $L_{\text{peak}}, M_{\text{Ni}}, M_{\text{tot}} \& E_{\text{tot}}$ )
1990I	42.4	$0.11 \pm 0.02$	0.044	$3.7 \pm 0.7$	$1.1 \pm 0.1$	1,1,1
1993J	42.2	$0.08 \pm 0.02$	0.050	$\sim 3$	$\sim 1$	2,2,13
1994I	42.2	$0.065 \pm 0.03$	0.041	$\sim 0.9$	$\sim 1.0$	3,3,7
1997dq	42.2	$0.15 \pm 0.03$	0.095	$\sim 8-10$	10-20	5,5,5
1997ef	42.2	$0.135 \pm 0.025$	0.085	$\sim 8-10$	10-20	4,5,5
1998bw	42.8	$0.49 \pm 0.04$	0.079	$\sim 14$	$\sim 60$	3,3,15
2002ap	42.1	$0.073 \pm 0.02$	0.058	2.5-5	4-10	3,3,14
2003jd	42.8	$0.36 \pm 0.04$	0.057	$3 \pm 0.5$	$7^{+3}_{-2}$	3,3,3
2004aw	42.4	$0.21 \pm 0.03$	0.084	3.5-8.0	3.5-9.0	3,16,16
2006aj	42.7	$0.20 \pm 0.04$	0.040	$\sim 2$	$\sim 2$	3,12,12
2007Y	42.1	$0.06 \pm 0.01$	0.048	$\sim 0.5$	$\sim 0.1$	8,8,8
2007gr	42.2	$0.08 \pm 0.02$	0.046	1.5-3	1.5-3	10,11
2007ru	42.9	0.4	0.045	$1.3^{+1.1}_{-0.8}$	$5^{+4.7}_{-3.0}$	9,9,9
2008D	42.2	$0.09 \pm 0.02$	0.057	$\sim 7$	$\sim 6$	4,4,4
2008ax	42.3	$0.08 \pm 0.02$	0.040	3-6	$\sim 1$	6,6,6

**Table 4.1.:** Peak luminosities,  $^{56}\text{Ni}$  masses, the ratio  $\beta \equiv M_{\text{Ni}} (M_{\odot})/L_{\text{Bol},42}$ , the total ejecta mass, and the total kinetic energy for 15 SECC-SNe taken from the literature (see references). Typically  $\beta \approx 0.06$  with a dispersion of roughly 70%. References: <sup>1</sup>Elmhamdi et al. (2004), <sup>2</sup>Bartunov et al. (1994), <sup>3</sup>Valenti et al. (2008), <sup>4</sup>Mazzali et al. (2008), <sup>5</sup>Mazzali et al. (2004), <sup>6</sup>Pastorello et al. (2008), <sup>7</sup>Sauer et al. (2006), <sup>8</sup>Stritzinger et al. (2009), <sup>9</sup>Sahu et al. (2009), <sup>10</sup>Hunter et al. (2009), <sup>11</sup>Valenti et al. (2008), <sup>12</sup>Mazzali et al. (2006), <sup>13</sup>Nomoto et al. (1993), <sup>14</sup>Mazzali et al. (2002), <sup>15</sup>Nakamura et al. (2000), <sup>16</sup>Taubenberger et al. (2006).

## 4.1. Data Set

We collected nebular spectra of 56 SECC-SNe. This sample includes all the spectra presented by Matheson et al. (2001), Modjaz et al. (2008), and Taubenberger et al. (2009) for which a spectral fit was possible. The most important criteria for selection were a reasonable signal-to-noise ratio and a spectral coverage of at least the region between 6000 and 6500 Å. Most spectra range from 4000 to 10000 Å, allowing modelling of the Fe-group, oxygen, calcium, and carbon lines. If we found evidence for an underlying continuum, we tried to remove it using a linear fit. When several nebular spectra were available for a given SN, we chose the one closest to 200 days, although the precise epoch has little influence as long as the spectrum is nebular, as shown in Section 4.3.

Unfortunately, most of the spectra are not properly flux-calibrated. If an estimate of the  $^{56}\text{Ni}$  mass was available in the literature for SNe with uncalibrated spectra, we used these values (Table 1). For the remaining SNe with uncalibrated spectra we tried to estimate the  $^{56}\text{Ni}$  mass from the light curve. We emphasise that the exact  $^{56}\text{Ni}$  mass is not important for our study, as we show in Section 4.3.

For several SNe only one light-curve point exists (generally the detection magnitude in the  $V$  or  $B$  bands, or unfiltered). To obtain a (very crude) estimate of the  $^{56}\text{Ni}$  mass from this single data point we employed the following procedure. For the SNe with known  $^{56}\text{Ni}$  mass and bolometric peak luminosity, the ratio of bolometric peak luminosity (in units of  $10^{42}$  ergs) to  $^{56}\text{Ni}$  mass (in units of  $M_{\odot}$ ) can be calculated. This ratio varies between 0.040 and 0.095, with a rather uniform distribution (see Table 1), which reflects the variety of light-curve widths of different SNe (e.g., SNe with broader light curves have more  $^{56}\text{Ni}$  for the same peak luminosity). From the estimates of the  $^{56}\text{Ni}$  mass and the peak luminosity of these SNe, we can derive a relation

$$M_{\text{Ni}}(M_{\odot}) \approx 0.058 L_{\text{peak},42}. \quad (4.1)$$

This estimate should be compared with a similar one obtained for SNe Ia by Stritzinger et al. (2006), who found  $M_{\text{Ni}} (M_{\odot}) = 0.050 L_{\text{peak},42}$ . The difference probably arises from the different densities and compositions of SNe Ia and SECC-SNe.

To estimate the peak luminosity from the measured magnitude, we first tried to determine the bolometric luminosity at the time of detection. For some SNe an estimate for both the Milky Way and host-galaxy absorption is available in the literature. For most SNe, however, only the former is known (Schlegel et al. 1998). In this case we

SN	$m$	$A_V$ (mag)	$m - M$ (mag)	$\Delta d$	$\log(L_{\text{peak}})$	$M_{\text{Ni}}$	References ( $m, A_V$ )
1983N	11.3 <sub>V</sub>	0.51 ± 0.05	28.02 ± 0.3	0 ± 5	42.45 <sup>+0.31</sup> <sub>-0.22</sub>	0.17 <sup>+0.43</sup> <sub>-0.11</sub>	31,31
1985F	12.1 <sub>B</sub>	0.70	29.72	0 ± 4	43.08 <sup>+0.33</sup> <sub>-0.25</sub>	0.73 <sup>+1.91</sup> <sub>-0.49</sub>	1,2
1987M	-	-	-	-	43.00 <sup>+0.18</sup> <sub>-0.18</sub>	0.60 <sup>+0.42</sup> <sub>-0.25</sub>	3
1990B	-	2.64/5.46	-	-	-	0.2	34
1990U	15.8 <sub>V</sub>	1.6	32.64	0 ± 12	42.93 <sup>+0.44</sup> <sub>-0.20</sub>	0.51 <sup>+1.91</sup> <sub>-0.32</sub>	4,5
1990W	14.8 <sub>V</sub>	0.55	31.43	0 ± 3	42.43 <sup>+0.60</sup> <sub>-0.14</sub>	0.16 <sup>+0.93</sup> <sub>-0.09</sub>	6,*
1990aa	17.0 <sub>N</sub> ± 0.5	0.175	34.13	7 ± 7	42.50 <sup>+0.80</sup> <sub>-0.20</sub>	0.19 <sup>+1.84</sup> <sub>-0.12</sub>	32,*
1990aj	-	-	-	-	-	0.2	33
1991A	18.0 <sub>N</sub>	1.3	33.54	1 ± 10	42.19 <sup>+0.31</sup> <sub>-0.11</sub>	0.094 <sup>+0.233</sup> <sub>-0.051</sub>	5,5
1991L	-	-	-	-	-	0.2	35
1991N	13.9 <sub>N</sub>	0.097	31.29	5 ± 5	42.53 <sup>+0.56</sup> <sub>-0.06</sub>	0.20 <sup>+1.06</sup> <sub>-0.10</sub>	36,*
1995bb	-	-	-	-	-	0.2	37
1996D	18.2 <sub>V</sub>	0.509	34.04	0 ± 7	42.10 <sup>+0.68</sup> <sub>-0.14</sub>	0.07 <sup>+0.53</sup> <sub>-0.04</sub>	38,*
1996N	-	-	-	-	-	0.2	29
1996aq	14.7 <sub>V</sub>	0.129	32.20	0 ± 4	42.61 <sup>+0.62</sup> <sub>-0.14</sub>	0.24 <sup>+1.48</sup> <sub>-0.14</sub>	7,*
1997B	16.5 <sub>N</sub>	0.243	33.17	10 ± 3	42.40 <sup>+0.52</sup> <sub>-0.06</sub>	0.15 <sup>+0.70</sup> <sub>-0.07</sub>	39,*
1997X	13.5 <sub>N</sub>	0.091	31.15	4 ± 4	42.61 <sup>+0.54</sup> <sub>-0.06</sub>	0.25 <sup>+1.21</sup> <sub>-0.12</sub>	40,*
2000ew	14.9 <sub>N</sub>	0.147	30.16	14 ± 7	41.88 <sup>+0.60</sup> <sub>-0.06</sub>	0.05 <sup>+0.26</sup> <sub>-0.02</sub>	41,*
2001ig	-	-	-	-	-	0.13 <sup>+0.02</sup> <sub>-0.02</sub>	8
2003bg	15.0 <sub>N</sub>	0.096	31.24	14 ± 7	42.25 <sup>+0.60</sup> <sub>-0.06</sub>	0.11 <sup>+0.61</sup> <sub>-0.07</sub>	10,*
2003dh	-	-	-	-	-	0.4 <sup>+0.15</sup> <sub>-0.1</sub>	9
2004ao	14.9 <sub>N</sub>	0.348	32.35	0 ± 4	42.56 <sup>+0.54</sup> <sub>-0.06</sub>	0.22 <sup>+1.06</sup> <sub>-0.11</sub>	13,*
2004dk	17.6 <sub>N</sub>	0.522	32.15	-10 ± 10	41.87 <sup>+0.66</sup> <sub>-0.06</sub>	0.044 <sup>+0.298</sup> <sub>-0.021</sub>	15,*
2004gk	13.3 <sub>N</sub>	0.10	31.02 (Virgo)	0 ± 5	42.56 <sup>+0.56</sup> <sub>-0.06</sub>	0.22 <sup>+1.13</sup> <sub>-0.11</sub>	14,*
2004gq	15.5 <sub>N</sub>	-	-	-4 ± 3	-	0.2	30
2004gt	14.9 <sub>N</sub>	0.22 ± 0.03	31.84	-3 ± 5	42.36 <sup>+0.17</sup> <sub>-0.07</sub>	0.14 <sup>+0.21</sup> <sub>-0.07</sub>	11,12
2004gv	17.6 <sub>N</sub>	0.110	34.50	0 ± 7	42.38 <sup>+0.60</sup> <sub>-0.06</sub>	0.14 <sup>+0.83</sup> <sub>-0.07</sub>	27,*
2005N	-	-	-	-	-	0.2	42
2005bf	-	-	-	-	-	0.05 <sup>+0.03</sup> <sub>-0.03</sub>	26
2005kl	14.6 <sub>N</sub>	>> 1	-	-	-	0.2	22,28
2006F	16.7 <sub>N</sub>	0.629	33.70	7 ± 7	42.63 <sup>+0.60</sup> <sub>-0.06</sub>	0.26 <sup>+1.47</sup> <sub>-0.12</sub>	19,*
2006T	17.4 <sub>N</sub>	0.246	32.68	-11 ± 2	42.07 <sup>+0.58</sup> <sub>-0.14</sub>	0.07 <sup>+0.383</sup> <sub>-0.04</sub>	16,*
2006gi	16.3 <sub>N</sub>	0.080	33.18	3 ± 5	42.28 <sup>+0.56</sup> <sub>-0.06</sub>	0.11 <sup>+0.59</sup> <sub>-0.06</sub>	17,*
2006ld	16.0 <sub>N</sub>	0.057	33.74	9 ± 4	42.73 <sup>+0.54</sup> <sub>-0.06</sub>	0.33 <sup>+1.60</sup> <sub>-0.16</sub>	18,*
2007C	15.9 <sub>N</sub>	0.140	32.15	2 ± 4	42.03 <sup>+0.54</sup> <sub>-0.06</sub>	0.065 <sup>+0.317</sup> <sub>-0.032</sub>	20,*
2007I	18.0 <sub>N</sub>	0/1.5	34.75 ± 0.25	10 ± 6	42.33 <sup>+0.82</sup> <sub>-0.10</sub>	0.13 <sup>+1.33</sup> <sub>-0.07</sub>	21,*
2007bi	18.3 <sub>N</sub>	0/1.5	38.8	0 ± 10	43.64 <sup>+0.86</sup> <sub>-0.06</sub>	2.6 <sup>+29.4</sup> <sub>-1.3</sub>	23,*
2007ce	17.4 <sub>N</sub>	0/1.5	36.37	5 ± 3	43.12 <sup>+0.72</sup> <sub>-0.12</sub>	0.80 <sup>+6.33</sup> <sub>-0.44</sub>	43,*
2007rz	16.9 <sub>N</sub>	0.660	33.59	7 ± 7	42.52 <sup>+0.60</sup> <sub>-0.06</sub>	0.20 <sup>+1.14</sup> <sub>-0.10</sub>	24,*
2007uy	16.9 <sub>N</sub>	0.075	32.48	-7 ± 7	41.84 <sup>+0.60</sup> <sub>-0.20</sub>	0.041 <sup>+0.239</sup> <sub>-0.026</sub>	25,*
2008aq	-	-	-	-	-	0.2	44

**Table 4.2.:** Observed magnitude ( $V$ -band,  $B$ -band,  $N =$  unfiltered CCD), extinction (in the  $V$  band), distance modulus, epoch, estimated peak luminosity, and  $^{56}\text{Ni}$  mass for 41 SECC-SNe, together with references for the magnitude and absorption. For SNe 1987M, 2001ig, 2003dh, and 2005bf, estimates for the  $^{56}\text{Ni}$  mass *or* luminosity are available and referenced. The uncertainty on the epoch was taken from Modjaz et al. (2008) and Taubenberger et al. (2009), if available, or estimated from the detection report. SNe without estimate for absorption are referenced with “\*.” For SNe 2007ce, 2007I, and 2007bi, we have no information about the host galaxy, so we assumed an absorption between 0 and 1.5 mag (unfiltered). SN 2004gk is a member of the Virgo cluster and we therefore took the Virgo distance modulus for this SN, as no reliable estimate for the distance of the host galaxy is available. References: <sup>1</sup>Tsvetkov (1986), <sup>2</sup>Begelman & Sarazin (1986), <sup>3</sup>Nomoto et al. (1990), <sup>4</sup>Clocchiatti & Wheeler (1997), <sup>5</sup>Gomez & Lopez (1994), <sup>6</sup>Elias et al. (1990), <sup>7</sup>Nakano et al. (1996), <sup>8</sup>Silverman et al. (2009), <sup>9</sup>Deng et al. (2005), <sup>10</sup>Wood-Vasey & Chassagne (2003), <sup>11</sup>Monard et al. (2004), <sup>12</sup>Maund et al. (2005), <sup>13</sup>Singer & Li (2004), <sup>14</sup>Quimby et al. (2004), <sup>15</sup>Graham & Li (2004), <sup>16</sup>Monard (2006), <sup>17</sup>Itagaki et al. (2006), <sup>18</sup>Frieman (2006), <sup>19</sup>Dimai & Villi (2006), <sup>20</sup>Puckett et al. (2007), <sup>21</sup>Jin et al. (2007), <sup>22</sup>Dimai & Migliardi (2005), <sup>23</sup>Nugent (2007), <sup>24</sup>Parisky & Li (2007), <sup>25</sup>Blondin & Calkins (2008), <sup>26</sup>Maeda et al. (2007), <sup>27</sup>Monard et al. (2004), <sup>28</sup>Taubenberger et al. (2005) but absorption highly uncertain, assume a  $^{56}\text{Ni}$  mass of  $0.2 M_{\odot}$ , <sup>29</sup>Williams et al. (1996) but no light-curve information, assume a  $^{56}\text{Ni}$  mass of  $0.2 M_{\odot}$ , <sup>30</sup>Pugh et al. (2004) but no distance information available, assume a  $^{56}\text{Ni}$  mass of  $0.2 M_{\odot}$ , <sup>31</sup>Clocchiatti et al. (1996), <sup>32</sup>Perlmutter et al. (1990), <sup>33</sup>McNaught et al. (1991) but no light-curve information available, assume a  $^{56}\text{Ni}$  mass of  $0.2 M_{\odot}$ , <sup>34</sup>Clocchiatti et al. (2001) but distance and reddening highly uncertain, assume a  $^{56}\text{Ni}$  mass of  $0.2 M_{\odot}$ , <sup>35</sup>Pollas & Maury (1991) but no light-curve information, assume a  $^{56}\text{Ni}$  mass of  $0.2 M_{\odot}$ , <sup>36</sup>Filippenko & Korth (1991), <sup>37</sup>Tokarz et al. (1995) but no light-curve information available, assume a  $^{56}\text{Ni}$  mass of  $0.2 M_{\odot}$ , <sup>38</sup>Drissen et al. (1996), <sup>39</sup>Gabrijelcic et al. (1997), <sup>40</sup>Nakano et al. (1997), <sup>41</sup>Puckett et al. (2000), <sup>42</sup>Schmidt et al. (2005) but no light-curve information, assume a  $^{56}\text{Ni}$  mass of  $0.2 M_{\odot}$ , <sup>43</sup>Quimby et al. (2007), <sup>44</sup>Brown et al. (2008) but no light-curve information and no detailed epoch information, assume a  $^{56}\text{Ni}$  mass of  $0.2 M_{\odot}$ .

assume a host-galaxy absorption between 0 and 1.0 mag (unfiltered) and treat this range as an uncertainty affecting the estimate. If the Milky Way absorption is not known as well, we assume an uncertainty between 0 and 1.5 mag (unfiltered). Unfiltered magnitudes are treated as bolometric,  $V$ -band magnitudes are converted to bolometric magnitudes using  $m_{\text{Bol}} = m_V - 0.3 \pm 0.2$ , and  $B$ -band magnitudes are converted using  $m_{\text{Bol}} = m_B - 0.8 \pm 0.4$ . For the distance moduli and the errors in the distance we took the values listed in NED<sup>1</sup> for the SN host galaxies (Virgo+GA+Shapley). We then estimated the epoch of detection (which is close to maximum light for most of the SNe of our sample) and the uncertainty in this value from the references given in Table 2. Comparing to light curves of well-observed SNe we determined the value and uncertainty of the peak luminosity, including uncertainties related to absorption, conversion from filtered to bolometric luminosity, and the lack of a well-sampled light curve. Combining this estimate with Equation (4.1), we obtained  $^{56}\text{Ni}$  masses for all 56 SNe of our sample. These are listed in Tables 1 and 2. The possible error of this method is very large, spanning roughly a factor of 20. This uncertainty estimate is very conservative. For most SNe the actual error should be much smaller. However, it is sufficient for our purposes as we show in the Section 4.3.

## 4.2. Spectral Modelling

The spectra were modelled using NC3D, however in a one-dimensional setup. The general principle of such modelling is that different velocity shells are characterised by different element abundances and densities, which lead to different ratios of line fluxes in each shell. The total emissivity of a shell is controlled by the energy deposition, which depends on the density and the  $^{56}\text{Ni}$  mass of the shell and the neighbouring ones. Therefore, each shell has a certain emissivity integrated over all wavelengths and a characteristic line profile caused by the Doppler shift. Each line in the emerging spectrum is the result of the superposition of single components from each shell, with different characteristic widths. A change of the emissivity of one line results in a variety of profile variations of other lines which have to be modelled iteratively until the complex shape of the full spectrum is reproduced. As a complicated structure must be found in order to produce a certain spectrum, the method is quite reliable in determining the velocity field of the ejecta.

We start modelling each spectrum using a SECC-SN model used by Mazzali et al. (2002) for SN 2002ap. Such a model contains all of the information about density, mass, velocity, and element abundances. We correct the  $^{56}\text{Ni}$

<sup>1</sup><http://nedwww.ipac.caltech.edu/forms/byname.html>

SN	Type	Epoch (days)	ID	$v_\alpha$ (km s <sup>-1</sup> )	$v_{50}$ (km s <sup>-1</sup> )	Ref.
1983N	Ib	226	Y	3797	2630	*
1985F	Ib/c	280	Y	4920	2456	*
1987M	Ic	141	Y	5486	3701	*
1990B	Ic	140	N	5405	5091	*
1990I	Ib	237	Y	4828	2899	*
1990U	Ic	184	Y	3488	3021	*
1990W	Ib/c	183	Y	4803	3425	*
1990aa	Ic	141	?	4216	4368	*
1990aj	Ib/c	150-250	?	5122	3034	*
1991A	Ic	177	Y	5262	3636	*
1991L	Ib/c	100-150	N	4140	3316	*
1991N	Ic	274	Y	4278	3239	*
1993J	Iib	205	Y	4029	3070	*
1994I	Ic	147	Y	5057	3967	*
1995bb	Ib/c	150-400	Y	5154	4410	*
1996D	Ic	214	Y	5228	3624	*
1996N	Ib	224	N	3736	3047	*
1996aq	Ib	226	N	5846	3451	*
1997B	Ic	262	Y	4801	3317	*
1997X	Ic	103	Y	4680	3420	*
1997dq	BL-Ic	217	Y	4594	3361	*
1997ef	BL-Ic	287	Y	4681	2733	*
1998bw	BL-Ic	201	Y	6340	3602	*
2000ew	Ic	122	N	4184	3001	*
2001ig	Iib	256	N	5027	3241	Silverman et al. (2009)
2002ap	BL-Ic	185	Y	6219	3729	*
2003bg	BL-Iib	279	N	4736	3205	Hamuy et al. (2009)
2003dh	BL-Ic	229	?	4342	3085	Bersier et. al. (in prep.)
2003jd	BL-Ic	317	N	6850	5593	*
2004ao	Ib	191	N	4555	3158	Modjaz et al. (2008)
2004aw	Ic	236	Y	5007	3234	*
2004dk	?	333	Y	5465	4338	Modjaz et al. (2008)
2004gk	Ic	225	Y	4623	3171	Modjaz et al. (2008)
2004gq	Ib	297	Y	6697	3039	Modjaz et al. (2008)
2004gt	Ic	160	N	4513	3371	*
2004gv	Ib/c	299	Y	4792	3158	Modjaz et al. (2008)
2005N	Ib/c	70-120	N	4001	3591	*
2005bf	Ib	209	N	3864	3628	Modjaz et al. (2008)
2005kl	Ic	160	Y	5074	3365	Modjaz et al. (2008)
2006F	Ib	314	N	4491	2966	Mazzali
2006T	?	371	N	4202	4436	*
2006aj	BL-Ic	204	Y	6540	5100	*
2006gi	?	148	Y	4589	3180	*
2006ld	Ib	280	N	4086	3182	*
2007C	Ib	165	N	4787	3520	*
2007I	BL-Ic	165	N	6085	3277	*
2007Y	Ib	270	Y	4331	3025	Stritzinger et al. (2009)
2007bi	PI?	360	Y	5487	3756	Mazzali
2007ce	BL-Ic	310	Y	6172	4461	Matheson
2007gr	Ic	158	Y	4480	3228	Valenti et al. (2009)
2007ru	BL-Ic	200	Y	5811	3981	Sahu et al. (2009)

SN	Type	Epoch (days)	1D	$v_\alpha$ (km s <sup>-1</sup> )	$v_{50}$ (km s <sup>-1</sup> )	Ref.
2007rz	Ic	292	?	4998	3785	Mazzali
2007uy	Ib	111	Y	6103	4563	Mazzali
2008D	BL-Ib	86	N	5847	4040	Mazzali
2008aq	I Ib	>130	Y	4119	2885	Matheson
2008ax	I Ib	246	N	4100	2821	Taubenberger et al. (2010)

**Table 4.3.:** SN type (classified by early-phase spectra), the epoch of the spectra (relative to maximum light), and the characteristic velocities  $v_\alpha$  (Equation 4.3) and  $v_{50}$  (Equation 4.4) both corrected by 5% per 100 days. The maximum errors of  $v_\alpha$  and  $v_{50}$  are estimated to be  $\pm 14\%$  and  $\pm 10\%$ , respectively. SNe marked with “Y” are fit by the 1D shell modelling quite well. For SNe marked with “N” the central parts of the line profiles are not reproduced well and therefore probably could be improved with multi-dimensional modelling ( $v_\alpha$  would not change much, as  $v_\alpha$  is dominated by the outer parts of the line profiles, where most of the kinetic energy is located). For SNe marked with “?” the spectra are too noisy to categorise as “Y” or “N.” In total we have 12 BL-SNe (2 of them are GRB hypernovae), 17 regular SNe Ic (27 with BL-Ic), 12 regular SNe Ib (13 with BL-Ib), 4 regular SNe I Ib (5 with BL-I Ib), 1 possible PI SN, and 10 SNe for which the classification is unclear (they are certainly of the SECC-SN type). See Taubenberger et al. (2009) for spectra referenced by “\*.”

mass to the values listed in Tables 1 and 2, and we scale the synthetic spectrum to match the observed one.

A clear modelling of the Fe-group lines is impossible for most nebular spectra because these lines are generally weak and are therefore affected by noise and background. The oxygen line is therefore taken as a tracer for the <sup>56</sup>Ni distribution. This means that the <sup>56</sup>Ni zone extends out to the point where the oxygen line can no longer be separated clearly from the background. Hence, a narrow oxygen line results in a more central <sup>56</sup>Ni distribution in our models, but it is important to note that this assumption may not exactly reflect the situation in real SNe. This may cause some epoch-dependent error which we try to quantify by comparing the time dependence of line widths in our models and the observed line widths (see Section 4.3). Above the <sup>56</sup>Ni/O zone we set the density to zero, as this region cannot be probed with the nebular approach. We discuss this in more detail in Section 4.3.

Other elements, such as O, Ca, and C, are distributed over the velocity shells until the line profiles are matched. We pay special attention to fitting the O line, since oxygen is typically the most abundant element in stripped-envelope SECC-SNe.

The modelling process yields the abundances, masses, and velocities which best reproduce the observed spectra (see Figures 4.1 and 4.2 for two examples). The mass and velocity distribution can then be integrated to obtain the total mass and kinetic energy of the model. The ratio of core kinetic energy (in units of 10<sup>50</sup> ergs) to core mass (in units of M<sub>⊙</sub>) is termed  $\alpha$  in this chapter:

$$\alpha \equiv \frac{E_{\text{kin},50}}{M_{\text{ej}}(M_\odot)}. \quad (4.2)$$

This parameter is measured for all 56 SECC-SNe of our sample and is converted to a characteristic velocity (see Table 3),

$$v_\alpha = \left( \frac{2\alpha 10^{40}}{M_\odot[\text{g}]} \right)^{1/2} [\text{km s}^{-1}]. \quad (4.3)$$

The largest uncertainty in the estimate of  $\alpha$  is caused by the background. This background results from observational uncertainties (for example from the subtraction of host-galaxy light) but also from physical processes, which are not treated by the nebular code. Recombination radiation and UV fluorescence can produce weak continua between the strong, characteristic nebular emission lines. The kinetic energy is dominated by the outer parts of the oxygen line and these are superposed on this background, which is difficult to distinguish. To quantify the uncertainty that this causes, we tried different fits for several spectra (see Figure 4.1 and 4.2 for two examples). We found that, depending on the background assumed, variations of up to  $\pm 15\%$  in  $\alpha$  can occur, which translates into an uncertainty of  $\sim 7\%$  in  $v_\alpha$ . An exact treatment of this problem is difficult, as background subtraction is arbitrary to some degree. Therefore, based on this uncertainty, we estimate an error of 7% in  $v_\alpha$ .

As we show in Section 4.2, the line width slowly evolves with time, causing  $v_\alpha$  to decrease by roughly 5% every 100 days. To handle this problem, we corrected  $v_\alpha$  by  $(1 + 0.05(t[\text{days}] - 200)/100)$  and assume that this causes an additional error of  $\pm 5\%$  in  $v_\alpha$ .

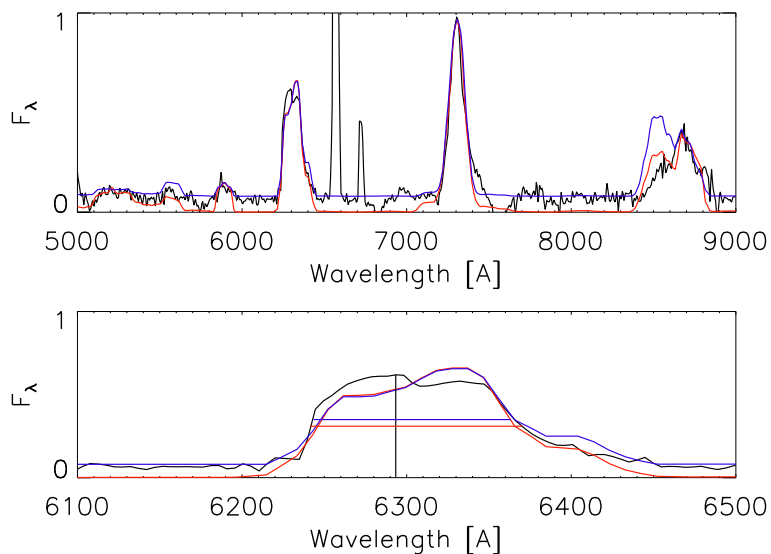


**Figure 4.1.:** Nebular spectrum of SN 1990U ( $v_\alpha = 3450(\text{blue})/3633(\text{red}) \text{ km s}^{-1}$ ) at  $t = 184$  days (black) (upper panel) and the oxygen doublet [O I]  $\lambda\lambda 6300, 6364$  isolated (lower panel). Two models are shown in blue and red, illustrating the uncertainty in the background. This spectrum is the one with the lowest  $v_\alpha$  in our sample (narrow oxygen line). The characteristic velocity is  $v_{50} = 2996(\text{blue})/3124(\text{red}) \text{ km s}^{-1}$ . The horizontal lines show the full width at half-maximum intensity (FWHM).

In addition to  $v_\alpha$ , we also measure the half width of the oxygen doublet [O I]  $\lambda\lambda 6300, 6364$  at half-maximum intensity (HWHM),  $\Delta_{50}$ , for all SNe of our sample. This can be directly converted to a velocity via the redshift

$$v_{50} = \frac{\Delta_{50}}{6300} c, \quad (4.4)$$

where  $c$  is the speed of light and  $\Delta_{50}$  is given in  $\text{\AA}$  units. This is another characteristic velocity of the SN core ejecta, which can be compared to  $v_\alpha$  (see Figure 4.3). There seems to be a linear trend between  $v_{50}$  and  $v_\alpha$ , as expected; exceptions are mostly caused by specific features of some line profiles, as discussed in detail in Section 4.3.

Estimating  $v_{50}$  has the advantage that it can be done easily and it does not require modelling. The disadvantage is that  $v_{50}$  contains some small contribution of the [O I]  $\lambda 6364$  line which causes some error. Since the ratio of [O I]  $\lambda 6300$  to [O I]  $\lambda 6364$  is  $\sim 3$  in the nebular phase, this error is small; it depends on the exact shape of the individual lines, but it should be  $< 20\%$  in the worst case, as we found by superposing Gaussians. More importantly, it is influenced by the shape of the inner line profile (which in some SNe has a double- or even triple-peaked shape) much more than by  $v_\alpha$ . In addition,  $v_{50}$  measures the velocity at one point (half height), while  $v_\alpha$  is the result of an integration over the entire line profile and includes the nonlinear weighting of different emission regions. The background causes some uncertainty in the estimate of  $v_{50}$ . We measure  $v_{50}$  for several SNe while varying the assumptions about the background, and estimate an uncertainty of  $\sim 5\%$ . Moreover, we apply the same time-dependent correction as for  $v_\alpha$  and assume an additional error as for  $v_\alpha$  ( $\pm 5\%$ ). Adding the possible errors due to background,  $^{56}\text{Ni}$  mass estimate, and time evolution of the line width, we estimate a maximum error of  $\pm 14\%$  for  $v_\alpha$  and  $\pm 10\%$  for  $v_{50}$ , which does not necessarily mean that  $v_{50}$  gives a more accurate estimate of the core velocity.

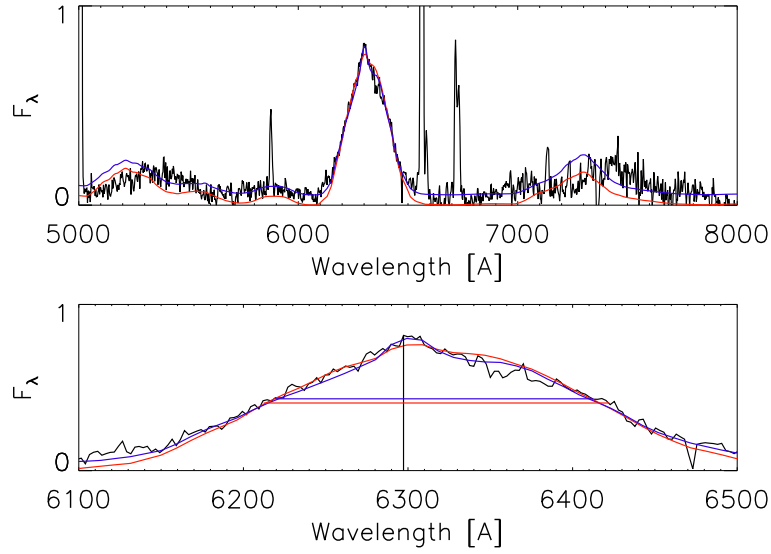


**Figure 4.2.:** Nebular spectrum of the BL-SN 2006aj ( $v_\alpha = 6542(\text{blue})/6870(\text{red}) \text{ km s}^{-1}$ ) at  $t = 204$  days (black) (upper panel) and the oxygen doublet [O I]  $\lambda\lambda 6300, 6364$  isolated (lower panel). Two models are shown in blue and red, illustrating the uncertainty in the background. This spectrum has one of the highest  $v_\alpha$  in our sample (broad oxygen line). The characteristic velocity  $v_{50} = 4992(\text{blue})/5190(\text{red}) \text{ km s}^{-1}$ . The horizontal lines show the FWHM.

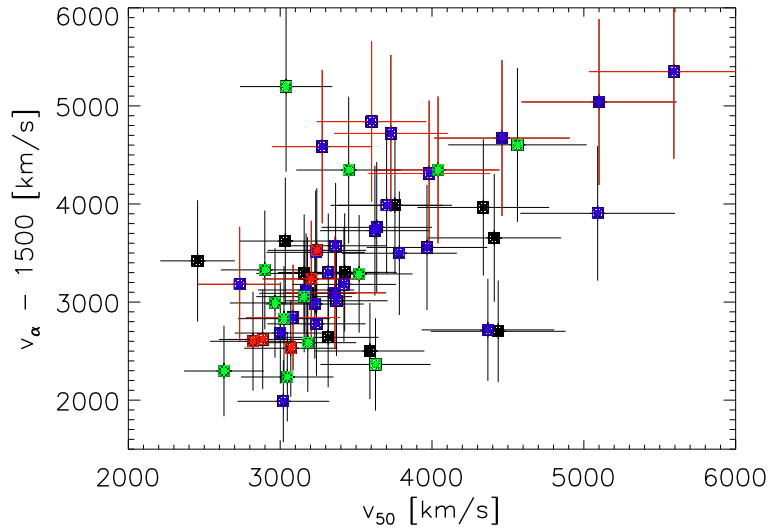


**Figure 4.3.:** The characteristic velocities  $v_{50} [\text{km s}^{-1}]$  vs.  $(v_\alpha - 1500 \text{ km s}^{-1})$ . Both characteristic velocities seem to correlate (as expected). The offset by  $\sim 1500 \text{ km s}^{-1}$  is caused by the different velocities cutoffs used to calculate  $v_{50}$  (half height) and  $v_\alpha$  (full line profile). BL-SNe are shown in red. SNe Ic are marked with blue, SNe Ib with green, and SNe Iib with red dots. Even taking into account the substantial errors, it is obvious that BL-SNe have a large scatter of characteristic core velocities. The data point at the upper right is SN 2003jd (see Table 3). The four BL-SNe at low characteristic velocities are SNe 1997ef, 1997dq, 2003dh, and 2003bg. The intermediate characteristic velocity BL-SNe are (from the left to the right) SNe 2007I, 1998bw, 2002ap, 2008D, 2007ce, and 2006aj. The three BL-SNe 2007I, 1998bw, and 2002ap fall off the  $v_\alpha/v_{50}$  relation owing to the strong broadening toward the base of their [O I]  $\lambda\lambda 6300, 6364$  line.



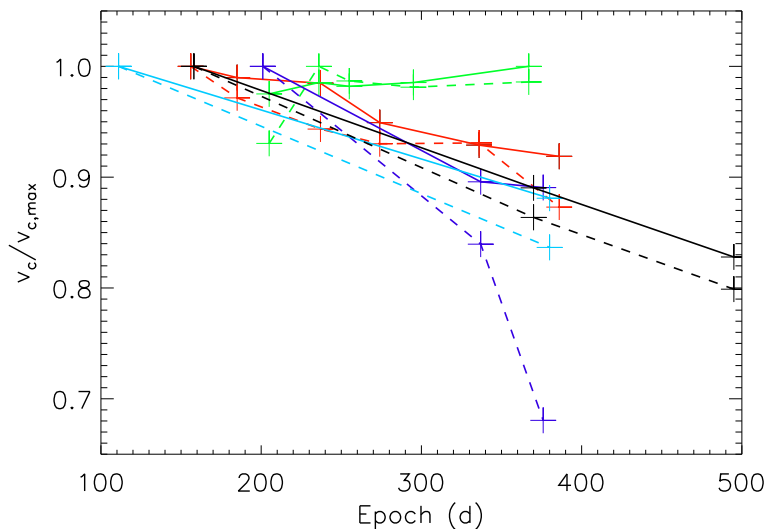


**Figure 4.4.:** Temporal evolution of the normalised characteristic core velocities  $v_\alpha$  (full line) and  $v_{50}$  (dashed line) for SNe 2002ap (red), 1993J (green), 1998bw (blue), 2007uy (light blue), and 2007gr (black). One can see that variations are rather small, about 5% per 100 days. The rapid drop of  $v_{50}$  of SN 1998bw is caused by the “knot” at half height of the oxygen-line profile, which “drops below” half height in the late phase. The increase of line width with time in SN 1993J must be some background effect (note the rise of the red wing at late times, due to H $\alpha$  emission; Figure 4.5) which could not be subtracted. For SNe 1993J, 1998bw, and 2002ap, similar temporal evolution was found by [Taubenberger et al. \(2009\)](#).

## 4.3. Discussion

### 4.3.1. Tests

In order to ensure that the estimates of  $v_\alpha$  are reliable, it is useful to verify that the data do not show behaviours that are not included in our modelling. Since the spectra that we used were obtained at very different SN epochs, it is vital that  $v_\alpha$  does not depend strongly on SN epoch. Figure 4.4 shows the time evolution of  $v_\alpha$  for five SNe with high-quality nebular spectra at several different epochs. The temporal evolution of  $v_\alpha$  is in fact weak, at most  $\sim 10\%$  over 200 days, which is comparable to the general modelling uncertainty. Figure 4.5 shows the corresponding evolution of the line profiles for three of these SNe. In Figure 4.6,  $v_\alpha$  is plotted against SN epoch for the entire sample; no strong time dependence is seen. For  $v_{50}$  the situation is similar. However, as can be seen for example in SN 1998bw (see Figures 4.5 and 4.4), small features in the line profile can have disturbing effects on  $v_{50}$ . The influence of epoch on the characteristic velocities will be more fully discussed below.

To test whether the often highly uncertain estimate of the  $^{56}\text{Ni}$  mass influences  $v_\alpha$ , we alternatively increased and reduced the  $^{56}\text{Ni}$  mass by a factor of five, therefore spanning a factor of 25 in  $^{56}\text{Ni}$  mass for several randomly selected SNe of our sample. This corresponds roughly to the maximum uncertainty in the  $^{56}\text{Ni}$  mass estimates. We found that  $v_\alpha$  depends only weakly on  $^{56}\text{Ni}$  mass: the difference is always less than 2%. For example, when changing the  $^{56}\text{Ni}$  mass of SN 1987M by a factor of 25, from 0.6 to 0.024  $M_\odot$ ,  $v_\alpha$  increased by only 1.3%, which is considerably smaller than other modelling uncertainties. Figure 4.7 shows  $v_\alpha$  against  $^{56}\text{Ni}$  mass; there is clearly no correlation. We conclude that the maximum error introduced by the uncertainty in the  $^{56}\text{Ni}$  mass is  $\pm 2\%$ . The independence of  $v_\alpha$  on  $^{56}\text{Ni}$  mass is discussed in more detail below.

### 4.3.2. Discussion of the Method

We obtained characteristic velocities for 56 SECC-SNe. Before we turn to the results we discuss our methodology. In Section 4.1 we tried to determine the  $^{56}\text{Ni}$  mass for 29 SNe in our sample without calibrated spectra. A typical uncertainty in  $^{56}\text{Ni}$  mass is a factor of 5–10 up and a factor of 2–3 down. The uncertainty upward is mainly caused by

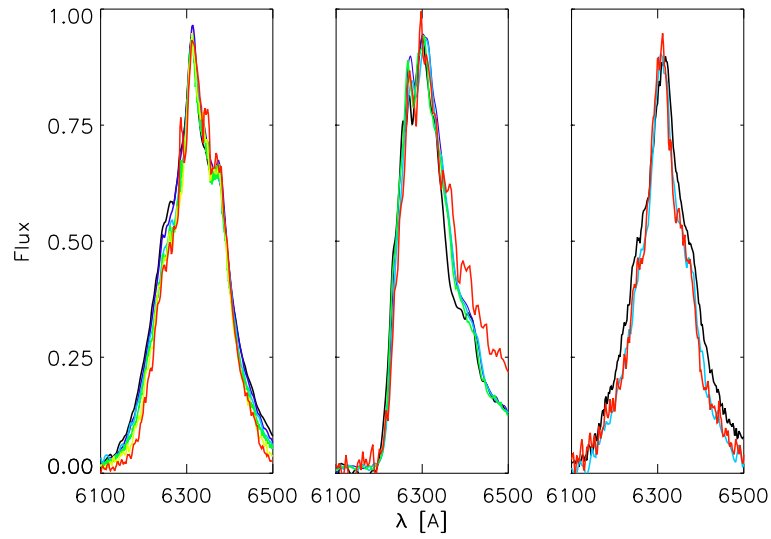


**Figure 4.5.:** The [O I]  $\lambda\lambda$ 6300, 6364 line profiles (left to right) of SN 2002ap (day 156, black; day 185, blue; day 237, violet; day 274, green; day 336, yellow; day 386, red), SN 1993J (day 205, black; day 236, blue; day 255, green; day 295, yellow; day 367, red), and SN 1998bw (day 201, black; day 337, red; day 376, blue). The temporal evolution is quantified in Figure 4.4.

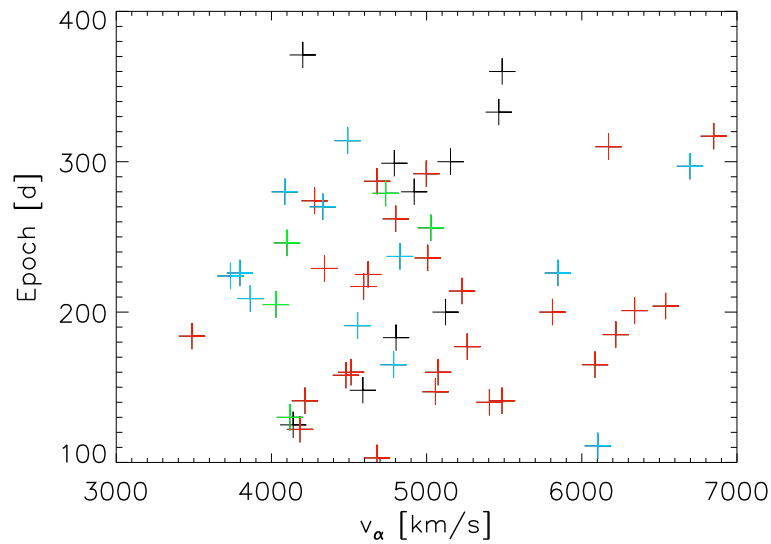


**Figure 4.6.:** The epoch (days after maximum light) vs. characteristic velocity  $v_\alpha$  ( $\text{km s}^{-1}$ ) for all SNe at epochs listed in Table 3. SNe Ic are shown in red, SNe Ib in blue, and SNe IIB in green. SNe without type classification are shown in black. There is no correlation between epoch and characteristic velocity.

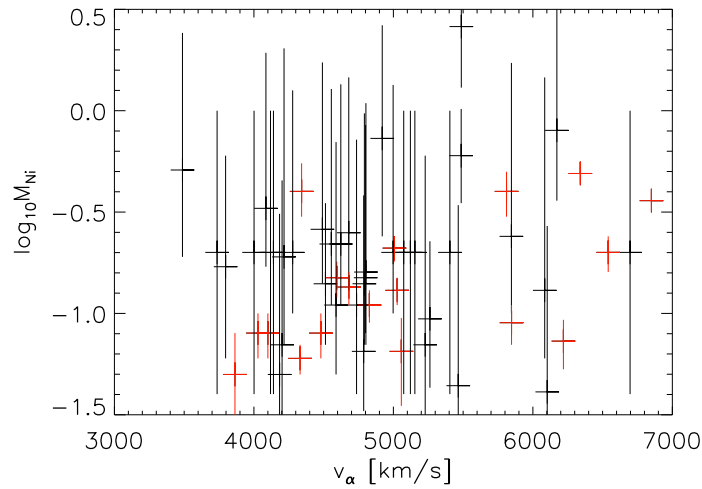


**Figure 4.7.:** The logarithm of  $^{56}\text{Ni}$  mass (in solar mass units) against the characteristic velocity  $v_\alpha$ . No relation is seen for the full sample. There might be a weak correlation for the SNe with  $^{56}\text{Ni}$  mass estimates taken from the literature (shown in red), where the errors in the  $^{56}\text{Ni}$  mass are much smaller. The mean  $^{56}\text{Ni}$  mass of observed SECC-SNe seems to lie around  $0.20 M_\odot$  ( $0.176 M_\odot$  for  $^{56}\text{Ni}$  mass estimates taken from the literature,  $0.225 M_\odot$  for the  $^{56}\text{Ni}$  mass estimates in this section), with a broad diversity. Neglecting the possible PI-SN 2007bi,  $^{56}\text{Ni}$  masses range from  $0.05 M_\odot$  to  $0.80 M_\odot$ . Because of the large uncertainties of our estimates, these upper and lower limits are inaccurate.

the uncertainty in absorption and epoch. There are also uncertainties in distance, magnitude, converting magnitude to bolometric luminosity and finally to  $^{56}\text{Ni}$  mass, which are smaller. The  $^{56}\text{Ni}$  masses might be systematically over- or underestimated and one should be cautious when using these values. The  $^{56}\text{Ni}$  masses listed in the literature (18 SNe) have an average of  $0.176 M_\odot$ , while the SNe with  $^{56}\text{Ni}$  masses estimated in this thesis have an average  $^{56}\text{Ni}$  mass of  $0.225$  (28 SNe, excluding 9 SNe where we could not estimate a  $^{56}\text{Ni}$  mass and excluding a possible PI-SN). Considering the relatively small numbers, the agreement is reasonable but might indicate a small systematic over-estimate of  $^{56}\text{Ni}$  mass. In any case, as shown in Section 4.2, an uncertainty of a factor of 25 in  $^{56}\text{Ni}$  mass will not influence our core velocity estimates significantly.

We checked for possible correlations between  $^{56}\text{Ni}$  mass and  $v_\alpha$ . This could be important in two different ways. First, the uncertain estimate of the  $^{56}\text{Ni}$  mass might introduce some error in the determination of  $v_\alpha$ . This is not the case, however, as shown in Section 4.2. Increasing the  $^{56}\text{Ni}$  mass by a constant factor throughout the ejecta will increase the energy deposited in any shell by the same factor; hence, the relative contribution of each shell to the emission will remain constant. As the emitted energy per particle also remains rather constant (the mass of other elements must be increased accordingly to the  $^{56}\text{Ni}$  mass), the spectrum of each shell does not change much. Therefore, the emerging spectrum is nearly constant apart from small differences arising from the small shift of line ratios in each shell (resulting, for example, from changes of the ionisation balance).

Second, there could be a physical correlation between  $^{56}\text{Ni}$  mass and core ejecta velocities. For the full sample, this does not seem to be the case, as shown in Figure 4.7. However, the large uncertainties in the  $^{56}\text{Ni}$  mass make a stringent conclusion impossible. There might be a weak correlation for the subgroup of 18 SECC-SNe with  $^{56}\text{Ni}$  masses taken from the literature (the uncertainties in these estimates should be much smaller), but the situation is not entirely clear owing to the substantial scatter.

Given that in most spectra we cannot determine the  $^{56}\text{Ni}$  velocity very accurately (in SECC-SN nebular spectra Fe-group lines are usually weak, strongly overlapping, and cannot be easily separated from the background), we can draw no conclusion about possible relations between  $^{56}\text{Ni}$  mass and Fe-group element velocities, which might differ from light-element velocities in aspherical SN models. However, there is no correlation between the total kinetic energy or the total ejecta mass and the characteristic core velocity (for the 15 SNe listed in Table 1). A weak correlation of the ratio  $(E_{\text{ej,tot}}/M_{\text{ej,tot}})^{1/2}$  with the characteristic core velocity is found, albeit with large scatter (see

Figure 4.8).

The epoch at which a SN reaches its nebular phase generally depends on the mass and the ejecta velocity. Some of the spectra are quite early ( $\sim 90$  days after maximum light), though they all seem to be sufficiently nebular to be treated with our modelling. The epochs of the spectra vary between 100 and 400 days (after maximum light), and we have shown in Section 4.2 that this large span of epochs will not influence the results much. From detailed modelling of five SNe with good spectral coverage in the nebular phase (extending over 200 days), we can estimate that the characteristic velocity may decrease by  $\sim 5\%$  every 100 days. This is caused by the decreasing importance of the outer layers, which become less luminous.

In principle, if the behaviour of the positrons and the detailed distribution of  $^{56}\text{Ni}$  were known, we could reproduce this line-width evolution. However, since these parameters are unknown, it is necessary to make some assumptions about both properties. As described in Section 4.2, we assumed that both the  $^{56}\text{Ni}$  distribution and the positron deposition trace the oxygen line profile, leading to an oxygen line with constant width (since we assume local deposition of positron energy). This systematic error causes the discrepancy between the evolution of line width with epoch observed and the constant line width in the modelling, and it is taken into account in our treatment of temporal line-width evolution. Since this temporal evolution is weak, oxygen and  $^{56}\text{Ni}$  cannot be strongly separated in the observed SNe and our modelling approach appears to resemble the physical situation quite well (e.g., a very central  $^{56}\text{Ni}$  distribution would cause a rapid decrease of line width with time).

To enable a direct comparison to a parameter which can be obtained without any detailed modelling, we calculated the half width at half-maximum intensity of the oxygen doublet [O I]  $\lambda\lambda 6300, 6364$ . These two lines are separated by  $\sim 64 \text{ \AA}$ , which translates to a velocity of  $\sim 3000 \text{ km s}^{-1}$ . With decreasing density the intensity ratio of the two lines will shift from 1:1 to 1:3 (Li & McCray 1992, Chugai 1992), and in the nebular phase the ratio should lie somewhere between 1:2 and 1:3. The error in the characteristic velocity caused by the superposition of these two lines will therefore be small.

In Section 4.2 we already mentioned the advantages of both  $v_\alpha$  and  $v_{50}$ . While  $v_\alpha$  is time consuming to compute,  $v_{50}$  is less exact in characterising the velocity of the central ejecta. In Figure 4.3 one can see a rather linear trend between both characteristic velocities, as expected. There are, however, some outliers. The SNe in the upper-left corner (where  $v_\alpha - 1500 \text{ km s}^{-1} \gg v_{50}$ ) are SNe 1998bw, 2004gq, and 2007I. Both BL-SNe (SN 1998bw, 2007I) have very convex line profiles with a broad base and a sharp peak. SN 2004gq, the most extreme outlier, also has a convex shape; in addition, it shows a kink in the line profile, which explains the large difference between  $v_\alpha$  and  $v_{50}$  for this case. The SNe in the lower-right region (where  $v_\alpha - 1500 \text{ km s}^{-1} \ll v_{50}$ ) are SNe 1990aa, 1990B, 2005bf, and 2006T. SN 1990aa has a prominent “spike” exactly at half height in the blue wing of the line profile, artificially increasing  $v_{50}$  without affecting  $v_\alpha$ . SN 1990B has a very steep blue wing. SNe 2005bf and 2006T both have double-peaked [O I] profiles with a very steeply falling blue wing. The width at half height is almost the same as at the base of the line, which explains the low  $v_\alpha/v_{50}$  ratio (see Figure 4.9 for the different line profiles). These examples demonstrate how  $v_{50}$  can give a misleading picture of the characteristic core velocity in some cases. Hence, while in general  $v_{50}$  seems to be a good proxy of core velocity, it should not be used if the [O I] profile shows broad double peaks, spikes, and kinks, or unusually steep or convex wings.

Both estimates of characteristic velocity are affected by the presence of an underlying continuum, which can either be the host galaxy or residual continuum emission from the SN. It is often difficult to distinguish the continuum from the SN spectrum. We tried to overcome this problem setting a characteristic minima around the oxygen line to zero flux by removing some linear function from the spectrum. However, the continuum in most cases is probably not represented by a linear function. Thus, some additional flux is almost always present in the region of an emission line, causing an error in the modelling procedure and in the determination of the half height. Consequently, it is not possible to obtain a single “best” result for a given spectrum. Depending on the quality and the specific shape of a spectrum, there might be a variety of possible background subtractions. To cope with this problem, we tried to model the extrema of what seemed plausible subtractions — of course a rather arbitrary approach. We modelled several different SNe in this manner to get a quantitative estimate of the typical uncertainty and found that an error of  $\pm 7\%$  should cover the plausible range (e.g., see Figures 4.1 and 4.2, where the differences in characteristic velocity for the models shown are about 5%).

Another general uncertainty which we cannot quantify is introduced by possible global asphericities of the SN ejecta. In such a case the projected velocities might be considerably lower than the actual ejecta velocities, so the SN kinetic energy may be underestimated. As long as the ejecta geometry and inclination are unknown, this problem could not be removed by three-dimensional (3D) modelling either.

For 19 SNe ( $\sim 35\%$  of our sample), the shell modelling approach is not adequate to fit the central parts of the

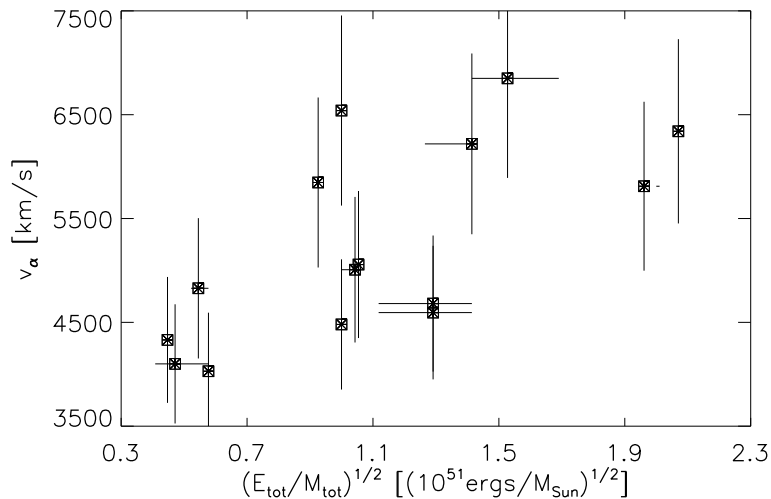


**Figure 4.8.** The characteristic velocity  $v_\alpha$  [ $\text{km s}^{-1}$ ] against the ratio  $(E_{\text{ej,tot}}/M_{\text{ej,tot}})^{1/2} [(10^{51} \text{ ergs}/M_\odot)^{1/2}]$ , which is a proxy for the outer ejecta velocity. There seems to be a weak correlation; however, the scatter is large and there is almost no predictive power in that relation.

oxygen doublet. This suggests that at least 35% of the SECC-SNe of our sample might be aspherical in the very centre (for other explanations, see e.g. [Milisavljevic et al. 2010](#)). Of course, asphericities cannot be ruled out for the rest of our sample, even if the shell modelling approach was sufficient to obtain a good fit to the full line profile. As  $v_\alpha$  is dominated by the outer parts of the line profile, a discrepancy between the model and the observation in the central parts of the line does not cause large errors in  $v_\alpha$ .

## 4.4. Results

Normal SNe of different types seem to have quite similar average core velocities  $v_\alpha$ :  $4402 \text{ km s}^{-1}$  ( $\sigma_v = 403 \text{ km s}^{-1}$ ) for SNe IIb (5 objects),  $4844 \text{ km s}^{-1}$  ( $\sigma_v = 935 \text{ km s}^{-1}$ ) for SNe Ib (13), and  $5126 \text{ km s}^{-1}$  ( $\sigma_v = 816 \text{ km s}^{-1}$ ) for SNe Ic (27). SNe Ic have an average  $v_\alpha$  only slightly higher (5%) than that of SNe Ib and  $\sim 15\%$  higher than that of SNe IIb. SNe BL-Ic have on average a higher  $v_\alpha$ :  $5685 \text{ km s}^{-1}$ , and a similar scatter ( $\sigma_v = 824 \text{ km s}^{-1}$ ) to type Ib and Ic SNe. The sample of SNe BL-Ic comprises 12 SNe — 10 of Type Ic, 1 of Type Ib, and 1 of Type IIb. The uncertainties are rather large, but as long as there is no systematic over- or underestimate for one of these groups the ratio of their averages should be a reliable quantity.

We have shown that if there is a physical correlation between  $^{56}\text{Ni}$  mass and characteristic core velocity it is weak. There also seems to be no correlation between total ejecta mass or kinetic energy and core velocity. There is only a weak correlation between the ratio of total kinetic energy to total ejecta mass and core velocity. On average, SNe with higher outer ejecta velocities have higher core velocities, but this trend is weak and shows a large scatter (see Figure 4.8).

[Matheson et al. \(2001\)](#) found that SNe Ic have significantly higher kinetic energy to mass ratios than SNe Ib, as measured from the line width at half maximum. First we compare the SNe contained in [Matheson et al. \(2001\)](#) and our sample. We find that the velocity estimates of [Matheson et al. \(2001\)](#) and  $v_{50}$  in this section agree rather well (to within  $\sim 10\%$ ) for most SNe, consistent with the estimate of the general uncertainty. The difference is probably caused by the different sizes of the two samples (2 SNe Ib and 12 SNe Ic in [Matheson et al. \(2001\)](#); 13 SNe Ib and 27 SNe Ic in this section). The listing of line widths at different epochs in [Matheson et al. \(2001\)](#) seems to confirm that line width is rather constant after the nebular phase has been reached (as discussed above).

[Taubenberger et al. \(2009\)](#) give the FWHM for 39 SECC-SNe, obtained by fitting the  $[\text{O I}] \lambda\lambda 6300, 6364$  lines with Gaussians. The absolute values and temporal evolution of these velocities are consistent with our  $v_{50}$  estimates: almost all velocities obtained by Gaussian fitting agree with  $v_{50}$  to 10% or better, which is within the estimated errors for  $v_{50}$ . Velocities obtained with Gaussian fitting are often slightly lower than  $v_{50}$ , probably because of

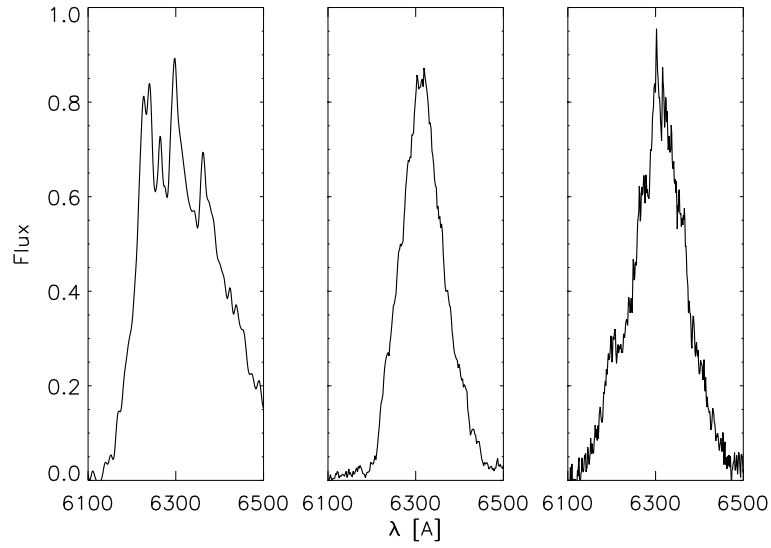


**Figure 4.9.:** Left: SN 1990B, whose steep blue wing causes a small ratio of  $v_{\alpha}$  and  $v_{50}$ . Middle: SN 1983N, which shows an average ratio of  $v_{\alpha}$  and  $v_{50}$ . Right: SN 2004gq, whose convex shape causes a large ratio of  $v_{\alpha}$  to  $v_{50}$ , which is additionally increased by the small notch in the blue wing.

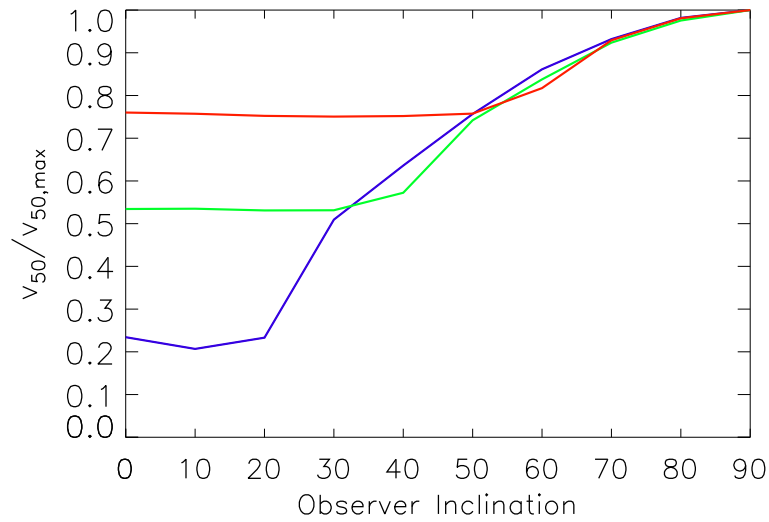


**Figure 4.10.:** Simulated evolution of normalised  $v_{50}$  with observer inclination (in  $^{\circ}$ ,  $0^{\circ}$  polar,  $90^{\circ}$  equatorial view) for a  $^{56}\text{Ni}/\text{O}$  disc with opening angles of  $20^{\circ}$  (blue, lower line),  $40^{\circ}$  (green, central line), and  $60^{\circ}$  (red, upper line). Opening angles of only  $20^{\circ}$  would cause very low projected velocities, which seem not to be observed. Opening angles between  $40^{\circ}$  and  $60^{\circ}$  seem to be able to explain the observed range of projected velocities, and are consistent with the distribution of high and low characteristic BL-SNe (see Figure 3).

the contribution of [O I]  $\lambda 6364$  to  $v_{50}$ . The average velocity for SNe BL-Ic (6 objects) from Gaussian fitting is  $\sim 3670 \pm 860 \text{ km s}^{-1}$ , while the average  $v_{50}$  is  $\sim 4010 \pm 600 \text{ km s}^{-1}$  for these six objects. Since we expect  $v_{50}$  to be slightly higher than velocities obtained from Gaussian fitting, these estimates are consistent.

The velocities of SNe BL-Ic are on average only 10% higher than those of regular SNe Ic. Interestingly, four BL-SNe have core velocities typical of regular SNe. For two of them (SNe 1997ef, 2003dh) the spectra are extremely noisy, so the errors could in principle be larger than the estimated 14% (although we do not expect that), which would allow higher velocities. On the other hand, for the two other SNe BL-Ic with low core velocities (SNe 1997dq, 2003bg) the spectra are rather good, and high core velocities can clearly be ruled out. Since SNe 1997ef and 1997dq are very similar (Mazzali et al. 2004) in light curve and spectral behaviour, it seems likely that our estimate for SN 1997ef (which agrees very well with that for SN 1997dq) is also correct. SN 2003dh has a very small  $v_{\alpha}$ .

For the GRB-SN 2003dh we might observe a projection effect. Given that a GRB was detected, we probably observed the SN close to the poles. If the central region contained an oxygen-rich disc expanding preferentially near the equatorial plane, the projected velocity of the [O I] line would be much smaller for a pole-on view. For example, if the disc had an opening angle of  $45^\circ$ , the projected velocity would be  $\sim 70\%$  of the radial ejecta velocity, which would mean that SN 2003dh would have been observed to have a “regular” (relatively high) BL-SN core velocity had it been observed close to the equator. It is not clear whether the other three BL-SNe with low  $v_{\alpha}$  can be explained in a similar way. One would expect roughly one third of all BL-SNe to be observed close to the poles and two thirds close to the equator, which is roughly consistent with 4 slow, 7 intermediate, and 1 fast BL-SN (Figure 9 shows that there is a rather steep transition from slow to fast between  $40^\circ$  and  $80^\circ$ ).

The ‘disc’ model presented here is only a toy model demonstrating the effect of geometry. Other deformations of the SN core could have similar effects, as long as the dense core ejecta have different velocities in different directions. Such core deformations can be caused by hydrodynamical instabilities, as for example by the standing accretion shock instability (e.g. Janka et al. 2007). However, there are predictions that GRB-SNe or SNe hosting a ‘failed’ GRB may contain structures in their cores quite similar to the ‘disc’ model presented here (e.g. Maeda & Nomoto 2003, Burrows et al. 2005, Nagataki 2009). In such scenarios Fe-group elements are produced preferentially in the polar direction along the path of the GRB propagation, leaving a ‘disc’ of oxygen rich material in the equatorial region.

As the asphericity can be much weaker in the outer layers of the SN than in the centre, this geometrical interpretation is not in conflict with the early-time classification. For SN 1998bw, Tanaka et al. (2007) have shown that the classification as BL-SN (from the early spectra) is not affected much by possible ejecta asphericities.

To test whether this scenario is plausible, we computed 3D nebular spectra of equatorial oxygen discs with different opening angles for several observer inclinations using NC3D. For our simulations we use a spherical grid with  $\sim 6000$  cells. We simulate discs of  $^{56}\text{Ni}$  and oxygen reaching out to  $10,000 \text{ km s}^{-1}$  with opening angles of 20, 40, and 60 degrees. Varying the observer angle in  $10^\circ$  steps from the pole to the equator, we calculate  $v_{50}$  for all three disc opening angles. As can be seen in Figure 4.10, oxygen discs with opening angles between  $40^\circ$  and  $60^\circ$  would be able to explain the observed difference of BL-SNe core velocities and would also roughly agree with the ratio of low and high  $v_{\alpha}$  BL-SNe cores. Discs with larger opening angles would result in smaller variations of the characteristic velocity, while very thin discs would cause larger differences. Of course, there might be some different explanations (e.g., different density profiles of the SN progenitors might cause different ratios of outer and inner velocities), but the geometric explanation is the most straightforward, especially as asphericities are expected for a substantial fraction of SECC-SNe (e.g., Maeda et al. 2008).

It is important to note that GRB-SNe 1998bw and 2006aj both have rather high  $v_{\alpha}$ . In the scenario described above, we argued that GRB-SNe might show low inner ejecta velocities, as one would observe them close from their poles. For GRB/XRF 060218 there is ongoing discussing whether it is a low-energy GRB or an X-ray flash (XRF). An XRF can be produced if the SN shock reaching the surface of the progenitor (shock break-out) runs into dense circum-stellar material. In this case shock break-out photons can be inversely Compton-scattered to high energies by repeated scatterings around the shock (first-order Fermi process), which can produce non-thermal, isotropic X-ray emission (e.g. Wang et al. 2007, Waxman et al. 2007, Suzuki & Shigeyama 2010). In this case the observed X-ray emission would allow no conclusions about the observer’s inclination. Alternatively, and this refers to SN 1998bw as well, SN-GRBs might have larger opening angles than estimated for high-redshift GRBs (the determination of GRB opening angles is highly uncertain anyway, since it is not clear whether the only known method to do so, by measuring jet breaks, is reliable). Therefore, these two objects may challenge the purely geometrical interpretation presented in this thesis. Studying the inner ejecta of future GRB-SNe will shed some

light on this issue.

SN	$\Delta$ [Å] (this work)	$\Delta$ [Å] Milisavljevic et al. (2010)
1985F	$58 \pm 4$	
1990B	$65 \pm 10 / 65 \pm 10$	
1990U	$48 \pm 10$	
1990aa	$45 \pm 10 / 61 \pm 6$	
1990aj	$49 \pm 6$	
1996N	$65 \pm 10$	
1996aq	$63 \pm 6$	
2000ew	$59 \pm 6$	
2002ap	$58 \pm 4$	
2003bg	$38 \pm 8$	
2003jd	$100 \pm 20$	$64 \pm 5$
2004ao	$64 \pm 10$	$65 \pm 3$
2004dk	$72 \pm 10$	
2004gt	$64 \pm 8$	
2005N	$50 \pm 10$	
2005bf	$50 \pm 20$	
2005kl	$65 \pm 10$	$65 \pm 4$
2006ld	$42 \pm 6 / 61 \pm 8$	
2006T	$70 \pm 20$	$63 \pm 3$
2007C	$52 \pm 10 / 50 \pm 10$	
2007I	$45 \pm 10$	
2007bi	$47 \pm 6$	
2008D	$45 \pm 10$	
2008ax	$61 \pm 4$	$64 \pm 1$

**Table 4.4.:** Peak separation measured in this work and by Milisavljevic et al. (2010). Two values are given if three peaks are observed; the separation is then measured from one peak to the next. For all SNe but SN 2003jd the estimates agree rather well. For SN 2003jd the difference is caused by the fact that Milisavljevic et al. (2010) did not measure the separation of the two largest peaks.

In SECC-SNe nebular spectra, the [O I]  $\lambda\lambda 6300, 6364$  doublet often has a double or even triple peaked emission profile. Recently, Milisavljevic et al. (2010) studied these peaks for 20 SECC-SNe and found that they are sometimes separated by  $\sim 64$  Å. Since this coincides with the doublet separation, Milisavljevic et al. (2010) concluded that the multi-peaked line profiles might be caused by the doublet-nature of [O I]  $\lambda\lambda 6300, 6364$ , rather than by ejecta geometry.

There are several problems with this interpretation. First, the [O I]  $\lambda\lambda 6300, 6364$  doublet is optically thin at typical nebular densities of SECC-SNe and therefore a line ratio of 3:1 is expected. Secondly, the observed double-peaks are usually centred around  $6300$  Å and not located at  $6300$  and  $6363$  Å. Thirdly, there are triple-peaks, which cannot be explained by a doublet. And, finally, in our sample there are 24 SNe with clear multi-peaked [O I]  $\lambda\lambda 6300, 6364$  profiles. Measuring their peak separation  $\Delta$  (see Table 4), we find that most double-peaks are not separated by  $64$  Å.

For SNe 2004ao, 2005kl, 2006T, and 2008ax our results agree with those of Milisavljevic et al. (2010). For SN 2003jd, Milisavljevic et al. (2010) did not measure the separation of the two largest peaks, while we do, which explains the different value given in this section.

Although about 50% of the SNe might be consistent with a separation of  $64$  Å (within the large uncertainties), the other 50% are not. For SNe 1985F and 2002ap it seems likely that the second (very weak) peak is caused by the [O I]  $\lambda 6364$  line, since the first peak is roughly at  $6300$  Å while the second is at  $\sim 6360$  Å. For SNe 1990U, 1991aj, 2000ew, 2003jd, 2004ao, 2004gt, 2006T, 2007I, 2007bi, and 2008ax, the two peaks are of similar strength and are centred around  $6300$  Å. The separation observed in SNe 1990U, 1991aj, 2003jd, 2007I, and 2007bi is clearly not consistent with  $64$  Å. For the remaining 12 SNe the situation seems less clear and we refer to Milisavljevic et al.



(2010) for an explanation alternative to geometry. However, geometry could explain all these observations well.

Interpreting the separation of these peaks as a geometrical effect, one obtains typical velocities between  $2000 \text{ km s}^{-1}$  and  $4000 \text{ km s}^{-1}$  ( $1000 \text{ km s}^{-1}$  to  $2000 \text{ km s}^{-1}$  when considering half width) which is of the same order as the characteristic core velocities measured in this chapter. Therefore the observed clustering around  $\sim 3000 \text{ km s}^{-1}$  (close to the  $64 \text{ \AA}$  doublet line separation) is likely a coincidence caused by the typical velocity of the SNe cores. Since the interpretation presented by Milisavljevic et al. (2010) would also require unusually high densities and also has other problems (see above), it seems very unlikely that the double-peaked [O I]  $\lambda\lambda 6300, 6364$  doublet is not caused by geometry in SNe Ib and Ic. For SNe Iib we find an alternative explanation in Section 6, which is however not in conflict with the presence of asymmetries.

## 4.5. Summary

We estimated  $^{56}\text{Ni}$  masses for 29 SNe for which  $^{56}\text{Ni}$  masses were not previously known. Their average agrees with the average of 18 SECC-SN  $^{56}\text{Ni}$  masses estimated before rather well, however there might be a small systematic over-estimate of the  $^{56}\text{Ni}$  mass in this work. Individual estimates might be quite erroneous given the poor quality of the data set. We then measured characteristic velocities for 56 SECC-SN cores, which range from  $3000 \text{ km s}^{-1}$  to  $7000 \text{ km s}^{-1}$  ( $v_\alpha$ ). Several BL-SNe with high-velocity outer ejecta have high-velocity cores as well, but some BL-SNe do not. We have shown that this might be due to ejecta asphericities, which are expected theoretically and might have been detected by different methods before. We found that the average core velocities of SNe Iib are slightly lower than core velocities of SNe Ib and SNe Ic. SNe Ib and Ic have very similar average core velocities. SNe Iib show much less variance ( $\sigma_v \approx 400 \text{ km s}^{-1}$ ) of their core velocities than SNe Ib and Ic ( $\sigma_v \approx 850 \text{ km s}^{-1}$ ).

There seems to be no strong dependence of core velocity on  $^{56}\text{Ni}$  mass. We also checked for correlations between total ejecta mass or kinetic energy and the core velocity and found none. There is only a weak correlation between the ratio of total kinetic energy to total mass and the core velocity (BL-SNe have the highest core velocities on average, but the scatter is so large that there is almost no predictive power). Therefore, although the total mass of a SN might be estimated (if the spectrum is flux calibrated), it is not possible to estimate the SN total kinetic energy from a nebular spectrum with good accuracy, since the core velocity seems to correlate with the outer ejecta velocities only weakly.

The uncertainties in our estimates are rather large. They are caused by the general properties of the method (background subtraction, reddening, time evolution of line width, uncertainty on epoch,  $^{56}\text{Ni}$  distribution, and  $^{56}\text{Ni}$  mass) and are difficult to improve upon when only limited high-quality data are available that cover different SECC-SNe at several different epochs. Therefore more and better data is needed.



## 5. Oxygen Recombination in Stripped-Envelope Core-Collapse Supernovae

In the previous section we have studied the core velocity of 56 SECC-SNe by modelling [O I]  $\lambda\lambda 6300,6363$ , which is by far the strongest emission line in the nebular phase of SECC-SNe. This doublet line is commonly used in the literature to study SECC-SN properties (e.g. Li & McCray 1992, Mazzali et al. 2005, Maeda et al. 2007, Modjaz et al. 2008, Taubenberger et al. 2009, Milisavljevic et al. 2010, Maurer et al. 2010). Since O I is the most abundant ion in CC-SNe (Type Ic, Ib), beside hydrogen (Type II) and helium (Type II, IIb), and since it is the strongest emitter in the nebular phase of SECC-SNe, understanding the formation of its lines is of special importance.

The [O I]  $\lambda\lambda 6300,6363$  doublet is formed by thermal electron excitation of the O I  $2p(^1D)$  state. Higher quantum states ( $n \geq 3$ ) cannot be excited by thermal electrons sufficiently because of the large ratio of excitation energy ( $\sim 9$  eV) and electron temperature ( $\sim 0.4$  eV). However, in most SECC-SNe, the permitted line O I  $\lambda 7774$  [ $3p(^3S) \rightarrow 2p(^3P)$ ] can be observed clearly. It is commonly assumed that this line is powered by oxygen recombination. Since previous studies of central oxygen have focused almost exclusively on [O I]  $\lambda\lambda 6300, 6364$  it is useful to investigate whether extending the analysis to other oxygen lines gives a consistent picture. Furthermore, this can improve the accuracy of the oxygen mass estimate, which is the most abundant element in SECC-SNe.

To investigate the formation of permitted O I lines in detail, in this section temperature-dependent effective recombination coefficients for neutral oxygen are calculated using available atomic data. Missing atomic data are computed in a temperature range typical for SN nebulae using a quantum defect method. The formation of O I recombination lines is investigated using a toy model. Recombination physics and data are implemented in NC3D to derive core ejecta models for two of the best studied SNe Type Ic, 1998bw and 2002ap from modelling their nebular emission spectra so that oxygen recombination line formation is computed consistently with oxygen forbidden line emission. While SN 2002ap can be explained well by a one-dimensional shell model, this seems not to be possible for GRB-SN 1998bw, for which a two-dimensional model is found.

In Section 5.1 temperature-dependent effective recombination rates are obtained for the  $n = 3$  & 4 levels of neutral oxygen and some quantities relevant for oxygen recombination and emission-line formation in CC-SN nebulae are estimated. A one-dimensional shell model for SN 2002ap is described in Section 5.2 and a two-dimensional model for SN 1998bw in Section 5.3 emphasising the role of the O I  $7774 \text{ \AA}$  line. Results are discussed in Section 5.4.

### 5.1. Oxygen lines in the nebular phase of CC-SNe

In this section temperature-dependent effective recombination rates are obtained for the 3s, 3p and 3d triplet and quintet states of neutral oxygen. These rates are used in the nebular code to calculate oxygen recombination line emission. These levels are responsible for O I  $7774, 8446, 9264$  and  $11287 \text{ \AA}$  line emission (see Figure 5.1 for illustration). We further investigate the relevant processes for oxygen recombination and absorption line formation in the nebular phase of CC-SNe.

Recombination into the 2p singlet states is not important in the CC-SN nebular phase. About 80 – 90% of the radioactive energy is deposited in thermal electrons, while only 10 – 20% goes into ionisation (see below). Since the 2p singlet states can be efficiently excited by thermal electron collisions, the population of these levels is predominantly determined by this process.

#### 5.1.1. Effective recombination rates for neutral oxygen

Di-electronic recombination is much weaker than radiative recombination [roughly by a factor of 5 (Nussbaumer & Storey 1983) at 10000 K and decreasing rapidly with temperature] and is not included when calculating the recombination fractions. At high electron densities collisional transitions between excited states can become important. However, for the electron densities expected in the nebular phase ( $n_e < 10^{10} \text{ cm}^{-3}$ ), this effect is weak. At high

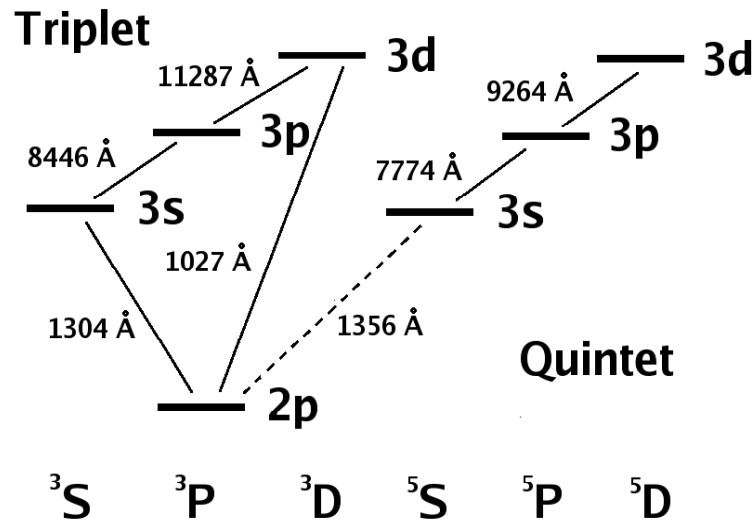


**Figure 5.1:** Neutral oxygen levels that are potentially interesting for the nebular phase of CC-SNe. The singlet states (which are responsible for the nebular oxygen forbidden-line emission) and states with  $n \geq 4$  are not shown. The 2p, 3p and 3d states can be subdivided into several  $j$  sub-states, which are not shown to keep the illustration clear. The wavelengths given represent the mean wavelengths of emission. Lines emitted by the different  $j$  sub-states differ slightly from the values given. For example, the line we refer to as O I 7774 Å in this section consists of three lines at wavelengths 7771.94, 7774.17 and 7775.39 Å. While all transitions indicated by solid lines are permitted with radiative rates of order  $10^{7-8} \text{ s}^{-1}$ , the  $3s(^5S)$  to  $2p(^3P)$  transition (spin-forbidden; dashed line) has a radiative rate of order  $10^3 \text{ s}^{-1}$  only.

electron densities ( $n_e \sim 10^{10} \text{ cm}^{-3}$ ) and low temperatures ( $T \leq 3000\text{K}$ ) collisional recombination can become important (e.g. see Storey & Hummer 1995). However, during the nebular phase only the combinations high density, high temperature (early) and low density, low temperature (late) are important and the contribution of collisional recombination is weak (e.g.  $\sim 20\%$  at  $n_e \sim 10^9 \text{ cm}^{-3}$  and  $T \sim 5000\text{K}$ ).

Therefore we only consider radiative recombination. We are interested in which fraction of recombining electrons reaches a certain atomic level, whether by direct recombination or cascading from higher states. It had been noted by Julienne et al. (1974), Chung et al. (1991) that high quantum levels ( $n \sim 20$ ) might be important to calculate the recombination cascade. In the literature recombination coefficients and radiative rates are available for neutral oxygen up to maximum quantum numbers  $n \sim 10$  (see e.g. TIPTOPbase<sup>1</sup>, NIST<sup>2</sup>).

For azimuthal quantum numbers  $l \geq 3$  one can use the hydrogenic approximation, however for the s, p and d orbitals this should be avoided (e.g. Chung et al. 1991). Therefore, we obtained radiative recombination coefficients and radiative rates for all s, p and d levels of oxygen up to  $n = 20$  using a quantum defect method (QDM) (Bates & Damgaard 1949, Seaton 1958, Burgess & Seaton 1960).

The potential of the atomic core and the inner electrons approaches the asymptotic form  $1/r$  quickly (see Section 2.2.2). The wave functions of the excited states can be described by a hydrogen-like solution, with the difference that the quantum energy levels are shifted owing to the unknown structure of the core potential. This shift of energy levels is described by the quantum defect (defined as the difference between the real and 'effective' principal quantum number) and can be measured in experiments or is determined by more sophisticated calculations.

The wave functions calculated by the QDM are described with sufficient accuracy at radii larger than a few (atomic units) and therefore the QDM is reliable as long as the main contribution of the transition integrals comes from sufficiently large radii and there is no strong cancellation in the integrand. Especially for ground state transitions, where contributions from small radii are important, the QDM is therefore not reliable.

<sup>1</sup><http://cdsweb.u-strasbg.fr/topbase/>

<sup>2</sup><http://www.nist.gov/index.html>

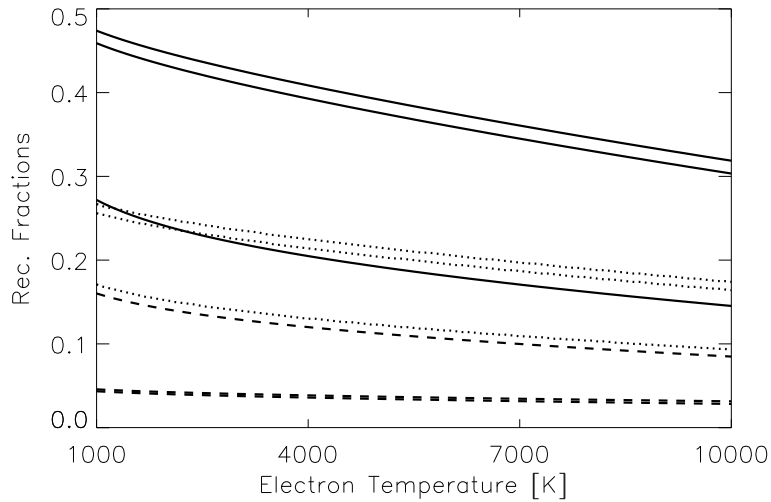


**Figure 5.2.:** Temperature-dependent normalised effective recombination fractions. The quintet states (3d, 3p, 3s from bottom to top) are shown by solid lines. Triplet states (3p, 3s, 3d from bottom to top; note that 3p and 3s do overlap) for the case of optically thin ground state transitions are shown by dashed lines. Triplet states (3d, 3p, 3s from bottom to top) for the case of optically thick ground state transitions are shown by dotted lines.

To improve the calculation, we numerically integrate the electron wave equation (e.g. [Seaton 1958](#))

$$\left[ \frac{d^2}{dr^2} - \frac{l(l+1)}{r^2} - V(r) + E \right] P(E, l; r) = 0 \quad (5.1)$$

inwards, starting with the solution obtained by the QDM at large radii and using a Thomas-Fermi potential

$$V(r) = \frac{2N}{r} \exp(-Z^{1/3}r) + \frac{2(Z-N)}{r} \quad (5.2)$$

where  $Z$  is the charge of the nucleus and  $N$  the number of core electrons. This integration is not part of the QDM, but increases the accuracy of the calculation. The Thomas-Fermi potential gives the correct asymptotic behaviour of the atomic potential for  $r \rightarrow 0$  and  $r \rightarrow \infty$  ([Burke & Robb 1975](#)). The result of this integration is a behaviour of the wave-function for  $r \rightarrow 0$  different than predicted by the QDM. For most transitions the contribution from small radii is approximately zero and therefore the calculated rates are not influenced by this correction. For the transitions which are influenced by the inner parts of the wave function we achieve better agreement with oxygen atomic data provided in the literature at low quantum numbers ( $n < 10$ ).

The difference for ground state radiative transitions relative to NIST recommended data is always less than 50% and the agreement increases considerably with the quantum number of the excited states. For ground state transitions from levels  $n > 5$  the disagreement becomes less than 10%. For transitions between excited states the maximum difference to NIST recommended data is 40% with most transitions agreeing at the 10% level or better. Whenever the disagreement was worse than 10% we replaced our data with the values from the literature. We compared our direct and effective recombination coefficients to [Julienné et al. \(1974\)](#), [Chung et al. \(1991\)](#) and found good agreement (better than 10%), as we did for the effective recombination rates at 1160 K. Our total recombination rate agrees with the value given by [Chung et al. \(1991\)](#) to 1% at 10000 K. However compared to [Aldrovandi & Pequignot \(1973\)](#) our total recombination rate is  $\sim 25\%$  too low. It was noted by [Julienné et al. \(1974\)](#) that neglecting the  $n > 20$  levels might cause an underestimate of  $\sim 20\%$  of the total recombination rate (at temperatures around 1000 K; the effect becomes smaller at higher temperatures). More importantly [Aldrovandi & Pequignot \(1973\)](#) used a hydrogenic approximation for all atomic states, which leads to an overestimate of the recombination rate ([Chung et al. 1991](#)). A comparison to a recent calculation from [Badnell \(2006\)](#) shows that our total radiative recombination rates agree to their results within 15%. To handle that deviation, we normalise our result.

We calculate the ratio of the effective recombination rates of the  $n = 3$  levels to the total recombination rate into excited states and find that this ratio varies only weakly with the number of levels included (it changes by  $\sim 1\%$

State	1000K	2000K	3000K	4000K	5000K	6000K	7000K	8000K	9000K	10000K
3s( <sup>3</sup> S)*	4.6(-2)	4.2(-2)	4.0(-2)	3.8(-2)	3.7(-2)	3.6(-2)	3.4(-2)	3.3(-2)	3.2(-2)	3.1(-2)
3p( <sup>3</sup> P)*	4.3(-2)	4.0(-2)	3.8(-2)	3.6(-2)	3.5(-2)	3.4(-2)	3.2(-2)	3.0(-2)	2.9(-2)	2.8(-2)
3d( <sup>3</sup> D)*	1.6(-1)	1.4(-2)	1.3(-1)	1.2(-1)	1.1(-1)	1.1(-1)	1.0(-1)	9.4(-2)	8.9(-2)	8.5(-2)
3s( <sup>3</sup> S)	2.7(-1)	2.5(-1)	2.4(-1)	2.3(-1)	2.2(-1)	2.1(-1)	2.0(-1)	1.9(-1)	1.8(-1)	1.7(-1)
3p( <sup>3</sup> P)	2.6(-1)	2.4(-1)	2.3(-1)	2.1(-1)	2.0(-1)	2.0(-1)	1.9(-1)	1.8(-1)	1.7(-1)	1.6(-1)
3d( <sup>3</sup> D)	1.7(-1)	1.5(-1)	1.4(-1)	1.3(-1)	1.2(-1)	1.2(-1)	1.1(-1)	1.0(-1)	9.8(-2)	9.3(-2)
3s( <sup>5</sup> S)	4.7(-1)	4.5(-1)	4.3(-1)	4.1(-1)	3.9(-1)	3.8(-1)	3.6(-1)	3.5(-1)	3.3(-1)	3.2(-1)
3p( <sup>5</sup> P)	4.6(-1)	4.3(-1)	4.1(-1)	3.9(-1)	3.8(-1)	3.6(-1)	3.5(-1)	3.3(-1)	3.2(-1)	3.0(-1)
3d( <sup>5</sup> D)	2.7(-1)	2.4(-1)	2.2(-1)	2.1(-1)	1.9(-1)	1.8(-1)	1.7(-1)	1.6(-1)	1.5(-1)	1.5(-1)
4s( <sup>3</sup> S)*	6.9(-3)	7.0(-3)	7.0(-3)	6.8(-3)	6.6(-3)	6.4(-3)	6.2(-3)	6.0(-3)	5.7(-3)	5.5(-3)
4p( <sup>3</sup> P)*	9.0(-3)	9.1(-3)	9.0(-3)	8.7(-3)	8.4(-3)	8.1(-3)	7.8(-3)	7.5(-3)	7.1(-3)	6.8(-3)
4d( <sup>3</sup> D)*	4.2(-2)	4.0(-2)	3.8(-2)	3.7(-2)	3.5(-2)	3.3(-2)	3.1(-2)	2.9(-2)	2.8(-2)	2.6(-2)
4d( <sup>3</sup> F)*	8.5(-2)	6.8(-2)	5.9(-2)	5.1(-2)	4.6(-2)	4.1(-2)	3.8(-2)	3.4(-2)	3.1(-2)	2.8(-2)
4s( <sup>3</sup> S)	3.8(-2)	3.8(-2)	3.7(-2)	3.6(-2)	3.4(-2)	3.3(-2)	3.2(-2)	3.0(-2)	2.9(-2)	2.7(-2)
4p( <sup>3</sup> P)	5.2(-2)	5.2(-2)	5.1(-2)	4.9(-2)	4.7(-2)	4.5(-2)	4.3(-2)	4.1(-2)	3.9(-2)	3.6(-2)
4d( <sup>3</sup> D)	4.5(-2)	4.4(-2)	4.2(-2)	4.0(-2)	3.8(-2)	3.6(-2)	3.4(-2)	3.2(-2)	3.0(-2)	2.9(-2)
4d( <sup>3</sup> F)	8.6(-2)	6.9(-2)	5.9(-2)	5.2(-2)	4.7(-2)	4.2(-2)	3.8(-2)	3.5(-2)	3.2(-2)	2.9(-2)
4s( <sup>5</sup> S)	6.8(-2)	6.9(-2)	6.7(-2)	6.5(-2)	6.3(-2)	6.1(-2)	5.8(-2)	5.5(-2)	5.3(-2)	5.0(-2)
4p( <sup>5</sup> P)	8.1(-2)	8.1(-2)	8.0(-2)	7.7(-2)	7.4(-2)	7.1(-2)	6.8(-2)	6.5(-2)	6.1(-2)	5.8(-2)
4d( <sup>5</sup> D)	7.1(-2)	6.8(-2)	6.5(-2)	6.2(-2)	5.9(-2)	5.6(-2)	5.3(-2)	5.0(-2)	4.7(-2)	4.4(-2)
4d( <sup>5</sup> F)	1.4(-1)	1.1(-1)	9.8(-2)	8.6(-2)	7.7(-2)	7.0(-2)	6.3(-2)	5.8(-2)	5.3(-2)	4.8(-2)

**Table 5.1.:** Effective normalised recombination fraction of O I for triplet and quintet states of O I  $n = 3$  & 4. The rates are normalised on the total radiative recombination rate of [Badnell \(2006\)](#). States indicated by \* show the case of optical thin ground state transitions. Values in brackets indicate a power of 10, e.g.  $a(b) = a \cdot 10^b$ .

(3s), 1% (3p) and 8% (3d) when using a maximum quantum number of  $n = 20$  instead of  $n = 10$  and is not too sensitive to uncertainties in the atomic data (see below), while the total recombination rate is (it increases by 15 - 30% depending on temperature when using a maximum quantum number  $n = 20$  instead of  $n = 10$ ).

Since fitting formulae for the total and ground state recombination rates are available in the literature, we can obtain the total recombination rate into excited states and normalise our effective recombination rates to the total radiative recombination rate. We call this the normalised effective recombination fraction.

The recombination rates used for this normalisation are the total recombination rate of [Badnell \(2006\)](#)

$$R_{OI} = A \left[ \sqrt{\frac{T}{T_0}} \left(1 + \frac{T}{T_0}\right)^{1-B'} \left(1 + \frac{T}{T_1}\right)^{1+B'} \right]^{-1} \text{cm}^3 \text{s}^{-1} \quad (5.3)$$

with  $B' = B + C \exp(-\frac{T_2}{T})$ ,  $A = 6.622 \cdot 10^{-11}$ ,  $B = 0.6109$ ,  $C = 0.4093$ ,  $T_0 = 4.136$ ,  $T_1 = 4.214 \cdot 10^6$  and  $T_2 = 8.770 \cdot 10^4$  and the (direct) ground state recombination rate of [Pequignot \(1990\)](#)

$$R_{GS} = (1.174 + 0.2463x + 0.2144x^2 - 0.0621x^3) \times 10^{-13} T_4^{-0.5} \text{cm}^3 \text{s}^{-1} \quad (5.4)$$

with  $x = \log(1 + T_4)/\log(2)$  and  $T_4 = T/10000$  K. These normalised effective recombination fractions are shown in Figure 5.2 for  $n = 3$ .

In Table 5.1 the normalised effective recombination fractions for triplet and quintet states of O I  $n = 3$  & 4 are shown. For the triplet states we show calculations for the cases of optical thin \* and thick ground states. These numbers have to be multiplied by the total radiative recombination rate to obtain the effective recombination rates. Since the total radiative recombination rate also contains a direct ground state component and since lower levels contain cascade contributions from the higher levels these fractions do not add up to one.

To obtain the effective recombination coefficient for a certain line one has to weigh the upper level by the corre-

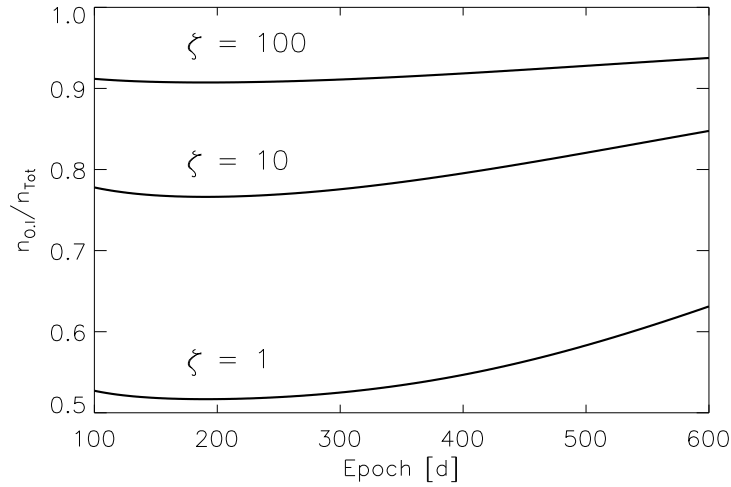


**Figure 5.3.:** The ratio  $n_{OI}/n_{Tot}$  for different clumping factors ( $\zeta = 1, 10, 100$  from bottom to top) calculated for the test model described in Section 5.1.4. Since clumping increases recombination the fraction of neutral oxygen increases with  $\zeta$ .

spending radiative rates<sup>3</sup>. As an example, we calculate the normalised effective recombination coefficient  $f_{6157}$  of the quintet  $4d(^5D) \rightarrow 3p(^5P)$  6157 Å line at 1000K. The radiative rate from  $4d(^5D)$  to  $3p(^5P)$  is given by  $A_{6157} = 7.62(+6) \text{ s}^{-1}$  and the radiative rate  $4d(^5D)$  to  $4p(^5P)$  is given by  $A_{26511} = 6.44(+6) \text{ s}^{-1}$  and therefore

$$f_{6157} = f_{4d(^5D)} \frac{A_{6157}}{A_{6157} + A_{26511}} = 3.8(-2) \quad (5.5)$$

which agrees well with the value given by [Julienne et al. \(1974\)](#) at 1160K.

Since there are uncertainties in our atomic data we want to quantify their influence. We randomly vary all the radiative rates obtained by the QDM by a value between  $\pm 20\%$  and the recombination rates obtained by the QDM by a value between  $\pm 50\%$  several times. This should be larger than the typical error, at least for excited states. The resulting deviations from the standard values are typically a few percent, often  $\ll 5\%$ .

## 5.1.2. Recombination line formation

With the effective recombination rates shown in Table 5.1 it is possible to calculate the strength of all [O I]  $n = 3$  & 4 lines due to recombining electrons.

The population of excited oxygen levels by recombination is implemented in the one dimensional ([Mazzali et al. 2001, 2007](#)) and three dimensional version ([Maurer et al. 2010](#)) of our nebular code and will be used in Sections 5.2 and 5.3 to calculate synthetic recombination lines for SNe 1998bw and 2002ap.

However, to obtain insight into the formation of these lines it is useful to derive some estimates for the recombination line formation. Below, we estimate the strength of the O I 7774 Å line. This is the strongest non-ground state (NGS) recombination line thanks to its high effective recombination rate and transition energy [ $3p(^5P)$  to  $3s(^5S)$ ]. Ground state recombination line observations are usually not available since most spectra reach a minimum wavelength of 3000 Å – 4000 Å only.

The ionisation rate can be calculated using the concept of 'work per ion' (e.g. [Axelrod 1980](#)), which describes the energy lost to thermal electrons in order to produce one ionisation. The ionisation rate per atom and ion is then given by

$$Y_{OI} = \frac{L_{Dep}}{N_{Tot} W_{OI}} \quad (5.6)$$

<sup>3</sup><http://www.nist.gov/index.html>

where  $L_{\text{Dep}}$  is the total deposited luminosity,  $N_{\text{Tot}}$  is the total number of atoms and  $W_{\text{OI}}$  is the energy lost to thermal electrons per ionisation and can be estimated by comparing the ionisation cross-section with atomic and plasma loss functions (more details are given in Section 3.3.3).

During the first several hundred days of a SN, ionisation balance is a valid assumption (Axelrod 1980), therefore

$$Y_{\text{OI}}(1 + \mathcal{R})n_{\text{OI}} = Y'_{\text{OI}}n_{\text{OI}} = R_{\text{OI}}n_e\zeta n_{\text{OII}} \quad (5.7)$$

where  $\mathcal{R}$  is the recycling fraction (recombination radiation causes further ionisation and  $\mathcal{R}$  is expected to have a value between 0.3 and 0.5; Axelrod 1980) and  $\zeta$  is the clumping factor (explained in more detail below), defined as the inverse of the filling factor (Li & McCray 1992).

Since oxygen is the dominant element in CC-SNe cores [ $\sim 55\%$  in SN 2002ap and  $\sim 75\%$  in SN 1998bw, as obtained from our modelling in Sections 5.2 and 5.3; see also Mazzali et al. (2001, 2007)] and the degree of ionisation of oxygen is rather high (roughly 10 – 50%; Figure 5.3) it is a reasonable simplification to neglect all elements besides the iron-group elements and oxygen when calculating the ionisation balance and to assume that all electrons are provided by oxygen and by iron, which is assumed to be 100% singly ionised. Therefore

$$Y'_{\text{OI}}n_{\text{OI}} \sim R_{\text{OI}}(n_{\text{OII}} + n_{\text{Fe}})\zeta n_{\text{OII}} \quad (5.8)$$

which gives

$$\begin{aligned} \frac{n_{\text{OI}}}{n_{\text{Tot}}} &\sim 1 - \frac{n_{\text{Fe}}}{n_{\text{Tot}}} - \frac{R_{\text{OI}}n_{\text{Fe}}\zeta + Y'_{\text{OI}}}{2R_{\text{OI}}n_{\text{Tot}}\zeta} \\ &\times \left( -1 + \sqrt{1 + \frac{4Y'_{\text{OI}}R_{\text{OI}}(n_{\text{Tot}} - n_{\text{Fe}})\zeta}{(R_{\text{OI}}n_{\text{Fe}}\zeta + Y'_{\text{OI}})^2}} \right) \\ &\sim 1 - \frac{n_{\text{Fe}}}{n_{\text{Tot}}} + \frac{R_{\text{OI}}n_{\text{Fe}}\zeta + Y'_{\text{OI}}}{2R_{\text{OI}}n_{\text{Tot}}\zeta} \\ &- \sqrt{\frac{Y'_{\text{OI}}(n_{\text{Tot}} - n_{\text{Fe}})}{R_{\text{OI}}n_{\text{Tot}}^2\zeta}}, \quad \frac{Y'_{\text{OI}}(n_{\text{Tot}} - n_{\text{Fe}})}{R_{\text{OI}}n_{\text{Tot}}^2\zeta} \gg 1 \\ &\sim 1 - \frac{n_{\text{Fe}}}{n_{\text{Tot}}} \\ &- \frac{Y(n_{\text{Tot}} - n_{\text{Fe}})}{(R_{\text{OI}}n_{\text{Fe}}\zeta + Y'_{\text{OI}})n_{\text{Tot}}}, \quad \frac{Y'_{\text{OI}}(n_{\text{Tot}} - n_{\text{Fe}})}{R_{\text{OI}}n_{\text{Tot}}^2\zeta} \ll 1 \end{aligned} \quad (5.9)$$

In Figure 5.3 this ratio is computed for a test model described in Section 5.1.4 using clumping factors of 1, 10 and 100. The total luminosity of any recombination line X of oxygen relative to the total deposited luminosity is then given by

$$\begin{aligned} \frac{L_X}{L_{\text{Dep}}} &= Y'_{\text{OI}}n_{\text{OI}}V E_X f_X L_{\text{Dep}}^{-1} \\ &= (1 + \mathcal{R}) \frac{E_X f_X}{W_{\text{OI}}} \left( \frac{n_{\text{OI}}}{n_{\text{Tot}}} \right) \end{aligned} \quad (5.10)$$

where  $E_X$  is the energy and  $f_X$  is the normalised effective recombination fraction of the line. Usually one can assume  $4Y'_{\text{OI}}R_{\text{OI}}n_{\text{Tot}}\zeta \gg (R_{\text{OI}}n_{\text{Fe}}\zeta + Y'_{\text{OI}})^2$ ; see Section 5.1.4.  $L_{\text{Dep}}$  (e.g. Axelrod 1980) and all other variables (besides the temperature) can be calculated for any ejecta model and Equation 5.10 can be evaluated directly. The temperature can be determined by balancing heating and cooling taking into account several hundred emission lines (therefore an exact estimate of the temperature is difficult) and varies between 8000 K and 2000 K at the epochs of interest (100 to 600 days). A sufficiently exact estimate can be obtained assuming a constant temperature of  $\sim 4000$  K (see Section 5.1.4).

The luminosity of any oxygen recombination line is directly proportional to the normalised effective recombination fraction  $f_X$  and the energy of the transition  $E_X$  [eV]. The recombination line luminosity is influenced only weakly by the clumping factor  $\zeta$  (which changes the ionisation fraction). The oxygen NGS recombination lines



will be weak in general [taking  $n_{\text{OI}}/n_{\text{Tot}} \sim 0.5$ ,  $f_{7774} \sim 0.4$ ,  $E_{7774} \sim 1.6$  eV and  $W_{\text{OI}} \sim 75$  eV the strongest NGS oxygen recombination line (7774 Å) carries less than 1.0% of the total luminosity] and we will neglect all other NGS oxygen recombination lines in the rest of this section. They are calculated by the nebular code, but in the nebular spectra of SNe 1998bw and 2002ap no oxygen recombination lines other than 7774 Å can be identified.

### 5.1.3. Excitation of the O I 7774 Å line

We will find in Sections 5.2 and 5.3 that the luminosity provided by recombination is not sufficient to explain the observations of the 7774 Å line earlier than  $\sim 250$  days. Therefore, in this section we investigate other excitation mechanisms which might operate simultaneously with recombination.

Ground-state excitation by thermal electrons can clearly be ruled out. All transitions from  $n \geq 3$  to the ground state have energies larger than 9 eV, which makes thermal excitation by electrons of temperatures  $\sim 0.5$  eV ineffective.

Non-thermal excitation by the same electrons causing ionisation (which are produced by Compton-scattering of  $\gamma$ -rays emitted by  $^{56}\text{Co}$  decay) is also too weak. The ratio of the cross-sections for electron impact excitation and ionisation (at the high electron energies which are of interest here) can be approximated by (e.g. Rozsnyai et al. 1980)

$$\frac{\sigma_{n\ell \rightarrow n'\ell'}}{\sigma_{n\ell}} \sim 1.66 \frac{f_{n\ell \rightarrow n'\ell'} E_{n\ell}}{N_{n\ell} E_{n\ell \rightarrow n'\ell'}} \quad (5.11)$$

where  $E_{n\ell \rightarrow n'\ell'}$  is the transition energy,  $E_{n\ell}$  the ionisation energy,  $N_{n\ell}$  is the number of electrons in the shell  $n, \ell$  and  $f_{n\ell \rightarrow n'\ell'}$  the oscillator strength of the transition. For allowed ground state transitions of neutral oxygen the oscillator strengths are of the order of  $10^{-2}$  decreasing with increasing quantum number (Bell & Hibbert 1990). The total excitation rate into triplet states is  $\sim 5\%$  of the ionisation rate only. The excitation rates of quintet states by non-thermal (high-energetic) electrons is even lower, since the excitation cross-sections of spin-forbidden lines strongly decrease with electron energy, as compared to allowed transitions (e.g. Ralchenko et al. 2008).

Therefore, non-thermal excitation is not important compared to recombination for populating excited levels. In addition, if the O I 7774 Å line was excited by non-thermal electrons, one would expect the ratio of the line to the total luminosity to be approximately constant at all epochs, which is clearly not observed (this ratio in fact decreases considerably at late epochs).

Although it is generally assumed that the SN is optically thin during the nebular phase, some lines can still be optically thick (especially ground state transitions). As we show here, the optical depth of the 7774 Å transition is still high, even at epochs of  $\sim 200$  days because the  $3s(^5S)$  level is populated by recombining electrons.

We estimate the time-dependent optical depth of the 7774 Å line resulting from recombination taking into account the effective recombination rates, resonance scattering of the  $3s(^5S)$  to  $2p(^3P)$  transition as well as the recycling of ground state recombination radiation.

Based on Equations 5.8 and 5.9, the number density of the  $3s(^5S)$  state relative to the total density is approximately given by

$$\begin{aligned} \frac{n_{3s(^5S)}}{n_{\text{Tot}}} &\sim \frac{f_{3s(^5S)} R_{\text{OI}} (n_{\text{Fe}} + n_{\text{OII}}) \zeta n_{\text{OII}}}{(A' + C) n_{\text{Tot}}} \\ &\sim \frac{f_{3s(^5S)} Y'_{\text{OI}} \tau \left(\frac{n_{\text{OI}}}{n_{\text{Tot}}}\right)}{A}, \quad A \gg A' \gg C \\ &\sim (1 + \mathcal{R}) \frac{f_{3s(^5S)} \tau_0 L_{\text{Dep}} \left(\frac{n_{\text{OI}}}{n_{\text{Tot}}}\right)^2 \zeta}{AVW_{\text{OI}}} \end{aligned} \quad (5.12)$$

defining  $A'$  as the reduced (due to self-absorption) radiative rate

$$A' = A \frac{1 - \exp(-\tau)}{\tau} \sim \frac{A}{\tau}, \quad \tau \gg 1 \quad (5.13)$$

from the  $3s(^5S)$  to the ground state, where  $\tau$  is the Sobolev optical depth of this ground state transition

$$\tau \sim \frac{\lambda_{1355}^3 t g_{3s(^5S)} A_{1355} n_{\text{OI}} \zeta}{8\pi g_{2p(^3P)}} \sim \tau_0 \zeta n_{\text{OI}}, \quad n_{\text{OI}} \gg n_{3s(^5S)} \quad (5.14)$$

with the ground state transition wavelength  $\lambda_{1355} = 1355 \text{ \AA}$ ,  $t$  the epoch in seconds,  $V$  the volume in  $\text{cm}^3$ ,  $A_{1355}$  the radiative rates from the  $3s(^5S)$  to the ground state (note that the ground state is split into three  $j$  sub-levels and appropriate weights have to be used; also the radiative rates of these  $j$  sub-state transitions differ). The weights of the upper and lower states are  $g_{3s(^5S),2p(^3P)}$ ;  $f_{3s(^5S)}$  is the normalised effective recombination fraction into the  $3s(^5S)$  state and  $C$  is the de-excitation rate due to thermal electrons which is much smaller than  $A/\tau$ . The  $3s(^5S)$  to  $2p(^3P)$  transition is spin-forbidden but dipole-allowed and therefore collisional rates are weaker than radiative rates by several orders in magnitude (van Regemorter 1962) for typical SN nebular densities. For  $n_{O}\zeta > 10^9 \text{ cm}^{-3}$  this assumption breaks down since  $C$  and  $\tau$  will increase with density and clumping factor.

Equation 5.12 can be used to calculate the Sobolev optical depth of the  $7774 \text{ \AA}$  line

$$\tau_{3s(^5S)} \sim \frac{\lambda_{7774}^3 t g_{3p(^5P)} A_{7774} n_{3s(^5S)} [\zeta]}{8\pi g_{3s(^5S)}}, \quad n_{3s(^5S)} \gg n_{3p(^5P)} \quad (5.15)$$

with the transition wavelength  $\lambda_{7774} = 7774 \text{ \AA}$ ,  $t$  the epoch in seconds,  $A_{7774}$  the radiative rates from the  $3p(^5P)$  to the  $3s(^5S)$  state (note that the  $3p(^5P)$  state is split into three  $j$  sub-levels and appropriate weights have to be used) and  $g_{3p(^5P),3s(^5S)}$  the weights of the upper and lower states. Again we compare this estimate with numerical results from NC3D in Section 5.1.4.

At this point it is important to review the concept of clumping in more detail. It is assumed that the ejecta are distributed into small ‘‘blobs’’ with size much smaller than the typical scale of the SN, covering the SN volume homogeneously (e.g. Li & McCray 1992). Therefore, although the optical depth is increased locally in the emitting region, the global optical depth of the SN remains constant. This means that, when scattering radiation from remote regions of the SN, the opacity is not influenced directly by clumping. On the other hand, when scattering radiation in the emission region, the optical depth increases proportionally to the clumping factor.

In addition, there is an increase of the ratio  $\frac{n_{3s(^5S)}}{n_{\text{tot}}}$  (see Equation 5.12), which results from the increased self-absorption of ground state transition radiation. Therefore, even when scattering radiation from remote regions, clumping increases the optical depth and so it does influence the  $7774 \text{ \AA}$  resonance scattering of background radiation.

The  $3p(^5P)$  state is separated from the  $3s(^5S)$  state by  $\sim 1.6 \text{ eV}$ , therefore thermal electron excitation is possible, but the population of the  $3s(^5S)$  state by thermal electron excitation is too low. Therefore the state must be populated by recombining electrons.

The thermal electron excitation coefficient from  $3s(^5S)$  to  $3p(^5P)$  is given by

$$C_{3p(^5P)} \sim 8.6 \times 10^{-6} \frac{n_e \zeta}{T^{1/2}} \frac{\Omega_{7774}}{g_{3s(^5S)}} \exp\left(-\frac{E_{7774}}{kT}\right) \equiv C_0 n_e \zeta \quad (5.16)$$

where all constants have the same meaning as in Equation 5.15,  $E_{7774}$  is the energy corresponding to  $7774 \text{ \AA}$  and  $\Omega_{7774} = 25.1/40.2$  (at 5000/10000 K; Bhatia & Kastner 1995) is the effective collision strength of the  $O \text{ I } 7774 \text{ \AA}$  transition. One can compare the population of the  $3p(^5P)$  state due to thermal electron collisional excitation and recombination respectively by calculating their ratio

$$\begin{aligned} \mathcal{R}_{3p(^5P)} &= \frac{C_{3p(^5P)} n_{3s(^5S)}}{Y_{O \text{ I}} n_{O \text{ I}} f_{3p(^5P)}} \\ &= (1 + \mathcal{R}) C_0 \frac{f_{3s(^5S)}}{f_{3p(^5P)}} \frac{\tau_0}{A} (n_{\text{Tot}} - n_{O \text{ I}}) n_{O \text{ I}} \zeta^2 \end{aligned} \quad (5.17)$$

The ratio of the  $O \text{ I } 7774 \text{ \AA}$  luminosity induced by thermal electron excitation compared to the total deposited luminosity is then given by

$$\begin{aligned} \frac{L_{3p(^5P)}}{L_{\text{Dep}}} &\sim (1 + \mathcal{R})^2 \frac{C_0 E_{7774} f_{3s(^5S)} \tau_0}{W_{O \text{ I}} A} \left(1 - \frac{n_{O \text{ I}}}{n_{\text{Tot}}}\right) n_{O \text{ I}}^2 \zeta^2 \\ &\sim 10^{-21} t[\text{days}] \left(1 - \frac{n_{O \text{ I}}}{n_{\text{Tot}}}\right) n_{O \text{ I}}^2 \zeta^2, \quad T = 5000 \text{ K} \end{aligned} \quad (5.18)$$

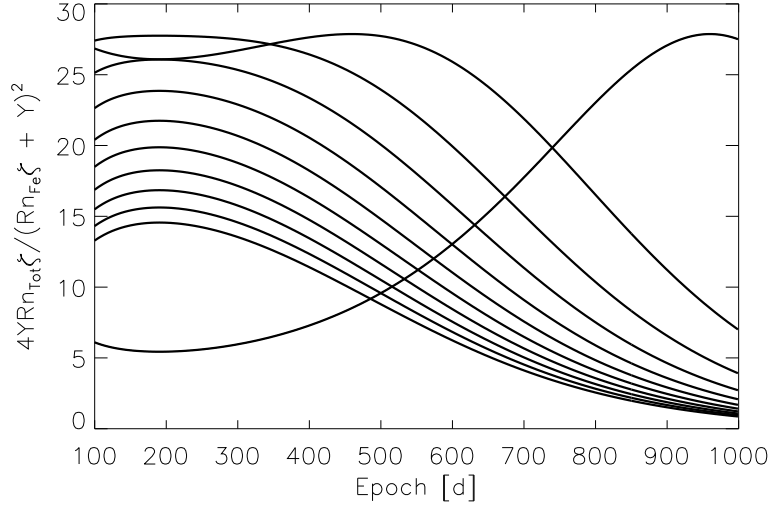


**Figure 5.4.:** The ratio  $4Y'_{O1}R_{O1}n_{Tot}\zeta / (R_{O1}n_{Fe}\zeta + Y'_{O1})^2$  for different clumping factors ( $\zeta = 1, 10, 20, 30, 40, 50, 60, 70, 80, 90$  and  $100$  from top to bottom) at 1000 days calculated for the same model as used in Figures 5.3, 5.5 and 5.6. For this model the ratio is much larger than one for any reasonable clumping factor (1 - 100) at epochs earlier than 600 days.

This estimate becomes invalid for  $n_{O1}\zeta > 10^9 \text{ cm}^{-3}$  since Equation 5.12 had been used for its derivation. Equation 5.18 is compared to results from our nebular code in Section 5.1.4. Whether collisional excitation of the O I 7774 Å line is negligible depends mainly on the temperature, which decreases with time, on the density of neutral oxygen, which decreases with  $t^{-3}$ , and on the clumping factor. Therefore, especially for early epochs (high temperature, high density) and for large clumping factors ( $\zeta \gg 1$ ) the O I 7774 Å line may be excited by thermal excitation of recombining electrons. Around 150 days the core (oxygen) density of CC-SNe is typically of order  $10^{7-8} \text{ cm}^{-3}$ , which gives  $\frac{L_{3p(5P)}}{L_{Dep}} \sim (10^{-5} \text{ to } 10^{-3})\zeta^2$  assuming a temperature of 5000 K.

From the above considerations it becomes clear that clumping influences the recombination line strength only weakly, but increases the effect of resonance scattering and thermal excitation of the O I 7774 Å transition strongly. For both processes the  $3s(5S)$  population is provided by recombination and not by thermal electron excitation from the ground level.

#### 5.1.4. Test Model

In Section 5.1.2 and 5.1.3 we have derived several estimates for quantities relevant for calculating O I 7774 Å nebular emission. To derive these estimates, we used some approximations. These are justified here by comparison to results from the nebular code, which are not based on these approximations and will show deviations as soon as our approximations fail. An important difference is introduced by the temperature. While the electron temperature is calculated considering hundreds of emission lines in the nebular code, this is not possible for our estimates and we use a temperature of 4000 K for the calculations.

To perform these tests we set up a test one-zone model with a total mass  $M_{Tot} \sim 0.5 M_{\odot}$ , an expansion velocity of 5000 km/s, containing 80% oxygen, 10%  $^{56}\text{Ni}$ ,  $\sim 9\%$  carbon, and other elements like calcium, magnesium and sodium.

Usually one can assume  $4Y'_{O1}R_{O1}n_{Tot}\zeta / (R_{O1}n_{Fe}\zeta + Y'_{O1})^2 \gg 1$ , which depends on the iron to oxygen ratio, the deposited luminosity, the electron temperature and the clumping factor. In Figure 5.4 we show this ratio for our test model using clumping factors of one to one hundred. At any epoch of interest (100 to 600 days) and for any clumping factor the assumption is valid. The assumption may fail for clumping factors  $\sim 1$  at lower densities and for higher  $^{56}\text{Ni}$  to oxygen ratios. For clumping factors  $\zeta \gg 1$  the assumption will hold for any plausible CC-SN scenario.

In Figures 5.5 and 5.6 we compare Equations 5.10 and 5.15 (temperature set to  $T = 4000 \text{ K}$ ) with the results obtained from our nebular code using our test model. The temperature is kept constant in the calculation, while it

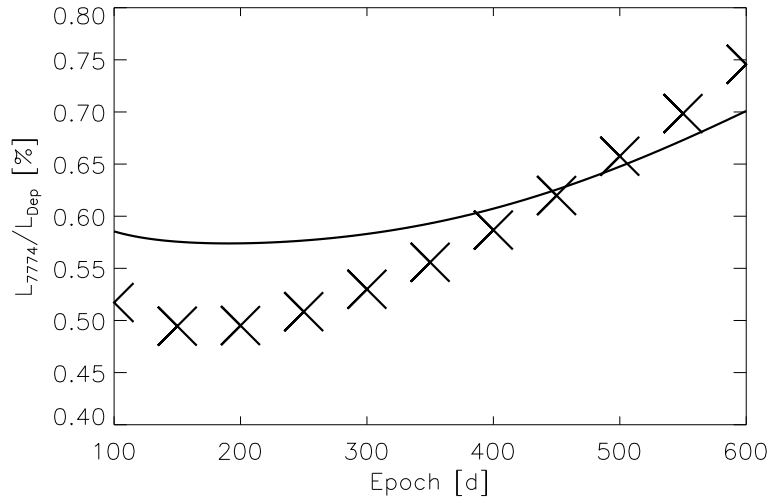


**Figure 5.5.:** The solid line is a computation of Equation 5.10 performed for the O I 7774 Å line assuming a constant temperature of 4000 K at all epochs for the one-zone model described in the text. The luminosity of this line is compared to the total deposited luminosity. The results are given in %. The recycling fraction was set to the ratio of ground state to total recombination rate at 4000 K. The crosses show data points obtained with the nebular code for the same model, where the temperature is computed at all epochs self-consistently and ionisation is treated in detail. Considering the large change of the temperature between 100 and 600 days (6800 K and 2800 K respectively) the agreement seems reasonable (note that the temperature calculated by the code drops below 4000 K around 450 days). The minimum around 200 days is present in both curves.

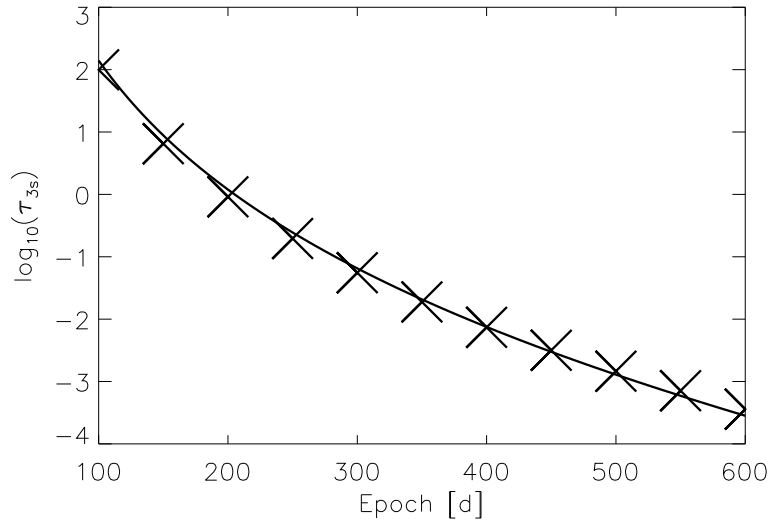


**Figure 5.6.:** The solid line shows a computation of Equation 5.15 performed for the logarithmic line opacity of the O I 7774 Å line assuming a constant temperature of 4000 K at all epochs for a one-zone model described in the text. The crosses show data points obtained with the nebular code for the same model, where the temperature is computed at all epochs self-consistently and ionisation is treated in detail. The agreement is good, especially around 450 days, when the simulated temperature drops below 4000 K, which we assumed in our calculation. The line optical depth is greater than one until day  $\sim 200$ .

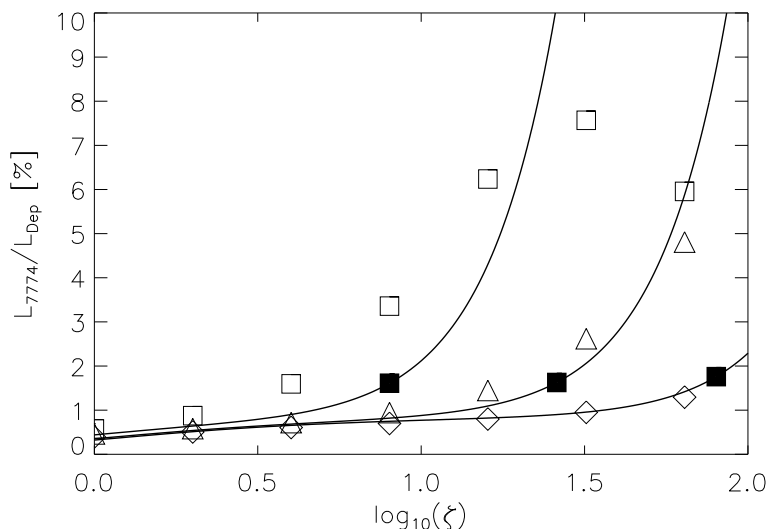


**Figure 5.7.:** The O I 7774 Å line luminosity from pure recombination and thermal excitation of recombining electrons relative to the total deposited luminosity in % for the test models described in the text using clumping factors between 1 and 100. Solid lines show estimates obtained from Equations 5.10 and 5.18 for oxygen densities of  $10^7$ ,  $10^{7.5}$  and  $10^8$   $\text{cm}^{-3}$  from bottom to top. Results from our nebular code are shown by diamonds ( $10^7$   $\text{cm}^{-3}$ ), triangles ( $10^{7.5}$   $\text{cm}^{-3}$ ) and squares ( $10^8$   $\text{cm}^{-3}$ ). The agreement is good. Small deviations are predominately caused by our rough approximation of the temperature. Filled squares mark  $n_{\text{O}}\zeta \sim 10^9$   $\text{cm}^{-3}$  where our estimates are expected to become inaccurate. At  $n_{\text{O}}\zeta > 10^{9.3}$   $\text{cm}^{-3}$  our approximation breaks down completely, but this regime is probably not important for the nebular phase of stripped CC-SNe. The 7774 Å luminosity increases with the increasing clumping until the density becomes high enough to depopulate the  $3s(^5\text{S})$  state by thermal electron collisions effectively.

is calculated self-consistently in the nebular code, influencing the recombination fraction and recombination rate. Also the ionisation of ions other than O I and Fe I has been neglected in the calculation. Despite the approximations, the agreement seems reasonable.

In Figure 5.7 we compare the O I 7774 Å flux from pure recombination and electron scattering of recombining electrons (Equations 5.10 and 5.18) to results obtained from our nebular code using variations of our test model. We set the epoch to 150 days and use oxygen densities of  $10^7$ ,  $10^{7.5}$  and  $10^8$   $\text{cm}^{-3}$ , which should cover the range expected for stripped CC-SNe. The oxygen fraction is again set to 80%. For our estimates We use a temperature of 5000 K (the temperature calculated by the nebular code varies between 4500 K and 6300 K for these models). The breakdown point of our estimate ( $n_{\text{O}}\zeta > 10^9$   $\text{cm}^{-3}$ ) is indicated by filled squares. Up to the breakdown point the agreement is good. For larger clumping factors the agreement is acceptable for  $n_{\text{O}}\zeta < 10^{9.3}$   $\text{cm}^{-3}$ . For larger clumping factors our estimate over predicts the 7774 Å luminosity. In this regime the population of the  $3s(^5\text{S})$  level is no longer controlled by the effective radiative rate but rather by collisional de-excitation by thermal electrons. It seems unlikely that such high density regimes can play a role in CC-SN nebulae.

### 5.1.5. Emission versus absorption line shapes

Since the [O I]  $\lambda\lambda$  6300,6363 doublet has often been used to probe the ejecta velocity and the geometry of CC-SNe cores it is interesting to study the profile of the [O I] 7774 Å line. If this line were caused by recombination or thermal excitation alone, one would expect that the shapes of the 6300, 6363 and 7774 Å lines should be at least approximately similar.

However, as we have shown above, O I 7774 Å might result from line scattering even at 200 days. At later times the line usually becomes very weak and it is difficult to use it to probe the ejecta geometry. The profile of a scattering dominated line depends on the flux distribution, so one cannot expect that the shape of the 6300, 6363 Å lines and the 7774 Å line will be even approximately similar.

To demonstrate this, we use a multi-dimensional Monte Carlo code. A photon background is generated and

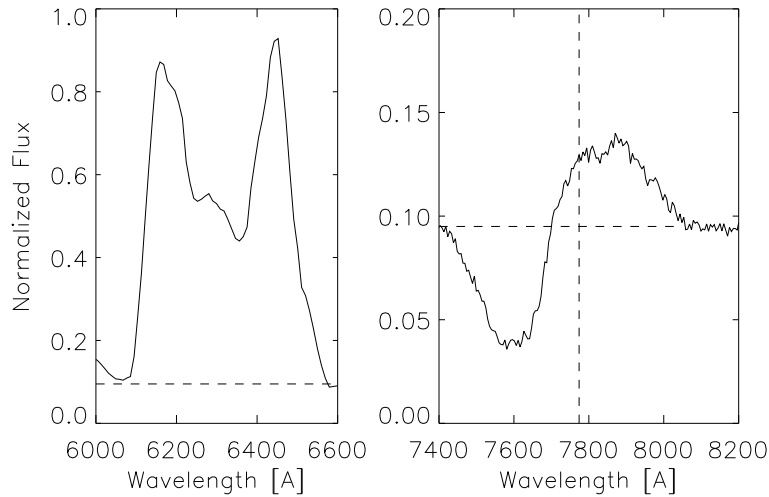


**Figure 5.8.** Left side: flux of a synthetic [O I]  $\lambda\lambda$  6300,6363 doublet for an asymmetric model (double-peaked shape). Right side: the 7774 Å line opacity calculated from this asymmetric model was used to calculate the flux of the absorption line at 7774 Å (dashed vertical line). The flux is normalised to an arbitrary constant. The formation of the absorption line strongly depends on the assumed background (indicated by the dashed horizontal line; it not only depends on the absolute background flux but also on the background rest-frame wavelength which determines the emission site) and therefore the absorption line shown would look different for a different background radiation field. The asymmetry has some influence on the absorption line, but the clear double-peaked shape of the [O I]  $\lambda\lambda$  6300,6363 doublet is not seen.

resonance-scattered in an (asymmetric) oxygen distribution (e.g. taken from a nebular model; the nebular code in its current version cannot simulate scattering processes). We calculate the [O I]  $\lambda\lambda$  6300,6363 doublet for an asymmetric oxygen model and use the 7774 Å line opacity calculated in the nebular code to compute the absorption of a broad-band background (3000 – 10000 Å) emitted in the inner region of the model SN. The formation of the absorption line is very sensitive to this background and therefore our results (see Figure 5.8) illustrate just one of many possibilities. As expected, the absorption line has quite a different shape than the emission line.

## 5.2. A shell model of SN 2002ap

After studying the formation of permitted oxygen lines in SECC-SNe in general, we now turn to two specific examples — SNe Ic 1998bw and 2002ap. These SNe are well studied and offer a large data set for nebular analysis. SN 2002ap is classified as a broad-lined SN of Type Ic. It had an ejected mass of  $\sim 2.5 M_{\odot}$  and a kinetic energy of  $\sim 4 \cdot 10^{51}$  ergs (Mazzali et al. 2007). The distance and reddening to SN 2002ap are only known approximately. To be consistent with previous work we use a distance modulus of  $\mu = 29.50$  mag and a reddening of  $E(B - V) = 0.09$  mag as done by Mazzali et al. (2002), Yoshii et al. (2003), Mazzali et al. (2007). The distance modulus  $\mu$  corresponds to a distance (in parsec [pc]; 1 pc =  $3.085 \times 10^{18}$  cm)

$$d = 10^{\frac{\mu}{5}+1} \text{ [pc]} \quad (5.19)$$

Reddening is caused by the scattering of light in the interstellar medium. The probability of this process is wavelength dependent reducing the relative strength of the blue component of a spectrum. The wavelength dependent modification of the flux  $F_{\lambda}$  owing to the reddening can be estimated according to Savage & Mathis (1979)

$$F_{\lambda} = 10^{-0.4E(B-V)[3.1+2(\lambda^{-1}-1.82)]} F_{\lambda,0} \quad (5.20)$$

where  $\lambda$  is the wavelength in  $\mu\text{m}$ . The distance modulus and the reddening are necessary to calculate a synthetic spectrum under the conditions of a terrestrial observer.

It is not clear whether SN 2002ap was a spherical symmetric event or not. Recently, [Maurer et al. \(2010\)](#) have shown that an asymmetry might be observable in all broad-lined CC-SNe, however this point is not clear yet. The spectra of SN 2002ap used in this work are those used by [Mazzali et al. \(2007\)](#).

[Mazzali et al. \(2007\)](#) found appropriate one-zone and shell models of the SN 2002ap nebular ejecta. We briefly summarise the main findings for the shell models here. Using a filling factor of 0.1 ( $\zeta = 10$ ) in the  $^{56}\text{Ni}$  rich regions, a total ejecta mass of  $\sim 2.5 M_{\odot}$  was found, containing roughly  $0.11 M_{\odot}$   $^{56}\text{Ni}$  and  $1.3 M_{\odot}$  of oxygen.

In contrast to this previous work, which aimed at modelling each spectrum individually, here we try to find one single  $^{56}\text{Ni}/\text{O}$  model which can produce the time evolution of the different spectra at all observed epochs consistently. Special attention is paid to reproducing the exact shape of the  $[\text{O I}] \lambda\lambda 6300,6363$  line profile, which is a tracer of the distribution of oxygen, the most abundant element of the nebula.

Using the same distance modulus and reddening as [Mazzali et al. \(2007\)](#) and clumping factors of 5 and 25 [we had to use a clumping factor of 1 for the innermost shell of the  $\zeta = 25$  model to avoid the formation of sharp high density lines which are not observed; [Mazzali et al. \(2007\)](#) had used a clumping factor of 10; this will be discussed in Section 5.4] we obtain models similar to the ones given in [Mazzali et al. \(2007\)](#) giving reasonable agreement with the observations at all epochs (see Figures 5.9 and 5.11). The forbidden oxygen lines are reproduced at all epochs by one and the same oxygen distribution, which provides evidence for the reliability of this model.

Our  $^{56}\text{Ni}$  zone with a total mass of  $\sim 1.2 M_{\odot}$  extends out to 8000 km/s, containing  $\sim 0.07 M_{\odot}$  of  $^{56}\text{Ni}$  (in agreement with [Mazzali et al. 2002](#)) and  $\sim 0.7 M_{\odot}$  of O. More mass is located at higher velocities, but the nebular modelling becomes inaccurate for the outer regions. The exact values depend on the clumping factor as well as on the  $^{56}\text{Ni}$  distribution, which is not known.

The  $\text{O I } 7774 \text{ \AA}$  line is excited by recombination and thermal electron excitation in our nebular modelling (no line scattering) and is too weak to explain the observations at 129 and 163 days using low clumping factors ( $\zeta \sim 5$ ). The  $\zeta = 25$  model can reproduce the observations of the  $\text{O I } 7774 \text{ \AA}$  line at 129 and 163 days better than the  $\zeta = 5$  model. This results from thermal electron scattering of  $3s(^5\text{S})$  electrons, which are provided by recombination. In general the  $\zeta = 5$  model reproduces the formation of the forbidden lines better than the  $\zeta = 25$  model at early epochs, since high density lines, which are not observed, form in the  $\zeta = 25$  model.

At days 192 and 229 both models produce too little flux at  $7774 \text{ \AA}$ , which is probably influenced by line scattering at these epochs (the optical depth of the inner shells of the  $\text{O I } 7774 \text{ \AA}$  line is high for both models at these epochs). The scattering process is not simulated and therefore the synthetic flux is too low.

At later epochs the  $\text{O I } 7774 \text{ \AA}$  line is consistently reproduced by recombination alone in both models when taking into account the uncertainty due to the background around  $7774 \text{ \AA}$ , which is not reproduced by the nebular code.

The optical depth of the  $7774 \text{ \AA}$  line is shown for all inner shells (five shells between 0 and 5000 km/s) of our  $\zeta = 5$  model in Figure 5.10. It does not fall below one before 210 days, indicating that there can be strong line scattering up to  $\sim 200$  days depending on clumping (for the  $\zeta = 25$  model the optical depth is higher and the  $\text{O I } 7774 \text{ \AA}$  line becomes optically thin later).

For clumping factors below 5 neither line scattering nor thermal excitation was strong enough to allow sufficient formation of the  $\text{O I } 7774 \text{ \AA}$  line before  $\sim 200$  days.

### 5.3. A 2D model of SN 1998bw

SN 1998bw is classified as a broad-lined SN of type Ic (ejected mass  $\sim 14 M_{\odot}$  and kinetic energy  $\sim 6 \cdot 10^{52}$  erg; [Nakamura et al. 2000](#)). We use a distance modulus of  $\mu = 32.89$  and an extinction of  $A_V = 0.2$  mag as given by [Patat et al. \(2001\)](#). SN 1998bw was accompanied by the low energy, long-duration GRB 980425. Due to this GRB-SN connection there are speculations that SN 1998bw was a highly aspherical event. These speculations are supported by polarisation measurements ([Kay et al. 1998](#), [Iwamoto et al. 1998](#), [Patat et al. 2001](#)), which were interpreted as a SN axis ratio of 2:1 ([Höflich et al. 1999](#)). Some indication for core ejecta asymmetry had also been found in the nebular spectra of SN 1998bw ([Mazzali et al. 2001](#)). The spectra of SN 1998bw used in this work are the same as used by [Mazzali et al. \(2001\)](#) originally presented by [Patat et al. \(2001\)](#).

The nebular phase of SN 1998bw has been well studied by means of nebular modelling ([Mazzali et al. 2001](#), [Maeda et al. 2006](#)). While [Mazzali et al. \(2001\)](#) attempted to model individual nebular spectra by one-zone models (concluding that this is insufficient), [Maeda et al. \(2006\)](#) computed two-dimensional synthetic nebular spectra for models obtained from hydrodynamical simulations, finding good agreement with spectra of individual epochs. However no model has so far described the time sequence of nebular spectra of SN 1998bw consistently.

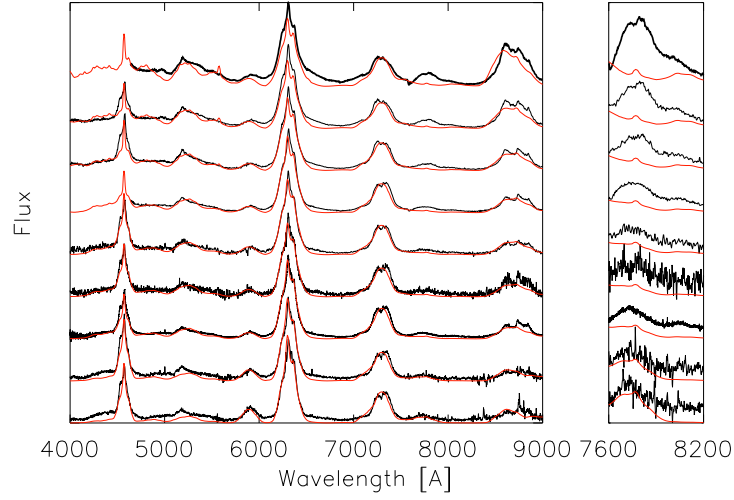


**Figure 5.9.:** SN 2002ap, models for a clumping factor  $\zeta = 5$ . Left side: normalised nebular spectra (from top to bottom: 129, 163, 192, 229, 245, 253, 281, 343 and 394 days after explosion) are shown in black with synthetic spectra on top in red. Right side: the region between 7600 Å and 8200 Å is enlarged to enable a comparison of observed (black) and synthetic (red) 7774 Å flux. At epochs of 129 to 229 days, the simulated flux is too low to match the observations. Beginning at 245 days, considering a constant off set caused by background-flux which is not reproduced by the synthetic spectrum, the synthetic 7774 Å line starts to become consistent with the observations.

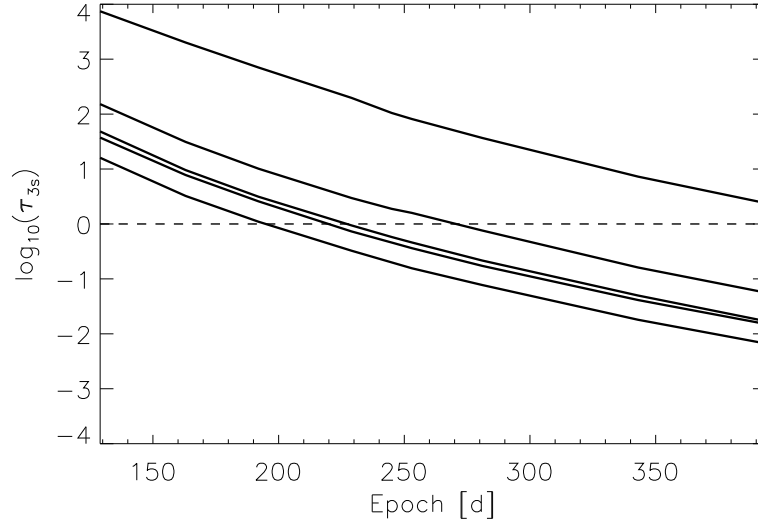


**Figure 5.10.:** SN 2002ap, models for a clumping factor  $\zeta = 5$ . The logarithm of the 7774 Å line optical depth in our model for the inner shells (from top to bottom: 0 – 1000 km/s, 1000 – 2000 km/s, 3000 – 4000 km/s, 4000 – 5000 km/s and 2000 – 3000 km/s). The 2000 – 3000 km/s shells contains very little oxygen in order to reproduce the narrow peak on top of the [O I]  $\lambda\lambda$  6300,6363 doublet lines and therefore it has low optical depth. Apart from the innermost shell, the optical depth drops below one around 220 days. This optical depth is calculated for scattering of remote emission radiation, which has a weaker dependence on the clumping factor than for local scattering.



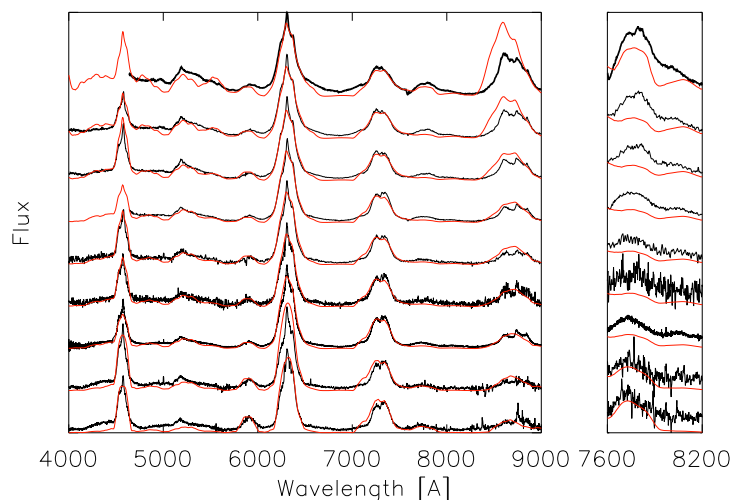


**Figure 5.11:** SN 2002ap, models for a clumping factor  $\zeta = 25$ . Left side: normalised nebular spectra (from top to bottom: 129, 163, 192, 229, 245, 253, 281, 343 and 394 days after explosion) are shown in black with synthetic spectra in red. Right side: the region between 7600 Å and 8200 Å is enlarged to enable a comparison of observed (black) and synthetic (red) 7774 Å flux. At epochs of 129 and 163 days, the simulated flux matches the observations at 7774 Å much better than for low clumping factors but in general the fit to the forbidden line emission is worse (e.g. the [O I] 5577 Å line and the Ca II IR-triplet line at  $\sim 8500$  Å become too strong at early epochs). Around 200 days line scattering seems necessary to explain the observed 7774 Å flux.

In this section we try to find a single two-dimensional model which is consistent with the full time evolution from 108 to 388 days after explosion. While successful models for individual epochs can be found even in one dimensional modelling, it seems impossible to model the time sequence of all spectra with a single one-dimensional model (in contrast to SN 2002ap, where this approach works well).

Since SN 1998bw is quite massive compared to other CC-SNe (like SN 2002ap for example), the transition to the nebular phase occurs at rather late times, although the ejecta expand at high velocities. The spectra at 108 and 139 days after explosion are not strictly nebular and therefore large deviations between the model and the observations are to be expected when trying to reproduce these spectra (especially at 108 days) with our nebular code.

When considering two dimensions one is immediately confronted with the problem that the parameter space is much larger [angular distribution of elements, observer inclination]. In addition, the computation time to obtain one synthetic spectrum increases dramatically. Since hundreds of spectra have to be computed to obtain a good model, this technical problem can make modelling unfeasible. Therefore some assumptions about the SN geometry have to be introduced.

There are several good arguments to assume that SN 1998bw might consist of some kind of two-dimensional 'jet + disc' structure, as described by for example by [Maeda et al. \(2006\)](#). Furthermore, since the SN was accompanied by a GRB, it seems likely that the observer inclination is not too far from polar, although this is uncertain since the opening angle of GRB 980425 is not known.

Therefore we work with a parametrised two-dimensional model which consists of a polar zone ( $0^\circ$  to  $45^\circ$ ) and an equatorial zone ( $45^\circ$  to  $90^\circ$ ). This simplification will introduce some error, since most likely it does not represent physical reality. However, it seems sufficiently exact to obtain an acceptable fit at all epochs with a single  $^{56}\text{Ni}/\text{O}$  model. A model with more degrees of freedom is highly degenerate anyway, since the information that can be extracted from a series of spectra  $F(\nu, t)$  is limited.

Because of this simplification the reliability of our model is in question, but this kind of uncertainty is inherent to all multi-dimensional modelling. We performed tests for viewing angles of  $0^\circ$ ,  $15^\circ$  and  $30^\circ$ . Using the smaller viewing angles the iron lines which are mainly produced in the jet-like structure become very narrow, which is not observed. Therefore we decided to use a viewing angle of  $30^\circ$ . However this might be a consequence of our

simplified geometry and therefore it is not possible to obtain valuable information about the observers inclination from our modelling approach.

Our model is roughly consistent with previous findings (Maeda et al. 2006). The polar zone contains  $\sim 0.24 M_{\odot}$  of  $^{56}\text{Ni}$  at velocities below 12000 km/s. The equatorial zone also contains  $\sim 0.24 M_{\odot}$  of  $^{56}\text{Ni}$  (note that the equatorial zone has more than twice the surface area of the polar zone), but located at velocities below  $\sim 8000$  km/s. The total mass below 12000 km/s is estimated to be  $\sim 2.7 M_{\odot}$  containing a total oxygen mass (below 12000 km/s) of  $\sim 2 M_{\odot}$ . There is a lot of material at higher velocities, but the nebular modelling becomes inaccurate for the outer regions because the density is too low.

Again we find that the O I 7774 Å line is not reproduced as due to recombination by our model with clumping  $\zeta = 1$  and  $\zeta = 5$ . Mazzali et al. (2001) and Maeda et al. (2006) had used a clumping factor of 10. This will be discussed in Section 5.4] for the spectra at 108, 139 and 214 days (see Figures 5.12 and 5.14). At 349 and 388 days we can reproduce the O I 7774 Å line consistently with the observations. There is some background around 7774 Å which is not reproduced by the nebular code sufficiently exactly. Shifting the oxygen recombination line upwards by the possible background, the agreement seems reasonable for both clumping factors. However the large background-line ratio makes an exact comparison impossible.

We tried to explain the formation of O I 7774 Å at the earlier epochs (108, 139 days) by increasing the clumping factor, which in turn increases the thermal electron excitation from the  $3s(^3S)$  to the  $3p(^3P)$  level. However, this does not seem to work. Both [O I] 5577 Å and the Ca II IR-triplet become very strong at clumping factors  $> 10$ , while the synthetic flux around 7774 Å increases but seems still too weak to explain the observations. Owing to the high density of SN 1998bw the nebular approach might be not suitable for such early epochs (the strong continuum which is observed is not reproduced). In addition there are uncertainties on the atomic data (especially the collision strengths), which may influence our conclusion.

In Figures 5.13 and 5.15 we show the opacity of the 7774 Å line for the five innermost shells for clumping factors of  $\zeta = 1$  and  $\zeta = 5$ . There will be 7774 Å line absorption up to  $\sim 200 - 300$  days depending on clumping.

Again, at least moderate clumping ( $\zeta \sim 5$ ) seems necessary in order to provide enough O I 7774 Å line opacity to reproduce the observations at 214 days.

## 5.4. Discussion

In Section 5.1.1 we have obtained normalised effective recombination fractions using available atomic data and computing missing atomic data. The agreement with atomic data available in the literature is good. Effective recombination rates had been given before by Julienne et al. (1974) at a temperature of 1160 K. These results are reproduced well. We extend the temperature range up to 10000 K, which should be an upper limit for temperatures of SN nebular ejecta between 100 and 600 days. Typical uncertainties in the atomic data seem to have small influence.

In Sections 5.1.2 and 5.1.3 we have obtained estimates for the formation of oxygen recombination lines and line absorption by the  $3s(^3S)$  state of neutral oxygen. We have shown that the luminosity of recombination lines is weak at any epoch. The influence of clumping on the recombination line is weak as well. Clumping will increase the recombination rate, but will decrease the number of O II ions at the same time. The total number of recombinations, which is equivalent to the total number of ionisations, will increase only slightly. Therefore clumping offers no direct way for increasing O I 7774 Å emission considerably.

We have shown that there is line scattering of 7774 Å photons even at very late epochs. This is possible because of the large number of ground state O I atoms, which resonantly scatter the UV radiation emerging from  $3s$  to  $2p$  transitions and slow down the de-population of the  $3s$  state. Combined with recombination this leads to a high population of the  $3s$  level, which in turn can resonantly scatter 7774 Å radiation. We have shown that, in contrast to the direct recombination line, the scattering line is very sensitive to clumping of the ejecta.

In addition, for high clumping factors, there may be thermal electron collisional excitation of the O I 7774 Å line at early epochs. However, it is in question whether these high clumping factors are realistic since high density lines, which are not observed, may form. Uncertainties in the atomic data, especially the collision strengths, may influence our results.

The considerations regarding the O I 7774 Å line are also in principle valid for the O I 8446 Å line [ $3s(^3S)$  to  $2p(^3P)$ ] with the difference that the effective recombination rate into the  $3s$  triplet state is smaller than into the quintet state. The optical depth of the 8446 Å line is therefore expected to be lower, which is still sufficient to cause

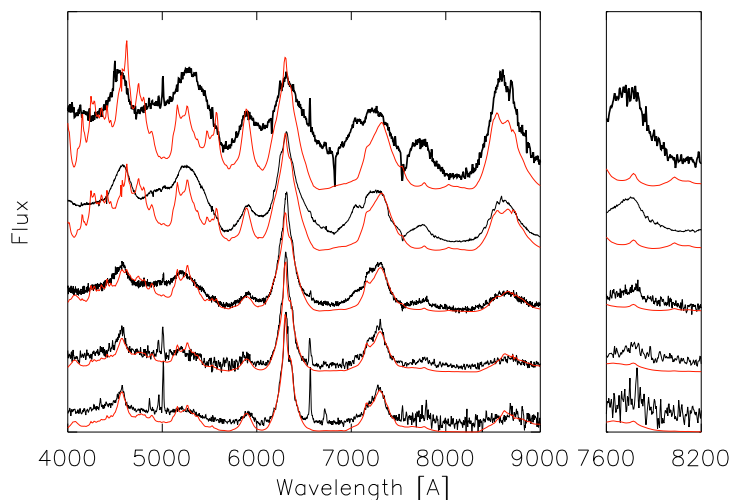


**Figure 5.12:** SN 1998bw, case of no clumping ( $\zeta = 1$ ). Left side: normalised nebular spectra of SN 1998bw (from top to bottom: 108, 139, 214, 349 and 388 days after explosion) are shown in black with the synthetic spectra in red. On the right side the region between 7600 Å and 8200 Å is enlarged to enable a comparison of observed (black) and synthetic (red) 7774 Å flux. The two earliest spectra (108, 139 days) of SN 1999bw are clearly not nebular and the agreement between observations and simulations is expected to be poor. However, the evolution of total and oxygen 6300 Å flux as well as the shape of the [O I]  $\lambda\lambda$  6300,6363 doublet line are reproduced at all epochs much better than by a one-dimensional model. At epochs of 108 to 349 days, the simulated flux is too low to match the observations of the 7774 Å line. At 388 days, considering the constant offset caused by some background flux which is not reproduced by the synthetic spectrum, the synthetic 7774 Å line seems to be consistent with the observations. Unfortunately the noise level is high and a detailed comparison is not possible.

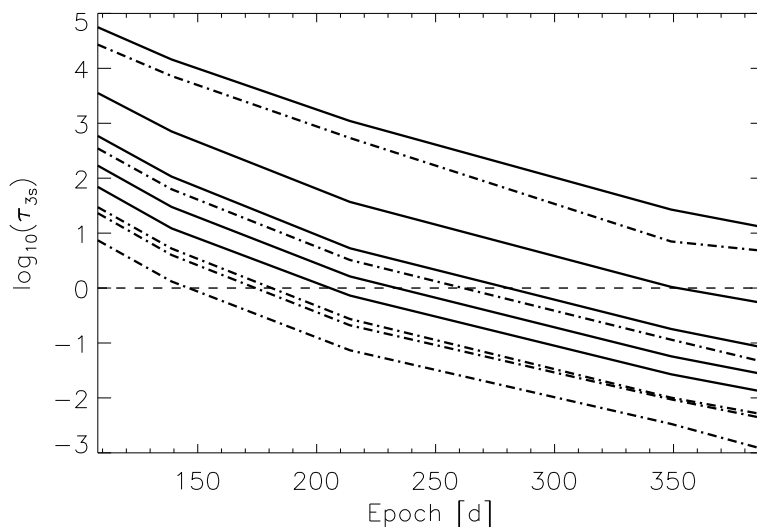


**Figure 5.13:** SN 1998bw, case of no clumping ( $\zeta = 1$ ). The logarithm of the 7774 Å line optical depth in our model for the inner shells (from top to bottom: 0 – 1000 km/s, 1000 – 2000 km/s, 2000 – 3000 km/s, 3000 – 4000 km/s and 4000 – 5000 km/s). Solid lines show the equatorial region, dotted lines the polar region. Apart from the innermost shell, the optical depth drops below one at  $\sim 210$  days. This optical depth is calculated for scattering remote emission radiation, which has a weaker dependence on the clumping factor than for local scattering.

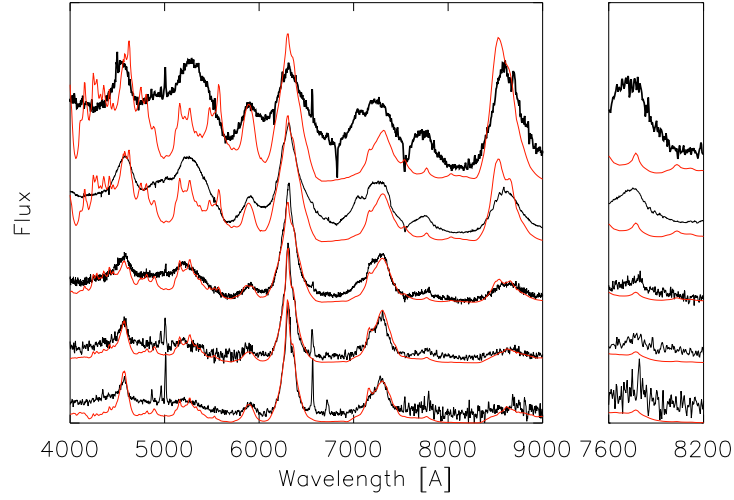


**Figure 5.14.:** SN 1998bw, case of clumping ( $\zeta = 5$ ). Left side: normalised nebular spectra (from top to bottom: 108, 139, 214, 349 and 388 days after explosion) are shown in black with the synthetic spectra in red. Right side: the region between 7600 Å and 8200 Å is enlarged to enable a comparison of observed (black) and synthetic (red) 7774 Å flux. The two earliest spectra (108, 139 days) of SN 1999bw are clearly not nebular and the agreement between observations and simulations is expected to be poor. However, the evolution of total and oxygen 6300 Å flux as well as the shape of the [O I]  $\lambda\lambda$  6300,6363 doublet line are reproduced at all epochs much better than by a one-dimensional model. At epochs of 108 to 349 days, the simulated flux is too low to match the observations of the 7774 Å line. At 388 days, considering the constant offset caused by some background flux which is not reproduced by the synthetic spectrum, the synthetic 7774 Å line seems to be consistent with the observations. Unfortunately the noise level is rather high and a detailed comparison is not possible.

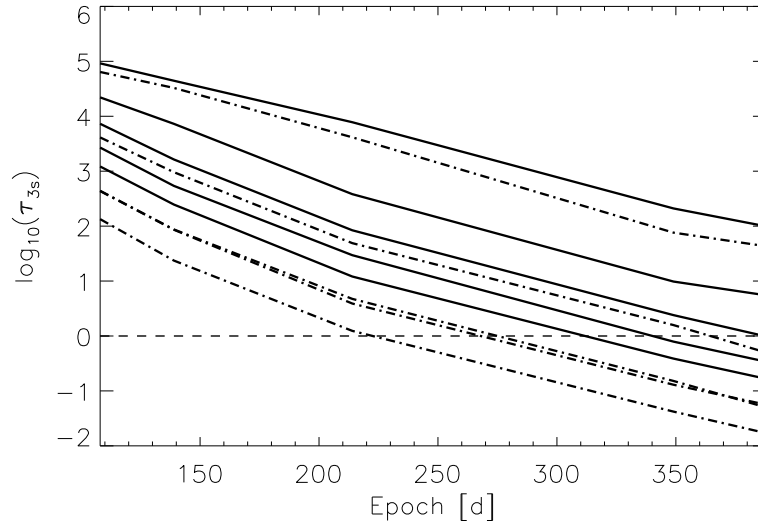


**Figure 5.15.:** SN 1998bw, case of clumping ( $\zeta = 5$ ). The logarithm of the 7774 Å line optical depth of our ejecta model for the inner shells (from top to bottom: 0 - 1000 km/s, 1000 - 2000 km/s, 2000 - 3000 km/s, 3000 - 4000 km/s and 4000 - 5000 km/s). Solid lines show the equatorial region, dotted lines the polar region. Apart from the innermost shell, the optical depth drops below one at  $\sim 310$  days. This optical depth is calculated for scattering remote emission radiation, which has a weaker dependence on the clumping factor than for local scattering.

line scattering at very early epochs. However, the 8446 Å line is blended with the blue wing of the [Ca II] IR-triplet, which can explain why no O I 8446 Å line is identified in SNe 1998bw and 2002ap.

We have shown that there is likely to be no other effective excitation mechanism than 'recombination + thermal excitation' or 'recombination + absorption' for O I  $n \geq 3$  levels. Thermal electron excitation of  $n \geq 3$  levels from the ground level is ineffective at typical nebular temperatures. Non-thermal electron excitation can also be ruled out. First, it is too weak and second, it would produce a temporal behaviour of the O I 7774 Å line which is not observed. As detailed modelling showed (Sections 5.2 and 5.3) absorption might be too weak to explain the observations as long as there is no clumping of the ejecta ( $\zeta \sim 5$ ). To enable thermal electron excitation even larger clumping factors seem necessary.

The concept of clumping has often been used in stellar wind and SN radiation physics (e.g. Li & McCray 1992, 1993a, Kozma & Fransson 1998, Mazzali et al. 2001, Maeda et al. 2006, Mazzali et al. 2007) without quantitative understanding of the physics behind ejecta clumping, therefore playing the role of a fitting factor. Li & McCray (1992) have modelled the ratio of the [O I]  $\lambda\lambda$  6300, 6363 doublet lines and Li & McCray (1993a) the Ca II emission of SN 1987A using a clumping factor of  $\sim 10$ . Mazzali et al. (2001), Maeda et al. (2006), Mazzali et al. (2007) have modelled the nebular spectra of SNe 1998bw and 2002ap finding that better fits to observations are obtained using clumping factors of  $\sim 10$  than when using no clumping. Our results are similar, but show some difference. We obtain good fits to all forbidden lines using clumping factors of 1 and 5 as well. The abundance of elements will change slightly depending on the value chosen.

This difference probably results mainly from our more accurate treatment of ionisation which increases the ionisation rate of carbon and oxygen considerably. This means that the electron density is increased, which can be mimicked by increasing the clumping factor and using lower ionisation rates. In general, it was found that for modelling nebular spectra of SECC-SNe with NC1D some clumping of the ejecta was needed. For SNe Ia a clumping factor  $\zeta = 1$  was found to be sufficient. Therefore it was thought that SECC-SNe might be clumped, while SNe Ia were not. However, the new treatment of ionisation (NC3D), developed in this thesis, allows a different interpretation of these findings. Since the old ionisation rates of Fe-group elements were approximately correct, while those of light elements like C and O were too low by factors of  $\sim 10$ , it becomes obvious why SECC-SN modelling required some clumping, while that of SNe Ia did not. Since SECC-SNe consist mainly of C and O, one had to introduce clumping to mimic the presence of stronger ionisation (clumping increases the local electron density), while in SNe Ia, which are dominated by Fe-group elements, this was not necessary.

Although this could eliminate the need for clumping found in some previous SECC-SN studies, this does not mean that SN ejecta are not clumped at all. The constraints we derived for the clumping factor of SNe 1998bw and 2002ap from the O I 7774 Å scattering line compare well to previous findings (e.g. Li & McCray 1992, Kozma & Fransson 1998). We found that a clumping factor of  $\sim 5$  seems necessary to provide sufficient opacity at 7774 Å. Clumping factors of  $\zeta > 10$  make it possible to model the O I 7774 Å emission at early epochs without line scattering, but may cause the formation of high density emission lines at early epochs (100 – 150 days). One example is the [O I] 5577 Å singlet line, which is observed to be weak. Since there are uncertainties on the atomic data it is not clear whether thermal electron excitation is important and whether the O I 7774 Å line at early epochs is dominated by line scattering or thermal electron excitation of recombining electrons.

At later epochs, between 150 and 250 days, the line is most likely a combination of line scattering and recombination radiation, since thermal electron excitation becomes too weak for any reasonable value of clumping. Around  $\sim 250$  days the O I 7774 Å line seems to become a true recombination line where the flux is mainly provided by the electrons cascading into the  $3p(^5P)$  level.

In Section 5.1.5 we have studied the expected profile of the [O I] 7774 Å line in light of our previous findings. As expected, the absorption and emission line shapes caused by a certain ejecta distribution can show important differences. Further, the profile of the absorption line depends on the background radiation field and one should be careful when using the shape of a scattering line for any kind of argumentation about ejecta geometry as long as it is not clear how this line is formed in detail.

In Sections 5.2 and 5.3 we obtained core ejecta models for SNe 1998bw and 2002ap. The primary goal of this modelling was not to re-derive ejecta properties, but to obtain reliable models for studying oxygen recombination consistently with other line formation. As a by-product we obtained estimates for the  $^{56}\text{Ni}$  and oxygen masses of the cores of these SNe. We find that SN 2002ap can be described very well by a one-dimensional shell model (as already found before), which does not necessarily mean that there is no asymmetry. Our  $^{56}\text{Ni}$  ( $\sim 0.07 M_{\odot}$ ) and oxygen mass estimates seem consistent with previous work. For SN 1998bw one-dimensional modelling seems to be insufficient to obtain an acceptable fit at all epochs using a single model. An acceptable fit is obtained with a

two-dimensional 'jet + disc' model (this had been found before). The fit could certainly be improved by increasing the degree of freedom of the model, but this would become extremely time-consuming. The model found in this work reproduces the observations at all epochs with increasing accuracy at later times, which is expected. The estimate of the  $^{56}\text{Ni}$  ( $\sim 0.48 M_{\odot}$ ) and oxygen mass are consistent with previous results.

Using these ejecta distributions we were able to reproduce the formation of O I 7774 Å at late epochs. There is enough line opacity at 7774 Å at early and intermediate nebular epochs to produce a strong scattering line. Since the background radiation field is important for the calculation of this absorption line, we were not able to show that our ejecta distribution reproduces the observations at early epochs exactly, however this seems likely. If there is strong clumping the O I 7774 Å line may be additionally excited by thermal electrons. The oxygen distribution inferred from forbidden line observations allows the reproduction of the allowed oxygen lines at late epochs. Since different physics are involved, this provides a test for the consistency of the nebular modelling approach, which is passed for SNe 1998bw and 2002ap.

Several other ions may produce absorption lines at wavelengths between 4000 and 10000 Å (the part of the spectrum that is usually observed). Since the abundance of these elements is much lower than that of oxygen, there will be no excited states with sufficient population to cause significant line scattering (an exception might be the Ca II IR-triplet). Allowed ground state transitions with energies between  $\sim 1$  and 3 eV are interesting since their optical depth can be high owing to the high radiative rates of allowed lines and to the possibly sufficiently high ground state populations of these low abundance elements. The elements of interest are Na I, Mg I and Ca II. These three elements have low quantum-level transitions with wavelengths of  $\sim 5890$  Å (Na I), 4570 Å (Mg I) and 3950 Å, 7300 Å and 8500 Å (Ca II), which can be present in sufficient amounts in SN nebulae. Iron group element lines, especially Fe II, may be optically thick as well. However, since these ions are complex we do not treat them explicitly here.

If  $0.01 M_{\odot}$  of Na I were to be distributed homogeneously within 5000 km/s, the optical depth of the Na I 5890 Å line would be  $\sim 6 \times 10^5$  at 200 days (this result is obtained by balancing thermal-electron excitation with radiative and collisional de-excitation analogously to Section 5.1.2), scaling linearly with Na I mass and with epoch  $t^{-2}$ .

If  $0.01 M_{\odot}$  of Mg I were to be distributed homogeneously within 5000 km/s, the optical depth of the Mg I 4570 Å line would be  $\sim 1$  at 200 days, scaling linearly with Mg I mass and with epoch  $t^{-2}$ .

Three Ca II lines might be seen in absorption even at late epochs ( $\sim 3950$  Å, 7300 Å and the IR-triplet 8500 Å). To estimate their strength, it is important to know the relative population of the Ca II 3d to 4s states, which can be approximated by

$$\frac{n_{3d}}{n_{4s}} \sim \frac{C_{4s \rightarrow 3d}}{A'_{3d \rightarrow 4s} + C_{3d \rightarrow 4s}} \quad (5.21)$$

where  $C_{4s \rightarrow 3d}$  and  $C_{3d \rightarrow 4s}$  are the collisional rates for the 4s to 3d transition and  $A'$  is the radiative rate from 3d to 4s, reduced due to resonance scattering.

If  $0.01 M_{\odot}$  of Ca II were to be distributed homogeneously within 5000 km/s, the optical depth of the Ca II 3950 Å and [Ca II] 7300 Å lines would be  $\sim 2 \times 10^5$  and  $\sim 0.02$  respectively, at 200 days, scaling linearly with the Ca II mass and with epoch  $t^{-2}$ . The optical depth of the Ca II IR-triplet depends on the population of the 3d state. Using the 7300 Å optical depth estimated above, the optical depth of the Ca II 8500 Å transition is  $\sim 430$  ( $n_e = 10^7$  and  $T = 5000$  K) at 200 days, with a stronger dependence on Ca II mass and epoch than the optical depths at 3950 Å and 8500 Å (see also Li & McCray 1993a, for a detailed discussion of Ca II line formation).

The exact mass of Na I, Mg I and Ca II is not well known, since estimates of their masses are not very accurate. However, typical masses in CC-SNe cores for Na, Mg and Ca might be of the order of  $0.01 M_{\odot}$ .

Therefore, even at late times ( $> 200$  days) there is strong line scattering at wavelengths between  $\sim 4000$  and 10000 Å. The Ca II 3950 Å, Na I 5890 Å and O I 7774 Å lines cause strong scattering in any reasonable scenario. The [Mg I] 4570 Å, O I 8446 Å and Ca II 8500 Å lines may have sufficient optical depth for line scattering, depending on epoch, degree of ionisation, total mass and clumping.

## 5.5. Summary

We have computed temperature-dependent effective recombination rates for neutral oxygen in a temperature range suitable for all types of SN nebulae (at epochs between 100 and 600 days). Since oxygen is the most abundant element in SNe Ib & Ic, oxygen lines are of special interest among other recombination lines.

We obtained core ejecta models for CC-SNe 1998bw and 2002ap. Similar models had been derived previously, however using the old treatment of ionisation. In this section we have studied the influence of the more accurate

ionisation treatment developed in this thesis. We found that clumping factors of the order of 10 required in previous studies of SNe 1998bw and 2002ap likely resulted from an inaccurate treatment of ionisation, since clumping can mimic increased ionisation rates. However, the main goal of the modelling presented in Sections 5.2 and 5.3 was to obtain accurate fits to the [O I]  $\lambda\lambda$  6300, 6363 doublet and consequently to the density profile of oxygen.

Using these oxygen profiles, the O I 7774 Å recombination line, which is the strongest observed recombination line, is calculated and compared to observations. We show that up to late epochs pure recombination is too weak to power O I 7774 Å. At earlier epochs the line is powered by scattering and possibly by thermal electron excitation of recombining electrons. In both scenarios the population of the  $3s(^5S)$  state by recombining electrons is the key to the O I 7774 Å emission.

We derived estimates for the strength of the O I 7774 Å line resulting from oxygen recombination, for the time-dependent optical depth of this line and for excitation of recombining electrons by thermal collisions. These estimates give insight into the formation of the O I 7774 Å line in CC-SNe. We have shown that while the recombination line strength depends on clumping very weakly, clumping does have a strong influence on the absorption and thermal electron excitation of this line.

Our results imply that the O I 7774 Å line should not be used as a tracer of the core ejecta before 250 days, unless one explicitly models the background radiation field and the recombination and absorption processes involved. Since the clumping factor can not be obtained with high accuracy and the background around 7774 Å seems to consist of a superposition of several weak lines this could become a difficult task. It is not clear which elements or ions produce the observed background flux in this region. Iron group elements seem to be promising candidates, but currently the accuracy of our calculations is not sufficient.

This is important for the geometrical interpretation of the [O I]  $\lambda\lambda$  6300, 6363 doublet. Sometimes, the O I 7774 Å line is single peaked, while the doublet is double-peaked. Although O I  $\lambda$  7774 is weak in general and can hardly be separated from the background, this could be taken as evidence against the geometrical interpretation of oxygen double-peaks. As it was shown here, forbidden and permitted O I lines can originate from different physical processes, which can invalidate such conclusions.





## 6. Hydrogen and Helium In Stripped-Envelope Core-Collapse Supernovae

In Section 4 we have determined core-velocities for a large sample of SECC-SNe. Evidence for core asymmetry has been found. In the previous section a more detailed analysis was performed for two SNe Ic, revealing further evidence for core asymmetry, at least in GRB-SN 1998bw. Extending the analysis to SNe IIb is important, since they mark the transition from SECC to SNe II. In this section we investigate possible asymmetries in SNe IIb in more detail.

Supernovae IIb contain large fractions of helium and traces of hydrogen, which can be observed in the early and late spectra. Estimates of the hydrogen and helium mass and distribution are mainly based on early-time spectroscopy and are uncertain since the respective lines have to be treated in NLTE (in contrast to the other elements). Constraining the mass and distribution of H and He is important to gain insight into the progenitor systems of these SNe.

Large amounts of hydrogen ( $\gg 1 M_{\odot}$ ) cause the progenitor to have an extended hydrogen envelope prior to explosion, which in turn leads to a broad peaked SN light curve (e.g. Grassberg et al. 1971). Since this is not observed in SNe of Type IIb there is an upper limit for the hydrogen mass of less than one solar mass (Nomoto et al. 1993, Utrobin 1994, Woosley et al. 1994). It is not clear how SNe IIb manage to keep just a thin layer of hydrogen.

While massive (and therefore hot, O-Type) stars ( $M > 25 M_{\odot}$ ) can blow off their hydrogen envelope by radiatively driven winds (e.g. Eldridge & Vink 2006), mass estimates for the progenitors of SNe IIb (e.g. Woosley et al. 1994, Mazzali et al. 2009, Silverman et al. 2009, Hamuy et al. 2009) suggest that they may not be massive enough to lose most of the H envelope via this process. Binary interaction can cause mass transfer between two interacting stars and would allow a Type IIb progenitor to lose most of its hydrogen (e.g. Woosley et al. 1994). There is observational evidence that the progenitors of SNe 1993J (Aldering et al. 1994, Maund et al. 2004, Maund & Smartt 2009), 2001ig (Ryder et al. 2006) [also see Kotak & Vink (2006) for an alternative interpretation of the SN 2001ig data] and 2008ax (Crockett et al. 2008) may have been part of binary systems.

There is evidence of shock interaction from nebular  $H\alpha$  (e.g. Chugai 1991, Patat et al. 1995, Houck & Fransson 1996, also see this work) as well as from radio (e.g. Fransson & Björnsson 1998, Soderberg et al. 2006, Chevalier & Soderberg 2010) and X-ray observations (e.g. Chevalier 1981, Soderberg et al. 2006, Nymark et al. 2009, Chevalier & Soderberg 2010), suggesting that at least some SNe IIb are surrounded by massive shell from stellar winds. This wind could also be produced by the massive companion star in the binary scenario.

At early phases of SNe IIb the energy emitted by  $H\alpha$  is probably provided by the radioactive decay chain  $^{56}\text{Ni} \rightarrow ^{56}\text{Co} \rightarrow ^{56}\text{Fe}$ . However, it was thought that in SN 1993J (Patat et al. 1995, Houck & Fransson 1996) at  $\sim 150$  days after explosion this mechanism becomes ineffective suggesting that an additional source of energy may be required to explain the observed  $H\alpha$  luminosities. This was further confirmed by the detection of a flattening of the  $H\alpha$  luminosity decay at late phases (Matheson et al. 2000). This could be inconsistent with radioactive decay, but may be explained by shock interaction. A similar result had been obtained for SNe II (Chugai 1991). However, Maurer et al. (2010) have shown that radioactive decay actually can power the late  $H\alpha$  emission in SNe 1993J, 2007Y and 2008ax, at least until  $\sim 350$  days after the explosion.

Shock interaction can also be detected through radio and X-ray observations. As the SN ejecta propagate into the circumstellar medium, they are decelerated, creating internal energy which is dissipated by radiative processes. There are several solutions for different scenarios of shock interaction (e.g. Chevalier 1981, Suzuki & Nomoto 1995, Fransson & Björnsson 1998), but a clear interpretation of the observations is often difficult. Micro-physical processes (e.g. the formation of magnetic fields) are poorly understood, and it is not clear in detail how the energy released by the shock is transferred into radiation. The SN envelope and circumstellar density profiles are not known and have to be treated as free parameters. Several authors found evidence for inhomogeneous wind structures and deviations from wind-like density profiles of the external medium (e.g. Fransson 1994, van Dyk et al. 1994, Suzuki & Nomoto 1995). This may however be an artefact of an inaccurate treatment of shock physics (Fransson & Björnsson 1998, 2005). A very careful treatment of shock interaction seems necessary to obtain reliable results (e.g.

Fransson & Björnsson 1998).

For this thesis, we implemented a NLTE treatment of hydrogen and helium in the three-dimensional nebular code (NC3D). Ionisation, recombination, (non-)thermal electron excitation and  $H\alpha$  line scattering are taken into account to compute the formation of  $H\alpha$ , which is by far the strongest H line observed in the nebular spectra of SNe I Ib. Other lines of H and He are also computed but are rarely identified in the nebular phase.

Nebular observations are available for very few SNe I Ib. To our knowledge there are nebular spectra of SNe 1993J, 2001ig, 2003bg, 2006T, 2008aq and 2008ax. The quality of the SN 2006T spectrum is poor. For SN 2008aq there is no light curve and therefore there are no flux-calibrated spectra. Therefore, neither SNe are included in our analysis.

Nebular models are computed for the Type I Ib SNe 1993J, 2001ig, 2003bg and 2008ax as well as for SN 2007Y, which shows  $H\alpha$ . Although early time  $H\alpha$  absorption features are observed, SN 2007Y was classified as a SN I Ib by [Stritzinger et al. \(2009\)](#), who argued there is very little hydrogen in the envelope and that the late  $H\alpha$  emission is powered by shock interaction. On the other hand, [Chevalier & Soderberg \(2010\)](#) found that the  $H\alpha$  emission of SN 2007Y must be powered by radioactive decay before 300 days after explosion. SN 2007Y is included in our analysis to investigate this contradiction and a possible re-classification. Optical spectra exist for all SNe of our sample, and there is one IR nebular observation of SN 2008ax, which allows an exploration of its helium mass and distribution.

Asphericities in the inner and outer ejecta are evident in at least some CC-SNe. Three indicators are velocity differences of Fe and lighter element lines at late times (e.g. [Mazzali et al. 2001](#)), polarisation measurements (e.g. [Höflich 1991](#)) and double-peaked or asymmetric emission line profiles (e.g. [Mazzali et al. 2005](#), [Maeda et al. 2008](#), [Modjaz et al. 2008](#), [Taubenberger et al. 2009](#), [Maurer et al. 2010](#)). Indirect evidence also emerges from a comparison of the inner and outer ejecta velocities ([Maurer et al. 2010](#)). In this section we find evidence that SN 2008ax is a non-spherical event.

We develop a three-dimensional model for SN 2008ax. We obtain estimates for the total mass and kinetic energy in good agreement with the results from light-curve modelling found in the literature. We further derive abundances of He, C, O, Ca and  $^{56}\text{Ni}$ . Estimates of the H mass are difficult but some constraints are derived. We demonstrate that  $H\alpha$  absorption is probably responsible for the double-peaked profile of the [O I]  $\lambda\lambda$  6300, 6363 doublet in several SNe I Ib and present a mechanism alternative to shock interaction for generating late-time  $H\alpha$  emission of SNe I Ib.

In [Section 6.1](#) we describe the implementation of hydrogen and helium in NC3D. In [Section 6.2](#) we describe a three-dimensional model of SN 2008ax, give some estimates for the total mass and kinetic energy and compare them to results available in the literature. In [Section 6.3](#) we present nebular models for the SNe 1993J, 2001ig, 2003bg, 2007Y. Since nebular models for these SNe are available in the literature already and since we cannot determine their helium density we concentrate on their  $H\alpha$  emission. In [Section 6.4](#) we present a scenario alternative to shock interaction for explaining strong late-phase  $H\alpha$  emission. In [Section 6.5](#) the results are discussed.

## 6.1. H and He in the nebular phase

In this section we describe the implementation of hydrogen and helium in NC3D.

### 6.1.1. Hydrogen

A full NLTE treatment of hydrogen is implemented in our three-dimensional nebular code. We obtain radiative transition and ionisation rates for the hydrogen atom from analytical solutions available in the literature (e.g. [Burgess 1965](#)). Collisional rates for allowed transitions between excited levels  $n > 3$  are unimportant, but are included using an approximation ([van Regemorter 1962](#)). Collisional rates between quantum levels  $n = 1, 2$  and 3 are taken from [Scholz et al. \(1990\)](#), [Callaway \(1994\)](#). The 2s level is additionally connected to the ground state by two-photon decay, and the 2s and 2p levels are coupled by electron and proton collisions.

Hydrogen is ionised by non-thermal electrons (produced by Compton scattering of  $^{56}\text{Co}$  radioactive decay  $\gamma$ -radiation) and by UV-radiation emitted by helium if hydrogen and helium are mixed. The electron impact ionisation rate can be obtained comparing the atomic and electronic loss-functions with the ionisation cross-sections (e.g. [Axelrod 1980](#), [Maurer & Mazzali 2010](#)). Thermal electron collisional ionisation and recombination is not important. Excitation by non-thermal electrons is important. We compute non-thermal electron excitation rates using the

approximation of [Rozsnyai et al. \(1980\)](#).

We compare our hydrogen and helium ionisation and non-thermal excitation rates to calculations from Hachinger et. al. (in prep.) who calculate non-thermal ionisation and excitation rates solving an energy balance equation derived from the Spencer-Fano equation ([Xu & McCray 1991](#), [Lucy 1991](#)). Although these methods are quite different, the thermal excitation and ionisation rates at various electron and atomic densities agree to 10% – 20% for both hydrogen and helium.

For levels with principal quantum number  $n > 5$  we only consider recombination (these levels are almost completely depopulated and have no influence on the nebular spectrum), while a full NLTE (de-)excitation treatment is performed for lower levels.

The  $n = 2$  level of H can effectively scatter the background radiation field. This is a very important process in SNe IIb ([Houck & Fransson 1996](#)) since  $H\alpha$  comes into resonance with the [O I]  $\lambda\lambda$  6300, 6363 doublet, which carries an important fraction of the nebular flux. The optical depth of transitions between levels  $n \geq 3$  is too low to cause observable line scattering at late epochs.

Clumping of hydrogen is usually neglected in SNe IIb ([Patat et al. 1995](#), [Houck & Fransson 1996](#), [Mazzali et al. 2009](#)), but it can increase the optical depth of  $H\alpha$  considerably. Under certain conditions, as we show in Section 6.4, it can also increase the  $H\alpha$  emission significantly.

### 6.1.2. Helium

Accurate atomic data for He are available in the literature (e.g. see TIPTOPbase <sup>1</sup>, NIST <sup>2</sup>). For technical reasons it was more convenient for us to calculate the He radiative transition and ionisation rates using a quantum defect method ([Bates & Damgaard 1949](#), [Seaton 1958](#), [Burgess & Seaton 1960](#)) [also see [Maurer & Mazzali \(2010\)](#) for an application to oxygen], which is very accurate for helium. The disagreement between the calculations and NIST recommended data is a few percent in the worst case, having no observable influence on the line calculations.

Thermal electron excitation rates for all quantum levels  $n < 4$  are taken from [Berrington & Kingston \(1987\)](#). The  $2s(^1S)$  level is connected to the ground state by two-photon emission (2PE) (e.g. [Drake et al. 1969](#)), which turns out to be important in the nebular phase of SNe of Type IIb (in the early phase radiative excitation of the 2p levels allows effective de-excitation via the  $2p \rightarrow 1s$  transition, which can be more important than 2PE then).

Helium is mainly ionised by non-thermal electrons (see hydrogen). The recombination rates into all levels  $n \leq 4$  are calculated by simulating recombination into and cascading from excited levels  $n \leq 30$ . Levels with  $n \leq 4$  are treated in full NLTE. Non-thermal electron excitation is important and is included using the approximation of [Rozsnyai et al. \(1980\)](#).

Helium can be observed in emission during the nebular phase of SNe IIb since its mass is large and since it is distributed down to a few thousand  $\text{km s}^{-1}$ . Owing to the large excitation potential of He ( $\sim 20$  eV), an important fraction of the deposited energy can be radiated away by other elements which may be present in small fractions. This means that the electron temperature decreases and the He lines become weaker while the other elements emit more strongly. Since all optical He lines are blended with lines only the IR He I 10830 Å and 20587 Å lines can be identified clearly (at least in SN 2008ax), which allows an estimate of the He mass and distribution. Since both lines are optically thick around 100 days after explosion, they can be influenced by line scattering.

### 6.1.3. Mixed H/He layers

We derive some estimates for the ionisation of hydrogen by non-thermal electrons and by the UV-radiation emitted by helium. We assume that H is mixed with He but not with other elements. Therefore the treatment presented is only valid if heavy elements are present in smaller fractions than hydrogen and helium. However, other elements with ionisation potentials below  $\sim 20$  eV would be affected in a way similar to hydrogen.

About 40% of all helium recombinations go directly to the ground state and cause another ionisation of helium and possibly of hydrogen. This recycling process increases the total ionisation rate but is not important for the rest of this subsection.

Electrons recombining to an excited state reach the ground state by two-photon emission (2PE) of the  $2s(^1S)$  state during the nebular phase. At early times, when the 2p levels are strongly excited by radiation, most electrons reach

<sup>1</sup><http://cdsweb.u-strasbg.fr/topbase/>

<sup>2</sup><http://www.nist.gov/index.html>

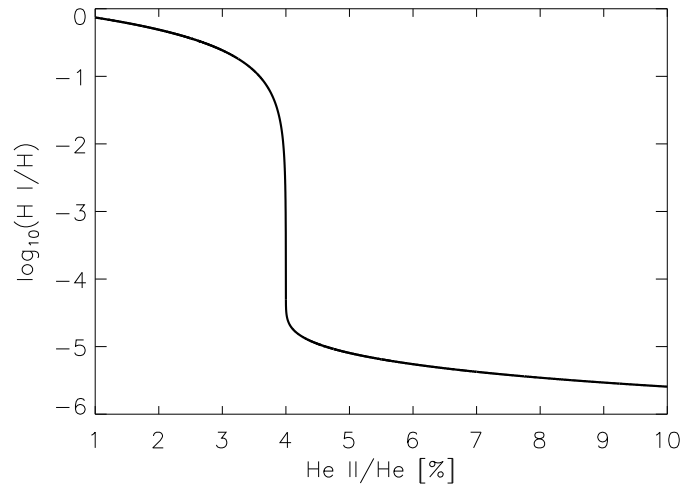


**Figure 6.1:** The logarithmic fraction of neutral hydrogen  $\frac{n_{\text{HI}}}{n_{\text{H}}}$  (full black line; Equation 6.6) as a function of the He II fraction  $\frac{n_{\text{HeII}}}{n_{\text{He}}}$  [%] for a helium dominated layer containing 2% of hydrogen, assuming  $f = 0.5$  and  $\xi_{\text{H}} = 0.1$ . The He density was set to  $10^8 \text{ g cm}^{-3}$ . There is a steep decrease of H I as soon as the fraction of He II increases above  $\frac{2}{f}\%$ . Changing the degree of ionisation of He by 1% only (from 4.5 to 3.5% in this example), the fraction of H I increases by a factor of  $10^4$ .

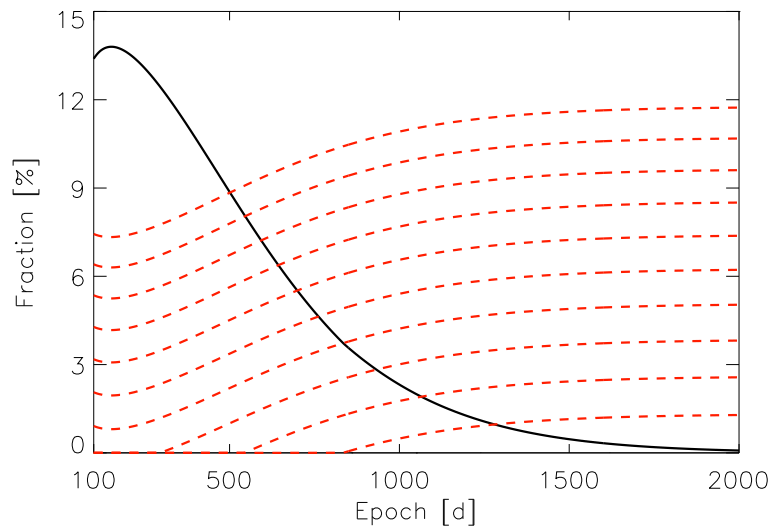


**Figure 6.2:** Toy model of a SN IIb. The time-dependent fraction  $\frac{n_{\text{HeII}}}{n_{\text{He}}}$  [%] (full black line; Equation 6.13) is shown for a model described in the text ( $M_{\text{He}} = 3 M_{\odot}$ ,  $M_{\text{Ni}} = 0.1 M_{\odot}$ ,  $f = 0.5$ ,  $T = 15000\text{K}$ ). The fraction  $\frac{n_{\text{HI}}}{n_{\text{H}} + n_{\text{He}}}$  [%] (dashed red line; Equation 6.6) is shown for hydrogen masses of 0.01 to  $0.1 M_{\odot}$  (bottom to top). There is no clumping of the H and He layer. The calculation starts at 100 days since at earlier epochs photospheric radiation may be important for ionising hydrogen and helium and our estimates become invalid. Although the model is highly simplified it demonstrates that depending on the ratio of hydrogen and helium the H I fraction can be approximately zero for the first 100 days and can increase rapidly at later epochs. This means that no  $\text{H}\alpha$  would be observed at early epochs, while strong  $\text{H}\alpha$  emission or scattering is possible later.

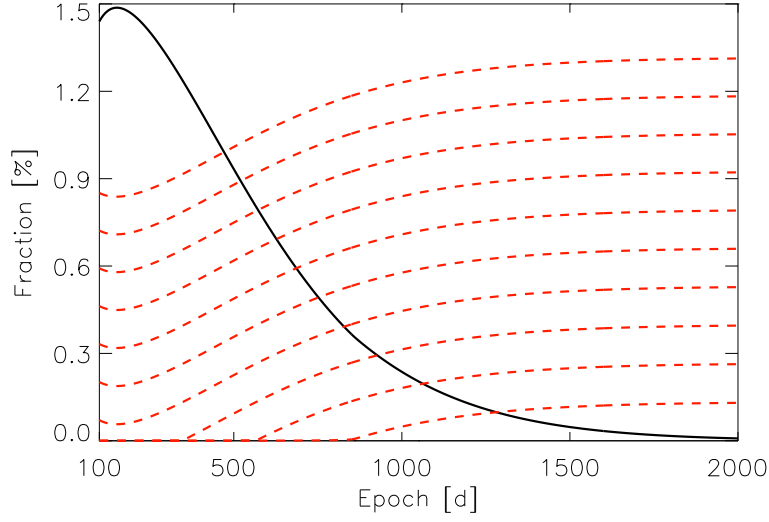


**Figure 6.3:** Toy model of a SN IIB. The time-dependent fraction  $\frac{n_{\text{He II}}}{n_{\text{He}}}$  [%] (full black line; Equation 6.13) is shown for a model described in the text ( $M_{\text{He}} = 3 M_{\odot}$ ,  $M_{\text{Ni}} = 0.1 M_{\odot}$ ,  $f = 0.5$ ,  $T = 15000\text{K}$ ). The fraction  $\frac{n_{\text{H I}}}{n_{\text{H}} + n_{\text{He}}}$  [%] (dashed red line; Equation 6.6) is shown for hydrogen masses of 0.001 to 0.01  $M_{\odot}$  (bottom to top). The clumping factor of the H and He layer is set to 100, which reduces the degree of ionisation strongly. The calculation starts at 100 days since at earlier epochs photospheric radiation may be important for ionising hydrogen and helium and our estimates become invalid. Although the model is highly simplified it demonstrates that depending on the ratio of hydrogen and helium the H I fraction can be approximately zero for the first 100 days and can increase rapidly at later epochs. This means that no  $\text{H}\alpha$  would be observed at early epochs, while strong  $\text{H}\alpha$  emission or scattering is possible later.

the ground state via the 2p levels.

In the case of 2PE approximately 30% of the ground state transition radiation can ionise hydrogen (the two photons are created with energies between 0 and 20.6 eV; the chance of producing a photon with  $E > 13.6$  eV is  $\sim 30\%$ ; Drake et al. 1969) and in the case of 2p transitions 100%. Therefore, we assume that a fraction  $f$  (0.3 – 1.0) of all He recombinations into excited states can ionise a hydrogen atom.

The total ionisation rate of hydrogen is then determined by non-thermal electron ionisation and by radiative ionisation from He recombination radiation. The non-thermal electron ionisation rates of neutral hydrogen and helium are given by (e.g. Axelrod 1980)

$$Y = Y_{\text{H I, He I}} = \frac{L_{\text{Dep}}}{N_{\text{Tot}} W_{\text{H I, He I}}} \quad (6.1)$$

where  $N_{\text{Tot}}$  is the total number of atoms and  $W_{\text{H I, He I}}$  is the work per ion of hydrogen and helium, which depends on the ratio of electrons to atoms and on the absolute atomic density (weakly).

For simplicity we assume  $W_{\text{H I}} = W_{\text{He I}}$  in this section, which will cause an error of  $\sim 30\%$  on the ionisation rates of H and He in the worst case.

During the first few hundred days the SN is in ionisation equilibrium (e.g. Axelrod 1980) and the ionisation balance of hydrogen can be estimated as

$$Y(n_{\text{He I}} D_{\text{H I}} f + n_{\text{H I}}) = R_{\text{H I}}(n_{\text{He II}} + n_{\text{H II}}) \zeta n_{\text{H II}} \quad (6.2)$$

where  $D_{\text{H I}} f$  is the fraction of He recombination radiation ionising hydrogen with

$$D_{\text{H I}} = 1 - \exp(-\sigma_{\text{H}} \Delta R n_{\text{H I}}) \quad (6.3)$$

where  $\sigma_{\text{H}}$  is the ionisation cross-section of H at  $\sim 20$  eV and  $\Delta R$  is some characteristic width of the He shell. The ionisation balance of helium can be written as

$$Y n_{\text{He I}} = R_{\text{He I}}(n_{\text{He II}} + n_{\text{H II}}) \zeta n_{\text{He II}} \quad (6.4)$$

Setting  $R = R_{\text{HI}} = R_{\text{HeI}}$  (which is a good approximation) one obtains

$$D_{\text{HI}} n_{\text{HeI}} f + n_{\text{HI}} = \frac{n_{\text{HeI}}}{n_{\text{HeII}}} (n_{\text{H}} - n_{\text{HI}}) \quad (6.5)$$

The exact solution of Equation 6.5 is given by

$$n_{\text{HI}} = \xi_{\text{H}}^{-1} W \left( \frac{n_{\text{HeI}} n_{\text{HeII}}}{n_{\text{He}}} \xi_{\text{H}} f \exp \left[ - \frac{n_{\text{HeI}} \xi_{\text{H}} (n_{\text{H}} - f n_{\text{HeII}})}{n_{\text{He}}} \right] \right) + \frac{n_{\text{HeI}}}{n_{\text{He}}} (n_{\text{H}} - f n_{\text{HeII}}) \quad (6.6)$$

where  $W(x) \equiv \sum_{n=1}^{\infty} \frac{(-n)^{n-1}}{n!} x^n$  is the Lambert  $W$  function. In approximation, the deposition fraction  $D_{\text{HI}}$  is given by

$$D_{\text{HI}} = \begin{cases} 1 & \sigma_{\text{H}} \Delta R n_{\text{HI}} \gg 1 \\ \sigma_{\text{H}} \Delta R n_{\text{HI}} \equiv \xi_{\text{H}} n_{\text{HI}} & \sigma_{\text{H}} \Delta R n_{\text{HI}} \ll 1 \end{cases} \quad (6.7)$$

The ionisation cross section of hydrogen is  $\sim 2 \cdot 10^{-18} \text{ cm}^2$  at 20 eV and the SN radius is of the order of  $10^{16} \text{ cm}$  during the first few hundred days, which means that  $\xi_{\text{H}}$  will be of order  $0.01 - 0.1 \text{ cm}^3$ . The number density of neutral hydrogen is then given by

$$\frac{n_{\text{HI}}}{n_{\text{H}}} = \begin{cases} \frac{n_{\text{HeI}}}{n_{\text{He}}} \left( 1 - f \frac{n_{\text{HeII}}}{n_{\text{H}}} \right) & \xi_{\text{H}} n_{\text{HI}} \gg 1 \\ \frac{n_{\text{HeI}}}{n_{\text{He}} + n_{\text{HeI}} n_{\text{HeII}} f \xi_{\text{H}}} \sim (f n_{\text{HeII}} \xi_{\text{H}})^{-1} & \xi_{\text{H}} n_{\text{HI}} \ll 1 \end{cases} \quad (6.8)$$

The degree of ionisation of hydrogen increases rapidly as soon as the hydrogen number density becomes similar to the number density of He II times  $f$  (see Figure 6.1).

A factor of 10 or less in the hydrogen abundance can make a difference of several orders in magnitude in the degree of ionisation. Also, a small change in the ionisation balance of He can have serious influence on the ionisation balance of H. A simple example is given by a helium layer containing 2% hydrogen and  $\frac{2.5}{f}\%$  He II. Hydrogen is ionised to  $\gg 99\%$  then. If the amount of He II decreases to  $\frac{1.5}{f}\%$  (a decrease of the ionisation fraction is expected at late epochs; see Figures 6.2 and 6.3) the H II fraction decreases to less than 10%. **Without changing the physical conditions significantly, the fraction of H I can change by several orders in magnitude.**

To obtain some rough estimate of the electron temperature in a He-dominated layer containing some small fraction of hydrogen, we calculate the temperature-dependent ratio of collisional excitation and recombination  $\mathcal{R}$ . The thermal electron excitation coefficient from  $n = 2$  to  $n = 1$  is given by

$$C_{12} \sim 8.6 \times 10^{-6} \frac{n_e}{T^{1/2}} \frac{\Omega_{21}}{g_1} \exp\left(-\frac{E_{\text{Ly}\alpha}}{kT}\right) \equiv C_0 n_e \quad (6.9)$$

where  $\Omega_{21}$  is the effective collision strength of the hydrogen  $n = 1$  to  $n = 2$  transitions given by Scholz et al. (1990) and  $f_2, g_1$  are defined in Section 6.4. This gives

$$\begin{aligned} \mathcal{R} &= \frac{C_{12} \xi n_{\text{HI}}}{R n_e \xi n_{\text{HeII}} f_2} \\ &= \frac{C_0}{R f_2} \left( \frac{n_{\text{H}}}{n_{\text{HI}}} - 1 \right)^{-1} \end{aligned} \quad (6.10)$$

While  $C_0$  increases with temperature  $R$  decreases and  $\frac{C_0}{R f_2}$  is approximately one at  $\sim 11000\text{K}$ . Since hydrogen must be excited by thermal collisions effectively in order to produce a significant contribution to the total luminosity,  $\mathcal{R}$  must be  $\gg 1$ . Therefore the temperature must be higher than  $\sim 10000\text{K}$ , depending on the H I fraction.

At temperatures of  $\sim 20000\text{K}$  (which are reached for low fractions  $\frac{n_{\text{HI}}}{n_{\text{H}}} < 0.1$ ; this implies  $n_{\text{HI}} \leq n_{\text{HeII}} \ll n_{\text{HeI}}$ ) thermal excitation of He becomes important, the above estimate becomes invalid and the relative importance of H I emission decreases as compared to He I. Therefore, the temperature should be  $\sim 10000 - 15000 \text{ K}$  in order to allow effective H I emission.

We can use this temperature estimate to calculate the temporal evolution of He II and therefore H I for a toy model of the SN ejecta. Of course this temperature estimate is not exact, but it is sufficient to demonstrate how the absolute fractions  $\frac{n_{\text{He II}}}{n_{\text{He}}}$  and  $\frac{n_{\text{H I}}}{n_{\text{H}} + n_{\text{He}}}$  in a helium dominated layer can evolve with time (see Figures 6.2 and 6.3).

The deposited energy can be estimated analytically if the He density is known. For simplicity we assume that  $X$  solar masses of He and  $Y$  solar masses of  $^{56}\text{Ni}$  are distributed within a sphere of velocity  $v$  homogeneously (of course this is in conflict with our assumption that He is mixed with small fractions of heavy elements only, but this is a toy model only and He and  $^{56}\text{Ni}$  could be separated on small scales). At nebular epochs (say,  $> 100$  days), when most of  $^{56}\text{Ni}$  has decayed to  $^{56}\text{Co}$ , the deposited luminosity is given by

$$L_{\text{Dep}}(t) \sim 1.3 \times 10^{43} \exp\left(-\frac{t[\text{d}]}{111.4}\right) M_{^{56}\text{Ni}} [M_{\odot}] f_{\text{Dep}} \text{ ergs s}^{-1} \quad (6.11)$$

where  $f_{\text{Dep}}$  is the deposition function, which can be calculated analytically for a homogeneous sphere (e.g. [Axelrod 1980](#)). For three solar masses of helium and a  $^{56}\text{Ni}$  mass of  $\sim 0.1 M_{\odot}$  distributed homogeneously in a sphere of  $10000 \text{ km s}^{-1}$  the luminosity deposited around 350 days is  $\sim 10^{39.5} \text{ ergs s}^{-1}$  while the  $\text{H}\alpha$  luminosity of SN 2008ax at this epoch is  $\sim 10^{38.5} \text{ ergs s}^{-1}$  only ([Taubenberger et al. 2010](#)).

Since the ionisation potential of He is high and since we assumed that it is the predominant element, helium is mainly ionised by non-thermal electrons

$$\mathcal{R}_{\text{He}} Y_{\text{He}} n_{\text{He I}} = R_{\text{He}} \zeta (n_{\text{He II}} + n_{\text{H II}}) n_{\text{He II}} \quad (6.12)$$

where  $\mathcal{R}_{\text{He}} \sim 1.5$  is the recycling fraction of helium. This gives

$$\begin{aligned} \frac{n_{\text{He II}}}{n_{\text{He}}} &\sim \frac{R_{\text{He}} \zeta n_{\text{H II}} + \mathcal{R}_{\text{He}} Y_{\text{He}}}{2R_{\text{He}} \zeta n_{\text{He}}} \\ &\times \left( -1 + \sqrt{1 + 4 \frac{\mathcal{R}_{\text{He}} Y_{\text{He}} R_{\text{He}} \zeta n_{\text{He}}}{(R_{\text{He}} \zeta n_{\text{H II}} + \mathcal{R}_{\text{He}} Y_{\text{He}})^2}} \right) \end{aligned} \quad (6.13)$$

We compute Equations 6.6 and 6.13 for the toy model described above. We assume that 50% of all He recombinations into excited states can ionise a hydrogen atom ( $f = 0.5$ ) and vary the hydrogen mass between 0.01 and  $0.1 M_{\odot}$ . The temporal evolution of the H I fraction is shown in Figure 6.2. Depending on the ratio of hydrogen and helium the fractions of H I can increase dramatically between 100 and 1000 days. This means that  $\text{H}\alpha$  scattering or emission can appear at late epochs, without any hydrogen being detected at earlier times. In Equation 6.6 and 6.13 we assumed ionisation equilibrium, which may become invalid at epochs of  $\sim 500$  days and later. Therefore, we underestimate the He II fraction at very late epochs. However, qualitatively the effect is the same, since H I ionisation is related to He II recombination even at 1000 days and later.

## 6.2. SN 2008ax

Nebular spectra of SN 2008ax are available at 131, 149, 266, 280 and 359 days after explosion. The spectrum at 131 days covers the range between 9000 and  $25000 \text{ \AA}$ . The other spectra cover a range between 5000 and  $10000 \text{ \AA}$ . For the modelling we use a distance modulus of  $\mu = 29.92 \pm 0.29 \text{ mag}$  and a reddening of  $E(B - V) = 0.4 \pm 0.1 \text{ mag}$  (see [Taubenberger et al. 2010](#)). Also see [Pastorello et al. \(2008\)](#), [Chornock et al. \(2010\)](#) for observations and discussion of SN 2008ax.

There is observational evidence for asymmetry in SN 2008ax. The double-peaked profiles of the He I IR 10830 and  $20587 \text{ \AA}$  lines can be interpreted as a torus-shaped distribution of helium ([Taubenberger et al. 2010](#), [Chornock et al. 2010](#)). In addition, the blue wing of these lines is stronger, which can be interpreted as an asymmetry along the line of sight, but may also be a scattering effect. We place the observer in the equatorial plane, which is necessary to produce the double-peaked He profiles in this model.

The choice of this geometry (see Figure 6.4 for illustration) is motivated by the observations but is probably not unique. Different geometries may reproduce acceptable fits to the observations as well.

In contrast to the He IR lines (see Figure 6.5), most other lines are single peaked (see Figure 6.6). This is expected, since heavy elements are concentrated in the core. An exception is the [O I]  $\lambda\lambda 6300, 6363$  doublet ([Taubenberger et al. 2010](#)). While we agree that the profile of these lines may be shaped by geometry in other types of CC-SNe

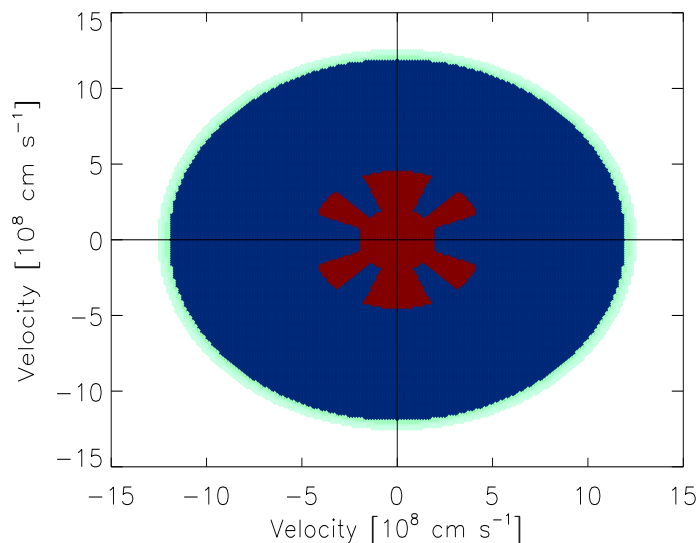


**Figure 6.4:** Illustration of the three-dimensional model of SN 2008ax, described in the text. The model has a weak asymmetry along the equatorial plane which is not indicated in this plot. Regions drawn in red colour are rich in heavy elements and contain no helium. Regions indicated in blue are helium-rich. The outermost region, indicated in green, is hydrogen-dominated. The x-axis is associated with the equator. In the centre (below  $4500 \text{ km s}^{-1}$ ), heavy elements (red) are concentrated towards the pole, while ejecta containing helium (blue) are concentrated in the equatorial regions.

(e.g. [Mazzali et al. 2005](#), [Maeda et al. 2008](#), [Modjaz et al. 2008](#), [Taubenberger et al. 2009](#), [Maurer et al. 2010](#)), we think that in SNe IIB  $H\alpha$  line scattering is responsible for the splitting of the [O I]  $\lambda\lambda$  6300, 6363 doublet (also see Section 6.3 for other SNe IIB).

The velocity of the  $H\alpha$  absorption minimum saturates at  $\sim 12500 \text{ km s}^{-1}$  about 40 days after explosion. This is usually interpreted as the lower boundary of hydrogen. Since hydrogen in lower layers may be strongly ionised (see Section 6.1.3), this estimate is somewhat uncertain. It may rather be the lower boundary of H I but not of H II.

We can reproduce the double-peaked profile of the [O I]  $\lambda\lambda$  6300, 6363 doublet very well placing less than  $0.1 M_{\odot}$  of hydrogen between  $12000$  and  $12500 \text{ km s}^{-1}$  (see Figure 6.6). An exact estimate of the H mass is not possible since shock interaction or clumping may be important in this region. This can explain why other lines, like [O I]  $5577 \text{ \AA}$  are single-peaked. This is discussed in more detail in Section 6.5.

Our model consists of 128 angular and 8 radial cells (spherical geometry; 1024 cells in total). The radial cells have outer boundaries at  $2000$ ,  $2800$ ,  $4500$ ,  $6000$ ,  $6600$ ,  $9500$ ,  $12000$  and  $12500 \text{ km s}^{-1}$ . This choice relates to the physical properties of our model for SN 2008ax.

Below  $2000 \text{ km s}^{-1}$  the ejecta are spherically symmetric. This innermost part of the SN is dominated by  $^{56}\text{Ni}$ , oxygen and calcium. The total mass and mass fractions in this zone are quite uncertain, but their contribution to the global properties of the SN is small. No He is present ( $< 10^{-4} M_{\odot}$ ).

The region between  $2000$  and  $2800 \text{ km s}^{-1}$  is similar to the innermost part, but some cells, preferentially in the equatorial plane, contain small fractions of He ( $\sim 10^{-3} M_{\odot}$ ). The bulk of the oxygen, calcium and carbon of SN 2008ax is located in this region. In contrast to calcium, carbon is probably not present below  $2000 \text{ km s}^{-1}$ . The confinement of C to a thin low velocity layer is in agreement with theoretical predictions (e.g. [Nomoto et al. 1993](#)).

The region between  $2800$  and  $4500 \text{ km s}^{-1}$  is dominated by oxygen and  $^{56}\text{Ni}$  in some cells and by He in others. This separation improves the reproduction of the observations. On the one hand He emission can be observed down to  $2000 \text{ km s}^{-1}$  and the He IR line ratio suggests that there is no strong mixing with heavy elements (which decreases the electron temperature and influences the strength and ratio of the He I  $10830$  and  $20587 \text{ \AA}$  lines). On the other hand, the iron lines observed are much broader than  $2800 \text{ km s}^{-1}$ . Placing all the  $^{56}\text{Ni}$  mass necessary to reproduce the observed flux below  $2800 \text{ km s}^{-1}$  causes too narrow and too strong Fe emission lines. A good



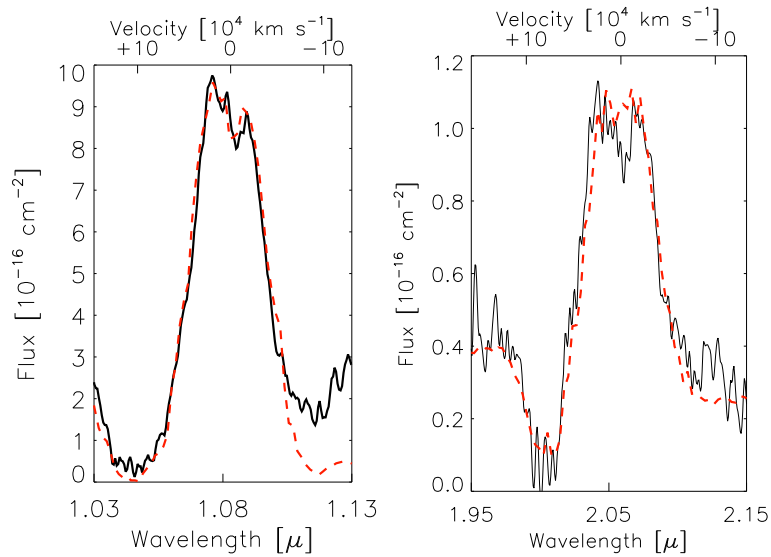


**Figure 6.5:** IR spectrum of SN 2008ax at 131 days after explosion. The He I 10830 Å line is shown on the left and the He I 20587 Å line is shown on the right. The observations are shown in black while the synthetic flux is shown by the dashed red line. The synthetic flux is obtained using the three-dimensional model described in the text. Since almost no background flux is produced by our nebular code near 20000 Å we added some constant flux at the level of the observations between 19000 and 22000 Å to allow He I 20587 Å line scattering. In contrast to the optical He lines, the 10830 Å and 20587 Å lines can be identified clearly, which allows a determination of the He density field. Two kinds of asymmetry can be observed. First, the double-peaked nature suggests a torus-shaped distribution of He. Second, the blue side of the profiles of both lines is stronger, which suggests an asymmetry along the line of sight.

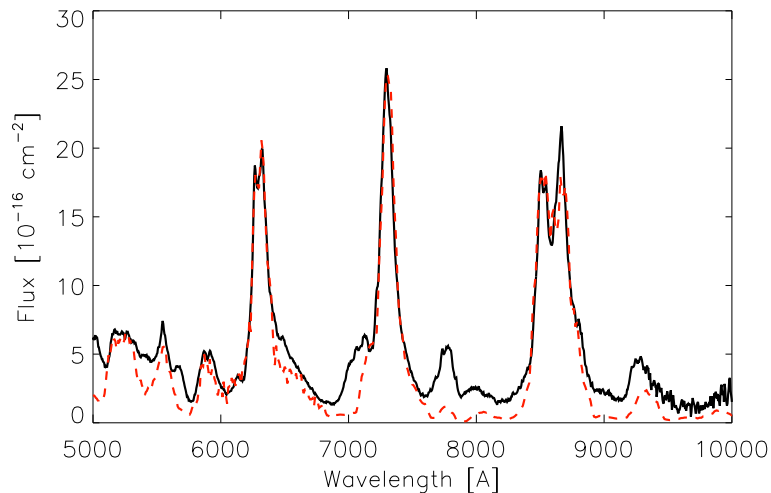


**Figure 6.6:** Optical spectrum of SN 2008ax at 149 days after explosion. Observations are shown in black while the synthetic flux is shown by the dashed red line. The synthetic flux is obtained using the three-dimensional model described in the text. Although the He I IR lines are shaped by the torus-like He distribution, all other lines are single peaked, since the heavy elements are concentrated in the core. There seems to be continuum flux, especially between 7000 and 10000 Å, which is not reproduced. This is because of the epoch (149 days), which is too early for a strictly nebular treatment.

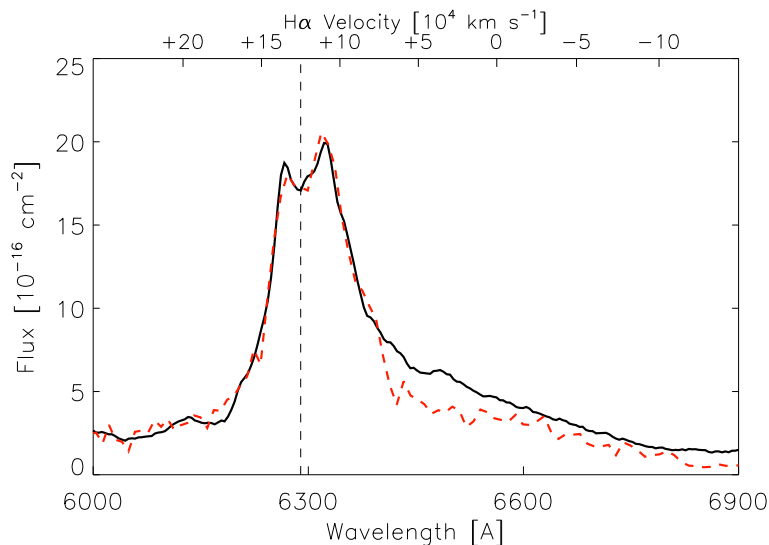


**Figure 6.7:** Optical spectrum of SN 2008ax at 149 days after explosion. Observations are shown in black while the synthetic flux is shown by the dashed red line. The synthetic flux is obtained using the three-dimensional model described in the text. The (double) peak of the [O I]  $\lambda\lambda$  6300, 6363 doublet profile is caused by  $H\alpha$  absorption between  $\sim 12000$  and  $12500 \text{ km s}^{-1}$ . The  $H\alpha$  absorption minimum is indicated by the vertical dashed line.

compromise is found by allowing a separation of the  $^{56}\text{Ni}$  and He-rich ejecta. Large-scale structures of burned and unburned material are not unexpected depending on the explosion scenario. The He rich cells contain some fraction of carbon, oxygen, sodium and calcium (in total  $\sim 30\%$ ). These elements are strongly excited by the energy absorbed by the He layer.

The material above  $4500 \text{ km s}^{-1}$  is dominated by helium, which constitutes most of the mass of SN 2008ax. The He rich layer reaches out to at least  $\sim 9500 \text{ km s}^{-1}$ . The composition and density of the zone between  $9500$  and  $12000 \text{ km s}^{-1}$  is not clear. The absorption profile of the He I IR lines suggests that there is no He I 20587 Å line scattering above  $\sim 10000 \text{ km s}^{-1}$  (see Figure 6.5). An upper limit to the He mass in this region is  $\sim 0.05 M_{\odot}$ . The observation of the [O I]  $\lambda\lambda$  6300, 6363 doublet shows that there is no strong  $H\alpha$  line scattering below  $12000 \text{ km s}^{-1}$  (see Figure 6.6). A possible solution may be that there is some He (of the order of  $0.1 M_{\odot}$ ) in this region, but mixed with small fractions of neutral elements, like H I. In this case continuum destruction of He I 584 Å photons could reduce the optical depth of the He I 20587 Å line significantly (Chugai 1987, Li & McCray 1995). This effect strongly depends on the composition of the He layer. However, since the mass in this region is expected to be low, the effect on our total mass estimate would presumably be less than 10%. The estimate of the kinetic energy could be influenced more strongly.

The 266, 280 and 359 day  $H\alpha$  observations cannot be reproduced using any reasonable amount of hydrogen (of the order of  $0.1 M_{\odot}$ ). It seems likely that some additional mechanism of  $H\alpha$  emission becomes important between 150 and 200 days after explosion, as in SN 1993J (Houck & Fransson 1996). In Section 6.4 we propose a mechanism, based on mixing and clumping of hydrogen and helium. Shock interaction is also a possibility and is discussed in Section 6.5.

The O I 7774 Å line is reproduced well at 266 days and later but is too weak at 149 days after explosion, which is expected (Maurer & Mazzali 2010) since there is no clumping of the ejecta in our model.

The He I 10830 Å line may contain some contribution from Si and S lines. However, in SN 2008ax this contribution is weak. It seems likely that He I 20583 Å and possibly He I 10830 Å are influenced by line scattering. Both lines have optical depths larger than one around 130 days after explosion. However, it is not clear if there is enough flux that can be scattered. Our nebular code produces almost no emission on the blue side of both lines. However, at least for He I 20587 Å this is in conflict with the observations, which show some background flux around 20000 Å. Since the spectrum at 131 days is probably not completely nebular, it is not surprising that certain features of the spectrum are not reproduced well (also see the background flux in the optical spectrum at 149 days). The formation

	He M <sub>⊙</sub>	C M <sub>⊙</sub>	O M <sub>⊙</sub>	Ca M <sub>⊙</sub>	Ni M <sub>⊙</sub>	M <sub>Tot</sub> M <sub>⊙</sub>	E <sub>K</sub> 10 <sup>51</sup> ergs
A	2.0	0.09	0.51	0.005	0.10	2.7	≥ 0.9
B	2.7	0.07	0.40	0.002	0.07	3.3	≥ 1.2

**Table 6.1.:** SN 2008ax. (A) Best fit three-dimensional model (B) All <sup>56</sup>Ni confined below 2800 km s<sup>-1</sup>; inconsistent with nebular Fe-group line observations. Hydrogen is not included in the total mass and kinetic energy estimate in both models but should be of the order of 0.1 M<sub>⊙</sub> and 10<sup>50</sup> ergs.

	μ mag	E(B - V) mag	M <sub>56Ni</sub> M <sub>⊙</sub>	M <sub>Tot,ej</sub> M <sub>⊙</sub>	E <sub>K</sub> 10 <sup>51</sup> ergs	Reference
A	29.92 ± 0.29	0.4 ± 0.1	0.10 <sup>+0.05</sup> <sub>-0.03</sub>	2.8 <sup>+1.2</sup> <sub>-0.9</sub>	1.0 <sup>+1.1</sup> <sub>-0.3</sub>	This work
B	29.92 ± 0.29	0.4 ± 0.1	0.07–0.15	4.6 ± 2.5	1.0–10	Taubenberger et al. (2010)
C	29.92	0.3	~ 0.06* [0.07]	~ 2.9* [3.3]	~ 0.5* [0.6]	Roming et al. (2009)
D	29.92	0.3	~ 0.11* [0.13]	~ 2.3* [2.7]	~ 1.5* [1.7]	Tsvetkov et al. (2009)
E	29.92 ± 0.29	0.3	0.07* – 0.11* [0.08 - 0.13]	3* – 6* [3 – 7]	~ 1.0* [1.2]	Pastorello et al. (2008)

**Table 6.2.:** Properties of SN 2008ax obtained by different methods: (A) Multi-dimensional nebular modelling (B) one-zone light-curve calculation (C) semi-analytical light-curve modelling (D) numerical light-curve modelling using the radiation transport code STELLA on a SN IIB explosion model (E) light-curve comparison of SN 2008ax and SN 1993J. Estimates (B), (C), (D) and (E) are obtained from the light-curve. Although no errors are given, (D) is probably the most reliable light-curve based estimate. \*Please note that (C), (D) and (E) are computed for E(B - V) = 0.3 mag instead of 0.4 mag. In rough approximation a comparison can be made by multiplying all quantities of (C), (D) and (E) by a factor of 1.15. These values are given in brackets.

of the background is discussed in more detail in Section 7.

To handle this problem we introduce some artificial background flux between 19000 and 22000 Å at the flux level of the observations. This allows the He I 20587 Å line to increase by line scattering. However, since this background is completely artificial, one can not expect that the modelling is accurate.

The masses estimated for He, C, O, Ca and <sup>56</sup>Ni are shown in Table 1. The uncertainties on these estimates should be of the order of (several) 10%. Other elements carry larger uncertainties. We also compute the total mass and kinetic energy, excluding hydrogen. Our best-fit three-dimensional model is listed Table 1, row (A). Since some SN IIB models predict a confinement of <sup>56</sup>Ni to quite low velocities (Nomoto et al. 1993), we additionally show an estimate obtained by placing all <sup>56</sup>Ni below 2800 km s<sup>-1</sup> (B), which is, however, in conflict with the Fe-group emission line observations.

A comparison of the total mass of models (A) and (B) shows that the uncertainties owing to the distribution of <sup>56</sup>Ni is about half a solar mass. However, since model (B) stands in clear contradiction to the nebular Fe-group emission line observations model (A) has to be preferred. There are also uncertainties from He I background scattering, clumping and from the atomic data. Additionally, we may underestimate the mass in the outer regions.

Owing to all the uncertainties described above, we estimate a total mass between 2.2 and 3.2 M<sub>⊙</sub> and a <sup>56</sup>Ni mass between 0.10 and 0.12 M<sub>⊙</sub>. A lower limit on the kinetic energy is 0.9 · 10<sup>51</sup> ergs (for a total mass of 2.7 M<sub>⊙</sub>). Since small amounts of high velocity H and He could increase the total kinetic energy considerably we estimate a total kinetic energy between 0.7 and 1.7 · 10<sup>51</sup> ergs (for a total mass between 2.2 and 3.2 M<sub>⊙</sub>).

In addition there is some uncertainty (~ 40%) owing to extinction (we used E(B - V) = 0.4 ± 0.1 mag) and distance (9.6 ± 0.3 Mpc). Since these uncertainties would influence the total mass and the <sup>56</sup>Ni mass estimate simultaneously we assume that the uncertainty owing to distance and extinction is ~ 20% on each of these quantities. Thus we estimate (including 0.1 M<sub>⊙</sub> of hydrogen with a kinetic energy of 10<sup>50</sup> ergs) a total mass of 2.8<sup>+1.2</sup><sub>-0.9</sub> M<sub>⊙</sub>, a total <sup>56</sup>Ni mass of 0.10<sup>+0.05</sup><sub>-0.03</sub> and a total kinetic energy 1.0<sup>+1.1</sup><sub>-0.3</sub> · 10<sup>51</sup> ergs.

In Table 2 we compare our estimates to results from other groups. Taubenberger et al. (2010) obtain estimates from one-zone-modelling of the light curve. They estimate a total mass of ~ 4.6 M<sub>⊙</sub>, a kinetic energy of 6 · 10<sup>51</sup> ergs and a <sup>56</sup>Ni mass of 0.1 M<sub>⊙</sub>. The estimates of the total mass and kinetic energy are larger than found in this work. The uncertainties estimated by Taubenberger et al. (2010) are large and the results agree within these uncertainties.

SN	$v_{\text{phot,H}\alpha}$ km s <sup>-1</sup>	$v_{\text{neb,H}\alpha}$ km s <sup>-1</sup>	$M_H$ $M_{\odot}$	Reference
1993J	~ 10000	≤ 11000	~ 0.2	Woosley et al. (1994)
2001ig	~ 13500	~ 13200	–	Maund et al. (2007)
2003bg	~ 13000	~ 12800	≥ 0.05	Mazzali et al. (2009)
2007Y	~ 10000	≤ 11000	–	Taubenberger et al. (2010)
2008ax	~ 12500	~ 12200	–	Taubenberger et al. (2010)

**Table 6.3.:** The velocity of the absorption minimum of H $\alpha$  at ~ 40 days after the explosion ( $v_{\text{phot,H}\alpha}$ ) taken from the literature and the velocity of the H $\alpha$  derived from the [O I]  $\lambda\lambda$  6300, 6363 doublet profile in this work ( $v_{\text{neb,H}\alpha}$ ). A physical connection between both velocities seems likely, confirming that the profile of the [O I]  $\lambda\lambda$  6300, 6363 doublet is strongly influenced by H $\alpha$  absorption.

Roming et al. (2009) model the light-curve of SN 2008ax using a combination of an analytical light-curve model and a Monte-Carlo routine. Our results are roughly consistent, however the kinetic energy estimated by Roming et al. (2009) seems to be too low in general. This has also been found by Taubenberger et al. (2010).

A comparison to Tsvetkov et al. (2009) shows that our results agree rather well. Since the extinction was estimated to be lower in the work of Tsvetkov et al. (2009) we multiply their results by a factor of 1.15 for comparison. This gives 0.127  $M_{\odot}$  of  $^{56}\text{Ni}$ , a total mass of 2.7  $M_{\odot}$  and a kinetic energy of  $1.7 \cdot 10^{51}$  ergs. We may underestimate the kinetic energy but our results agree within the errors.

Our estimates for the  $^{56}\text{Ni}$  and total mass, as well as for the kinetic energy are also consistent with the results of Pastorello et al. (2008).

### 6.3. Other SNe of Type IIb

Nebular models for SNe 1993J (Houck & Fransson 1996), 2001ig (Silverman et al. 2009), 2003bg (Mazzali et al. 2009) and 2007Y (Stritzinger et al. 2009) exist but a treatment of helium was not possible, since there are no IR nebular spectra (Houck & Fransson 1996 included He in their analysis but had no IR observations for comparison). An exact treatment of hydrogen is also difficult since it is observed as H $\alpha$ , which may be influenced by scattering, clumping and shock interaction.

Therefore, we restrict our analysis to the question: can H $\alpha$  be powered by radioactive energy deposition, as described by Houck & Fransson (1996)? The answer to this question is less model dependent than estimating element masses or distributions. At late epochs (> 200 days) the SN ejecta are illuminated homogeneously by  $\gamma$ -radiation (since the  $\gamma$ -optical depth is low) and asymmetries in the  $^{56}\text{Ni}$  or hydrogen distribution are not very important. In addition we can obtain some constraints on the H and He distribution from early and late-time line-width observations. The maximum H mass is restricted by light curve observations and should be less than one solar mass (Nomoto et al. 1993, Utrobin 1994, Woosley et al. 1994).

Early time observations show that all SNe of our sample have absorption minima of H $\alpha$  between 13000 and 20000 km s<sup>-1</sup> during the first days after explosion. The velocity of these absorption minima decreases rapidly in the following tens of days and bottoms out at ~ 10000 – 13000 km s<sup>-1</sup> in all SNe around 30 – 40 days after explosion. This saturation behaviour is usually interpreted as the lower boundary of the hydrogen layer. However, there may be some hydrogen at lower velocities if it is ionised completely in the early phase of the SN (see Section 6.1.3). We show that there is an intriguing link between the velocity of the early time H $\alpha$  absorption minimum and the profile of the [O I]  $\lambda\lambda$  6300, 6363 doublet for all SNe of our sample (see Table 6.3).

Whether a double-peaked [O I]  $\lambda\lambda$  6300, 6363 doublet is formed or not, depends on the velocity of the optically thick H $\alpha$ . The optimum H $\alpha$  velocity to produce a double-peaked O [I] profile is ~ 12000 km s<sup>-1</sup> since then the absorption minimum of H $\alpha$  for 6300 Å lies right at the centre of the [O I]  $\lambda$  6300 line profile, which corresponds to the centre of the SN (bulk of oxygen).

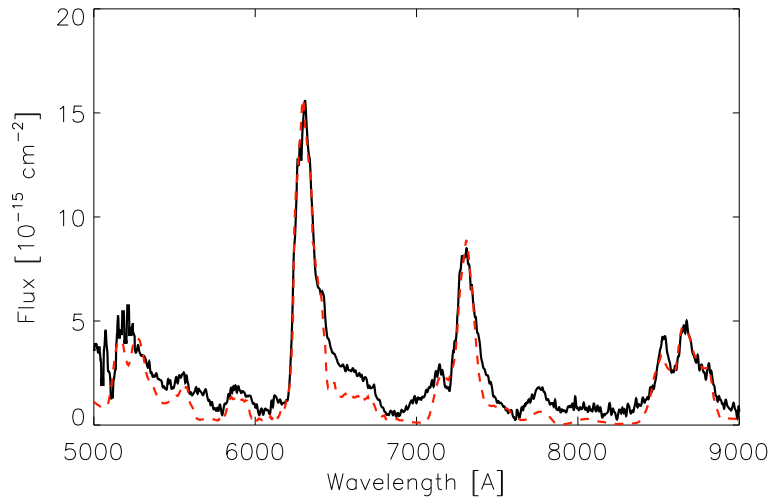


**Figure 6.8.:** Optical spectrum of SN 1993J at 206 days after explosion (black line). The synthetic flux (red dashed line) is produced using  $0.2 M_{\odot}$  of hydrogen distributed between 7000 and 10000  $\text{km s}^{-1}$ .  $H\alpha$  is not reproduced with sufficient strength. The [O I]  $\lambda\lambda$  6300, 6363 doublet is single peaked, since hydrogen is located below 11000  $\text{km s}^{-1}$ .

### 6.3.1. SN 1993J

Nebular spectra of SN 1993J have been modelled before, investigating the formation of the  $H\alpha$  line in detail (Houck & Fransson 1996). We repeat this analysis to test whether our results are in agreement with previous findings. We have spectra at 118, 172, 206, 237, 256, 300 and 363 days after explosion. While the 118 day spectrum is not strictly nebular, all the later ones are. The spectra cover a range between 4000 and 10000 Å but no IR observations are available. For the modelling we use a distance modulus of  $\mu = 27.72$  mag and an extinction of  $E(B - V) = 0.18$  mag (Houck & Fransson 1996).

Houck & Fransson (1996, see their Figure 1) have shown that a model consisting of a heavy element core ( $0 - 3400 \text{ km s}^{-1}$ ), a He layer ( $3400 - 7800 \text{ km s}^{-1}$ ) and a hydrogen dominated layer ( $> 7800 \text{ km s}^{-1}$ ) containing  $\sim 25\%$  of He can produce synthetic spectra consistent with the nebular observations of SN 1993J (except  $H\alpha$  at late epochs).

Using a model similar to the one presented by Houck & Fransson (1996) we can reproduce the evolution of the heavy element lines of SN 1993J at all epochs between 118 and 363 days (e.g. see Figure 6.8). The hydrogen mass of SN 1993J was estimated to be  $0.2 M_{\odot}$  (Woosley et al. 1994, Houck & Fransson 1996). Using this hydrogen mass we come to the same conclusions as Houck & Fransson (1996). The synthetic  $H\alpha$  flux and the observations become inconsistent between 150 and 200 days after explosion. This is usually interpreted as the time of the transition to a shock interaction dominated phase (e.g. Patat et al. 1995, Houck & Fransson 1996).

The [O I]  $\lambda\lambda$  6300, 6363 line in SN 1993J is not double-peaked. As we have shown for SN 2008ax, the double-peaked oxygen profile is possibly the result of  $H\alpha$  absorption. Since the optically thick  $H\alpha$  of SN 1993J has a velocity  $< 11000 \text{ km s}^{-1}$  (see Table 3), the oxygen line is not split by the  $H\alpha$  absorption minimum. This is discussed in more detail in Section 6.5.

### 6.3.2. SNe 2001ig & 2003bg

For SN 2003bg there is a H mass estimate of  $\sim 0.05 M_{\odot}$  obtained from early-time absorption modelling (Mazzali et al. 2009), while there is no estimate of the H mass of SN 2001ig.

We have nebular spectra of SN 2001ig at 256, 309 and 340 days after explosion. The spectra cover a range between 4000 and 10000 Å. For the modelling we use a distance modulus of  $\mu = 30.5$  mag and an extinction of  $E(B - V) = 0.011$  mag (Silverman et al. 2009).

For SN 2003bg we have nebular spectra at 264 and 301 days after explosion. The spectra cover a range between 4000 and 10000 Å. For the modelling we use a distance modulus of  $\mu = 31.68$  mag and an extinction of  $E(B -$

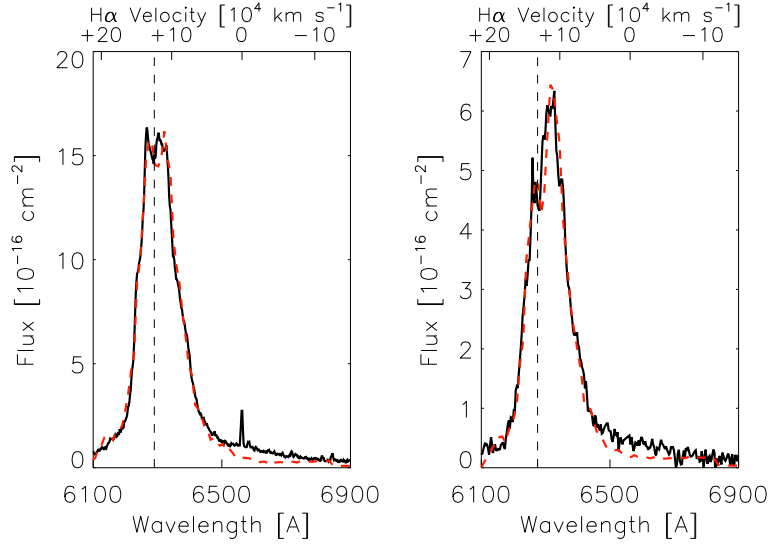


**Figure 6.9:** Left: Optical spectrum of SN 2001ig at 340 days after explosion. Right: Optical spectrum of SN 2003bg at 301 days after explosion. The band shown (6100 to 6900 Å) is dominated by the [O I]  $\lambda\lambda$  6300, 6363 doublet. The observations are shown by the black lines. The red dashed lines show the synthetic flux obtained using  $\sim 0.3 M_{\odot}$  of hydrogen and a **one-dimensional** model. Hydrogen causes some weak line scattering of the oxygen-dominated flux around 6300 Å, creating the double peaked profile of the oxygen doublet, but does not provide enough H $\alpha$  flux to explain the observations around 6560 Å. The double peaked oxygen profile is not caused by geometry, but by H $\alpha$  absorption around 13200 km s $^{-1}$  (SN 2001ig) and 12800 km s $^{-1}$  (SN 2003bg). The H $\alpha$  absorption minima are indicated by the vertical dashed lines.

$V$ ) = 0.02 mag (Mazzali et al. 2009).

Although the nebular H $\alpha$  flux is weak in both SNe, we find that it cannot be reproduced using reasonable amounts of hydrogen. In contrast to the H $\alpha$  emission, the absorption can be reproduced well. The [O I]  $\lambda\lambda$  6300, 6363 doublet is often used to investigate asymmetries of CC-SNe cores. However, in the case of SNe I Ib there is strong evidence that the profile of the oxygen line is not shaped by geometry alone but also by absorption (see Section 6.2). To reproduce the oxygen profiles of SN 2001ig and 2003bg we have to place  $\sim 0.3 M_{\odot}$  of hydrogen between 13000 and 13500 km s $^{-1}$  (SN 2001ig) and 12600 and 13000 km s $^{-1}$  (SN 2003bg) which is roughly consistent with the early-time absorption minimum of H $\alpha$  (see Table 3) of these SNe.

Although we can reproduce the absorption features well, it seems unlikely that  $0.3 M_{\odot}$  of hydrogen are necessary to reproduce the observations if there is some additional mechanism of H $\alpha$  excitation (e.g. shock interaction). This may be expected, since H $\alpha$  emission is underestimated in our models.

### 6.3.3. SNe 2007Y

Although H $\alpha$  absorption was detected in its early spectra, SN 2007Y was classified as a SN Ib (Stritzinger et al. 2009). While these H $\alpha$  features would be sufficient to classify SN 2007Y as a Type I Ib, there is more evidence for the presence of hydrogen since there is strong H $\alpha$  emission in the nebular phase. Stritzinger et al. (2009) argue that the emission is caused by shock interaction, but Chevalier & Soderberg (2010) claim that the circumstellar density of SN 2007Y is too low to produce the H $\alpha$  luminosities observed before 300 days after explosion.

The nebular spectra cover a range between 4000 and 10000 Å. For the modelling we use a distance modulus of  $\mu = 31.43$  mag and an extinction of  $E(B - V) = 0.112$  mag (Stritzinger et al. 2009). There is no IR nebular spectrum.

The H $\alpha$  flux can be reproduced neither at 248 nor at 288 days using reasonable amounts of hydrogen. We therefore conclude that the H $\alpha$  flux of SN 2007Y cannot result from radioactive energy deposition as described by Houck & Fransson (1996) even if it was a SN I Ib and that some other mechanism is needed. To avoid a double-peaked profile of the [O I]  $\lambda\lambda$  6300, 6363 doublet, the hydrogen must be concentrated below 11000 km s $^{-1}$ . This is in perfect

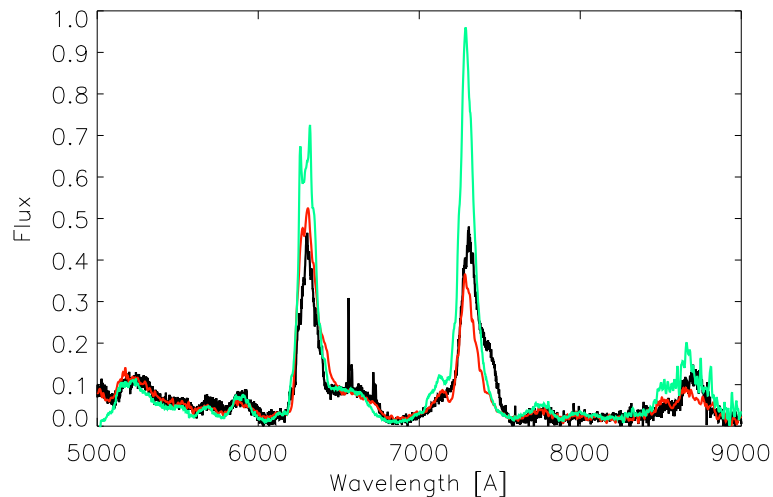


**Figure 6.10:** Optical spectra of SNe 1993J (256 days; red line), 2007Y (248 days; black line) and 2008ax (266 days; green line). The spectra are scaled by arbitrary constants. Apart from the [O I]  $\lambda\lambda$  6300, 6363 doublet and the [Ca II] emission the spectra agree extremely well. The ratio of  $H\alpha$  to oxygen emission is strongest in SN 2007Y, which is surprising since this SN was classified as SN Ib, while SNe 1993J and 2008ax were classified as Type IIB. SN 2007Y has the strongest nebular ratio of  $H\alpha$  to oxygen (and total) flux ever detected in a stripped CC-SN. The [O I]  $\lambda\lambda$  6300, 6363 doublet is single-peaked, which is expected if the bulk of hydrogen is located below  $11000 \text{ km s}^{-1}$ .

agreement with observations of the early-time  $H\alpha$  absorption minimum (see Table 6.3).

SN 2007Y has the highest  $H\alpha$  to [O I]  $\lambda\lambda$  6300, 6360 doublet flux ratio (and also total flux) of all five SNe (see Figure 6.10). Unless a serious amount of hydrogen has been accumulated from a thick circumstellar wind afterwards, which is unlikely, SN 2007Y must have had a significant fraction of H in its outer layers at the time of explosion. In addition,  $H\alpha$  is observed at  $\sim 15000 \text{ km s}^{-1}$  during the first days after explosion.

Therefore, SN 2007Y is most likely a SN of Type IIB similar to SN 1993J and SN 2008ax. Then it is important to understand why the early time  $H\alpha$  absorption was weak (Stritzinger et al. 2009). A simple explanation may be that the hydrogen of SN 2007Y is more mixed with helium than the hydrogen of SN 1993J and 2008ax. In this case hydrogen could be ionised more strongly at early times, which means that there is hydrogen but no H I. Thorough mixing of hydrogen and helium could also explain the strong, low-velocity  $H\alpha$  emission observed at late epochs (see Section 6.4). This is discussed in more detail in Section 6.5.

## 6.4. An alternative to shock interaction

To our knowledge there are only three stripped CC-SNe (SNe 1993J, 2007Y, 2008ax) which show strong, box-shaped  $H\alpha$  emission in their nebular phase. It is commonly assumed (e.g. Filippenko et al. 1994, Patat et al. 1995, Houck & Fransson 1996) that the box-shaped  $H\alpha$  emission of SN 1993J is caused by shock interaction.

Houck & Fransson (1996) have shown that radioactive energy deposition is too weak to produce strong  $H\alpha$  emission at late epochs. Their analytical estimates do not depend on the SN 1993J model explicitly and should be valid for any SN IIB with moderate amounts of H ( $\sim 0.1 M_{\odot}$ ). One may therefore conclude that the same mechanism operating in SN 1993J is also at work in SNe 2007Y and 2008ax. However, for SN 2008ax there are several problems connected to the shock-interaction interpretation of its  $H\alpha$  nebular emission (Taubenberger et al. 2010). In SN 2007Y shock interaction is not expected at all (Chevalier & Soderberg 2010).

In this section we present an alternative mechanism for powering late nebular  $H\alpha$  emission. This mechanism may explain how late-time  $H\alpha$  emission can be powered by radioactive decay without any need for shock interaction, solving the problems mentioned above. This is possible, since we include the effect of thermal electron hydrogen excitation, which was neglected by Houck & Fransson (1996) and propose a certain ejecta configuration, which is required. The mechanism is simple but needs special conditions to operate, which could explain why strong nebular

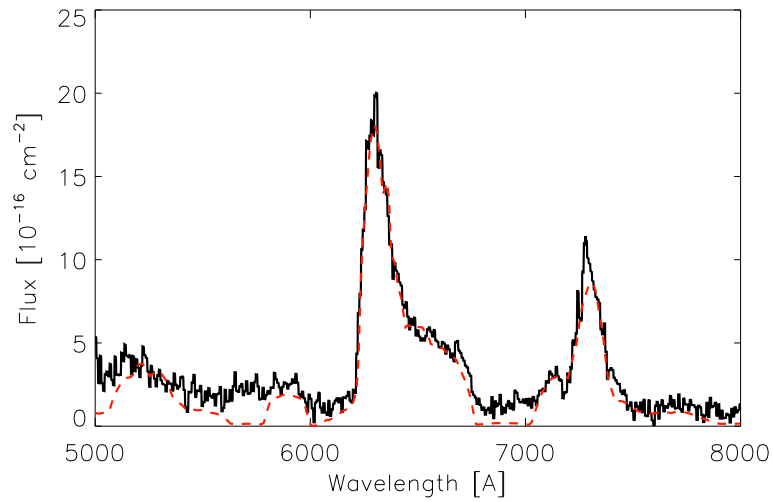


**Figure 6.11.:** Optical spectrum of SN 1993J at 363 days after explosion (black line). The synthetic flux (red dashed line) was produced by a one-dimensional model containing  $2 M_{\odot}$  of He and  $0.2 M_{\odot}$  of hydrogen. H and He are mixed and distributed out to  $\sim 10000 \text{ km s}^{-1}$ . A clumping factor of the He layer of  $\zeta = 200$  was used. As expected the [O I]  $\lambda\lambda$  6300, 6363 doublet is single peaked.

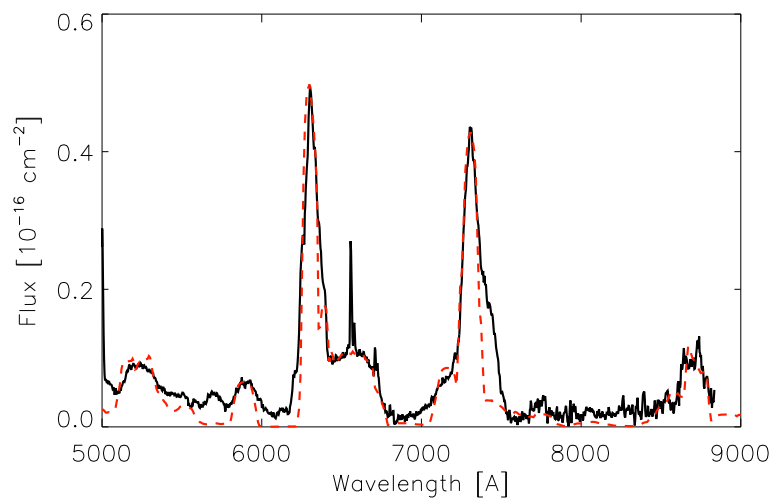


**Figure 6.12.:** Optical spectrum of SN 2007Y at 288 days after explosion (black line). The synthetic flux (red dashed line) was produced by a one-dimensional model containing  $1.5 M_{\odot}$  of He and  $0.1 M_{\odot}$  of hydrogen. H and He are mixed and distributed out to  $\sim 10500 \text{ km s}^{-1}$ . A clumping factor of the He layer of  $\zeta = 100$  was used. As expected the [O I]  $\lambda\lambda$  6300, 6363 doublet is single peaked.



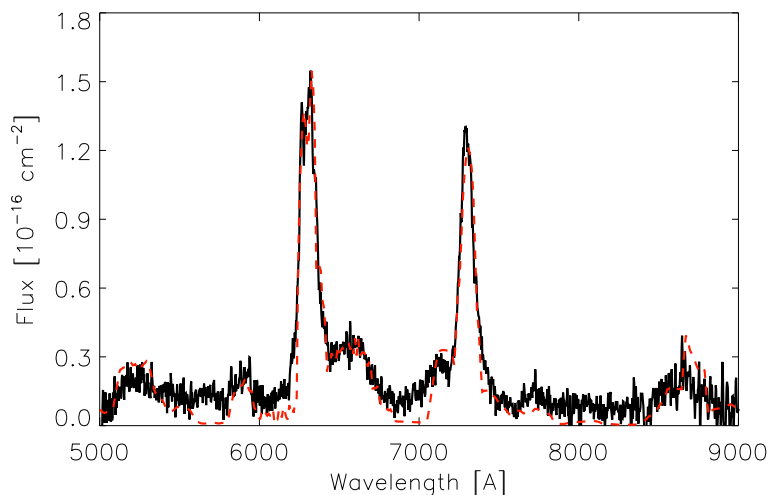


**Figure 6.13.:** Optical spectrum of SN 2008ax at 359 days after explosion (black line). The synthetic flux (red, dashed line) was produced using a one-dimensional model. A clumping factor of the He layer of  $\zeta \sim 100$  was used. While the  $H\alpha$  emission is produced by tiny fractions of H in the He layer below  $12000 \text{ km s}^{-1}$ , the double-peaked profile of the [O I]  $\lambda\lambda$  6300, 6363 doublet is again produced by  $H\alpha$  absorption between  $12000$  and  $12500 \text{ km s}^{-1}$  (also see Figure 6.7).

$H\alpha$  emission is rare in stripped CC-SNe (this may also be explained by shock interaction).

We assume that a small fraction of hydrogen (of the order of 1%) is mixed into a helium-dominated layer. The degree of H ionisation will lie between 1 and almost 100% depending on the ionisation state of helium, since He recombination can ionise hydrogen strongly (see Section 6.1.3). There is a sharp transition between complete and almost no ionisation of hydrogen, if the hydrogen mass is comparable to the mass of He II. In such a situation, when the degree of ionisation of helium decreases with time, as it does naturally, large amounts of neutral hydrogen can be produced in regions where no H I had been present at earlier epochs (this is explained in more detail in Section 6.1.3). Therefore, the H I fraction in the He dominated layer can increase from approximately zero to, say, 2% of the total mass within several hundred days. Up to this epoch an observer would not even know about hydrogen in these regions since H II cannot be observed, except by extremely weak recombination radiation.

It is important to note that the energy deposited in the He-rich regions (at least in SN 2008ax, but probably also in SNe 1993J and 2007Y) is  $\sim 10$  times larger than the energy emitted in  $H\alpha$ . This means that if only 10% of the deposited energy was transformed into  $H\alpha$ , shock interaction would not be needed to explain the late-time  $H\alpha$  emission.

Under typical nebular conditions  $\sim 70\%$  of the energy deposited in a He rich layer by radioactive decay is stored in thermal electrons. It is therefore clear that emission from this region is dominated by thermal electron collisional excitation and not by recombination. If heavy elements (C, O, Na, etc.) are mixed into the He layer in sufficient fractions, they can be excited by thermal electrons and cool the gas efficiently. In this case  $H\alpha$  is predominantly produced by recombination, which is much too weak to explain the late time  $H\alpha$  flux (Houck & Fransson 1996, they neglected thermal electron excitation of hydrogen). Since this scenario would produce high-velocity optical lines (e.g. oxygen or sodium), which are not observed, helium cannot be mixed with heavy elements strongly (at least in SN 2008ax; see Section 6.2).

If the gas consists of hydrogen and helium only, or if heavier elements are singly ionised to almost 100%, which would be the case if the fraction of these elements was lower than the fraction of He II, thermal electrons cannot cool effectively until they reach high enough temperatures to excite hydrogen ( $\sim 10000\text{K}$ ; see Section 6.1.3). In this scenario 99% of the thermal electron energy is radiated away by Ly $\alpha$  emission and therefore lost to the UV. About 1% is converted into  $H\alpha$ , which is too small by a factor of  $\sim 10$  to explain the  $H\alpha$  observations.

At this point clumping could become important. We use the symbol  $\zeta$  for the clumping factor, which is defined as the inverse of the filling factor [see Maurer & Mazzali (2010) for more details]. A clumping factor  $\zeta$  means that the density is increased by a factor of  $\zeta$  locally, while the global density remains constant.

A helium layer containing small amounts of hydrogen can emit much more than 1% of its thermal electron energy in  $H\alpha$  if clumping is strong, since clumping increases the excitation of H I to  $n = 2$  & 3, and the self-absorption optical depth of the H I ground state transitions.

Summarising, this means that, if hydrogen and helium are mixed in suitable fractions and clumped strongly, radioactive energy deposition can power  $H\alpha$  completely without any additional source of energy. We present some estimates here, which support this idea.

Since the excitation potential of hydrogen is  $\sim 10$  eV lower than that of helium, the thermal electron collisional excitation rates of hydrogen are approximately  $\exp(10\text{eV}/kT) \sim 10^{5-3}$  times (at 10000 – 20000K) higher than those of helium. Unless there are  $\sim 10^{5-3}$  times more He I than H I atoms  $\sim 70\%$  of the total energy deposited in helium will be radiated away by hydrogen and He IR lines (the other 30% will go into non-thermal electron excitation and recombination radiation, mainly UV).

It is clear that, as long as H is ionised completely ( $\gg 99\%$ ),  $H\alpha$  emission and scattering are extremely weak. There is no  $H\alpha$  scattering since there is no  $Ly\alpha$  self-absorption if there is no H I, which means that the H I  $n = 2$  level is depopulated strongly. Moreover, there is almost no  $H\alpha$  emission, since only  $\sim 20\%$  of the deposited energy go into ionisation. This energy is mainly emitted by He I recombination radiation and  $Ly\alpha$ , which means that the fraction of deposited energy emitted by  $H\alpha$  is less than one percent. Thermal electrons cool predominantly by exciting He I, since the temperature increases to more than 15000K.

We derive a rough estimate for the dependence of  $H\alpha$  emission on clumping. We consider effective recombination into the hydrogen levels  $n = 2$  and 3, thermal electron (de-) excitation between the ground state and the levels  $n = 2$  and  $n = 3$ , and radiative transitions from H I  $n = 3$  to  $n = 2$  and from  $n = 2$  to  $n = 1$ . We neglect radiative transitions from H I  $n = 3$  to  $n = 1$ , since this rate is small owing to self-absorption. We also neglect thermal excitation from H I to  $n = 2$  to  $n = 3$ , which may contribute to the population of the H I  $n = 3$  level but is less important than direct excitation from the ground state. We only consider the situation where enough H I is present to cool the gas efficiently ( $\frac{n_{\text{HI}}}{n_{\text{He}}} > 0.1\%$ ), which means that the H I ground state transitions are highly self-absorbed.

To calculate the formation of  $H\alpha$  the population of the  $n = 2$  state of H I has to be estimated

$$\begin{aligned} n_{\text{HI},2} &\sim \frac{C_{12}\zeta[+If_2]}{A_{21}\tau_{21}^{-1}\zeta^{-1} + C_{21}\zeta} n_{\text{HI},1}, & \tau_{21} \gg 1 \\ &\propto \zeta^2, & \zeta \sim 1, C_{12} > I \\ &\propto \zeta^0, & \zeta \gg 1 \end{aligned} \quad (6.14)$$

where  $C_{ij}$  are the thermal electron collisional rates between the  $n = i$  and  $j$  states of H I (e.g. Callaway 1994),  $I$  is the total ionisation rate (non-thermal electrons and photo-ionisation; see Section 6.1.3),  $f_n$  are the fractions of recombining electrons, cascading into the H I  $n$  states and

$$\tau_{21} = \frac{\lambda_{Ly\alpha}^3 t g_2 A_{21}}{8\pi g_1} n_{\text{HI},1}, \quad n_{\text{HI},1} \gg n_{\text{HI},2} \quad (6.15)$$

is the Sobolev optical depth of the H I ground state, with  $\lambda_{Ly\alpha} \sim 1216 \text{ \AA}$  the wavelength of  $Ly\alpha$ ,  $g_n$  the statistical weights of the  $n$  states of H I and  $A_{21}$  the radiative rate of  $Ly\alpha$ . Depending on the number density of the H I ground state the  $n = 2$  state can be thermally populated ( $C_{21}\zeta \gg \frac{A_{21}}{\tau_{21}\zeta}$ ) at moderate clumping factors ( $\zeta \sim 10$ ) already. The  $H\alpha$  optical depth is given by

$$\begin{aligned} \tau_{H\alpha} &\sim \frac{\lambda_{H\alpha}^3 t g_3 A_{32}}{8\pi g_2} n_{\text{HI},2}, & n_{\text{HI},2} \gg n_{\text{HI},3} \\ &\propto \zeta^2, & \zeta \sim 1 \\ &\propto \zeta^0, & \zeta \gg 1 \end{aligned} \quad (6.16)$$

where  $\lambda_{H\alpha} \sim 6563 \text{ \AA}$  is the wavelength of  $H\alpha$  and  $A_{32}$  is the radiative rate of  $H\alpha$ .  $\tau_{H\alpha}$  increases with clumping at low clumping factors, but then saturates as soon as the de-population of the H I  $n = 2$  level is dominated by collisional

de-excitation. In rough approximation the ratio of the  $H\alpha$  to the  $Ly\alpha$  luminosity is given by

$$\begin{aligned}
\frac{H\alpha}{Ly\alpha} &\sim \frac{E_{H\alpha} n_{H1,3} A'_{32}}{E_{Ly\alpha} n_{H1,2} A'_{21}} \\
&\sim \frac{E_{H\alpha} C_{13}\zeta[+If_3]}{E_{Ly\alpha} C_{12}\zeta[+If_2]} \\
&\times \left(1 + \frac{C_{21}\tau_{21}\zeta^2}{A_{21}}\right) \left(1 + \frac{C_{31}\tau_{H\alpha}\zeta^2}{A_{32}[1 - \exp(-\tau_{H\alpha}\zeta)]}\right)^{-1} \\
&\sim 0.03 \cdot \exp\left(-\frac{E_{H\alpha}}{kT}\right), \quad \zeta \sim 1, C_{1j} > I \\
&\sim F(T, n_e, n_H, n_{HII}, \zeta), \quad \zeta \gg 1
\end{aligned} \tag{6.17}$$

where  $A'_{ij}$  denotes the self-absorbed radiative transition rates between the  $n = i$  and  $j$  states of H I.

Clumping can increase the relative strength of  $H\alpha$  significantly. High clumping factors ( $\zeta \gg 1$ ) increase the  $H\alpha$  optical depth less effectively than they do the  $H\alpha$  luminosity, while moderate clumping factors increase both. An estimate for the time-dependent density  $n_{H1}$  is available (see Section 6.1.3).

A numerical computation of the processes described above can be performed using NC3D. In Figures 6.11, 6.12 and 6.13 we show models of SN 1993J (363 days), 2007Y (288 days) and SN 2008ax (359 days) using the mechanism described above (radioactive decay energy; mixing of H and He; strong clumping). Since the late  $H\alpha$  emission of SNe 2001ig and 2003bg is much weaker it is clear that the late  $H\alpha$  emission of these SNe can be reproduced in a similar way. For SN 1993J we use the He mass estimate of Woosley et al. (1994). For SN 2007Y we assume that the He mass is a bit smaller than in SN 1993J. For SN 2008ax the He mass is estimated in Section 6.2. For SN 1993J I use a helium mass of  $2 M_{\odot}$ , a hydrogen mass of  $0.2 M_{\odot}$  and a clumping factor  $\zeta \sim 200$ , for SN 2007Y we use a helium mass of  $1.5 M_{\odot}$ , a hydrogen mass of  $0.1 M_{\odot}$  and a clumping factor  $\zeta \sim 100$  and for SN 2008ax we use a helium mass of  $2 M_{\odot}$ , a hydrogen mass of  $0.2 M_{\odot}$  and a clumping factor of  $\zeta \sim 100$ . Most of the hydrogen is concentrated in a thin shell at high velocities, while tiny fractions are mixed into the lower velocity helium. It is difficult to decide whether clumping, the helium or the hydrogen mass should be increased to obtain a reproduction of the spectra. Several combinations are possible. Additionally, the outer region could be influenced by shock interaction. Therefore it is not possible to derive a hydrogen or helium mass estimate from this procedure. It seems however clear that small amounts of hydrogen are sufficient to reproduce late  $H\alpha$  emission (which is usually not possible Houck & Fransson 1996), if there is strong clumping ( $\zeta \sim 100$ ).

It is important to note that we could not reproduce the temporal evolution of the  $H\alpha$  line using this mechanism with NC3D. We can find models that reproduce the observations at any epoch, but no model describing the observations at all epochs consistently. This is discussed in Section 6.5.

## 6.5. Discussion

### 6.5.1. Late $H\alpha$ emission

We have investigated the formation of  $H\alpha$  in the nebular phase of five SNe IIb (re-classifying SN 2007Y as SN IIb). We find that radioactive energy from  $^{56}\text{Ni}$  decay is not sufficient to power the  $H\alpha$  emission observed at late nebular epochs ( $> 200$  days), as long as the energy deposited in the He layer cannot be tapped. This finding is consistent with the work of Houck & Fransson (1996) for SN 1993J, but raises the question of which mechanism causes the observed  $H\alpha$  flux.

In Section 6.4 we have shown that a combination of mixing and strong clumping could solve this problem. It is not clear whether such high clumping factors are realistic. Furthermore, we could not reproduce the temporal evolution of  $H\alpha$  using this mechanism. This may be because of several reasons. First, there is a degeneracy between the hydrogen and the helium mass and clumping and it is not clear which combination has to be chosen. Secondly, as can be seen from Equation 6.17, the strength of  $H\alpha$  is very sensitive to the electron density and temperature at clumping values of the order 100. In addition,  $n_{H[1,II]}$  is extremely sensitive to mixing and clumping. The composition has to be known at the one percent level or better. Our nebular code is expected to be less accurate. We do not treat UV-radiation transport explicitly, the ionisation of hydrogen by helium is treated in approximation

only and in general there are uncertainties owing to the atomic data and owing to the incomplete description of the physical scenario. Asymmetries of the ejecta can further complicate the problem.

Since the radioactive scenario appears to have problems, it may be worth considering the most common interpretation, i.e. that late SN IIb  $H\alpha$  emission is the result of shock interaction. An extensive discussion of several shock interaction scenarios for SN 2008ax can be found in [Taubenberger et al. \(2010\)](#). However, as pointed out by [Taubenberger et al. \(2010\)](#), there are several problems within all these scenarios. Shock interaction has difficulties explaining why  $H\alpha$  emission is observed at low velocities in SN 2007Y and SN 2008ax (see [Taubenberger et al. 2010](#)). Moreover, there are contradictions between X-ray and  $H\alpha$  observations, if both are interpreted as shock interaction (see SNe 2003bg, 2007Y). These problems may arise from an incomplete understanding of the influence of the shock radiation on the ejecta or from an inaccurate treatment of the physical parameters determining the shock properties (e.g. the SN outer density structure).

The shock interaction model can explain why strong  $H\alpha$  emission at late times is rare in SN IIb and has the advantage that it may explain a flattening of the late  $H\alpha$  light curve, which is observed in SN 1993J and possibly in SN 2008ax. However, this has never been shown quantitatively. Nor has it been shown that shock interaction can reproduce late  $H\alpha$  emission in detail in any SN IIb at all.

The mechanism presented in Section 6.4 can explain the formation of low velocity  $H\alpha$  in SNe 2007Y and 2008ax, which is observed. It can further explain the absence of high velocity  $H\alpha$  emission, again consistent with the observations, since in this scenario the  $H\alpha$  emission traces the He distribution. It can explain why SN 2007Y, has strong  $H\alpha$  emission, although [Chevalier & Soderberg \(2010\)](#) claim that there is extremely weak shock interaction in SN 2007Y. It can explain why SN 2003bg has no strong  $H\alpha$  emission, although [Chevalier & Soderberg \(2010\)](#) claim that there is strong shock interaction in SN 2003bg. Since the model needs some fine tuning it can explain why strong late time  $H\alpha$  is rare in SNe IIb.

There may well be some other mechanism (not clumping; still mixing of H and He), which emits in  $H\alpha$  energy absorbed by the He layer. If it was possible to use  $\sim 10\%$  of the energy of a massive He shell to excite  $H\alpha$  without producing any other strong optical lines, the late-time  $H\alpha$  emission could be explained by radioactive energy deposition alone.

### 6.5.2. Nebular line profiles of SNe IIb

Usually, double-peaked line profiles are interpreted as toroidal ejecta distributions. While we agree with this interpretation in general (e.g. for SN Ib/c; see also Section 6.2) we think that the situation may be different in SNe IIb. We have shown that, taking the 40 day (after explosion)  $H\alpha$  absorption minimum velocity as lower boundary of the bulk of hydrogen (as it is usually done) we can explain the peak profile of the [O I]  $\lambda\lambda$  6300, 6363 doublet for all five SNe of our sample consistently by  $H\alpha$  absorption.

Since  $H\alpha$  absorption causes a split of the [O I]  $\lambda\lambda$  6300, 6363 doublet if it is located around  $12000 \text{ km s}^{-1}$ , and since the position of  $H\alpha$  influences the position of this split, we can infer the radial distribution of H I from fitting the [O I]  $\lambda\lambda$  6300, 6363 doublet profile. For all five SNe of our sample the  $H\alpha$  velocity measured with this method agrees very well with the early-time  $H\alpha$  minimum velocity (see Table 3). It seems unlikely that this is coincidence.

The outer  $H\alpha$  region could be optically thick even at late epochs (e.g. excited by shock interaction), which could explain why the profile of the [O I]  $\lambda\lambda$  6300, 6363 doublet does not change its shape significantly at late epochs. For example, the reverse shock of SN 2008ax could be located around  $12000 \text{ km s}^{-1}$  at 359 days after the explosion ([Taubenberger et al. 2010](#)).

### 6.5.3. SN 2008ax

We have derived a three-dimensional model of SN 2008ax. Two kinds of asymmetries may be observed. First the He IR lines are double-peaked, which is most easily explained by a torus shaped He distribution. Secondly, the blue sides of the He lines appear to be stronger than the red sides.

We find a total ejecta mass of  $\sim 3 M_{\odot}$ , containing about  $0.1 M_{\odot}$  of  $^{56}\text{Ni}$  and expanding with a kinetic energy of  $\sim 10^{51}$  ergs, which is consistent with findings from light curve and early-time  $H\alpha$  absorption modelling (Table 2). We find a helium mass of  $\sim 2 M_{\odot}$  and derive the abundances of heavier elements such as carbon or oxygen (Table 1).

While most of the heavy element mass is confined to velocities below  $4500 \text{ km s}^{-1}$ , helium is predominantly found between  $4500$  and probably  $12000 \text{ km s}^{-1}$ . The outer boundary is uncertain. Some helium is present below

4500 km s<sup>-1</sup>. We find that a separation of helium and heavy elements, at least between 2000 and 4500 km s<sup>-1</sup>, improves the reproduction of the He IR lines.

Since our nebular code does not reproduce the continuum flux observed around 20000 Å, we added some artificial background to allow He I 20587 Å line scattering. There seems to be no He I 20587 Å line scattering above ~ 10000 km s<sup>-1</sup>, while the He I 10830 Å line would not be in conflict with higher helium velocities. The observations of the He I 20587 Å line place an upper limit on the He mass between 9500 and 12000 km s<sup>-1</sup> of ~ 0.05 M<sub>⊙</sub>. It may well be that continuum destruction (e.g. by hydrogen), which could reduce the He I 20587 Å optical depth, is important. In this case the He mass in this region could be larger.

We can compare our results to SN IIB models of [Nomoto et al. \(1993\)](#) and [Woosley et al. \(1994\)](#). The [Nomoto et al. \(1993\)](#) models (also see [Houck & Fransson 1996](#)) predict a strong confinement of <sup>56</sup>Ni to low velocities (< 2000 km s<sup>-1</sup>). Other heavy elements are distributed in layers above the radioactive core. Most of the hydrogen is confined to a thin layer above the He layer. This He layer contains some traces of hydrogen and heavier elements. The models of [Woosley et al. \(1994\)](#) predict a broader distribution of <sup>56</sup>Ni in velocity space. Heavy elements dominate at low velocities but are also mixed into the He layer. Helium and hydrogen are mixed in the outer regions.

We find that <sup>56</sup>Ni is probably not as centrally confined as predicted by the [Nomoto et al. \(1993\)](#) models. On the other hand carbon seems to be confined to a thin shell on top of the iron core in agreement with these models. Since our core is deformed to an axis ratio of ~ 3:2 (see Figure 6.4), one probably cannot expect perfect agreement with the spherical symmetric models. The distribution of heavy elements seems rather consistent with the predictions in the core as well as in the He layers. Our results for hydrogen are inaccurate and therefore a comparison is difficult.

We compare the masses of He, C, O, Ca and <sup>56</sup>Ni of our SN 2008ax model to the 13C model of [Woosley et al. \(1994\)](#), which has been used by [Tsvetkov et al. \(2009\)](#) to reproduce the light curve of SN 2008ax. We find that our estimates of the He, C, Ca and <sup>56</sup>Ni mass agree at the 10% level. The estimate of the oxygen mass is larger by a factor of ~ 2 than predicted by the 13C model.

Thanks to its late time IR observations, SN 2008ax is the first SN IIB where the He density field can be determined from nebular observations. Other methods, such as light-curve modelling, provide poor information about element abundances or asphericities. Early-time modelling can determine the properties of the outer layers more accurately, but no information about the central region can be obtained. Therefore nebular IR observations (10000 to 22000 Å) of SNe Ib and IIB are highly desirable.

## 6.6. Summary

We have derived estimates related to hydrogen and helium line formation in the nebular phase of SNe IIB. We have shown that hydrogen can be highly ionised if it is mixed with helium in suitable ratios. This could explain why H $\alpha$  can sometimes be observed in the nebular phase but not at early times. This finding is of special interest for SN 2007Y.

From our analysis it seems likely that SN 2007Y is a SN IIB. The lack of strong H $\alpha$  absorption around 50 days after explosion may well be explained by strong mixing of H and He. Such mixing could also explain the formation of strong late time H $\alpha$ . Since we cannot determine the He distribution of SN 2007Y, this remains a speculation.

We have shown that radioactive energy deposition is insufficient to produce the late-time H $\alpha$  emission in all SNe IIB of our sample, as long as the energy of the helium layer cannot be tapped by H $\alpha$ .

Shock interaction may be observed in all SNe of our sample. There seem to be two types of late H $\alpha$  emission scenarios. Strong, box-shaped (SNe 1993J, 2007Y, 2008ax) and weak (SNe 2001ig, 2003bg) H $\alpha$ . The simplest explanation would seem to be strong and weak shock interaction, respectively. However, this is in conflict with findings of [Chevalier & Soderberg \(2010\)](#), at least for SNe 2003bg and 2007Y. It also seems difficult to explain the low velocity observations in H $\alpha$  by shock interaction ([Taubenberger et al. 2010](#)).

We presented an alternative mechanism to shock interaction, explaining late time H $\alpha$  emission by radioactive energy deposition. The right combination of mixing and clumping of hydrogen and helium has been shown to be able to reproduce the H $\alpha$  observations of all SNe of our sample at least up to 350 days after explosion. However, there are also some problems with this interpretation of late H $\alpha$  emission. Summarising, it is not clear how late H $\alpha$  is formed in SNe IIB. Therefore, we were not able to derive an estimate of the hydrogen mass for any SN of our sample.

We have shown that most likely the profile of the [O I]  $\lambda\lambda$  6300, 6363 doublet is influenced by H $\alpha$  absorption strongly. Hydrogen concentrations above ~ 11000 km s<sup>-1</sup> can cause double-peaked oxygen profiles, while slower

hydrogen can not. We have shown that observations of early-time  $H\alpha$  absorption minima and the corresponding oxygen line profiles are perfectly consistent with this interpretation for all five SNe of our sample.

This scenario also explains why other lines, like Ca II or [O I] 5577 Å, are single peaked in all SNe of our sample. An exception are the He lines of SN 2008ax, which show signs of asymmetry. It seems likely that at least the inner part of SN 2008ax is asymmetric. We have obtained a three-dimensional model of the SN 2008ax envelope. For the first time the helium mass of a SN I Ib has been determined from nebular modelling. We have obtained estimates of the total mass and kinetic energy of SN 2008ax in excellent agreement with results from light-curve modelling. Chemical abundances have been derived. The nebular model of SN 2008ax provides the opportunity to compare observations and theoretical SN I Ib models with unprecedented richness of detail.

## 7. Supernova 1987A

Supernova 1987A was discovered by Shelton and Duhalde on February 24, 1987 in the Large Magellanic Cloud (LMC; a nearby dwarf galaxy) close to the Tarantula Nebula. Its progenitor, the blue supergiant Sanduleak (Sk) -69 202, exploded about 170,000 years ago, the time light needs to travel from LMC to earth. Since SN 1604, which exploded in our own galaxy, SN 1987A has been the closest SN observed. Even neutrinos, emitted during the core-collapse, have been detected (e.g. [Bionta et al. 1987](#), [Hirata et al. 1987](#), [Aglietta et al. 1987](#)). Owing to its small distance from earth and the advanced astronomical facilities available at the end of the 20th century, SN 1987A is the best observed SN ever and therefore of special interest for any analysis of SN properties.



**Figure 7.1.:** Supernova 1987A about 10 years after the explosion observed with the Hubble Space Telescope.

SN 1987A is of Type II-P, but shows some irregularities. The fact, that its progenitor was a blue giant star came as a surprise, since Type II explosions were only expected from red supergiants. Such a progenitor could be explained, if Sk -69 202 had been metal poor (e.g. [Hillebrandt et al. 1987](#)), since metal deficiency makes it possible for a star to reach carbon burning as a blue giant ([Brunish & Truran 1982](#)). Also mixing of He into the hydrogen envelope, which influences the opacity of the stellar gas, could cause a transition from the red to the blue giant phase (e.g. [Saio et al. 1988](#), [Hillebrandt & Hoflich 1989](#)). Another possibility was that the progenitor could have suffered strong mass loss from stellar winds prior to the explosion ([Chevalier & Fransson 1987](#)) or it was influenced by binary interaction (e.g. [Fabian et al. 1987](#), [Hillebrandt & Meyer 1989](#)). Alternatively, the progenitor could have merged from two smaller stars several thousand years prior to the explosion (e.g. [Podsiadlowski et al. 1990](#)). The merger scenario could also explain the prominent rings (e.g. [Morris & Podsiadlowski 2007](#)) surrounding the remnant (see Figure 7.1). These rings (two large and one smaller ring) expand with approximately  $\sim 20 \text{ km s}^{-1}$  (larger rings) and  $\sim 10$

km s<sup>-1</sup> (smaller ring) into the circumstellar medium. From their velocity and distance to the centre of the explosion, their formation can be dated to about 20,000 – 30,000 years prior to the explosion. Therefore they were probably expelled by the blue giant progenitor during the final stage of stellar evolution and were illuminated by SN radiation later (e.g. [Mattila et al. 2010](#)). This is also supported by a chemical abundance analysis of the ring material (e.g. [Lundqvist & Fransson 1996](#)). Alternatively to the merger scenario the rings could also result from heating induced pressure gradients in a red supergiant wind (from a previous stellar evolution phase surrounding the blue supergiant [Meyer 1997](#)) or from a rapidly rotating single progenitor star (e.g. [Chita et al. 2008](#)).

Since its detection, SN 1987A has been the object of extensive investigation. Although SN 1987A certainly is a core-collapse event, so far, no compact remnant has been detected (e.g. [Manchester 2007](#)). SN 1987A is observed in numerous wave bands and various theoretical models of the explosion exist (e.g. [Woosley 1988](#), [Nomoto et al. 1988](#), [Arnett & Fu 1989](#)). Among all these studies there is also extensive interpretation of the nebular observations (e.g. [Chugai 1992](#), [Li & McCray 1992, 1995](#)) and general investigation of UV effects in the nebular phase of SNe II (e.g. [Li & McCray 1996](#)). Most importantly for this work, [Kozma & Fransson \(1998\)](#), [de Kool et al. \(1998\)](#) have treated the late spectra of SN 1987A by nebular modelling.

Summarising, the literature describes SN 1987A as a  $M_{\text{ej}} \sim 8 - 18 M_{\odot}$ ,  $E_{\text{kin}} \sim (1-2) \cdot 10^{51}$  ergs,  $M_{56} \sim 0.07 M_{\odot}$  Type II-P explosion (e.g. [Shigeyama & Nomoto 1990](#), [Kozma & Fransson 1998](#)). [Shigeyama & Nomoto \(1990\)](#) found that modelling the light curve of SN 1987A requires  $E_{\text{kin}}/M_{\text{ej}} \sim 1.1 \pm 0.3 \times 10^{50}$  ergs  $M_{\odot}^{-1}$ . X-ray observations indicate that about 60% of the <sup>56</sup>Co is confined within the inner 2  $M_{\odot}$  of the ejecta, while the rest is mixed out to at least 10  $M_{\odot}$  (e.g. [McCray 1993](#)). This is confirmed by light curve models, which also predict some high velocity <sup>56</sup>Co. It is expected that the heavier elements are concentrated in the core but possibly reach out to high velocities, forming 'bullets' of ejected core material (e.g. [Hammer et al. 2010](#)).

The hydrodynamical models used by [Shigeyama & Nomoto \(1990\)](#) to reproduce the SN 1987A light curve contain about 55% hydrogen and 45% helium in the hydrogen dominated outer layer. This was roughly confirmed by [Kozma & Fransson \(1998\)](#), who estimate a hydrogen mass of  $\sim 7.7 M_{\odot}$  and a helium mass of  $\sim 5.8 M_{\odot}$  in total. The heavy element core, which is expected to contain about 6  $M_{\odot}$  is confined below 2000 km s<sup>-1</sup> and consists of about equal parts of hydrogen, helium and oxygen ([Kozma & Fransson 1998](#)). Another 4  $M_{\odot}$  (mainly H and He) are expected between 2000 and 3200 km s<sup>-1</sup>, with some material at higher velocities ( $\sim 1$  and 4  $M_{\odot}$  between 3200 and 6300 km s<sup>-1</sup> [Shigeyama & Nomoto 1990](#)). At higher velocities the predictions become more uncertain, which is however not very important for the nebular phase, because of the low density of those regions. Typical clumping factors used by [Li & McCray \(1992, 1995\)](#), [Kozma & Fransson \(1998\)](#) are of the order of 1 to 100.

There is evidence for dust formation in SN 1987A between 350 and 600 days ([Lucy et al. 1989](#), [Li & McCray 1996](#), [Kozma & Fransson 1998](#), [de Kool et al. 1998](#)), which can explain the blue-shift of spectral lines observed at those epochs and could influence the line formation. This can however hardly be quantified ([Kozma & Fransson 1998](#)). The ejecta are possibly mixed or separated on small or large scales and could be clumped strongly, which has serious influence on line formation. [Kozma & Fransson \(1998\)](#) mention that there are serious uncertainties on their oxygen and other intermediate-mass element mass estimates. Similar conclusions about SN 1987A have been obtained by [de Kool et al. \(1998\)](#).

In Sections 4, 5 & 6 we have studied the ejecta of numerous SECC-SNe (type Ic, Ib, IIb). A useful next step was to extend the nebular analysis to hydrogen dominated SNe II, completing the nebular treatment of CC-SNe. Although some physics necessary to treat SNe II in all the detail are still missing, some of their properties may be derived at the current level of sophistication. To investigate the limitations of NC3D regarding hydrogen dominated SNe, in this section, we compare SN 1987A properties obtained using NC3D with the extensive data set available in the literature.

## 7.1. Nebular Modelling of SN 1987A

At the current state of development NC3D can treat the most important physics responsible for nebular hydrogen and helium line formation, but still neglects some effects, which become important for hydrogen dominated SNe II. Of the SN II physics which are not treated in NC3D, the most important one is UV transport, since the massive hydrogen/helium envelope emits in Ly $\alpha$  and other UV ground-state transitions strongly (e.g. [Li & McCray 1996](#), [Kozma & Fransson 1998](#), [de Kool et al. 1998](#)). This also became evident when analysing SN 1987A with NC3D (see below). For the modelling presented here, especially the missing reproduction of the strong continuum found in the SN 1987A nebular spectra poses some problems. Since the formation of IR emission lines is dominated by



UV fluorescence, the IR reproduction using NC3D is poor.

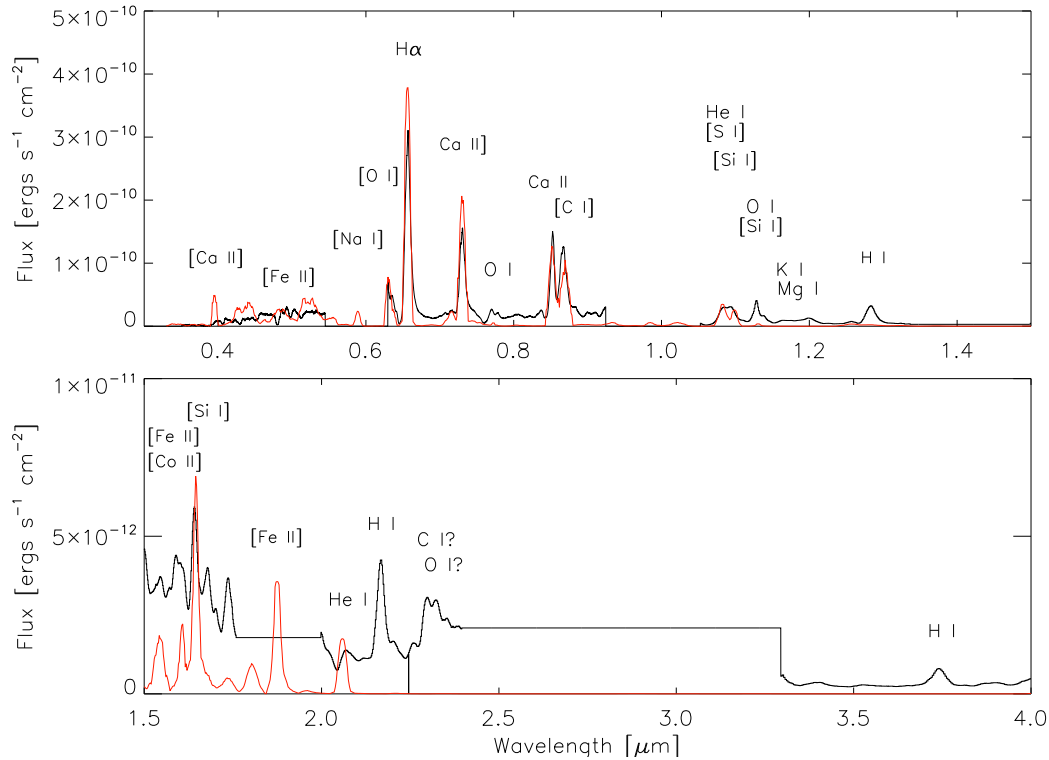


**Figure 7.2.:** Spectrum of SN 1987A at 255 days after the explosion. The observations are shown in black, while the synthetic spectrum is shown in red. The strong emission lines (e.g. [O I]  $\lambda\lambda$  6300, 6363, H $\alpha$ ) are reproduced well, but not the continuum flux (e.g. around 8000 Å). Especially, the fit to the IR above 1.1  $\mu\text{m}$  is poor. The IR line identification is taken from Meikle et al. (1989).

In addition, there are problems which are inherent to a nebular treatment of SNe II. First, nebular modelling of H and He is very sensitive to mixing (e.g. Kozma & Fransson 1998) and secondly, at late times dust formation, radio-actives other than  $^{56}\text{Co}$  as well as time-dependent effects become important. All these processes are difficult to quantify (e.g. Kozma & Fransson 1998, de Kool et al. 1998) since they can hardly be measured independently.

Since the SN 1987A envelope is very massive and slow, its density is high and one cannot expect a meaningful nebular treatment before 200 days after the explosion. Around 400 days after the explosion dust absorption can influence the line formation (Kozma & Fransson 1998) and at around 500 days the deposition of positron energy becomes increasingly important. Since this deposition process is strongly influenced by (possible) magnetic fields (see Section 1.3) and since the gas falls out of ionisation and heat equilibrium at later epochs, the nebular code becomes increasingly unreliable with time. In addition, light curve modelling (e.g. Suntzeff et al. 1991, Bouchet et al. 1991) has shown that an additional source of energy is needed between 700 and 1000 days after the explosion and later. The source of this energy is not known exactly, but is expected to consist of radioactive isotopes like  $^{44}\text{Ti}$  and time-dependent effects (Fransson & Kozma 1993).

Therefore, while an approximate treatment seems possible between 200 and, say, 600 days after the explosion, the most accurate results are expected between 200 and 400 days. We therefore use nebular spectra of SN 1987A at 255, 284 and 349 days after the explosion, kindly provided by Peter Meikle (Meikle et al. 1989). These spectra are of high quality and cover the UV, optical and IR between  $\sim 2000$  and  $20,000$  Å. The 255 and 284 spectra even extend to  $\sim 40,000$  Å. For the modelling we use a distance modulus of 18.5 mag and a reddening  $E(B - V) = 0.15$  mag (Suntzeff et al. 1991).

We derive a model (see Figures 7.2, 7.3 & 7.4) with  $M_{\text{tot}} \sim 13 M_{\odot}$  and a total kinetic energy of  $E_{\text{kin}} \sim 1.0 \cdot 10^{51}$  ergs  $\text{s}^{-1}$ . Since the nebular modelling becomes unreliable at low densities (high velocities), we may underestimate

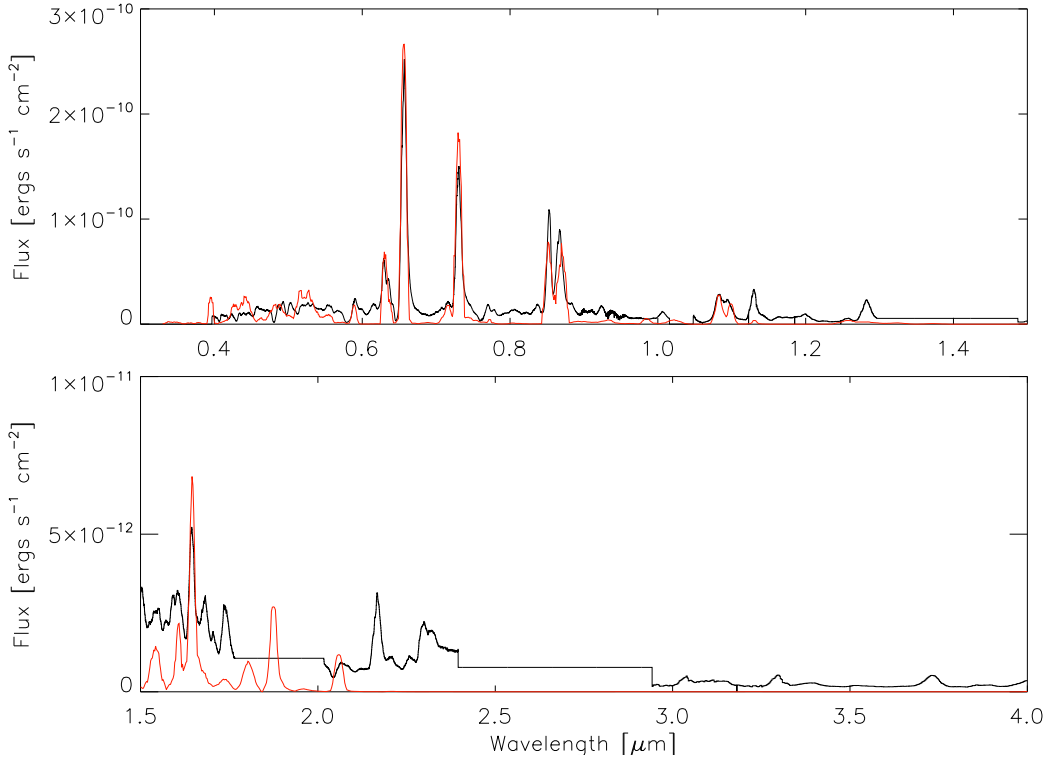


**Figure 7.3.:** Spectrum of SN 1987A at 284 days after the explosion. The observations are shown in black, while the synthetic spectrum is shown in red. The strong emission lines are reproduced, while the continuum is not. The fit to the IR above  $1.1 \mu\text{m}$  is poor. See Figure 7.2 for an identification of the strongest emission lines.

the total mass and kinetic energy slightly. The mass below  $2000 \text{ km s}^{-1}$  is  $5.5 M_{\odot}$  and there are  $5 M_{\odot}$  between  $2000$  and  $3200 \text{ km s}^{-1}$ . The ratio of H to He is about 7:5 and the  $^{56}\text{Co}$  mass used is  $M_{56} \sim 0.07 M_{\odot}$ . Therefore, the basic properties of the model are consistent with the literature (see above).

A draw-back of our nebular treatment is that the continuum-like flux between the strong emission lines (e.g. around  $8000 \text{ \AA}$ ) is not reproduced. This continuum is most likely created by UV effects (e.g. [Li & McCray 1996](#)), since UV excitation and consequent line-branching excite thousands of weak lines. Since the continuum is not reproduced the total flux of the synthetic model is lower by a factor of  $\sim 1.6$  than the observed one. To accommodate for this difference of flux we have to place a large fraction ( $\sim 40\%$ ) of the radioactive material at the highest velocities of our model ( $3200 - 5000 \text{ km s}^{-1}$ ) in order to obtain the observed line strengths. While the literature quotes  $60\%$  of the  $^{56}\text{Ni}$  to be located below  $2000 \text{ km s}^{-1}$ , in our model its only  $40\%$ . This means that in our model, the radioactive material is on average located at higher velocities, which decreases the deposition rate owing to the lower densities in these regions.

One can study this effect by observing the luminosity evolution between 250 and 350 days. The flux ratio of the observed spectra between 255 and 349 days is  $\sim 2.54$ . The ratio of radioactive  $^{56}\text{Co}$  emission is given by

$$\frac{\exp(-255/111.37)}{\exp(-349/111.37)} \sim 2.33 \quad (7.1)$$

The observed decrease of luminosity is slightly higher ( $\sim 10\%$ ) than the value expected from the  $^{56}\text{Co}$  decay alone (Equation 7.1), since there is some increasing fraction of  $\gamma$ -radiation escaping. Since the difference is small the deposition fraction does not change significantly between 250 and 350 days in SN 1987A. On the other hand, in the synthetic spectra the flux ratio over the same epochs is 2.96, which means that the  $\gamma$ -deposition fraction has decreased by about  $30\%$ . This indicates that the radioactive material in SN 1987A deposits at higher densities than in our model. We study this effect by moving  $0.3 M_{\odot}$  of the high velocity  $^{56}\text{Co}$  to the core, as in the light curve model

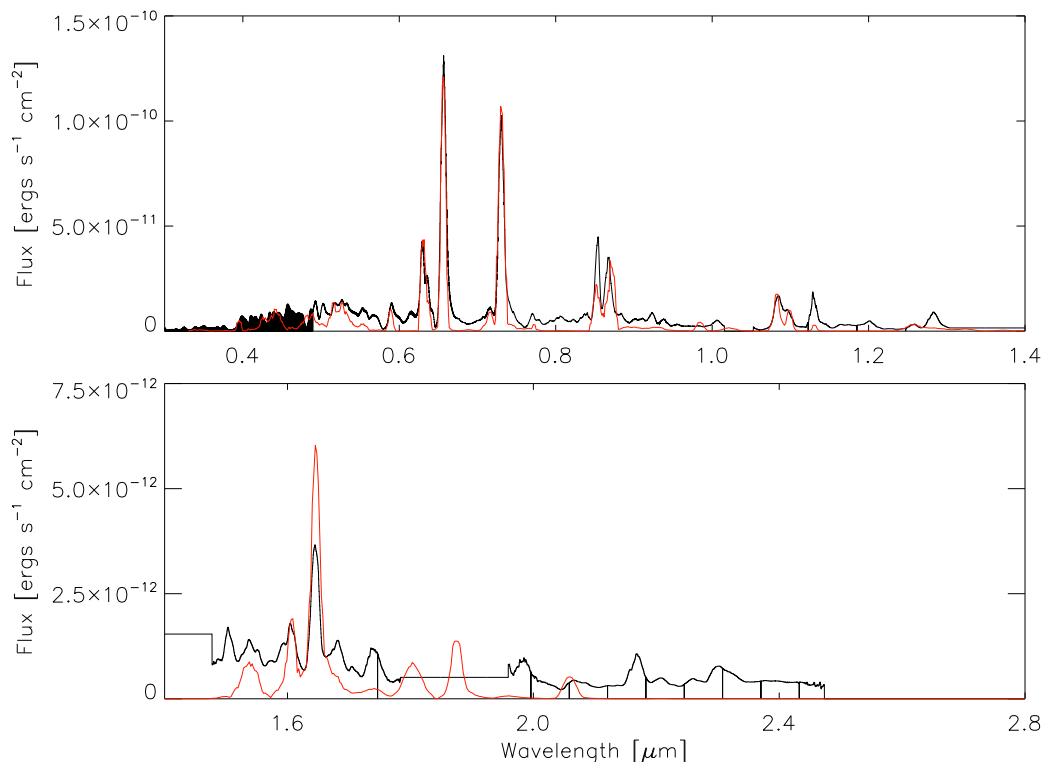


**Figure 7.4:** Spectrum of SN 1987A at 349 days after the explosion. The observations are shown in black, while the synthetic spectrum is shown in red. The strongest emission lines are reproduced well, while the continuum is not. See Figure 7.2 for an identification of the strongest emission lines.

of Shigeyama & Nomoto (1990). In this case the total flux is reproduced correctly (Table 7.1), but the strength of the strong emission lines is over-estimated seriously, since there is no continuum in the synthetic model.

Apart from the continuum problem, the strong emission lines (see Figures 7.2, 7.3 & 7.4) as well as the characteristic [Fe II] blends around 5000 Å and He I  $\lambda$  10830 can be reproduced by the high-velocity  $^{56}\text{Co}$  model. The double peaked feature at  $\sim 10800$  Å seems not to be the result of He asymmetry (as in SN 2008ax; Section 6), but rather seems to result from a blend of He I  $\lambda$  10830, [S I]  $\lambda$  10821 and [Si I]  $\lambda$  10991. This has also been found by Li & McCray (1993b), Kozma & Fransson (1998). The in generally weak IR lines are not reproduced well, which is however expected (Mazzali et al. 2010). While we can reproduce for example He I  $\lambda$  10830 & 20585 and [Si I]  $\lambda$  16455, which are efficiently excited by thermal electrons (and recombination in the case of He I), most of the emission features above 10000 Å are not seen in the synthetic spectra at all.

The poor reproduction of the IR band is a consequence of missing UV excitation. A clear example is the quite strong feature at  $\sim 11300$  Å, which is likely O I  $\lambda$  11287 [ $3d(^3D) \rightarrow 3p(^3P)$ ], since the O I  $3d(^3D)$  level (1027.76 Å) can strongly be excited by Ly $\beta$  (1025.72 Å). This can explain why O I  $\lambda$  11287 is stronger than O I  $\lambda$  7774 & 9264,

Epoch [d]	$F_{\text{obs}}$	$F_{\text{m1}}$	$F_{\text{m2}}$
255	2.146(-7)	2.282(-7)	1.450(-7)
284	1.751(-7)	1.709(-7)	1.049(-7)
349	8.438(-8)	8.437(-8)	4.883(-8)

**Table 7.1:** The flux [ $\text{ergs s}^{-1} \text{cm}^{-2}$ ] of the observed spectra  $F_{\text{obs}}$  and the models with  $\sim 60\%$  ( $F_{\text{m1}}$ ) and  $\sim 40\%$  ( $F_{\text{m2}}$ ) of all  $^{56}\text{Co}$  in the core at epochs of 255, 284 and 349 days after the explosion.

which is not expected from recombinative excitation (Maurer & Mazzali 2010) and is not observed in SNe Ib and Ic. Also the IR emission around 12800, 21700 and 35000 Å, which are most likely H I lines, must be excited by UV radiation, since recombination and thermal-electron excitation are too weak to reproduce any of these lines (see Figures 7.2, 7.3 & 7.4).

Our model contains  $M_C \sim 0.12 M_\odot$  of carbon,  $M_O \sim 0.4 M_\odot$  of oxygen, about  $M_{Si,S} \sim 0.01 M_\odot$  of silicon and sulphur and  $M_{Ca} \sim 0.12 M_\odot$  of calcium, while the models analysed by Kozma & Fransson (1998) contained  $M_C \sim 0.1 M_\odot$ ,  $M_O \sim 2.0 M_\odot$ ,  $M_{Si,S} \sim 0.1 M_\odot$ ,  $M_{Ca} \sim 0.01 M_\odot$ . Therefore the intermediate-mass element abundances derived agree only to about a factor of ten in the worst case, which means that the deviation can be rather significant. This huge uncertainty may partially be attributed to the UV treatment, clumping and uncertainties in the atomic data, but is expected in general in SNe II (Kozma & Fransson 1998) because of the strong influence of mixing with hydrogen and helium. Most of the energy absorbed by H and He is emitted by heavier elements if there is mixing, since the excitation potential of H and He is large. Therefore the inferred amount of heavy elements is extremely sensitive to mixing, if the H or He mass is larger than the mass of heavy elements.

Unfortunately, this kind of uncertainty is an inherent problem of Type II nebular modelling and it is doubtful that it can be solved by improvements of the nebular treatment alone. Analytical treatments of clump-formation or hydrodynamical simulations of SNe II explosions seem necessary to obtain this information.

## 7.2. Summary

Although the treatment of hydrogen-dominated SNe is expected to be not as accurate as the modelling of other CC-SNe and of SNe Ia, it seems useful to derive properties of a well-studied SN II using NC3D. The comparison of the derived properties to the literature reveals the current level of NC3D's accuracy with respect to hydrogen dominated SNe but also identifies the areas that need further development.

Therefore, in this section we derived an ejecta model of the well-studied SN II 1987A. Although some physics, necessary to treat hydrogen dominated SNe in all the necessary detail, are still missing, the global properties of the synthetic model derived are consistent with the values found in the literature. The total mass, density structure and kinetic energy, as well as the H and He fractions agree well with the values for example given by Shigeyama & Nomoto (1990), Kozma & Fransson (1998). This demonstrates that the basic properties of SNe II can currently be derived using NC3D. Further it would be possible to study ejecta asymmetries of SNe II. Although SN 1987A seems to show no signs of asphericity in the core, observations of other SNe II could reveal more interesting geometries, as for example discovered in SN Iib 2008ax (see Section 6).

The intermediate-mass and heavy element fractions of hydrogen-dominated SNe obtained from nebular modelling are in general uncertain (e.g. Kozma & Fransson 1998). Depending on the degree of mixing, H and He can emit most of the deposited energy in intermediate-mass and heavy element lines, which can mimic the presence of large amounts of these elements. Since this problem is inherent to nebular modelling, hydrodynamical simulations of SNe II explosions (e.g. Hammer et al. 2010) could give important information about the expected degree of mixing in the future.

Since several spectral features of SN 1987A (mainly the optical and the IR continuum) are not synthesised, the need for a more accurate treatment of SN II physics became evident. Therefore, the next step would be to implement a detailed treatment of UV processes. This would also increase the accuracy of other SN Type nebular spectra calculations, but requires more atomic data and fundamental changes in the structure of the code. The time-scale for such a development would be about one year. However, such improvement seems highly desirable.

Summarising, the current treatment of hydrogen rich supernovae by NC3D is in an advanced state. One can derive properties like H and He fractions, total mass or kinetic energy and study possible asymmetries. However, to synthesise the rather strong continuum emission observed in SNe II further development regarding the nebular physics is required. To derive intermediate-mass and heavy element fractions, information about mixing in SNe II is needed. Thanks to steadily improving simulations of SNe II explosions, such information is expected in the near future.

## 8. Conclusions

This thesis joins three important elements of nebular phase analysis. On the one hand, an advanced tool to study and analyse nebular spectra, the nebular code (NC3D; see Section 3.2) is improved and developed in respect to its reliability and adaptability. Beside the refinement of energy deposition and ionisation, the inclusion of recombination line formation, line scattering and two new elements (hydrogen and helium), the nebular code was extended to three-dimensions becoming a state-of-the-art tool to study supernova nebular spectra.

On the other hand, the new code is extensively used to investigate the physical properties of core-collapse supernovae. In Section 4 characteristic core velocities of 56 stripped-envelope core-collapse supernovae are obtained, by far the largest and most reliable data-set of this kind. In addition, we studied the O I  $\lambda\lambda$  6300, 6364 profiles of these supernovae regarding asymmetries and derive estimates of their  $^{56}\text{Ni}$  masses, which are however affected by large uncertainties. In Section 5 we investigate the formation of O I recombination lines in two well studied core-collapse supernovae and asphericities in the Type Ic supernova 1998bw, which is unambiguously associated with the long duration GRB 980425. The code is then used to perform an analysis of five supernovae Type IIb in Section 6. Of special interest is supernova 2008ax, which is well observed and belongs to the rare class of supernovae IIb showing strong box-shaped H $\alpha$  emission in their late phase. The helium mass estimate of this supernova is the first one ever obtained for a stripped-envelope core-collapse supernova from nebular modelling. Also, the model of supernova 2008ax is the only three-dimensional nebular model of an observed supernova derived so far. Finally, in Section 7 we derive properties of SN II 1987A consistent with the literature. This study completes the nebular treatment of core-collapse supernovae (Ic, Ib, IIb, II) and points the direction for further developments.

The third important aspect of this thesis is a theory based investigation of supernova nebular physics. In Section 5 the formation of O I recombination lines is studied in detail. In Section 6 we scrutinised the interplay of hydrogen and helium in supernovae IIb, in respect to helium induced photo-ionisation of hydrogen, hydrogen line excitation in mixed H/He layers and the influence of clumping on H $\alpha$ .

A fourth point, which is however of subordinate importance, is the computation of oxygen atomic data in a temperature range relevant for the nebular phase of core-collapse supernovae. These data have been provided to the public and could also be useful for other areas of physics.

Here, we will summarise where all these efforts have led. First of all, the data set of physical properties of stripped-envelope core-collapse supernovae obtained in Section 4 provides a representative characteristic, which can be used for further studies and comparison to theory. We compare these core-velocities to the ratio of kinetic energy and mass (if available in the literature) in Section 4, finding no strong correlation. In addition, supernovae classified as broad-lined (high velocity outer ejecta) show a wide span of core velocities. This is surprising, since one may have expected that inner and outer velocities are directly proportional. It is shown that this could be the effect of ejecta asperities and consequently a projection effect. The observed distribution of broad-lined supernova core velocities is consistent with a torus-like configuration with torus opening angles between  $\sim 40^\circ$  and  $60^\circ$ . This geometrical interpretation is interesting, since it could confirm the presence of strong asymmetries in the core of SECC-SNe independent of line-profile observations.

An alternative explanation could be that different supernovae (however of the same type) have different ejecta density profiles, which could influence the maximum radial velocities of the nebular line forming regions. Joining early and late time observations could be useful to shed light onto this issue. If one could obtain density profiles of the outer ejecta for a large number of these supernovae it might be possible to rule out or support density-based explanations.

Although the uncertainties on the  $^{56}\text{Ni}$  mass estimates obtained in Section 4 are large, it is expected that they have statistical relevance, since on average the errors are likely much smaller than the values quoted. These estimates demonstrate the large diversity among core-collapse supernovae and give some insights into their  $^{56}\text{Ni}$  mass function. This part of the work could be greatly improved by using flux calibrated spectra, since this would make it possible to derive  $^{56}\text{Ni}$  and total (core) masses more accurately. However, this would require light curves (photometry) of all these events, which often are not available. For a sub-sample of SECC-SNe, where more reliable estimates of the  $^{56}\text{Ni}$  mass are available in the literature, we demonstrate that there is likely no correlation between

$^{56}\text{Ni}$  mass and core velocity.

Finally, we studied the line profiles of O [I]  $\lambda\lambda$  6300, 6364. Recent claims about a non-geometrical origin of the double and triple peaked profiles observed in SNe Ib and Ic appear unlikely in the light of these findings. This is further evidence for a geometrical origin of multi-peaked line profiles and for the importance of ejecta asphericities in core-collapse supernovae. However, since related aspects of nebular line formation, like for example the time-dependent blue-shift of the O [I] doublet observed in some core-collapse supernovae are not understood yet, this needs further investigation.

In Section 5 we have studied the formation of O I recombination lines in the nebular phase. Since oxygen is the most abundant element in supernovae Ib and Ic and the second most abundant element in supernovae IIb (after helium) an accurate treatment of this element is of special importance. As it turned out, the simultaneous formation of forbidden and recombination lines is approximately compatible with the observations, but clumping of the ejecta is needed to become fully consistent at the earlier epochs. This is interesting, since the need for clumping has also been found in supernova 1987A to explain the line ratio of the O [I]  $\lambda\lambda$  6300, 6364 doublet. Other studies also have claimed the presence of clumping and observations of some supernova remnants reveal the presence of bullet-like over-densities. Those studies seem to favour clumping factors of the order of ten, however this estimate is highly uncertain. Unfortunately, the formation of clumps in supernova envelopes is not understood well and theoretical studies are rare. Although the line-formation based approach provides no definite answers at the current level of accuracy, it could contribute to the understanding of clump formation in supernova ejecta in the future.

The two-dimensional model of GRB-supernova 1998bw derived in Section 5 allows to test predictions about the interaction of GRBs with their associated supernovae. Although this model is certainly not unique, it demonstrates that a 'jet + disc' ejecta structure, which is expected in GRB scenarios, can explain the nebular observations well, while spherical symmetric models most likely cannot. Therefore, the nebular modelling supports the poorly tested theoretical foundations of GRB physics and gives some insights into the connection of GRBs and supernovae. Three-dimensional nebular modelling will provide one of the few criteria to decide about the physical relevance of hydrodynamical GRB-supernova models, which may be available in the near future.

In Section 6 we analyse the nebular phase of all the supernovae IIb with good nebular data available in the literature (five in total). Since sometimes the literature seems confused about the temporal evolution of hydrogen lines in supernovae IIb, we study their formation using a toy model. It is not very surprising that the large amount of helium expected in supernovae IIb can ionise small amounts of hydrogen completely by photo-ionisation processes, which can mimic the absence of hydrogen. The model describes the temporal evolution of hydrogen lines in supernovae IIb qualitatively and has been used to justify the need to correct the miss-classification of supernova 2007Y. Further improvements to this toy model are necessary to make quantitative predictions about the hydrogen to helium ratio from the temporal evolution of hydrogen lines. A numerical treatment (with the nebular code) is desirable, but needs an exact treatment of UV transport which is currently not implemented.

The idea that shock-interaction is responsible for the formation of strong, box-shaped  $\text{H}\alpha$  observed in some supernovae IIb was commonly accepted for more than one decade. However, there are good reasons to mistrust this interpretation. It was believed that the deposition of nuclear energy is not sufficient to power late  $\text{H}\alpha$  in supernovae IIb, making shock interaction an attractive source of energy. However, as it is shown in Section 6 the nuclear energy deposited in the helium shell would well be sufficient if it could be converted to  $\text{H}\alpha$  with an efficiency of  $\sim 10\%$ . Further, it is shown that very small fractions of hydrogen can emit most of the energy deposited in a helium shell if no other neutral elements are present. The mechanism to achieve the required  $\text{H}\alpha$  efficiency proposed in Section 6 is based on strong clumping of the ejecta. Since it is doubtful whether such high clumping factors are realistic, again, UV transport could be important, since it may supersede the need for strong clumping under certain conditions. However, unless one can treat the nebular UV transport explicitly, this remains a speculation.

Independently from these problems it seems likely that the energy emitted in  $\text{H}\alpha$  is initially deposited in the massive helium shell. Modelling the line profiles of all the relevant supernovae IIb (1993J, 2007Y, 2008ax) we demonstrate the consistency of this approach with the observations. Showing that small fractions of hydrogen in massive helium shells are sufficient to cause strong  $\text{H}\alpha$  emission together with the toy model studies of the temporal evolution of hydrogen lines combined to a consistent picture of the helium rich ejecta of supernovae IIb. Although this model needs further refinement, it improves our understanding of the chaining Type II  $\rightarrow$  IIb  $\rightarrow$  Ib and allows us to understand basic properties of SNe IIb.

More insights in the ejecta of supernovae IIb are provided by the nebular model of supernova 2008ax derived in Section 6. It is the only three-dimensional nebular model of a supernova available in the literature and can be used to obtain information about the core geometry of core-collapse supernovae with unprecedented richness of detail. We

---

found evidence for the separation of helium and the heavier elements in the core and a deformation of the innermost ejecta in the polar direction. These findings can be compared to hydrodynamical core-collapse models directly. For the first time the helium mass of a supernova IIb is derived from nebular observations. In addition the mass fractions of several elements like oxygen are derived, which can hardly be obtained from other methods. Since the nebular modelling becomes increasingly uncertain in the outer regions a complementary study of supernova 2008ax by means of early time modelling would be useful. Still, since there seems to be a sharp density break at the outer boundary of the helium rich layer, the nebular model obtained in Section 6 likely captures most of the mass and kinetic energy of supernova 2008ax. This makes nebular modelling an important tool to study the total mass and kinetic energy of this supernova, independent from the various light-curve based approaches found in the literature. Good agreement between the two methods is achieved.

Finally, we propose an alternative model for generating double-peaked O [I]  $\lambda\lambda$  6300, 6364 in supernovae IIb. Although, geometry is certainly important for line-profile formation it is shown in Section 6 that H $\alpha$  absorption can split the O [I] doublet under certain conditions. From this split a hydrogen velocity can be derived, which perfectly correlates with the hydrogen velocity obtained from early time observations. Besides geometry, this is the only serious explanation for double peaked O [I] doublets in supernovae IIb. Both effects can in principle exist in parallel. However, in supernovae IIb H $\alpha$  splitting seems to be the dominant effect, which is important if one tries to infer the ejecta geometry of SNe IIb from their nebular line profiles.

Summarising, we have studied a large number of aspects of stripped-envelope core-collapse supernovae by nebular modelling in this thesis. Beside obtaining physical parameters in great number and detail, we also addressed several theoretical issues of nebular line formation. Along with some deeper understanding, also the necessity for further investigation has emerged (see Section 6 & 7). Further improvements to the nebular code seem desirable.

Most importantly, the UV transport should be treated more carefully in the future. To this point, only the recycling of UV recombination radiation and photo-ionisation of hydrogen by helium TPE are treated in an approximate way. A detailed treatment of photo-ionisation and excitation (fluorescence) is however needed, especially for SNe Type II (see Section 7). Less urgent improvements include a detailed treatment of recombination for elements other than H, He and O, the inclusion of more elements and higher ionisation states or charge exchange reactions. All these modifications could probably be implemented on a time scale of one year. If this can be done all the physics that are likely to be important in the nebular phase of all types of SNe would be treated by the nebular code.

Because of their great importance for cosmology, GRB physics and other areas of astronomy, and a rapidly growing number of new observations, it seems highly desirable to amend our understanding of supernovae by all means. Although this point is obvious, this thesis demonstrates how much can be learnt from the interpretation of nebular observations, providing the link between theory and experiments. The three-dimensional code developed in this thesis can be used in the future to further study nebular physics and supernova ejecta geometry. Another application is the calculation of nebular spectra from hydrodynamical supernova models, which allows to compare theory and observations from the explosion model perspective. Therefore, the theoretical understanding of the details of nebular line formation is a key to compare physical models with reality. Although the nebular phase has been neglected during the last decades as compared to the early phase, more attention should be paid to this field in the future.





# Bibliography

- Abadi M. G., Navarro J. F., Steinmetz M., Eke V. R., 2003, *ApJ*, 591, 499
- Aglietta M., Badino G., Bologna G., Castagnoli C., Castellina A., Dadykin V. L., Fulgione W., Galeotti P., Kalchukov F. F., 1987, *Europhysics Letters*, 3, 1321
- Aldering G., Humphreys R. M., Richmond M., 1994, *AJ*, 107, 662
- Aldrovandi S. M. V., Pequignot D., 1973, *A&A*, 25, 137
- Alpher R. A., Bethe H., Gamow G., 1948, *Phys. Rev.*, 73, 803
- Amati L., Frontera F., Guidorzi C., 2009, *A&A*, 508, 173
- Argelander F. W. A., 1864, *Astronomische Nachrichten*, 62, 273
- Arnett W. D., 1969, *A&A Suppl.*, 5, 180
- Arnett W. D., Fu A., 1989, *ApJ*, 340, 396
- Arnett W. D., Truran J. W., Woosley S. E., 1971, *ApJ*, 165, 87
- Atkins P. W., 1970, *Molecular Quantum Mechanics*. Oxford University Press, London W.1, Ely House
- Axelrod T. S., 1980, PhD thesis, AA(California Univ., Santa Cruz.)
- Axford W. I., Leer E., Skadron G., 1977, in *International Cosmic Ray Conference Vol. 11 of International Cosmic Ray Conference, The Acceleration of Cosmic Rays by Shock Waves*. pp 132–+
- Baade W., 1943, *ApJ*, 97, 119
- Baade W., 1945, *ApJ*, 102, 309
- Baade W., Burbidge G. R., Hoyle F., Burbidge E. M., Christy R. F., Fowler W. A., 1956, *PASP*, 68, 296
- Baade W., Zwicky F., 1934a, *Proceedings of the National Academy of Science*, 20, 259
- Baade W., Zwicky F., 1934b, *Proceedings of the National Academy of Science*, 20, 254
- Badnell N. R., 2006, *ApJS*, 167, 334
- Bailer-Jones C. A. L., 2009, *International Journal of Astrobiology*, 8, 213
- Barbon R., Ciatti F., Rosino L., 1979, *A&A*, 72, 287
- Barkat Z., Rakavy G., Sack N., 1967, *Physical Review Letters*, 18, 379
- Bartunov O. S., Blinnikov S. I., Pavlyuk N. N., Tsvetkov D. Y., 1994, *A&A*, 281, L53
- Bate M. R., 2009, *MNRAS*, 392, 1363
- Bates D. R., Damgaard A., 1949, *Philosophical Transactions of the Royal Society of London. Series A, Mathematical and Physical Sciences*, 242, 101
- Begelman M. C., Sarazin C. L., 1986, *ApJL*, 302, L59
- Bell K. L., Hibbert A., 1990, *J. Phys. B: At. Mol. Opt. Phys.*, 23, 2673

- Benz W., Cameron A. G. W., Press W. H., Bowers R. L., 1990, *ApJ*, 348, 647
- Berrington K. A., Kingston A. E., 1987, *J. Phys. B: At. Mol. Phys.*, 20, 6631
- Bethe H. A., 1990, *Reviews of Modern Physics*, 62, 801
- Bethe H. A., Wilson J. R., 1985, *ApJ*, 295, 14
- Bhatia A. K., Kastner S. O., 1995, *ApJS*, 96, 325
- Bionta R. M., Blewitt G., Bratton C. B., Casper D., Ciocio A., 1987, *Physical Review Letters*, 58, 1494
- Blandford R. D., Ostriker J. P., 1980, *ApJ*, 237, 793
- Blinnikov S. I., 2010, *Physics of Atomic Nuclei*, 73, 604
- Blondin J. M., Mezzacappa A., DeMarino C., 2003, *ApJ*, 584, 971
- Blondin S., Calkins M., 2008, *Central Bureau Electronic Telegrams*, 1191, 2
- Bloom J. S., Prochaska J. X., 2006, in S. S. Holt, N. Gehrels, & J. A. Nousek ed., *Gamma-Ray Bursts in the Swift Era Vol. 836 of American Institute of Physics Conference Series, Constraints on the Diverse Progenitors of GRBs from the Large-Scale Environments*. pp 473–482
- Bodansky D., Clayton D. D., Fowler W. A., 1968, *ApJS*, 16, 299
- Bode M. F., 2010, *Astronomische Nachrichten*, 331, 160
- Borst L. B., 1950, *Phys. Rev.*, 78, 807
- Bouchet P., Danziger I. J., Lucy L. B., 1991, *AJ*, 102, 1135
- Branch D., Fisher A., Nugent P., 1993, *AJ*, 106, 2383
- Branch D., Livio M., Yungelson L. R., Boffi F. R., Baron E., 1995, *PASP*, 107, 1019
- Branch D., Nomoto K., Filippenko A. V., 1991, *Comments on Astrophysics*, 15, 221
- Brandt T. D., Tojeiro R., Aubourg É., Heavens A., Jimenez R., Strauss M. A., 2010, *AJ*, 140, 804
- Brown P. J., Immler S., The Swift Satellite Team 2008, *The Astronomer's Telegram*, 1403, 1
- Brunish W. M., Truran J. W., 1982, *ApJS*, 49, 447
- Buras R., Rampp M., Janka H., Kifonidis K., 2006, *A&A*, 447, 1049
- Burbidge E. M., Burbidge G. R., Fowler W. A., Hoyle F., 1957, *Rev. Mod. Phys.*, 29, 547
- Burbidge G. R., Hoyle F., Burbidge E. M., Christy R. F., Fowler W. A., 1956, *Physical Review*, 103, 1145
- Burger J. J., Stephens S. A., Swanenburg B. N., 1970, *A&A Suppl.*, 8, 20
- Burgess A., 1965, *MmRAS*, 69, 1
- Burgess A., Seaton M. J., 1960, *MNRAS*, 120, 121
- Burke P. G., Robb W. D., 1975, *Advances in Atomic and Molecular Physics*. Vol. 11, ACADEMIC PRESS New York, 111 Fifth Avenue, New York, New York 10003
- Burles S., Nollett K. M., Turner M. S., 2001, *ApJL*, 552, L1
- Burrows A., 1987, *ApJL*, 318, L57
- Burrows A., Goshy J., 1993, *ApJL*, 416, L75+

- Burrows A., Livne E., Dessart L., Ott C. D., Murphy J., 2006, *ApJ*, 640, 878
- Burrows A., Livne E., Dessart L., Ott C. D., Murphy J., 2007, *ApJ*, 655, 416
- Burrows A., Walder R., Ott C. D., Livne E., 2005, in R. Humphreys & K. Stanek ed., *The Fate of the Most Massive Stars* Vol. 332 of *Astronomical Society of the Pacific Conference Series*, *Rotating Core Collapse and Bipolar Supernova Explosions*. pp 350–+
- Callaway J., 1994, *Atomic Data and Nuclear Data Tables*, 57, 9
- Carroll S. M., Press W. H., Turner E. L., 1992, *ARA&A*, 30, 499
- Chan K., Lingenfelter R. E., 1993, *ApJ*, 405, 614
- Chandrasekhar S., 1931, *ApJ*, 74, 81
- Chevalier R. A., 1981, *ApJ*, 251, 259
- Chevalier R. A., Fransson C., 1987, *Nature*, 328, 44
- Chevalier R. A., Soderberg A. M., 2010, *ApJL*, 711, L40
- Chita S. M., Langer N., van Marle A. J., García-Segura G., Heger A., 2008, *A&A*, 488, L37
- Chornock R., Filippenko A. V., Li W., Marion G. H., Foley R. J., Modjaz M., Rafelski M., Becker G. D., de Vries W. H., Garnavich P., Jorgenson R. A., Lynch D. K., Malec A. L., 2010, *ArXiv e-prints*
- Chugai N. N., 1987, *Astrophysics*, 26, 53
- Chugai N. N., 1991, *MNRAS*, 250, 513
- Chugai N. N., 1992, *Soviet Astronomy Letters*, 18, 239
- Chung S., Lin C. C., Lee E. T. P., 1991, *Phys. Rev. A*, 43, 3433
- Clark D. H., Stephenson F. R., 1977, *The Historical Supernovae*. Pergamon Press GmbH, 6242 Kronberg-Taunus, Pferdstrasse 1, Frankfurt-am-Main
- Clifford F. E., Tayler R. J., 1965, *MEMRAS*, 69, 21
- Clocchiatti A., Suntzeff N. B., Phillips M. M., Filippenko A. V., Turatto M., Benetti S., Cappellaro E., 2001, *ApJ*, 553, 886
- Clocchiatti A., Wheeler J. C., 1997, in Ruiz-Lapuente P., Canal R., Isern J., eds, *NATO ASIC Proc. 486: Thermonuclear Supernovae New perspectives on Type Ic supernovae*. pp 863–+
- Clocchiatti A., Wheeler J. C., Benetti S., Frueh M., 1996, *ApJ*, 459, 547
- Colgate S. A., 1970, *A&A Suppl.*, 8, 457
- Colgate S. A., McKee C., 1969, *ApJ*, 157, 623
- Colgate S. A., White R. H., 1966, *ApJ*, 143, 626
- Conley A., Goldhaber G., Wang L., Aldering G., Amanullah R., Commins E. D., Fadeyev V., Folatelli G., Garavini G., 2006, *ApJ*, 644, 1
- Crockett R. M., Eldridge J. J., Smartt S. J., Pastorello A., Gal-Yam A., Fox D. B., Leonard D. C., Kasliwal M. M., Mattila S., Maund J. R., Stephens A. W., Danziger I. J., 2008, *MNRAS*, 391, L5
- Curran P. A., van der Horst A. J., Wijers R. A. M. J., 2008, *MNRAS*, 386, 859

- D'Avanzo P., Salvaterra R., 2010, in A. Comastri, L. Angelini, & M. Cappi ed., American Institute of Physics Conference Series Vol. 1248 of American Institute of Physics Conference Series, GRB 090423 as the new beacon at the frontier of the Universe. pp 55–58
- de Kool M., Li H., McCray R., 1998, *ApJ*, 503, 857
- Deng J., Tominaga N., Mazzali P. A., Maeda K., Nomoto K., 2005, *ApJ*, 624, 898
- Dimai A., Migliardi M., 2005, Central Bureau Electronic Telegrams, 300, 1
- Dimai A., Villi M., 2006, Central Bureau Electronic Telegrams, 364, 1
- Drake G. W., Victor G. A., Dalgarno A., 1969, *Physical Review*, 180, 25
- Dressler A., Faber S. M., 1990, *ApJ*, 354, 13
- Drissen L., Robert C., Dutil Y., Roy J.-R., Filippenko A. V., Cappellaro E., Patat F., 1996, *IAUCIRC*, 6317, 2
- Dunkley J., Komatsu E., Nolte M. R., Spergel D. N., Larson D., Hinshaw G., Page L., Bennett C. L., Gold B., Jarosik N., Weiland J. L., 2009, *ApJS*, 180, 306
- Eisenstein D. J., Zehavi I., Hogg D. W., Scoccamarro R., Blanton M. R., Nichol R. C., Scranton R., Seo H., Tegmark M., 2005, *ApJ*, 633, 560
- Eldridge J. J., Vink J. S., 2006, *A&A*, 452, 295
- Elias J., Phillips M., Suntzeff N., 1990, *IAUCIRC*, 5080, 2
- Elmhamdi A., Danziger I. J., Cappellaro E., Della Valle M., Gouiffes C., Phillips M. M., Turatto M., 2004, *A&A*, 426, 963
- Fabian A. C., Rees M. J., van den Heuvel E. P. J., van Paradijs J., 1987, *Nature*, 328, 323
- Ferrara A., Tolstoy E., 2000, *MNRAS*, 313, 291
- Fewell M. P., 1995, *American Journal of Physics*, 63, 653
- Filippenko A. V., 1988, *AJ*, 96, 1941
- Filippenko A. V., 1991, in A. Ray & T. Velusamy ed., *Supernovae and Stellar Evolution Photometric and Spectroscopic Classification of Supernovae*. pp 34–+
- Filippenko A. V., 1997, *ARA&A*, 35, 309
- Filippenko A. V., Korth S., 1991, *IAUCIRC*, 5234, 1
- Filippenko A. V., Matheson T., Barth A. J., 1994, *AJ*, 108, 2220
- Fink M., Hillebrandt W., Röpke F. K., 2007, *A&A*, 476, 1133
- Foley R. J., Matheson T., Blondin S., Chornock R., Silverman J. M., Challis P., Clocchiatti A., Filippenko A. V., Kirshner R. P., Leibundgut B., 2009, *AJ*, 137, 3731
- Fowler W. A., 1984, *Science*, 226, 922
- Fraley G. S., 1967, PhD thesis, CALIFORNIA INSTITUTE OF TECHNOLOGY.
- Fransson C., 1994, in R. E. S. Clegg, I. R. Stevens, & W. P. S. Meikle ed., *Circumstellar Media in Late Stages of Stellar Evolution Circumstellar interaction in supernovae*. pp 120–+
- Fransson C., Björnsson C., 1998, *ApJ*, 509, 861
- Fransson C., Björnsson C., 2005, in J.-M. Marcaide & K. W. Weiler ed., *IAU Colloq. 192: Cosmic Explosions, On the 10th Anniversary of SN1993J Modeling the Radio and X-ray Emission of SN 1993J and SN 2002ap*. pp 59–+

- Fransson C., Kozma C., 1993, *ApJL*, 408, L25
- Frieman J., 2006, *IAUCIRC*, 8766, 1
- Gabrijelcic A., Benetti S., Lidman C., 1997, *IAUCIRC*, 6535, 1
- Gal-Yam A., Mazzali P., Ofek E. O., Nugent P. E., Kulkarni S. R., Kasliwal M. M., Quimby R. M., Filippenko A. V., 2009, *Nature*, 462, 624
- Galama T. J., Vreeswijk P. M., van Paradijs J., Kouveliotou C., Augusteijn T., Patat F., Heise J., in 't Zand J., Groot P. J., Wijers 1999, *A&A Suppl. Ser.*, 138, 465
- Gamezo V. N., Khokhlov A. M., Oran E. S., Chtchelkanova A. Y., Rosenberg R. O., 2003, *Science*, 299, 77
- Gamow G., Schoenberg M., 1941, *Physical Review*, 59, 539
- Garcia-Senz D., Woosley S. E., 1995, *ApJ*, 454, 895
- Gehrels N., the Swift Team 2008, *Classical and Quantum Gravity*, 25, 184005
- Gomez G., Lopez R., 1994, *AJ*, 108, 195
- Gordon W., 1929, *An.d.Phys.*, 394, 1031
- Graham J., Li W., 2004, *Central Bureau Electronic Telegrams*, 75, 1
- Grassberg E. K., Imshennik V. S., Nadyozhin D. K., 1971, *A&A Suppl.*, 10, 28
- Green L. C., Rush P. P., Chandler C. D., 1957, *ApJS*, 3, 37
- Hammer N. J., Janka H., Müller E., 2010, *ApJ*, 714, 1371
- Hamuy M., Deng J., Mazzali P. A., Morrell N. I., Phillips M. M., Roth M., Gonzalez S., Thomas-Osip J., Krzeminski W., Contreras C., 2009, *ApJ*, 703, 1612
- Hanbury Brown R., Hazard C., 1952, *Nature*, 170, 364
- Hansen B., 2004, *Physics Reports*, 399, 1
- Haymes R. C., Walraven G. D., Meegan C. A., Hall R. D., Djuth F. T., Shelton D. H., 1975, *ApJ*, 201, 593
- Heger A., Fryer C. L., Woosley S. E., Langer N., Hartmann D. H., 2003, *ApJ*, 591, 288
- Heger A., Woosley S., 2005, in V. Hill, P. François, & F. Primas ed., *From Lithium to Uranium: Elemental Tracers of Early Cosmic Evolution* Vol. 228 of *IAU Symposium*, Nucleosynthesis of pair-instability supernovae. pp 297–302
- Heger A., Woosley S. E., 2002, *ApJ*, 567, 532
- Higdon J. C., Lingenfelter R. E., Ramaty R., 1998, *ApJL*, 509, L33
- Higdon J. C., Lingenfelter R. E., Rothschild R. E., 2009, *ApJ*, 698, 350
- Hillebrandt W., Hoefflich P., Weiss A., Truran J. W., 1987, *Nature*, 327, 597
- Hillebrandt W., Hofflich P., 1989, *Reports on Progress in Physics*, 52, 1421
- Hillebrandt W., Meyer F., 1989, *A&A*, 219, L3
- Hillebrandt W., Niemeyer J. C., 2000, *ARA&A*, 38, 191
- Hirata K., Kajita T., Koshiba M., Nakahata M., Oyama Y., 1987, *Physical Review Letters*, 58, 1490
- Höflich P., 1991, *A&A*, 246, 481

- Höflich P., Wheeler J. C., Wang L., 1999, *ApJ*, 521, 179
- Homeier D., Koester D., Hagen H., Jordan S., Heber U., Engels D., Reimers D., Dreizler S., 1998, *A&A*, 338, 563
- Houck J. C., Fransson C., 1996, *ApJ*, 456, 811
- Hoyle F., Fowler W. A., 1960, *ApJ*, 132, 565
- Hubble E., 1929, *Proceedings of the National Academy of Science*, 15, 168
- Hulse R. A., Taylor H. J., 1974, in *Bulletin of the American Astronomical Society Vol. 6 of Bulletin of the American Astronomical Society, Discovery of a Pulsar in a Close Binary System..* pp 453–+
- Hunter D. J., Valenti S., Kotak R., Meikle W. P. S., Taubenberger S., Pastorello A., Benetti S., Stanishev V., Smartt S. J., Trundle C., Arkharov A. A., 2009, *A&A*, 508, 371
- Iben Jr. I., Tutukov A. V., 1984, *ApJS*, 54, 335
- Iben Jr. I., Tutukov A. V., 1985, *ApJS*, 58, 661
- Iocco F., Mangano G., Miele G., Pisanti O., Serpico P. D., 2009, *Physics Reports*, 472, 1
- Itagaki K., Nakano S., Puckett T., Toth D., 2006, *IAUCIRC*, 8751, 2
- Iwamoto K., Mazzali P. A., Nomoto K., Umeda H., Nakamura T., Patat F., Danziger I. J., Young T. R., Suzuki T., Shigeyama T., Augusteijn T., Doublier V., Gonzalez J., Boehnhardt H., 1998, *Nature*, 395, 672
- Janka H., 2001, *A&A*, 368, 527
- Janka H., Langanke K., Marek A., Martínez-Pinedo G., Müller B., 2007, *Physics Reports*, 442, 38
- Jeffery D. J., 1993, *ApJ*, 415, 734
- Jin C. C., Cao Y., Bian F.-Y., Lou Y.-Q., Wang X. F., Wu Y., Yang Y., Newton J., Puckett T., Lee N., Li W., Joubert N., Madison D. R., Mostardi R., 2007, *IAUCIRC*, 8798, 1
- Johnson III W. N., Harnden Jr. F. R., Haymes R. C., 1972, *ApJL*, 172, L1+
- Julienne P., Davis J., Oran E., 1974, *J. Geophys. Res.*, 79, 2540
- Jullo E., Natarajan P., Kneib J., D’Aloisio A., Limousin M., Richard J., Schimd C., 2010, *Science*, 329, 924
- Kay L. E., Halpern J. P., Leighly K. M., Filippenko A. V., Barth A., Moran E. C., Leonard D. C., Magalhães A. M., Heathcote S., 1998, in *Bulletin of the American Astronomical Society Vol. 30 of Bulletin of the American Astronomical Society, Spectropolarimetry of the Peculiar Type IC Supernovae 1998bw and 1997ef.* pp 1323–+
- Keil W., Janka H., Mueller E., 1996, *ApJL*, 473, L111+
- Khokhlov A. M., 1991, *A&A*, 245, 114
- Komatsu E., Dunkley J., Nolte M. R., Bennett C. L., Gold B., Hinshaw G., Jarosik N., Larson D., Limon M., Page L., Spergel D. N., Halpern M., Hill R. S., Kogut A., Meyer S. S., Tucker G. S., Weiland J. L., Wollack E., Wright E. L., 2009, *ApJS*, 180, 330
- Kotak R., Vink J. S., 2006, *A&A*, 460, L5
- Kotake K., Sawai H., Yamada S., Sato K., 2004, *ApJ*, 608, 391
- Kouveliotou C., Meegan C. A., Fishman G. J., Bhat N. P., Briggs M. S., Koshut T. M., Paciesas W. S., Pendleton G. N., 1993, *ApJL*, 413, L101
- Kowalski M., Rubin D., Aldering G., Agostinho R. J., Amadon A., Amanullah R., Balland C., Barbary K., Blanc G., 2008, *ApJ*, 686, 749

- Kozma C., Fransson C., 1998, *ApJ*, 497, 431
- Krause O., Tanaka M., Usuda T., Hattori T., Goto M., Birkmann S., Nomoto K., 2008, *Nature*, 456, 617
- Larson R. B., 1985, *MNRAS*, 214, 379
- Leibundgut B., 2000, *AAPR*, 10, 179
- Leibundgut B., 2001, *ARA&A*, 39, 67
- Lemaître G., 1931, *Nature*, 127, 706
- Lennon M. A., Bell K. L., Gilbody H. B., Hughes J. G., Kingston M. J., Murray M. J., Smith F. J., 1988, *J.Phys.Chem.Ref.Data*, 17, 1285
- Leventhal M., MacCallum C. J., Stang P. D., 1978, *ApJL*, 225, L11
- Li H., McCray R., 1992, *ApJ*, 387, 309
- Li H., McCray R., 1993a, *ApJ*, 405, 730
- Li H., McCray R., 1993b, in *Bulletin of the American Astronomical Society Vol. 25 of Bulletin of the American Astronomical Society, The HeI Emission Lines of SN 1987A*. pp 1349–+
- Li H., McCray R., 1995, *ApJ*, 441, 821
- Li H., McCray R., 1996, *ApJ*, 456, 370
- Li W., Filippenko A. V., Treffers R. R., Riess A. G., Hu J., Qiu Y., 2001, *ApJ*, 546, 734
- Liebendörfer M., Rampp M., Janka H., Mezzacappa A., 2005, *ApJ*, 620, 840
- Lingenfelter R. E., Higdon J. C., Ramaty R., 2000, in R. A. Mewaldt, J. R. Jokipii, M. A. Lee, E. Möbius, & T. H. Zurbuchen ed., *Acceleration and Transport of Energetic Particles Observed in the Heliosphere Vol. 528 of American Institute of Physics Conference Series, Cosmic ray acceleration in superbubbles and the composition of cosmic rays*. pp 375–382
- Lingenfelter R. E., Higdon J. C., Rothschild R. E., 2009, *Physical Review Letters*, 103, 031301
- Livne E., Glasner A. S., 1990, *ApJ*, 361, 244
- Loewenstein M., 2006, *ApJ*, 648, 230
- Lotz W., 1970, *J. Opt. Soc. Am.*, 60, 206
- Lucy L. B., 1991, *ApJ*, 383, 308
- Lucy L. B., Danziger I. J., Gouiffes C., Bouchet P., 1989, in G. Tenorio-Tagle, M. Moles, & J. Melnick ed., *IAU Colloq. 120: Structure and Dynamics of the Interstellar Medium Vol. 350 of Lecture Notes in Physics*, Berlin Springer Verlag, *Dust Condensation in the Ejecta of SN 1987 A*. pp 164–+
- Lundmark K., 1919, *Astronomische Nachrichten*, 209, 369
- Lundqvist P., Fransson C., 1996, *ApJ*, 464, 924
- Lyutikov M., 2009, *ArXiv e-prints*: 0911.0349v3
- Maeda K., Kawabata K., Mazzali P. A., Tanaka M., Valenti S., Nomoto K., Hattori T., 2008, *Science*, 319, 1220
- Maeda K., Kawabata K., Mazzali P. A., Tanaka M., Valenti S., Nomoto K., Hattori T., Deng J., Pian E., Taubenberger S., Iye M., Matheson T., Filippenko 2008, *Science*, 319, 1220
- Maeda K., Kawabata K., Tanaka M., Nomoto K., Tominaga N., Hattori T., Minezaki T., Kuroda T., Suzuki T., Deng J., Mazzali P. A., Pian E., 2007, *ApJL*, 658, L5

- Maeda K., Nakamura T., Nomoto K., Mazzali P. A., Patat F., Hachisu I., 2002, *ApJ*, 565, 405
- Maeda K., Nomoto K., 2003, *ApJ*, 598, 1163
- Maeda K., Nomoto K., Mazzali P. A., Deng J., 2006, *ApJ*, 640, 854
- Maeda K., Tanaka M., Nomoto K., Tominaga N., Kawabata K., Mazzali P. A., Umeda H., Suzuki T., Hattori T., 2007, *ApJ*, 666, 1069
- Maio U., Ciardi B., Dolag K., Tornatore L., Khochfar S., 2010, *MNRAS*, 407, 1003
- Malesani D., Tagliaferri G., Chincarini G., Covino S., Della Valle M., Fugazza D., Mazzali P. A., Zerbi F. M., D'Avanzo 2004, *ApJL*, 609, L5
- Manchester R. N., 2007, in S. Immler, K. Weiler, & R. McCray ed., *Supernova 1987A: 20 Years After: Supernovae and Gamma-Ray Bursters Vol. 937 of American Institute of Physics Conference Series, Searching for a Pulsar in SN1987A*. pp 134–143
- Mannucci F., 2005, in M. Turatto, S. Benetti, L. Zampieri, & W. Shea ed., *1604-2004: Supernovae as Cosmological Lighthouses Vol. 342 of Astronomical Society of the Pacific Conference Series, Rates and Progenitors of Type Ia Supernovae*. pp 140–+
- Marek A., Janka H., 2009, *ApJ*, 694, 664
- Matheson T., 2004, in Höflich P., Kumar P., Wheeler J. C., eds, *Cosmic explosions in three dimensions The first direct Supernova/GRB connection: GRB 030329 / SN 2003dh*. pp 351–+
- Matheson T., Filippenko A. V., Barth A. J., Ho L. C., Leonard D. C., Bershadsky M. A., Davis M., Finley D. S., Fisher D., González R. A., Hawley S. L., Koo D. C., Li W., Lonsdale C. J., Schlegel D., Smith H. E., Spinrad H., Wirth G. D., 2000, *AJ*, 120, 1487
- Matheson T., Filippenko A. V., Li W., Leonard D. C., Shields J. C., 2001, *AJ*, 121, 1648
- Mattila S., Lundqvist P., Gröningsson P., Meikle P., Stathakis R., Fransson C., Cannon R., 2010, *ApJ*, 717, 1140
- Maund J. R., Smartt S. J., 2009, *Science*, 324, 486
- Maund J. R., Smartt S. J., Kudritzki R. P., Podsiadlowski P., Gilmore G. F., 2004, *Nature*, 427, 129
- Maund J. R., Smartt S. J., Schweizer F., 2005, *ApJL*, 630, L33
- Maund J. R., Wheeler J. C., Patat F., Wang L., Baade D., Höflich P. A., 2007, *ApJ*, 671, 1944
- Maurer J. I., Mazzali P. A., 2010, *MNRAS* accepted
- Maurer J. I., Mazzali P. A., Deng J., Filippenko A. V., Hamuy M., Kirshner R. P., Matheson T., 2010, *MNRAS*, 402, 161
- Maurer J. I., Mazzali P. A., Taubenberger S., Hachinger S., 2010, *MNRAS* accepted
- Mayall N. U., Oort J. H., 1942, *PASP*, 54, 95
- Mazzali P. A., Deng J., Hamuy M., Nomoto K., 2009, *ApJ*, 703, 1624
- Mazzali P. A., Deng J., Maeda K., Nomoto K., Filippenko A. V., Matheson T., 2004, *ApJ*, 614, 858
- Mazzali P. A., Deng J., Maeda K., Nomoto K., Umeda H., Hatano K., Iwamoto K., Yoshii Y., Kobayashi Y., Minezaki T., Doi M., Enya K., Tomita H., Smartt S. J., 2002, *ApJL*, 572, L61
- Mazzali P. A., Deng J., Nomoto K., Sauer D. N., Pian E., Tominaga N., Tanaka M., Maeda K., Filippenko A. V., 2006, *Nature*, 442, 1018



- Mazzali P. A., Kawabata K. S., Maeda K., Foley R. J., Nomoto K., Deng J., Suzuki T., Iye M., Kashikawa N., Ohya Y., Filippenko A. V., Qiu Y., Wei J., 2007, *ApJ*, 670, 592
- Mazzali P. A., Kawabata K. S., Maeda K., Nomoto K., Filippenko A. V., Ramirez-Ruiz E., Benetti S., Pian E., Deng J., Tominaga N., Ohya Y., Iye M., Foley R. J., 2005, *Science*, 308, 1284
- Mazzali P. A., Maurer I., Valenti S., Kotak R., Hunter D., 2010, *MNRAS*, pp 1078–+
- Mazzali P. A., Nomoto K., Cappellaro E., Nakamura T., Umeda H., Iwamoto K., 2001, *ApJ*, 547, 988
- Mazzali P. A., Nomoto K., Deng J., Maeda K., Tominaga N., 2005, in M. Turatto, S. Benetti, L. Zampieri, & W. Shea ed., 1604-2004: Supernovae as Cosmological Lighthouses Vol. 342 of *Astronomical Society of the Pacific Conference Series*, The Properties of Hypernovae in Gamma Ray Bursts. pp 366–+
- Mazzali P. A., Nomoto K., Patat F., Maeda K., 2001, *ApJ*, 559, 1047
- Mazzali P. A., Valenti S., Della Valle M., Chincarini G., Sauer D. N., Benetti S., Pian E., Piran T., D'Elia V., Elias-Rosa N., Margutti R., Pasotti F., Antonelli 2008, *Science*, 321, 1185
- McCray R., 1993, *ARA&A*, 31, 175
- McNaught R. H., della Valle M., Pasquini L., 1991, *IAUCIRC*, 5178, 1
- Meikle W. P. S., Spyromilio J., Varani G., Allen D. A., 1989, *MNRAS*, 238, 193
- Mészáros P., 2006, *Reports on Progress in Physics*, 69, 2259
- Meyer F., 1997, *MNRAS*, 285, L11
- Meynet G., Maeder A., 2005, *A&A*, 429, 581
- Milisavljevic D., Fesen R. A., Gerardy C. L., Kirshner R. P., Challis P., 2010, *ApJ*, 709, 1343
- Milne P. A., The L., Leising M. D., 1999, *ApJS*, 124, 503
- Minkowski R., 1940, *PASP*, 52, 206
- Minkowski R., 1941, *PASP*, 53, 224
- Miyaji S., Nomoto K., Yokoi K., Sugimoto D., 1980, *PASJ*, 32, 303
- Modjaz M., Kirshner R. P., Blondin S., Challis P., Matheson T., 2008, *ApJL*, 687, L9
- Modjaz M., Li W., Butler N., Chornock R., Perley D., Blondin S., Bloom J. S., Filippenko A. V., Kirshner R. P., Kocevski D., Poznanski D., Hicken M., Foley 2009, *ApJ*, 702, 226
- Moiseenko S. G., Bisnovatyi-Kogan G. S., Ardeljan N. V., 2006, *MNRAS*, 370, 501
- Monard L. A. G., 2006, *IAUCIRC*, 8666, 2
- Monard L. A. G., Quimby R., Gerardy C., Hoefflich P., Wheeler J. C., Chen Y.-T., Smith H. J., Bauer A., 2004, *IAUCIRC*, 8454, 1
- Moriya T., Tominaga N., Tanaka M., Maeda K., Nomoto K., 2010, *ApJL*, 717, L83
- Morris T., Podsiadlowski P., 2007, *Science*, 315, 1103
- Mott N. F., Massey H. S. W., 1950, *The Theory Of Atomic Collisions*. Oxford University Press, Amen House, London E.C. 4
- Mukhanov V., 2005, *Physical Foundations of Cosmology*. Cambridge University Press, The Edinburgh Building, Cambridge CB2 2RU, UK

- Muller E., 1990, *Journal of Physics G Nuclear Physics*, 16, 1571
- Nagataki S., 2009, *ApJ*, 704, 937
- Nahar S. N., 2005, *ApJS*, 158, 80
- Nakamura T., Maeda K., Iwamoto K., Suzuki T., Nomoto K., Mazzali P. A., Turatto M., Danziger I. J., Patat F., 2000, in Martens P. C. H., Tsuruta S., Weber M. A., eds, *Highly Energetic Physical Processes and Mechanisms for Emission from Astrophysical Plasmas Vol. 195 of IAU Symposium, Hypernovae: SNe 1997ef, 1998bw, and 1997cy*. pp 347–+
- Nakano S., Aoki M., Kushida R., Kushida Y., Benetti S., Turatto M., Augusteijn T., Reduzzi L., Clocchiatti A., 1996, *IAUCIRC*, 6454, 1
- Nakano S., Aoki M., Kushida Y., Kushida R., Suntzeff N. B., Clocchiatti A., Phillips M. M., Kim D.-W., Covarrubias R., Garnavich P., Kirshner R., Berlind P., 1997, *IAUCIRC*, 6552, 1
- Nava L., Ghisellini G., Ghirlanda G., Tavecchio F., Firmani C., 2006, *A&A*, 450, 471
- Niemeyer J. C., Hillebrandt W., 1995, *ApJ*, 452, 769
- Niemeyer J. C., Hillebrandt W., Woosley S. E., 1996, *ApJ*, 471, 903
- Nomoto K., 1982a, *ApJ*, 257, 780
- Nomoto K., 1982b, *ApJ*, 253, 798
- Nomoto K., 1984, *ApJ*, 277, 791
- Nomoto K., 1987, *ApJ*, 322, 206
- Nomoto K., Hashimoto M., 1986, *Progress in Particle and Nuclear Physics*, 17, 267
- Nomoto K., Iwamoto K., Suzuki T., Pols O. R., Yamaoka H., Hashimoto M., Hoflich P., van den Heuvel E. P. J., 1996, in J. van Paradijs, E. P. J. van den Heuvel, & E. Kuulkers ed., *Compact Stars in Binaries Vol. 165 of IAU Symposium, The Origin of Type Ib-Ic-IIb-III Supernovae and Binary Star Evolution*. pp 119–+
- Nomoto K., Kamiya Y., Nakasato N., Hachisu I., Kato M., 2009, in G. Giobbi, A. Tornambe, G. Raimondo, M. Limongi, L. A. Antonelli, N. Menci, & E. Brocato ed., *American Institute of Physics Conference Series Vol. 1111 of American Institute of Physics Conference Series, Progenitors of Type Ia Supernovae: Single Degenerate and Double Degenerates*. pp 267–276
- Nomoto K., Kondo Y., 1991, *ApJL*, 367, L19
- Nomoto K., Moriya T., Tominaga N., 2010, in K. Cunha, M. Spite, & B. Barbuy ed., *IAU Symposium Vol. 265 of IAU Symposium, Nucleosynthesis of the Elements in Faint Supernovae and Hypernovae*. pp 34–41
- Nomoto K., Shigeyama T., Filippenko A. V., 1990 Vol. 22 of *Bulletin of the American Astronomical Society, A Low Mass Helium Star Model for the Type Ic Supernova 1987M*. pp 1221–+
- Nomoto K., Shigeyama T., Kumaga S., Hashimoto M., 1988, *Proceedings of the Astronomical Society of Australia*, 7, 490
- Nomoto K., Sugimoto D., Neo S., 1976, *A&A Suppl.*, 39, L37
- Nomoto K., Suzuki T., Shigeyama T., Kumagai S., Yamaoka H., Saio H., 1993, *Nature*, 364, 507
- Nordhaus J., Burrows A., Almgren A., Bell J., 2010, *ArXiv e-prints*
- Nugent P. E., 2007, *Central Bureau Electronic Telegrams*, 929, 1
- Nussbaumer H., Storey P. J., 1983, *A&A*, 126, 75

- Nymark T. K., Chandra P., Fransson C., 2009, *A&A*, 494, 179
- Ober W. W., El Eid M. F., Fricke K. J., 1983, *A&A*, 119, 61
- Oppenheimer J. R., Volkoff G. M., 1939, *Physical Review*, 55, 374
- Paczynski B., 1973, *A&A*, 26, 291
- Pakmor R., Kromer M., Röpke F. K., Sim S. A., Ruiter A. J., Hillebrandt W., 2010, *Nature*, 463, 61
- Parisky X., Li W., 2007, *Central Bureau Electronic Telegrams*, 1158, 1
- Pastorello A., Kasliwal M. M., Crockett R. M., Valenti S., Arbour R., Itagaki K., Kaspi S., Gal-Yam A., Smartt S. J., Griffith R., Maguire K., Ofek E. O., Seymour N., 2008, *MNRAS*, 389, 955
- Pastorello A., Mattila S., Zampieri L., Della Valle M., Smartt S. J., Valenti S., Agnoletto I., 2008, *MNRAS*, 389, 113
- Patat F., Cappellaro E., Danziger J., Mazzali P. A., Sollerman J., Augusteijn T., Brewer J., Doublier V., Gonzalez J. F., Hainaut O., Lidman C., Leibundgut B., Nomoto K., Nakamura T., 2001, *ApJ*, 555, 900
- Patat F., Chugai N., Mazzali P. A., 1995, *A&A*, 299, 715
- Peebles P. J. E., 1966, *ApJ*, 146, 542
- Pequignot D., 1990, *A&A*, 231, 499
- Perlmutter S., Aldering G., Deustua S., Fabbro S., Goldhaber G., Groom D. E., Kim A. G., 1997, in *Bulletin of the American Astronomical Society Vol. 29 of Bulletin of the American Astronomical Society, Cosmology From Type IA Supernovae: Measurements, Calibration Techniques, and Implications*, pp 1351–+
- Perlmutter S., Aldering G., Goldhaber G., Knop R. A., Nugent P., Castro P. G., Deustua S., Fabbro S., Goobar A., 1999, *ApJ*, 517, 565
- Perlmutter S., Pennypacker C., Carlson S., Marvin H., Muller R., Smith C., 1990, *IAUCIRC*, 5087, 1
- Phillips M. M., 1993, *ApJL*, 413, L105
- Phillips M. M., Lira P., Suntzeff N. B., Schommer R. A., Hamuy M., Maza J., 1999, *AJ*, 118, 1766
- Pian E., Mazzali P. A., Masetti N., Ferrero P., Klose S., Palazzi E., Ramirez-Ruiz E., Woosley S. E., Kouveliotou C., Deng J., Filippenko A. V., Foley R. J., Fynbo J. P. U., 2006, *Nature*, 442, 1011
- Piran T., 2004, *Reviews of Modern Physics*, 76, 1143
- Podsiadlowski P., Joss P. C., Rappaport S., 1990, *A&A*, 227, L9
- Podsiadlowski P., Mazzali P., Lesaffre P., Han Z., Förster F., 2008, *New Astronomy Review*, 52, 381
- Pollas C., Maury A., 1991, *IAUCIRC*, 5200, 1
- Prochaska J. X., Bloom J. S., Chen H., Foley R. J., Perley D. A., Ramirez-Ruiz E., Granot J., Lee W. H., Pooley D., Alatalo K., Hurley K., 2006, *ApJ*, 642, 989
- Puckett T., Langoussis A., Garradd G. J., 2000, *IAUCIRC*, 7530, 1
- Puckett T., Orff T., Madison D., Li W., Itagaki K., Nakano S., Newton J., Kadota K., 2007, *IAUCIRC*, 8792, 2
- Pugh H., Li W., Manzini F., Behrend R., 2004, *IAUCIRC*, 8452, 2
- Quimby R., Gerardy C., Hoefflich P., Wheeler J. C., Shetrone M., Riley V., McGaha J., Kadota K., Nakano S., 2004, *IAUCIRC*, 8446, 1

- Quimby R., Odewahn S. C., Terrazas E., Rau A., Ofek E. O., 2007, *Central Bureau Electronic Telegrams*, 953, 1
- Racah G., 1942, *Phys. Rev.*, 62, 438
- Racusin J. L., Liang E., Burrows D. N., Falcone A., Morris D. C., Zhang B. B., Zhang B., 2008, in M. Galassi, D. Palmer, & E. Fenimore ed., *American Institute of Physics Conference Series Vol. 1000 of American Institute of Physics Conference Series, Swift X-ray Afterglows and the Missing Jet Break Problem*. pp 196–199
- Ralchenko Y., Janev R. K., Kato T., Fursa D. V., Bray I., de Heer F. J., 2008, *Atomic Data and Nuclear Data Tables*, 94, 603
- Ramaty R., Lingenfelter R. E., 1979, *Nature*, 278, 127
- Rampp M., Janka H., 2000, *ApJL*, 539, L33
- Rest A., Welch D. L., Suntzeff N. B., Oaster L., Lanning H., Olsen K., Smith R. C., Becker A. C., Bergmann M., Challis P., 2008, *ApJL*, 681, L81
- Rhoads J. E., 1998, in C. A. Meegan, R. D. Preece, & T. M. Koshut ed., *Gamma-Ray Bursts, 4th Huntsville Symposium Vol. 428 of American Institute of Physics Conference Series, Afterglows as diagnostics of gamma-ray burst beaming*. pp 699–703
- Riess A. G., Filippenko A. V., Challis P., Clocchiatti A., Diercks A., Garnavich P. M., Gilliland R. L., Hogan C. J., 1998, *AJ*, 116, 1009
- Riess A. G., Press W. H., Kirshner R. P., 1995, *ApJL*, 438, L17
- Riess A. G., Strolger L., Casertano S., Ferguson H. C., Mobasher B., Gold B., Challis P. J., Filippenko A. V., Jha S., Li W., 2007, *ApJ*, 659, 98
- Robertson B., Yoshida N., Springel V., Hernquist L., 2004, *ApJ*, 606, 32
- Roming P. W. A., Pritchard T. A., Brown P. J., Holland S. T., Immler S., Stockdale C. J., Weiler K. W., Panagia N., Van Dyk S. D., Hoversten E. A., Milne P. A., Oates S. R., Russell B., Vandrevala C., 2009, *ApJL*, 704, L118
- Rowan-Robinson M., 1985, *The cosmological distance ladder: Distance and time in the universe*
- Rozsnyai B. F., Jacobs V. L., Davis J., 1980, *Phys. Rev. A*, 21, 1798
- Ruiz-Lapuente P., Lucy L. B., 1992, *ApJ*, 400, 127
- Rybicki G. B., Hummer D. G., 1978, *ApJ*, 219, 654
- Rybicki G. B., Lightman A. P., 1979, *Radiative Processes in Astrophysics*. WILEY - INTERSCIENCE PUBLICATION, US, New York
- Ryder S. D., Murrowood C. E., Stathakis R. A., 2006, *MNRAS*, 369, L32
- Sahu D. K., Tanaka M., Anupama G. C., Gurugubelli U. K., Nomoto K., 2009, *ApJ*, 697, 676
- Saio H., Nomoto K., 1985, *A&A*, 150, L21
- Saio H., Nomoto K., 1998, *ApJ*, 500, 388
- Saio H., Nomoto K., 2004, *ApJ*, 615, 444
- Saio H., Nomoto K., Kato M., 1988, *ApJ*, 331, 388
- Sauer D. N., Mazzali P. A., Deng J., Valenti S., Nomoto K., Filippenko A. V., 2006, *MNRAS*, 369, 1939
- Savage B. D., Mathis J. S., 1979, *ARA&A*, 17, 73

- Scannapieco C., Tissera P. B., White S. D. M., Springel V., 2007, in A. Vallenari, R. Tantalò, L. Portinari, & A. Moretti ed., *From Stars to Galaxies: Building the Pieces to Build Up the Universe* Vol. 374 of *Astronomical Society of the Pacific Conference Series*, *Supernova Feedback and the Formation of Disk Galaxies*. pp 475–+
- Scannapieco E., Bildsten L., 2005, *ApJL*, 629, L85
- Schlegel D. J., Finkbeiner D. P., Davis M., 1998, *ApJ*, 500, 525
- Schlier O., 1935, *Astronomische Nachrichten*, 254, 181
- Schmidt B., Salvo M., Wood P., 2005, *IAUCIRC*, 8472, 2
- Scholz T. T., Walters H. R. J., Burke P. J., Scott M. P., 1990, *MNRAS*, 242, 692
- Schramm D. N., Turner M. S., 1998, *Rev. Mod. Phys.*, 70, 303
- Schwarzschild K., 1916, *Abh. Konigl. Preuss. Akad. Wissenschaften Jahre 1906,92*, Berlin, 1907, pp 189–196
- Seaton M. J., 1958, *MNRAS*, 118, 504
- Shen K. J., Kasen D., Weinberg N. N., Bildsten L., Scannapieco E., 2010, *ApJ*, 715, 767
- Shigeyama T., Nomoto K., 1990, *ApJ*, 360, 242
- Silverman J. M., Mazzali P., Chornock R., Filippenko A. V., Clocchiatti A., Phillips M. M., Ganeshalingam M., Foley R. J., 2009, *PASP*, 121, 689
- Singer D., Li W., 2004, *IAUCIRC*, 8299, 1
- Smith N., Li W., Foley R. J., Wheeler J. C., Pooley D., Chornock R., Filippenko A. V., Silverman J. M., Quimby R., Bloom J. S., Hansen C., 2007, *ApJ*, 666, 1116
- Sobolev V. V., 1960, *Moving envelopes of stars*
- Soderberg A. M., Chakraborti S., Pignata G., Chevalier R. A., Chandra P., Ray A., Wieringa M. H., Copete A., Chaplin V., 2010, *Nature*, 463, 513
- Soderberg A. M., Chevalier R. A., Kulkarni S. R., Frail D. A., 2006, *ApJ*, 651, 1005
- Spergel D. N., Verde L., Peiris H. V., Komatsu E., Nolte M. R., Bennett C. L., Halpern M., Hinshaw G., Jarosik N., Kogut A., Limon M., Meyer S. S., Page L., Tucker G. S., Weiland J. L., Wollack E., Wright E. L., 2003, *ApJS*, 148, 175
- Storey P. J., Hummer D. G., 1995, *MNRAS*, 272, 41
- Stritzinger M., Mazzali P., Phillips M. M., Immler S., Soderberg A., Sollerman J., Boldt L., Braithwaite J., Brown P., 2009, *ApJ*, 696, 713
- Stritzinger M., Mazzali P. A., Sollerman J., Benetti S., 2006, *A&A*, 460, 793
- Sullivan M., Conley A., Howell D. A., Neill J. D., Astier P., Balland C., Basa S., Carlberg R. G., Fouchez D., Guy J., Hardin D., Hook I. M., Pain R., 2010, *MNRAS*, 406, 782
- Suntzeff N. B., Phillips M. M., Depoy D. L., Elias J. H., Walker A. R., 1991, *AJ*, 102, 1118
- Suzuki A., Shigeyama T., 2010, *ApJ*, 719, 881
- Suzuki T., Nomoto K., 1995, *ApJ*, 455, 658
- Svensson K. M., Levan A. J., Tanvir N. R., Fruchter A. S., Strolger L., 2010, *MNRAS*, 405, 57
- Takiwaki T., Kotake K., Sato K., 2009, *ApJ*, 691, 1360

- Tanaka M., Maeda K., Mazzali P. A., Nomoto K., 2007, *ApJL*, 668, L19
- Taubenberger S., Navasardyan H., Maurer J. I., Zampieri L., Chugai N. N., Benetti S., X A., Y B., Z C., 2010, submitted to *MNRAS*
- Taubenberger S., Pastorello A., Mazzali P. A., Valenti S., Pignata G., Sauer D. N., Arbey A., Bärnbantner O., Benetti S., Della Valle A., Deng 2006, *MNRAS*, 371, 1459
- Taubenberger S., Pastorello A., Mazzali P. A., Witham A., Guijarro A., 2005, *Central Bureau Electronic Telegrams*, 305, 1
- Taubenberger S., Valenti S., Benetti S., Cappellaro E., Della Valle M., Elias-Rosa N., Hachinger S., 2009, *MNRAS*, 397, 677
- Thompson T. A., Burrows A., Pinto P. A., 2003, *ApJ*, 592, 434
- Tokarz S., Garnavich P., Geller M., Kurtz M., Berlind P., Prosser C., 1995, *IAUCIRC*, 6271, 1
- Tolman R. C., 1934, *Relativity, Thermodynamics, and Cosmology*
- Tominaga N., Umeda H., Maeda K., Nomoto K., Iwamoto N., 2008, in L. K. Hunt, S. Madden, & R. Schneider ed., *IAU Symposium Vol. 255 of IAU Symposium, Supernova Nucleosynthesis in the early universe*. pp 189–193
- Truran J. W., Arnett W. D., Cameron A. G. W., 1967, *Canadian Journal of Physics*, 45, 2315
- Truran J. W., Cameron A. G. W., 1971, *A&A Suppl.*, 14, 179
- Tsvetkov D. Y., Volkov I. M., Baklanov P., Blinnikov S., Tuchin O., 2009, *Peremennye Zvezdy*, 29, 2
- Tsvetkov Y. D., 1986, *Pis ma Astronomicheskii Zhurnal*, 12, 784
- Turatto M., Benetti S., Pastorello A., 2007, in S. Immler, K. Weiler, & R. McCray ed., *Supernova 1987A: 20 Years After: Supernovae and Gamma-Ray Bursters Vol. 937 of American Institute of Physics Conference Series, Supernova classes and subclasses*. pp 187–197
- Umeda H., Nomoto K., 2008, *ApJ*, 673, 1014
- Utrobin V., 1994, *A&A*, 281, L89
- Valenti S., Benetti S., Cappellaro E., Patat F., Mazzali P., Turatto M., Hurley K., Maeda K., Gal-Yam A., Foley R. J., Filippenko A. V., Pastorello A., Challis 2008, *MNRAS*, 383, 1485
- Valenti S., Elias-Rosa N., Taubenberger S., Stanishev V., Agnoletto I., Sauer D., Cappellaro E., Pastorello A., Benetti 2008, *ApJL*, 673, L155
- Valenti S., Pastorello A., Cappellaro E., Benetti S., Mazzali P. A., Manteca J., Taubenberger S., Elias-Rosa N., Ferrando 2009, *Nature*, 459, 674
- van Dyk S. D., Weiler K. W., Sramek R. A., Rupen M. P., Panagia N., 1994, *ApJL*, 432, L115
- van Regemorter H., 1962, *ApJ*, 136, 906
- Vanhala H. A. T., Cameron A. G. W., 1998, *ApJ*, 508, 291
- Wallace R. K., Woosley S. E., 1981, *ApJS*, 45, 389
- Wallerstein G., Iben I., Parker P., Boesgaard A. M., Hale G. M., Champagne A. E., Barnes C. A., Käppeler F., Smith V. V., Hoffman R. D., Timmes F. X., Sneden C., Boyd R. N., Meyer B. S., Lambert D. L., 1997, *Rev. Mod. Phys.*, 69, 995
- Wang X., Li Z., Waxman E., Mészáros P., 2007, *ApJ*, 664, 1026
- Waxman E., Mészáros P., Campana S., 2007, *ApJ*, 667, 351

- Webbink R. F., 1984, *ApJ*, 277, 355
- Wheeler J. C., 1977, *A&A Suppl.*, 50, 125
- Wheeler J. C., Harkness R. P., 1986, in B. F. Madore & R. B. Tully ed., *NATO ASIC Proc. 180: Galaxy Distances and Deviations from Universal Expansion Physical models of supernovae and the distance scale.* pp 45–54
- Whelan J., Iben Jr. I., 1973, *ApJ*, 186, 1007
- White M., 1998, *ApJ*, 506, 495
- White S. D. M., Rees M. J., 1978, *MNRAS*, 183, 341
- Whittaker E. T., Watson G. N., 1958, *A course of modern analysis.* University Press, Cambridge
- Wiggins D. J. R., Sharpe G. J., Falle S. A. E. G., 1998, *MNRAS*, 301, 405
- Williams A., Martin R., Germany L., Schmidt B., Stathakis R., Johnston H., 1996, *IAUCIRC*, 6351, 1
- Wilson J. R., Mathews G. J., Dalhed H. E., 2005, *ApJ*, 628, 335
- Wilson J. R., Mayle R., Woosley S. E., Weaver T., 1986, *Annals of the New York Academy of Sciences*, 470, 267
- Wood-Vasey W. M., Chassagne R., 2003, *IAUCIRC*, 8082, 1
- Woosley S., Janka T., 2005, *Nature Physics*, 1, 147
- Woosley S. E., 1988, *ApJ*, 330, 218
- Woosley S. E., Blinnikov S., Heger A., 2007, *Nature*, 450, 390
- Woosley S. E., Bloom J. S., 2006, *ARA&A*, 44, 507
- Woosley S. E., Eastman R. G., Weaver T. A., Pinto P. A., 1994, *ApJ*, 429, 300
- Woosley S. E., Taam R. E., Weaver T. A., 1986, *ApJ*, 301, 601
- Woosley S. E., Weaver T. A., 1986, *ARA&A*, 24, 205
- Woosley S. E., Weaver T. A., 1994, *ApJ*, 423, 371
- Woosley S. E., Zhang W., Heger A., 2003, in G. R. Ricker & R. K. Vanderspek ed., *Gamma-Ray Burst and Afterglow Astronomy 2001: A Workshop Celebrating the First Year of the HETE Mission Vol. 662 of American Institute of Physics Conference Series, The Central Engines of Gamma-Ray Bursts.* pp 185–192
- Xu Y., McCray R., 1991, *ApJ*, 375, 190
- Yoon S., Podsiadlowski P., Rosswog S., 2007, *MNRAS*, 380, 933
- Yoshii Y., Tomita H., Kobayashi Y., Deng J., Maeda K., Nomoto K., Mazzali P. A., Umeda H., Aoki T., Doi M., Enya K., Minezaki T., Suganuma M., Peterson B. A., 2003, *ApJ*, 592, 467
- Zatsepin V. I., Sokolskaya N. V., 2006, *A&A*, 458, 1





# Publications

1. J. I. Maurer, A. L. Watts, 2008:  
Ignition latitude and the shape of Type I X-ray bursts  
MNRAS, 383, 387
2. J. I. Maurer and 11 coauthors, 2010:  
Characteristic velocities of stripped-envelope core-collapse supernova cores  
MNRAS, 402, 161
3. J. I. Maurer, P. A. Mazzali, 2010:  
Oxygen Recombination in the nebular phase of supernovae 1998bw and 2002ap  
MNRAS, 408, 947
4. J. I. Maurer, P. A. Mazzali, S. Taubenberger, S. Hachinger, 2010:  
Hydrogen and helium in the late phase of SNe I Ib  
MNRAS, accepted
5. A. L. Watts, J. I. Maurer, 2007:  
Accretion rate and the occurrence of multi-peaked X-ray bursts  
A&A, 467, 33
6. P. A. Mazzali, J. I. Maurer, S. Valenti, R. Kotak, D. Hunter, 2010:  
The Type Ic SN 2007gr: a census of the ejecta from late-time optical-infrared spectra  
MNRAS, 408, 87
7. S. Taubenberger, H. Navasardyan, J. I. Maurer and 15 coauthors, 2010:  
The He-rich Stripped-Envelope Core-Collapse Supernova 2008ax  
MNRAS, submitted
8. M. Tanaka, P. A. Mazzali, V. S. Stanishev, J. I. Maurer, W. Kerzendorf, K. Nomoto, 2010:  
Abundance stratification in Type Ia supernovae - III.  
The normal SN 2003du  
MNRAS, accepted



# Curriculum Vitae

## personal data

name: Jakob Immanuel Maurer

address: Max-Planck-Institut für Astrophysik, Karl-Schwarzschild-Straße 1, 85741 Garching

birth: 28.Apr.1982 in Munich/Germany

nationality: German citizenship

## education

Grundschule Pastetten (1988 - 1992)

Franz-Marc-Gymnasium, Markt Schwaben (1992 - 2001)

Abitur at Franz-Marc-Gymnasium, Markt Schwaben (Jun.2001)

civil service (2001 - 2002)

## academic record

study of physics at Ludwig-Maximilians-Universität (LMU) Munich/Germany (Okt.2002 - Okt.2007)

Vordiplom in physics, LMU (Apr.2004)

diploma thesis at Max-Planck-Institut für Astrophysik, Munich/Germany (Okt.2006 - Okt.2007)

Diplom in physics, LMU (Nov.2007)

PhD student at Max-Planck-Institut für Astrophysik, Garching/Germany (Nov.2007 - Nov.2010)